NEUTRON SCATTERING FROM MOLECULAR METALLIC COMPOUNDS

A thesis submitted for the degree of

Doctor of Philosophy

to the

University of Oxford

William John Stead

University College, Oxford

Trinity Term 1986

Neutron Scattering from Molecular Metallic Compounds

W.J. Stead, University College, Oxford.
D. Phil.
Trinity Term, 1986.

The alkali metal graphite intercalates and the conducting polymers polyacetylene and polypyrrole are reviewed and compared.

Polyacetylene was synthesized by Luttinger's method and doped by exposure to caesium vapour. The doped and undoped polyacetylene were characterized by neutron powder diffraction. Hydrogen absorption and subsequent pyrolysis of caesium doped polyacetylene were studied. Mass spectrum analysis of the gases evolved at 300°C showed methane and other alkanes, indicating H_2 addition to the polymer chain followed by methane elimination. The graphite intercalates C_8Cs and $C_{24}Cs$ reacted irreversibly with acetylene, neutron powder diffraction indicating graphite and two new substances. Mass spectrum analysis of gases evolved on heating showed ethylene, butene and butadiene, suggesting a polymerization.

Polypyrrole was synthesized electrochemically and characterized by cyclic voltammetry. Gram quantities of polypyrrole doped with BF_4^- and ClO_4^- were prepared electrochemically under high vacuum conditions to achieve high purity and avoid oxygen doping. Perchlorate doped polypyrrole prepared in an oxygen-free environment proved dangerously unstable, especially when dry.

The neutron scattering law for a harmonic oscillator and the energy level splitting pattern of a 1-D rotor in a $\cos 3\theta$ hindering potential are reviewed and applied to solid acetonitrile. Intense lines in the neutron spectrum at 140 and 190 cm^{-1} are assigned to methyl group torsions with barriers to rotation of 400 and 734 cm^{-1}.

Hydrogen is reversibly physisorbed by intercalates $C_{24}K$, $C_{24}Rb$ and $C_{24}Cs$ at 100K to form compounds $C_{24}M(H_2)_2$. Neutron spectra of H_2, HD and D_2 physisorbed by $C_{24}Rb$ and $C_{24}Cs$ at energy transfers between 0.3-3 meV and 10-200 meV (1 meV = 8.065 cm^{-1}) were measured and assigned to rotational tunnelling and librations of hydrogen molecules in two sites of different dimensions. The $\cos 2\theta$ barriers to rotation were 57 and 78 meV respectively in $C_{24}Rb(H_2)_x$ and 51 and 78 meV in $C_{24}Cs(H_2)_x$. A structural model is proposed for the metal layers with the hydrogen molecules in the layers and perpendicularly oriented.

CONTENTS

INTRODUCTION : MOLECULAR METALS

The alkali metal graphite intercalation compounds and the conducting polymers polyacetylene and polypyrrole are some of the most widely studied members of the class of materials termed molecular metals. The primary characteristic of molecular metals is a high electrical and thermal conductivity. This conductivity is electronic in origin (not ionic), and stems from electron delocalization throughout the material. Conductivities vary enormously, but are typically of the order of 1-1000 S/cm (1 S = 1 Ω^{-1}), intermediate between semiconductors and metallic elements, and the term semi-metal is sometimes used. A conductivity chart is given as a guide (Table 1).

The delocalized electrons are highly polarizable and molecular metals are usually, though not always, characterized by charge transfer and unusual redox chemistry. They also tend to be highly anisotropic, since the electron delocalization usually occurs in one or two dimensions only; for this reason, they are sometimes referred to as "low dimensional solids". The properties of metals, insulators, semiconductors and semi-metals are described by Kittel[1] with a summary in the introductory chapter of Chien's book on polyacetylene[2].

Many types of molecular metals exist. A large number of substances besides alkali metals can be intercalated into graphite, and the number of conducting polymers is increasingly rapidly. There are also inorganic layered compounds such as the Group IVA, VA and VIA disulphides and diselenides and their intercalation compounds eg ZrS_2, TaS_2, $NbSe_2$, Li_xTiS_2 ($0 < x \leq 1$),[+] also intercalates of FeOCl and even boron nitride.

+ The Group IVA disulphides and diselenides become more conducting on intercalation. The Group VA disulphides and diselenides are metallic anyway, and intercalation reduces their conductivity (See Table 2). Lithium intercalation of TiS_2 can be exploited to make rechargeable batteries[3].

Table 1. Conductivities of Metals, Semiconductors and Insulators

(d indicates doped material) (ref [2])

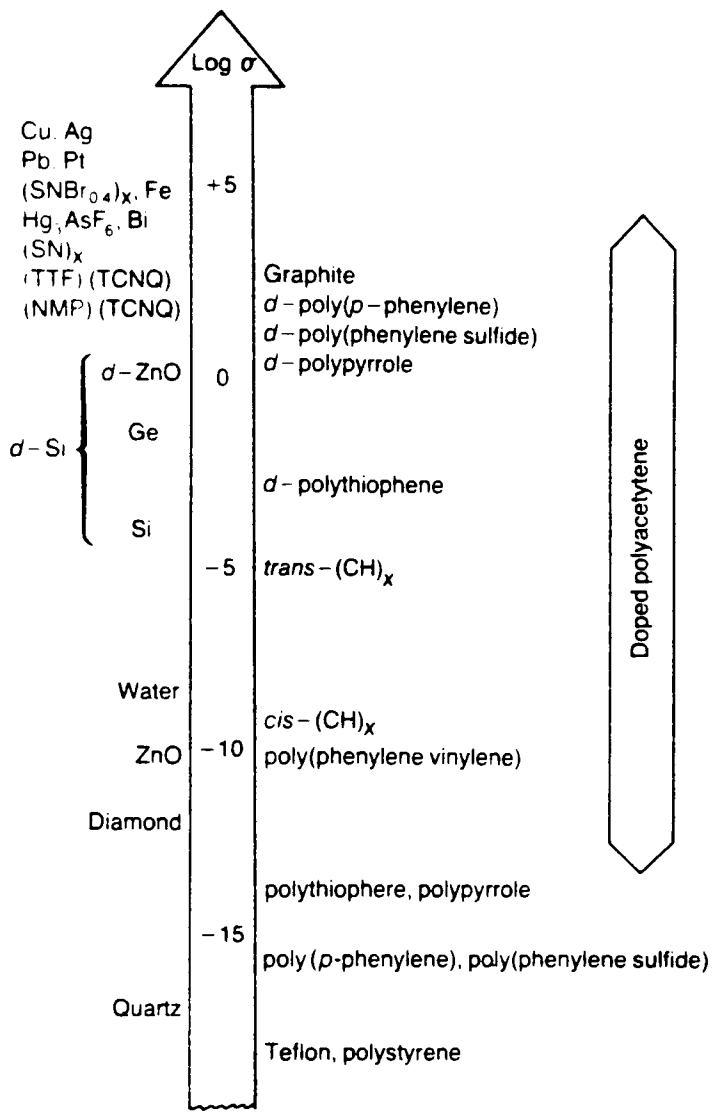

Chain compounds include polythiazyl $(SN)_x$ and its doped version $(SNBr_{0..4})_x$, square planar metal tetracyanoplatinates, charge transfer complexes such as TTF.TCNQ, TTF/Iodine and perylene/iodine, and even a one-dimensional form of graphite. In addition, there are the tungsten bronzes eg Na_xWO_3 ($0.3 < x < 1$) which form complex layer and channel structures. Some representative molecular metals are listed with conductivities and references in Table 2. Many of the layered compounds are reviewed by Gamble and Geballe[4], and the chain compounds by Miller[5].

In the graphite intercalates and the conducting polymers, the electron delocalization stems from a framework of carbon atoms with alternating double and single bonds. In the graphite intercalates, the carbon backbone consists of the two dimensional graphite layers with

oxidizing and reducing species accommodated between the graphite layers with accompanying charge transfer. In the conducting polymers, however, the π system is a one dimensional polymer chain; the redox species are accommodated either in channels between polymer chains, or in layers. The incorporation of oxidizing or reducing species between layers or chains of carbon atoms is characteristic of the carbon-based molecular metals. It is reversible, can occur either chemically or electrochemically, and is termed intercalation in the graphite compounds and doping in the conducting polymers. The difference in nomenclature should not, however, conceal the fact that the processes are essentially similar, and that many of the same redox agents are used in both cases eg AsF_5, Br_2 (oxidants); Li, K (reductants).

The charge transferred in the intercalation/doping process is up to $0.1e^-$ per carbon atom. This is not necessarily the same as the amount of dopant/intercalant which reacts, as extra neutral molecules can be incorporated without charge transfer. The term "doping", although commonly used, is somewhat misleading in this case, and should not be confused with its use with traditional inorganic semiconductors. (Some authors suggest "loading" instead.)

The extended π system, though a necessary condition, is not on its own sufficient for electronic conductivity, which is determined by the electron mobility at the Fermi energy[1]. Thus while graphite itself is a semi-metal, becoming more conducting on intercalation, undoped polyacetylene and polypyrrole are large band-gap semiconductors, owing to bond alternation, and only become conducting on doping. The conductivity of polyacetylene and polypyrrole can be altered over many orders of magnitude by choosing a suitable dopant at the correct concentration. (See conductivity chart.)

A further big difference between the graphite intercalates and the conducting polymers lies in the method used for the synthesis of the carbon framework and its effect on their structure and morphology. While the carbon framework of graphite occurs naturally as a regular crystal structure, in the case of the conducting polymers it is formed in a polymerization reaction from the monomer in solution or at an electrode. This means that while the graphite intercalates are highly ordered and give good diffraction patterns, the conducting polymers are poorly ordered and give mediocre to uselessly poor diffraction patterns, especially when doped. The aim of Part A, therefore, was to learn more about the structure of the doped conducting polymers by analogy with the graphite intercalates.

In Part B, the specific physical problem of the behaviour of secondary doping species H_2 and N_2 in alkali metal graphite intercalates is examined. Much disagreement has arisen over the structure of the metal layers in the graphite intercalates $C_{24}K$, $C_{24}Rb$ and $C_{24}Cs$ which, unlike C_8K, C_8Rb and C_8Cs, are disordered at room temperature, undergoing partial ordering at 100-200K. Since the $C_{24}M$ compounds physisorb hydrogen and other inert gases reversibly into the metal layers at temperatures below 100K, the dynamics of the absorbed hydrogen molecules have been used to determine the structure of the metal ions and to test the response of the alkali metal intercalant to the secondary doping. The dynamics depend only on the short range order round each hydrogen molecule, and the chosen method of inelastic incoherent neutron scattering takes advantage of the excellent scattering properties of the hydrogen nucleus.

Table 2. Some Molecular Metals and their Conductivities

Intercalates : Layer Compounds

Name	Repeating Unit	Dopant/ Intercalant	Concentration	σ S/cm	refs
graphite	C	-	-	2.5×10^{4}, 8	[6-8]
	C_8K	K^+	0.125	10^5, 3×10^3	
	$C_{48}K$	K^+	0.021	10^5, 25	
	C_6Li	Li^+	0.167	2.5×10^5, $1.5\text{-}2\times10^4$	
	$C_8(AsF_5)$	AsF_6^-	0.125	4×10^5, ?	[9,10]
TiS_2	TiS_2	-	-	70	[3,11]
	$LiTiS_2$	Li^+	1.0	200	
2H-TaS_2	TaS_2	-	-	6700, 500	[4,12]
	$TaS_2(py)_{0.5}$	pyridine	0.5	3300, 0.05	
FeOCl	FeOCl			10^{-7}	[4,13]
	$FeOCl(py)_{0.33}$	pyridine	0.33	0.5, ?	
Boron Nitride, BN		-	-	insulating	[14-16]
	$(BN)_4SO_3F$	FSO_3^-	0.25	conducting	
	$(BN)_{13}K$			?	

Complex Structure

sodium tungsten bronze, Na_xWO_3	x=0.48→0.88	$1.4\times10^{-4}\rightarrow5\times10^{-4}$		[4,17]

Conductivities refer to the value at 298K. Where two figures are shown, they refer to measurements parallel and perpendicular to the layers. In some cases, resistivities were quoted in the original reference. These have been converted to conductivities for ease of comparison. A method of measuring conductivities of highly anisotropic samples is described by Zeller et al[10].

Table 2. (cont'd) Some Molecular Metals and their Conductivities

Chain Compounds : Conducting Polymers

Name	Repeating Unit	Dopant/ Intercalant	Concentration	σ S/cm	refs
cis-polyacetylene	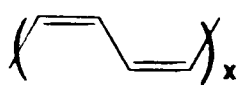			10^{-9}	[2]
trans-polyacetylene	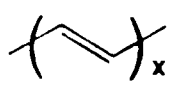			10^{-5}	[2]
neutral polypyrrole	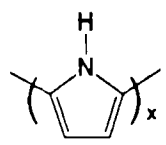			$<10^{-5}$	[18]
doped polyacetylene		AsF_6^-	0.1	1200	[2]
		Li^+	0.3	200	[2]
polypyrrole		ClO_4^-	0.3	60-200	[18]
polythiophene	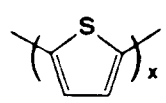	ClO_4^-	0.25	10-100	[19]
poly-p-phenylene	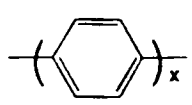	AsF_6^-		145	[2]
		K^+		7	[2]
polythiazyl	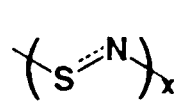	-		2000, 10	[20,21]
		Br	0.4	2×10^4, 40	[20,21]
polyperinaphthalene (1-D graphite)	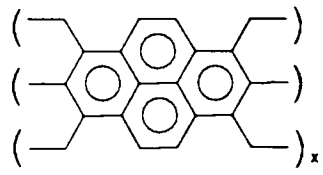	-		0.2-1100	[22]

Chain Compounds : Molecular Stacks

$Li_2[Pt(CN)_4].3H_2O$ 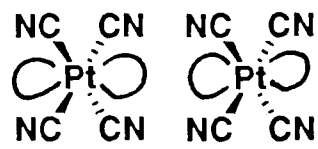			3×10^{-5}-3×10^{-4}, 3×10^{-7}	[23,24]
tetrathiofulvalene (TTF)/ tetracyano-p-quinodimethane (TCNQ) 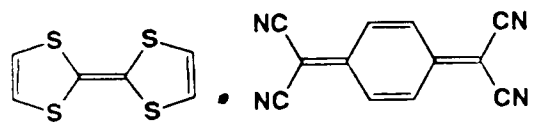			500	[2,25,26]
perylene 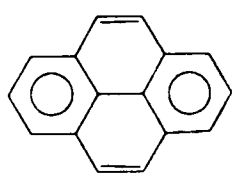	I_3^-	4.0	5-50	[20]
TTF	I^-	0.7	100-450	[20]

The conductivities of polyacetylene and polypyrrole with various dopants are considered in more detail in Tables 2.1 and 3.1.

PART A : CHEMICAL ASPECTS OF INTERCALATION

CHAPTER 1

THE GRAPHITE INTERCALATION COMPOUNDS

INTRODUCTION

A vast amount of literature has been and is being published about the graphite intercalates and a full review is not attempted here. Structural views up to 1982 are summarized in a review article by Solin[27]. A brief though dated general summary is given by Novikov and Vol'pin[28], with gas absorption and catalytic properties described by Boersma[29].

1.1 POSSIBLE INTERCALANTS

The graphite intercalates of the heavy alkali metals are the easiest to prepare since these metals do not form stable carbides and have relatively high vapour pressures. The compounds were originally prepared by equilibrating stoichiometric quantities of graphite and the intercalant at 300°C in a sealed tube so that the intercalant vapour diffused into the graphite. More common nowadays is Hérold's double bulb method in which the graphite and excess intercalant are heated to different temperatures, the product being determined by the graphite temperature (Section 1.2). Other methods of preparation are reviewed by Solin[27] and Novikov & Vol'pin[28]. Stoichiometries are traditionally given as C_8M, $C_{12n}M$ ($n \geq 2$) for M = K,Rb,Cs; $C_{6n}Li$ ($n \geq 1$). Sodium intercalates have proved difficult to prepare[28], and if a liquid amalgam of sodium and lithium is used, only the lithium will intercalate[27,30]. (Contrast sodium doping of polyacetylene - See Section 2.3.) Nevertheless, compounds such as $C_{56}Na$ have been reported[6]. No good explanation has been advanced for the exceptional behaviour of sodium. The stoichiometries, however, are now reckoned to be only approximate and can vary with sample conditions[27,31] (See also Sections 1.3, 1.4).

More recently, intercalates have been prepared from the heavier alkaline earth metals[32] and some lanthanides[33] eg C_6Sr, C_6Ba, C_6Eu, C_6Yb (cf C_6Li). (Contamination by the metal carbide is a problem here.) Mixed intercalates have also been prepared, both from two alkali metals eg $C_{16}KCs$ [34], $C_8K_{1-x}Rb_x$ [35,36], and from an alkali metal and a less electropositive metal eg C_4MHg, C_8MHg, $C_4MTl_{1.5}$ (M = K, Rb) [37]; also $C_{7.5}Na_xBa_y$ where $1.6 < x/y < 5$ [37].

In addition, a large number of electron acceptors will also form graphite intercalates. These have been reviewed by Stumpp[38] and fall into a number of categories. First, there are protonic acids eg H_2SO_4, HNO_3, SO_3, N_2O_5, CrO_3, PF_6^-. Second, there are the halogens chlorine and bromine and the interhalogen compounds (but not fluorides). Third, there is a wide range of transition metal, lanthanide, and B metal chlorides and bromides eg $FeCl_3$, $AlCl_3$, $SbCl_5$, and also metal and non-metal fluorides eg AsF_5, SbF_5. There are also some other metal compounds eg $Cu(NO_3)_2$, $Zn(NO_3)_2$. In spite of the greater variety of intercalants, these compounds are less well studied than the alkali metal compounds, the AsF_5 intercalate being the best known. Preparation is usually by direct combination, although electrochemical intercalation of strong acids such as HF [39], $HClO_4$ [39,40], H_2SO_4 [40], $ClSO_3H$ [40], CF_3CO_2H [40], H_3PO_4 [40], H_3AsO_4 [40], HIO_4 [40] and also AsF_5 [41] has also been reported. Stoichiometries vary even more than for electron donors eg $C_{8n}AsF_5$[42], $C_{5n}HNO_3$ [43] ($n \geq 1$), but of this, only ≈40% of the intercalant oxidizes the graphite, the rest diffusing in as neutral molecules to screen the charge[40,42] (cf water of crystallization in classical inorganic compounds).

1.2 THE CLASSICAL STAGING MODEL

Graphite consists of layers of flat sheets of conjugated hexagons stacked in an ABAB... sequence with only weak Van de Waals' forces

between the sheets (C-C in-plane distance = 1.4211Å [44], C-C interlayer distance = 3.35Å). On intercalation, the graphite swells as layers of intercalant are inserted between some or all of the graphite layers. Charge is simultaneously transferred to the carbon layers whose in-plane structure undergoes minimal change. The intercalated layers occur in a regular sequence, so that the compounds can be assigned a stage number n, where n is the number of graphite layers between each intercalated layer. Thus C_6Li and C_8M (M = K, Rb, Cs) are stage I, $C_{24}M$ is stage II as are both $C_{12}Li$ and $C_{18}Li$ (See Section 1.4.2), and $C_{36}M$ is stage III. stage I compounds are golden in colour, stage II compounds are dark blue, and higher stages are black. Fractional staging does not occur under normal conditions. The graphite stacking sequence is modified and the stacking orders for various stages of potassium intercalate are shown in Fig 1.2. Rubidium and caesium intercalates have similar structures. The very long c axis repeat distances are typical of the graphite intercalates and are clearly indicated in the 00ℓ lines in the powder diffraction pattern[45] (Fig 1.1). Compounds up to stage XV have been characterized in this way[6]. The c axis repeat distance is given by the formula

$$d_c \approx N[(n-1)d_1 + d_2] \quad n = 1,2... \qquad (1.1)$$

where N is an integer, n is the stage number, d_1 the distance between adjacent carbon planes (3.35Å), and d_2 the thickness of an intercalated layer. In C_8K, Rb, Cs the intercalated layer thicknesses are 5.40,[+] 5.68, 5.94 Å respectively.

In mixed intercalates with intercalants of different redox potentials, a sandwich structure forms with the less strongly

---

+ Rüdorff & Schulz's figure[45], also quoted by Solin[27]. Novikov & Vol'pin[28] give the C_8K interlayer spacing as 5.33Å.

Fig 1.1 Neutron powder diffraction pattern of Caesium Intercalates

Roman numerals give stage numbers.

Lines indexed on a single metal-metal c axis spacing

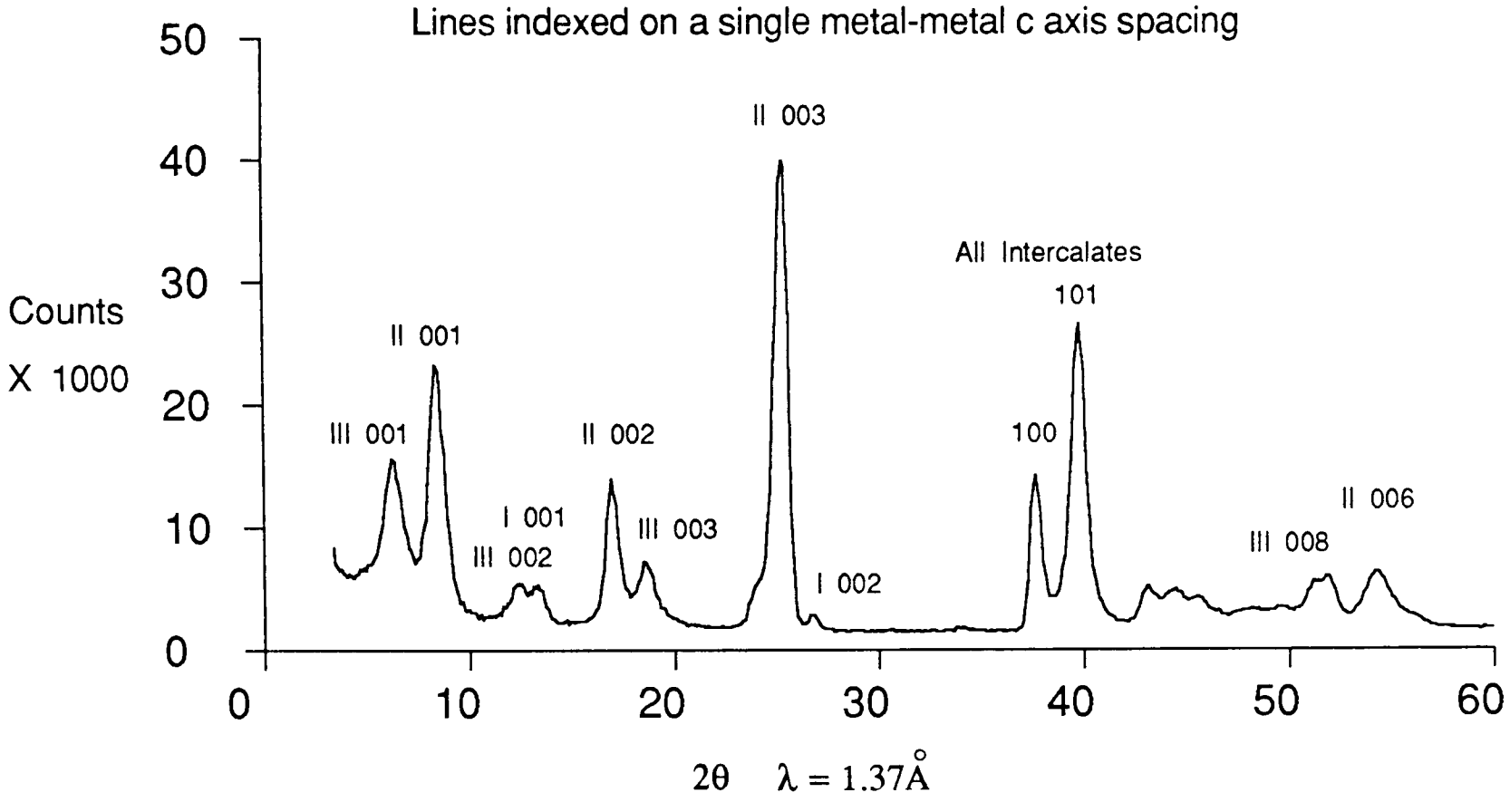

Fig 1.2 Stacking Sequences in Stage I to V Potassium Intercalates[27,45]

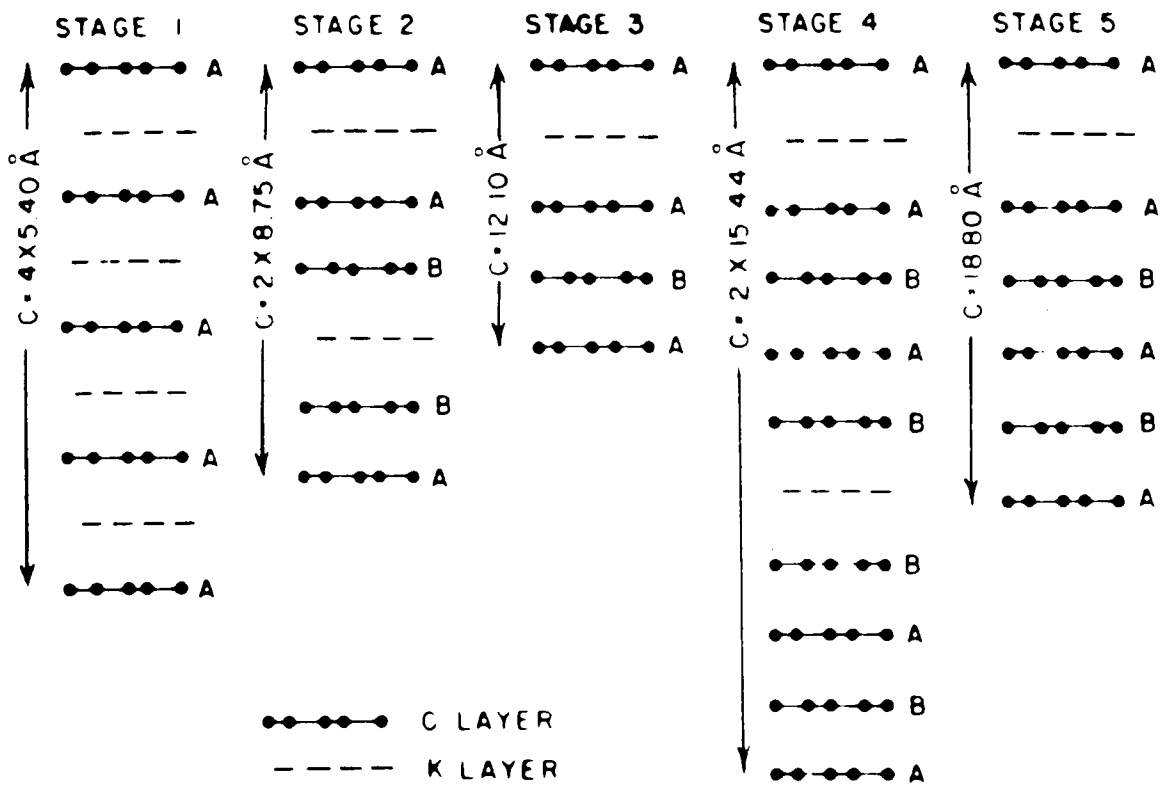

Distance between adjacent graphite layers = 3.35 A. Thickness of an intercalated layer = 5.40, 5.68, 5.94 A for M = K, Rb, Cs. Roman letters refer to graphite layer stacking sequence, Greek letters (Fig 1.3) to metal layer stacking sequence.

oxidizing/reducing element replacing a carbon layer. Thus the stacking sequence in the mercury mixed intercalates is $C^{\delta-}K^{\delta+}Hg^{\delta-}K^{\delta+}C^{\delta-}$ (Fig 1.4). This structure also occurs in thallium mixed intercalates[37], intercalates of many molecular electron acceptors eg $AlCl_3$, AsF_5[32], and also $C_8KH_{\frac{2}{3}}$ [47,48] (Section 1.5.1).

Further evidence for the stability of integral stages comes from Hérold's classic experiment[49] (repeated by Nixon and Parry[50]) in which excess potassium at a constant 250°C was equilibrated with graphite at temperatures between 250°C and 600°C in a double oven. The desorption curve showed plateaux at compositions C_8K, $C_{24}K$ and $C_{40}K$ corresponding to intercalates of stages I, II and III. (NB Both Hérold and Nixon & Parry only report data for potassium.) A similar effect was noted by Bottomley et al[40] during electrochemical intercalation of graphite with H_2SO_4 at constant current, when the voltage across the cell showed plateaux at compositions $C_{24}^{+}(HSO_4^{-})$, $C_{48}^{+}(HSO_4^{-})$ and $C_{72}^{+}(HSO_4^{-})$. (Neutral molecules are excluded in this stoichiometry, since the measurement was on the charge passed.)

The staging model does not define the bulk composition of each stage; C_6Li (stage I), C_8K (stage I), $C_{24}K$ (stage II), and $C_{24}(HSO_4)$ (stage I) each show a different in-plane packing density. The in-plane intercalate unit cell is classified $(n\times m)R\theta$ where n and m are cell dimensions and θ the angle of rotation, both relative to the graphite unit cell. The stage I intercalates C_8M show a $(2\times2)R0°$ structure with four different possible positions for the M^+ ions[45]. C_8K and C_8Rb stack $\alpha\beta\gamma\delta$ (Fig 1.3) but C_8Cs shows predominantly $\alpha\beta\gamma$ stacking[47,51]. C_6Li, on the other hand, adopts the more closely packed $(\sqrt{3}\times\sqrt{3})R30°$ structure, which has three possible positions for the M^+ ions[52] (Fig 1.5). The stacking sequence in this and all higher stage compounds is more complex.

Fig 1.3 3-D Structure of C_8K [ref 46 after ref 45]

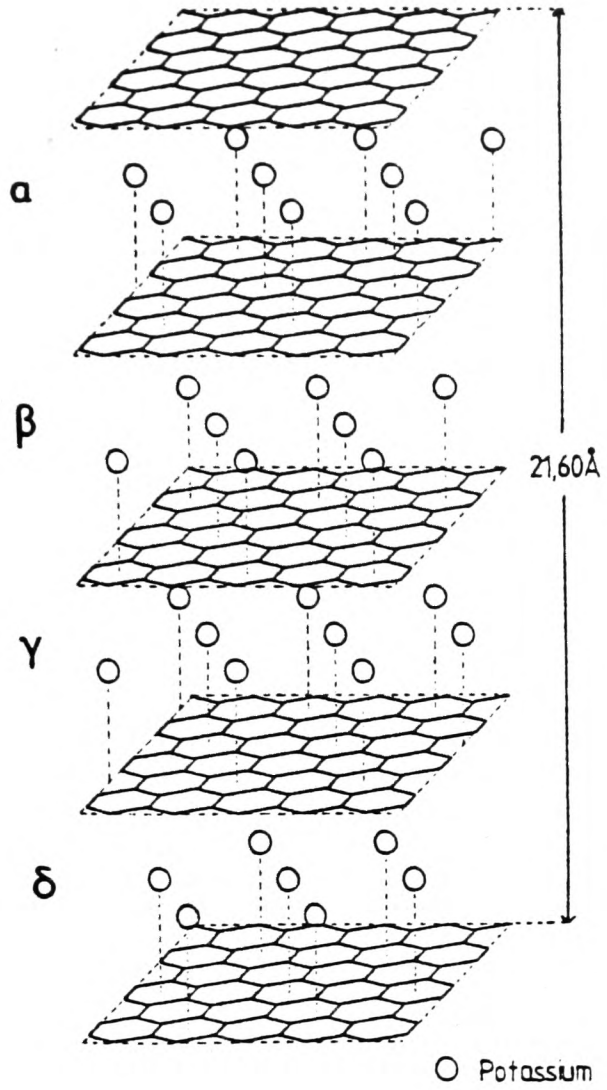

Fig 1.4 "Sandwich" structure of mixed Potassium/Mercury Intercalates[ref 37]

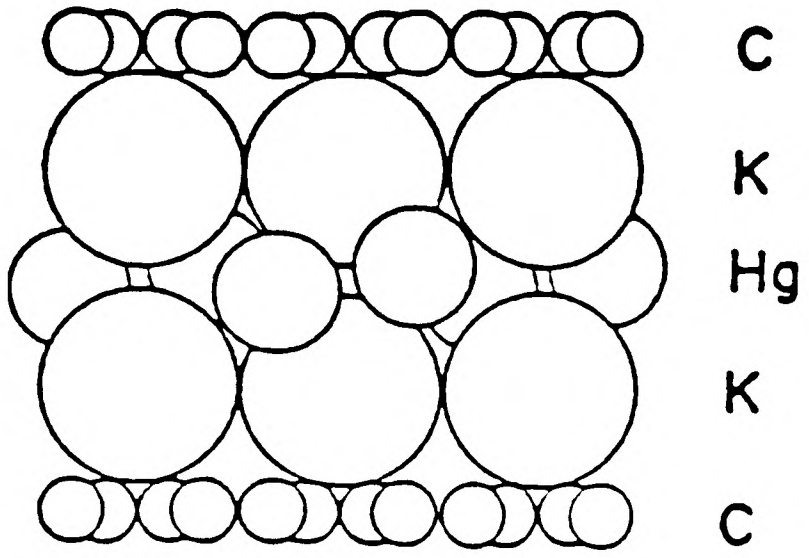

$C_8KH_{\frac{2}{3}}$ shows a similar structure. In metal chloride intercalates, the positions are reversed. M replaces Hg and Cl replaces K.

Fig 1.5 In-plane Structure of Stage I Intercalates[ref 27]

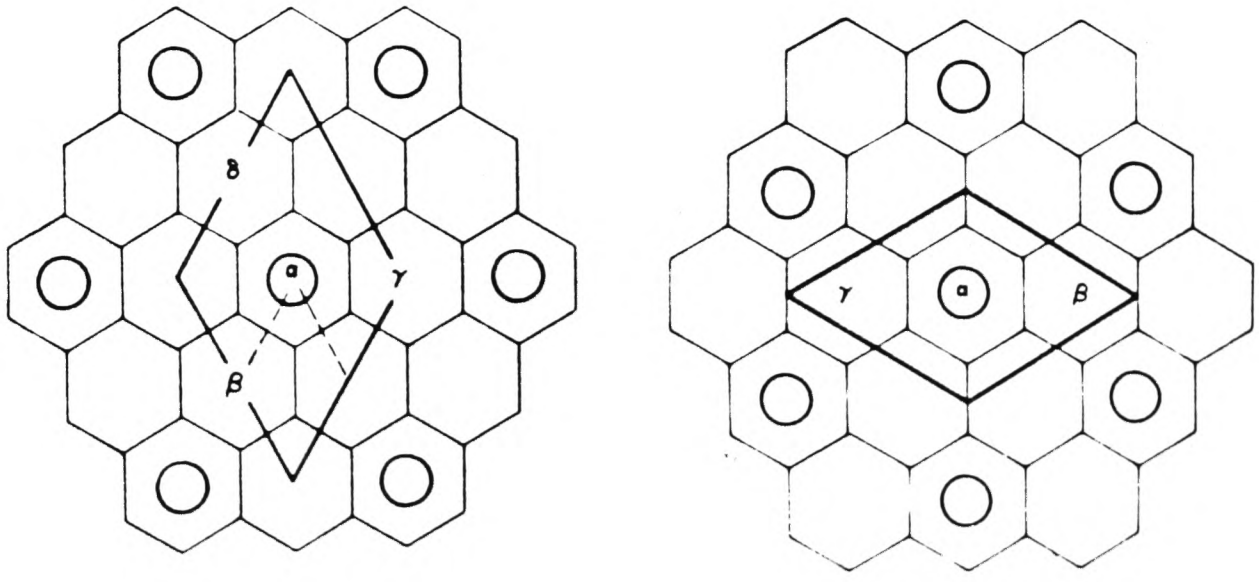

$(2\times2)R0°$ C_8M (M = K,Rb,Cs) $(\sqrt{3}\times\sqrt{3})R30°$ C_6Li

The corners of the hexagons represent carbon atoms and the circles metal ions. Equivalent positions for the metal ions are marked by Greek letters; this is not necessarily the same as the stacking order. The intercalate unit cell is marked in heavy black lines with the graphite unit cell dashed. The label shows the size of the intercalate unit cell and its angle of rotation relative to the graphite unit cell.

1.3 DEPARTURES FROM THE CLASSICAL MODEL

A neutron powder diffraction pattern of a mixture of C_8Cs, $C_{24}Cs$ and $C_{36}Cs$ has been shown in Fig 1.1. Using Equation 1.1, the thickness of an intercalated layer in $C_{24}Cs$ and $C_{36}Cs$ was found to be 6.01 to 6.02Å compared with 5.93Å in C_8Cs. This shows that while the classical staging model is broadly correct, the fine details of intercalation chemistry are more complex:-

1.3.1 Pure Staging

The stability of pure stages of the alkali metal graphite intercalates is illustrated by the fact that a poorly intercalated sample shows a mixture of pure stages with domains which are large on a molecular scale (>500Å), as in Fig 1.1 where three interpenetrating sets of **sharp** lines are seen (See also Nishitani et al[53]). The pure staging is caused by a combination of strong attraction between the intercalated layers and the adjacent graphite layers, and weak repulsion between the intercalated layers[54]. This effect is more marked in the alkali metal intercalates than in intercalates of $FeCl_3$ and other electron acceptors where stacking faults occur much more readily[55], and diffraction lines broadened by disorder are common[27,56].

A staging theory for the alkali metal intercalates has been developed and theoretical phase diagrams have been plotted by Safran[57] and by Millman and Kirczenow[54] as a function of temperature and chemical potential of the intercalant (ie the logarithm of the vapour pressure of the alkali metal) (See Fig 1.6). Several features of the analysis stand out: first, at high temperatures the stage I and stage II intercalates have a **range** of concentrations over which they are stable, so that there is no unique in-plane packing density. This has been observed for all C_8M and also for $C_{24}K$ (See Section 1.4.2). Second, each stage has a critical temperature above which it cannot exist; at very

Fig 1.6 Calculated Phase Diagram for the Intercalates [ref 57]

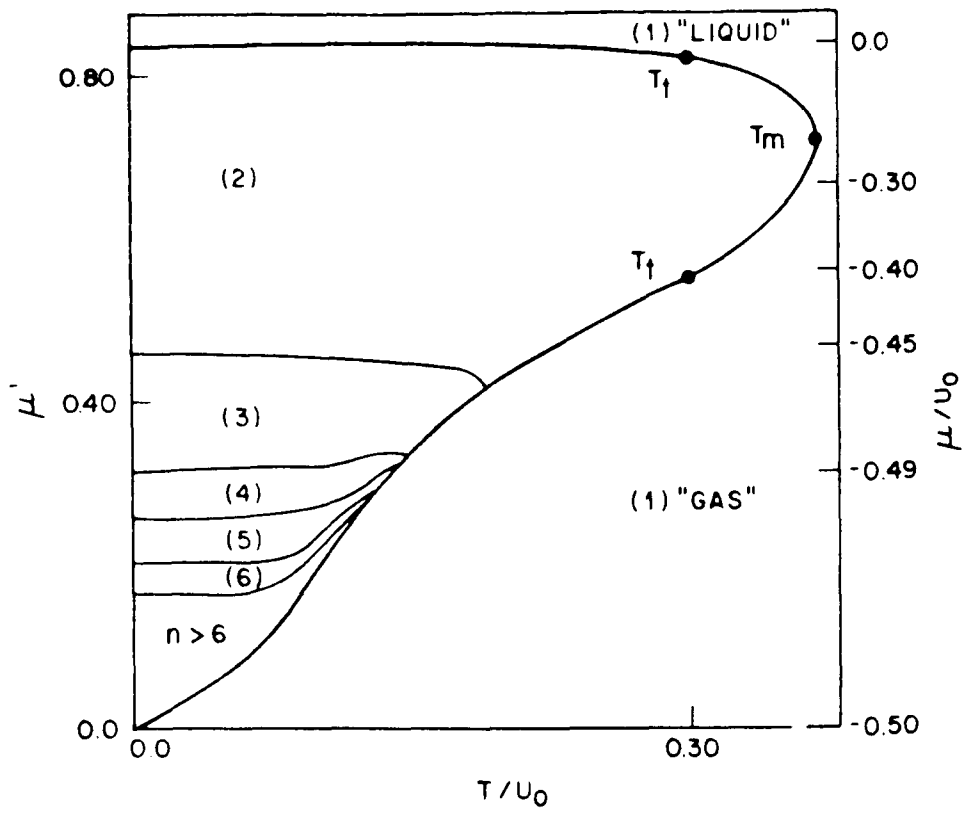

The stage numbers are shown in brackets with temperature on the x axis and the chemical potential on the y axis (NB log scale).

high temperatures, only stage I is stable over the full range of chemical potentials. This may explain why in Hérold's double bulb experiment, each higher stage is stable over a narrower and narrower temperature range. Third, an intermediate stage $\frac{3}{2}$ is predicted. This is not normally observed, although it has recently been reported in high pressure studies[53] (See Section 1.4.3).

1.3.2 Dynamics of Intercalation

While the formation of any stage of intercalate from graphite can easily be visualized, progression from one stage to a neighbouring stage causes problems. For example, in Hérold's double bulb experiment [49,50], $C_{24}K$ (stage II) was changed into $C_{36}K$ (stage III) by desorption of potassium. In the simple staging model, this would require removal and re-intercalation of whole sheets of potassium ions. However, Daumas and Hérold[58] de-intercalated C_8K and $C_{24}K$ using carbon monoxide, and by stopping the reactions at different times, obtained all the pure stages in turn from stage II to stage VI in spite of the fact that any

free potassium metal would have reacted preferentially with the carbon monoxide (See Section 1.5.3). Changes of stage without desorption of metal can also occur on application of pressure (Section 1.4.3) and chemisorption of hydrogen (Section 1.5.1). Daumas and Hérold postulated the existence of domain boundaries where the carbon layers bent and folded into each other, and that changes of stage were accomplished by moving the boundaries[58]. (The domains were, however, large enough to give sharp X-ray diffraction lines.) This folding of layers in mixed stage intercalates has been observed directly in a high resolution electron micrograph of an $FeCl_3$ intercalate[27,55]. By contrast, potassium intercalates undergoing stage transitions in situ show 00ℓ lines from pure stages only, showing that in this case, the boundaries of mixed stage are very narrow[53]. The model has also been the subject of a recent computer simulation which illustrates the growth of domains of different stages in a single sample[59].

1.3.3 Changes in the Graphite Structure

In the classical staging model, it is assumed that the carbon layers retain the graphite structure unchanged upon intercalation. While this is approximately true, there are changes associated with the accompanying transfer of charge. Nixon and Parry[44] measured the in-plane C-C bond length of potassium intercalates of stages I to VI to four decimal places and found that it varied smoothly with the concentration of potassium, the bond length in C_8K being greater by ≈0.01A than in graphite. Furthermore, if stage I were assigned a composition $C_{12}K$ instead of C_8K, the points, with the exception of graphite itself, lay on a straight line.

There has been a suggestion[60] that graphite layers might be inequivalent within a single stage of intercalate. DiCenzo et al[61,62] studied $C_{24}K$, $C_{48}K$ and $C_{60}K$ by XPS and found that although the C1s

linewidth decreased on increasing the stage number, the charge in the graphite layers appeared to be highly localized near the metal ions.

1.3.4 Degree of Ionization of the Intercalated Species and the Nature of the Bonding to the Graphite Layer

In the classical staging model, charge is transferred from the intercalant to the graphite layers; the exact degree of charge transfer and the nature of the bonding between the metal ions and the graphite layers remain controversial. Traditionally, it has been reckoned that the metal atoms in the stage I C_8M compounds were 0.6 ionized and that those in compounds of stage II and higher were fully ionized. Evidence for this includes optical absorption spectroscopy[63], T_1 and Knight shift measurements in ^{13}C and ^{133}Cs NMR [64,65], low temperature specific heat measurements[66] and theoretical band structure calculations[67]. Furthermore, if the metal atoms in C_8M **were** only partially ionized, they would be expected to bond covalently to the neighbouring graphite layers. The expansion in the distance between the graphite layers on intercalation to C_8K,Rb,Cs is only 2.05, 2.33, 2.98Å respectively, less than the diameters of the M^+ ions of 2.66, 2.98 and 3.30Å. This was attributed by Boersma[29] to covalent bonding between the metal ions and the graphite layers, as was the low c axis compressibility of C_8Cs [68]. Against this, DiCenzo's XPS study[61] suggested that the small chemical shift of the C1s level in $C_{24}K$, $C_{48}K$ and $C_{60}K$ might be attributed to incomplete ionization of metal atoms. On the other hand, a more recent valence band study of C_8K concluded that the lack of a K4s band was direct proof of complete charge transfer[69].

In C_6Li the ionization energy is greater and covalent bonding is reckoned to play a more important role[70-72]. Furthermore, a theoretical study[73] in which the c axis lattice constant and

compression and shear moduli were calculated for C_8M and C_6Li on the basis of complete charge transfer gave accurate predictions for C_8M only; for C_6Li, the lattice constant was 20% too large. Finally, ^{151}Eu Mössbauer spectra of C_6Eu suggest the presence of Eu^{2+} [74].

1.4 DEPENDENCE OF THE INTERCALATE STRUCTURE ON TEMPERATURE AND PRESSURE

1.4.1 Temperature Dependence of the Stage II Intercalates

While the three dimensional structure of the stage I intercalates, C_8M and C_6Li appears to be reasonably well determined at room temperature, the structure of the stage II intercalates is far from simple and has provoked endless controversy as summarized by Solin[27]. Since 1982 however, some progress has been made and a consensus is beginning to emerge.

The original proposal[45] for the in-plane structure of $C_{24}K$ was a $(\sqrt{12}\times\sqrt{12})R30°$ unit cell (Fig 1.7). This is a modification of the $(2\times2)R0°$ C_8M unit cell with regular defects and merely fulfills stoichiometry requirements. Room temperature X-ray diffraction patterns from single crystals of $C_{24}K$ [75-77], $C_{24}Rb$ [78,79] and $C_{24}Cs$ [80,81] show a diffuse **ring** of intensity corresponding to a metal-metal distance of 5.79, 6.05, 6.24Å for M = K,Rb,Cs.# These do not correspond to the distance between the centres of any two graphite hexagons and give stoichiometries $C_{22.0}K$, $C_{24.0}Rb$, $C_{25.5}Cs$. The nearest commensurate structure is the $(\sqrt{7}\times\sqrt{7})R19.1°$ structure with a metal-metal distance 6.51Å and a stoichiometry $C_{28}M$ (Fig 1.7). $C_{24}M$ gives a metal-metal distance 6.03Å.

The diffuse ring shows that there is no long range spatial correlation. Line shape analysis of the diffraction pattern from

---

These metal-metal distances are those listed by Suzuki[79] and appear to be the most reliable. Clarke originally claimed a Cs-Cs distance of 5.95 ± 0.1Å [81].

intercalated HOPG^{++} suggests a 2D **liquid**[80] (not a lattice gas[75,82]) with short-range triangular correlations and the metal ions **incommensurate** with the graphite lattice. The liquid-like behaviour has been supported by quasi-elastic neutron scattering measurements on $C_{24}Rb$ and $C_{24}Cs$ [82].

As a sample of intercalate is cooled from room temperature to liquid nitrogen temperature, the single crystal X-ray diffraction pattern changes radically. The diffuse ring of liquid-like scattering from the metal ions resolves itself into six pairs of spots, each pair rotated by an angle $\pm\phi$ from the directions of the graphite lattice, with the metal-metal distance remaining unchanged. For $C_{24}K$, Rb, Cs, ϕ is 8.5, 9.2, 14.5°## Furthermore, the difference between ϕ and 19.1° correlates with the mismatch in reciprocal space between the observed metal-metal distance and 6.51Å [84]. Kambe et al[85] claim to have observed a $(\sqrt{7}\times\sqrt{7})R19.1°$ lattice in a stage II rubidium intercalate by electron diffraction, but it is now thought that heating by the electron beam caused partial desorption of the metal[84].

The reason for this behaviour appears to be that at room temperature, the structure is determined entirely by the metal-metal potential, but that at low temperatures, the graphite potential becomes significant. Given the fact that below room temperature, the

---

++ X-ray diffraction patterns of intercalates have been measured from highly oriented pyrolytic graphite (HOPG) and single crystals, as well as from powder samples. HOPG has an ordered layer structure, but random orientation of the crystallites within each layer. Thus a diffraction pattern from intercalated HOPG with the c axis perpendicular to the incident beam will show a powder-like pattern of the hk0 lines only. (In powder samples, the 00ℓ lines dominate.) Single crystals, of course, show diffraction spots and give information on in-plane orientation. See also Mori et al[77].

Clarke's figures[80,84] collected by Suzuki[79] and those usually quoted. See paragraphs on $C_{24}Rb$, $C_{24}K$ for remeasured values.

metal:carbon ratio is fixed, the graphite potential could affect the structure in various ways. The incommensurate metal lattice could be modulated by a static distortion wave (SDW) with the periodicity of the graphite lattice, or it could break up into small commensurate domains separated by domain walls of a different packing density, or a mixture of macroscopic commensurate phases (eg (2×2)R0° + ($\sqrt{7}\times\sqrt{7}$)R19.1°) could separate out. (The theory of structures determined by two competing potentials is reviewed by Bak[86].) Originally, the mixture of phases was favoured[87,88], but recent X-ray patterns have found no evidence for this, and the SDW and domain models are now considered more likely. (A mathematical treatment unifying the SDW and domain models has recently been developed by Suzuki[89,90].) Each compound has two transition temperatures T_U and T_L (for C_{24}K, Rb, Cs, T_U = 124, 165, 225 K and T_L = 95, 106, 165 K)$^+$ and each transition temperature has associated with it resistivity[8] and specific heat[91] anomalies. (There is also a low temperature anomaly at 48K for C_{24}Rb [79,91] and 50K for C_{24}Cs [80] which has not yet been associated with structural changes.) Because the nature of the structural changes appears to vary slightly between intercalates, each compound is reviewed in turn.

In the case of C_{24}Cs[80,81,84,92], the in-plane diffraction ring resolves itself into spots at T_L, that is at 165K. Around this temperature (169-162K), there is a sharp increase in both the in-plane correlation, as shown by the hk0 lines, and the interlayer correlation as shown by the 10ℓ lines. However, the spots are visible very weakly at temperatures above T_L and they move steadily from the graphite 100 directions to ±14.5° as the sample is cooled from T_U to T_L. Thus there is reckoned to be some orientational but not positional ordering between

---

+ References K[76], Rb[79], Cs[80]. See also electron diffraction work by Kambe et al[88].

T_U and T_L. Below T_L there is short-range order, and the correlation lengths around 160K are 78A in plane and 250A interplane. (There is also a change from the metal layers stacking αβαβ... (hcp) above 160K to αβγαβγ... (fcc) below 160K.) Below 160K the in-plane ordering continues to increase, **but at the expense of the interplane ordering.** Winokur and Clarke[92] have interpreted this as interplane correlations driving the structure **towards** (but never quite reaching) an **ordered** structure in which hexagonal fragments of the $(\sqrt{7}\times\sqrt{7})R19.1°$ structure with 19 Cs^+ ions are bounded by domain walls (Fig 1.8). (This is slightly different from the authors' earlier structural proposal[84].) This structure, still controversial, is reminiscent of an earlier proposal by Parry[93] in which 7 atom fragments of the $(\sqrt{7}\times\sqrt{7})R19.1°$ structure existed in a (9×9) unit cell.#

In $C_{36}Cs$ [81,92], the results are qualitatively similar. However, T_L is 12K lower than for $C_{24}Cs$ and interplane ordering only starts to occur at 138K. As the temperature is further lowered, $C_{36}Cs$ undergoes more interplane disordering and less in-plane ordering than $C_{24}Cs$. This has been attributed to the weaker interlayer coupling.

In $C_{24}Rb$, the spots appear at 165K, that is at T_U. Between 110K and 165K, a single crystal study by Naiki and Yamada[94] measured $\phi = 14.0°$ with no temperature dependence.++ They observed two sets of satellites, the so-called ring-like and star-like reflections, which indexed on (9×9) and (8×8) unit cells respectively. As the star-like satellites had previously been observed by Kambe et al[85] at temperatures up to 620K,

---

Earlier proposals have tended to consist either of (8×8) or (9×9) unit cells with various probabilities of a metal ion occupying each graphite hexagon[93], or else a mixture of commensurate phases[87]. Suzuki has also applied the SDW model to $C_{24}Cs$ [89].

++ The authors, however, quote Clarke's figure of $\phi = 9.2°$ in a subsequent paper[95].

they were reckoned not to be concerned with the order-disorder transition. Both HOPG[79] and single crystal[94] c^* scans (scanning ℓ with h and k constant and non-zero) showed that the ring-like reflections had distinct selection rules of either $\ell = 3n$ or $\ell = 3n\pm1$, which suggested $\alpha\beta\gamma$ stacking.

Various low temperature structures for $C_{24}Rb$ have been suggested. The simplest is Naylor's model[96] in which 7 atom domains of the $(\sqrt{7}\times\sqrt{7})R19.1°$ structure are bounded by densely-packed domain walls (Fig 1.9). This is similar to Clarke's low temperature limiting structure for $C_{24}Cs$, but the domains are smaller, reflecting the greater degree of mismatch between the mean metal-metal distance and the $(\sqrt{7}\times\sqrt{7})R19.1°$ structure. Alternatively, Suzuki and Suematsu[89] have proposed a more complex 14 atom unit cell with a lower symmetry (Fig 1.10); this is a development of an earlier proposal by Yamada and Naiki[95].

Below 110K, that is T_L, there have been no single crystal measurements on $C_{24}Rb$ to date. c^* scans from HOPG[79] show new peaks appearing with no simple selection rules, indicating a more complex stacking sequence. Suzuki and Suematsu[89] suggest a repeating unit of nine C-Rb-C sandwiches.

In $C_{24}K$, the in-plane ordering transition also occurs at T_U, that is 122.9K [76,97], with T_L (95K) attributed to a change from $\alpha\beta\gamma$ stacking at high temperature to sixfold stacking at low temperature[97,98]. More recently, however, Mori et al[77] carefully measured the single crystal in-plane diffraction pattern of $C_{24}K$ at 100K and obtained ϕ = 7-7.5°. They explained the characteristic ring of twelve spots repeated round each graphite lattice point in terms of first, second and third order modulations of the **graphite** structure by the incommensurate potassium layers. This is the SDW alternative to the domain structure described

Fig 1.7 Idealized commensurate structures for the Stage II Intercalates

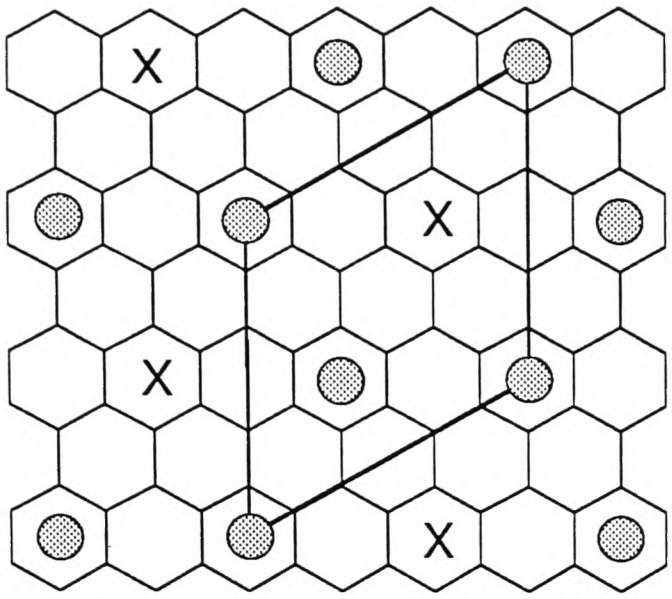

$(\sqrt{12} \times \sqrt{12})$ R30° Stoichiometry $C_{24}M$. If metal ions are inserted at X, the structure becomes (2 x 2) R0°.

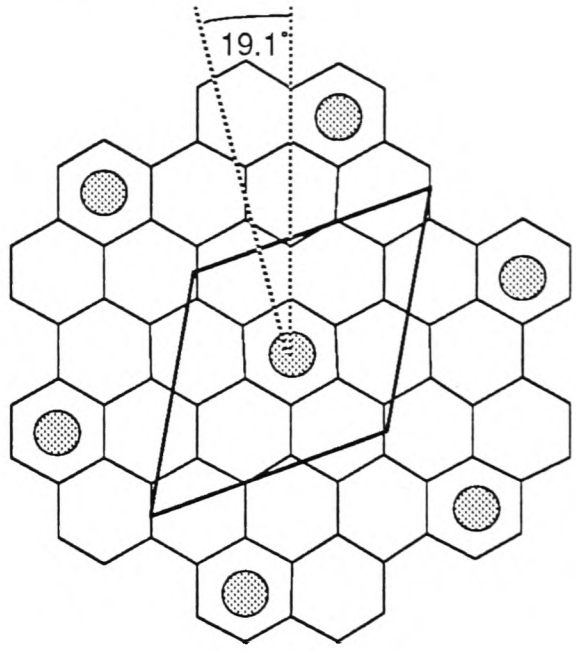

$(\sqrt{7} \times \sqrt{7})$R19.1° Stoichiometry $C_{28}M$ Metal - metal distance = 6.51Å.

Fig 1.8 Clarke's domain structure for $C_{24}Cs$ in the low temperature limit

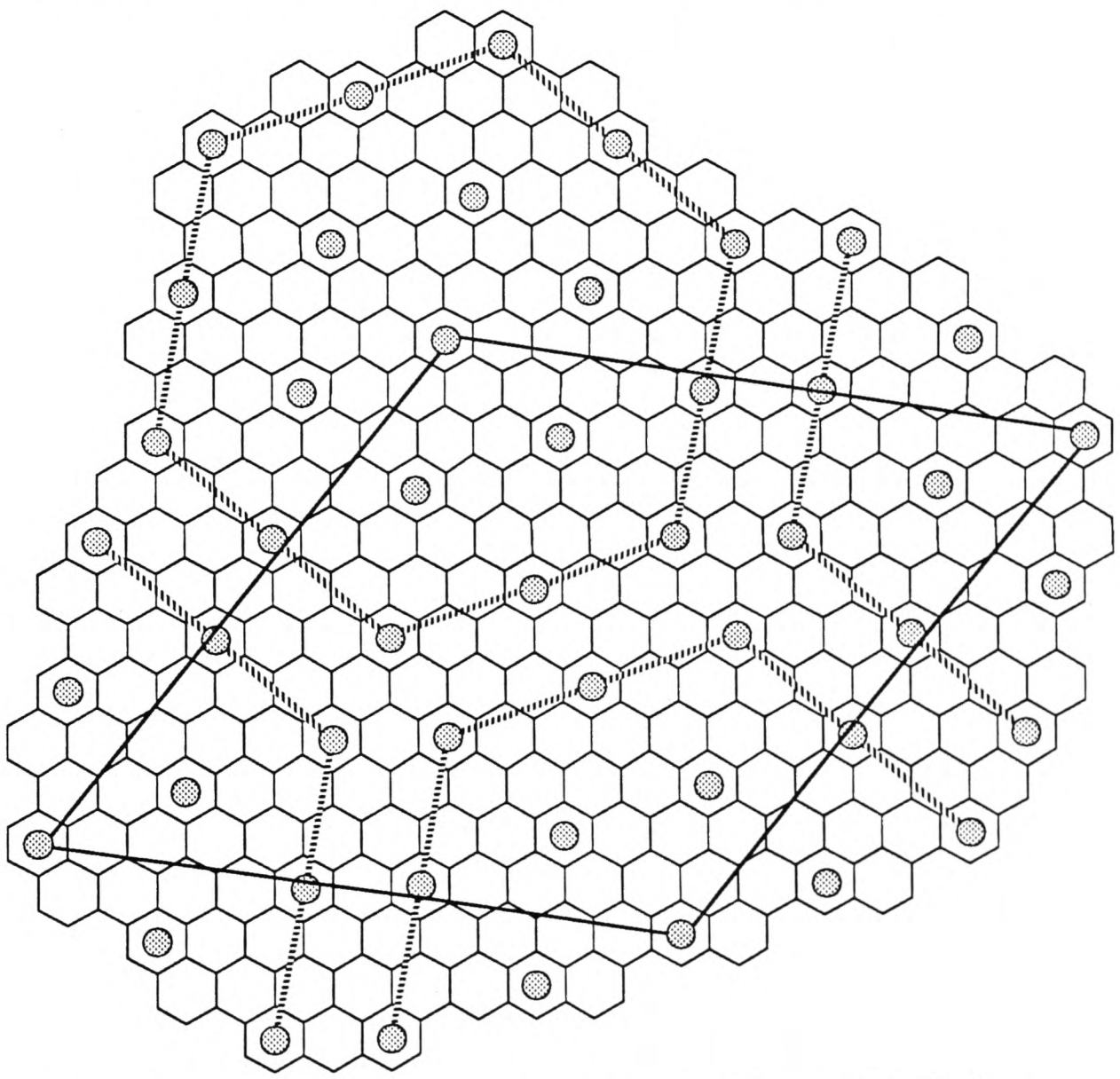

Stoichiometry $C_{26.1}Cs$, mean metal - metal distance = 6.28 Å, ϕ = 14.5°. The large hexagons are the walls of the 19 atom domains of $(\sqrt{7} \times \sqrt{7})$ R19.1° structure. To save space, only one domain has been shown in full. The large rhombus is the unit cell containing 19 metal ions. (Winokur and Clarke use a hexagonal unit cell of same size [92].)

Fig 1.9 Naylor's low temperature domain structure for $C_{24}Rb$

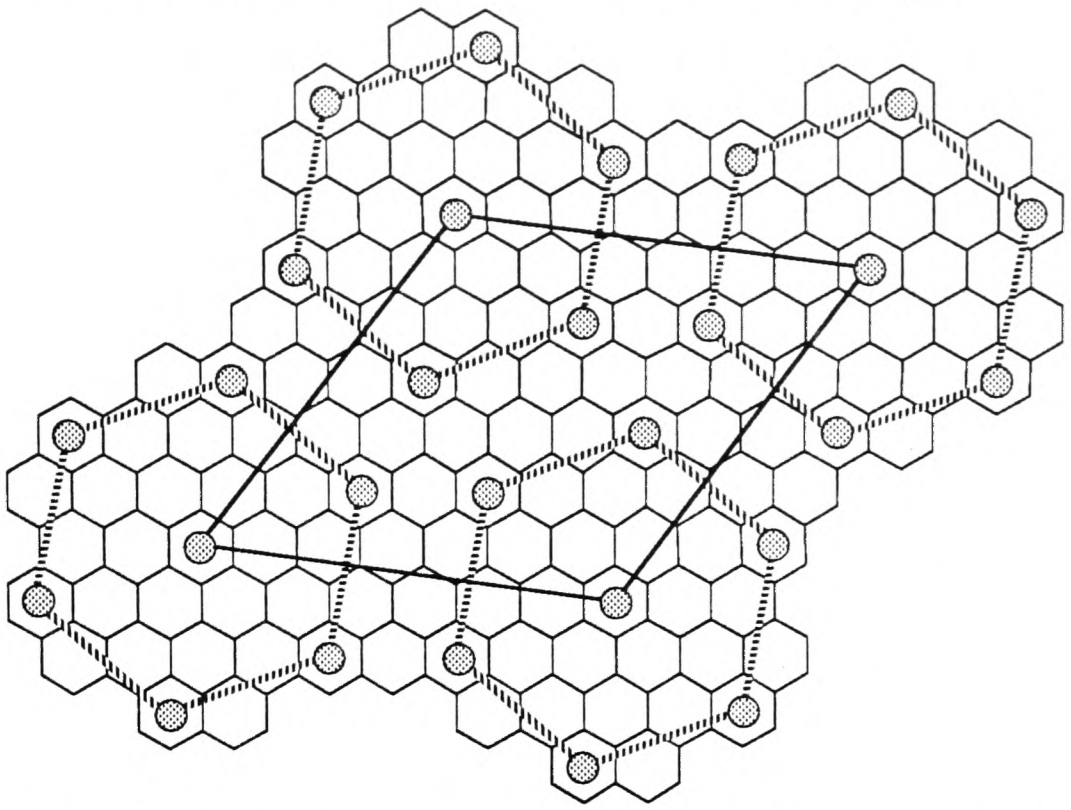

Stoichiometry $C_{24.6}Rb$, mean metal-metal distance 6.097 Å, $\phi = 11.5^{\circ}$. The large hexagons are the walls of the domains of $(\sqrt{7} \times \sqrt{7})$ R19.1° structure. The rhombus is the unit cell containing 7 metal ions.

Fig 1.10 Suzuki and Suematsu's Irregular Domain Structure for $C_{24}Rb$ between 165 and 110K.[ref 89]

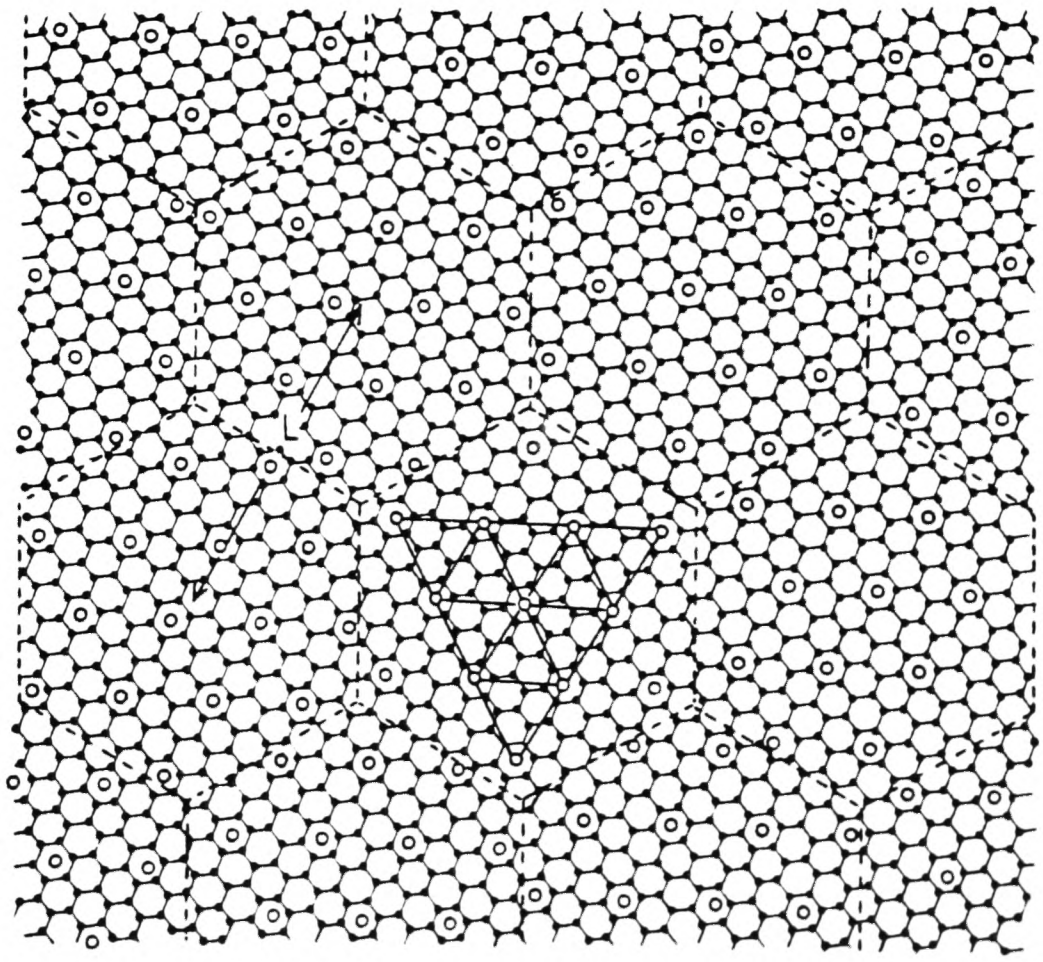

The open circles show the metal ions, and the dotted lines the underlying hexagonal (10×10)R21.3° domain superlattice. Note the irregularities along the domain walls.

for $C_{24}Cs$ and $C_{24}Rb$. Yamada and Naiki[95] have plotted domain size against ϕ and show that it would be inappropriate to apply the domain model to $C_{24}K$, since each domain would only contain one metal ion.

1.4.2 Temperature Dependence of the Stage I Intercalates

The stage I compounds also show order-disorder transitions at elevated temperatures (≈700K)[27]. Caswell[51,99] made a detailed study of C_8Cs and found a change to αβ stacking leading to a disordered phase with a liquid-like in-plane structure and a variable stoichiometry, denoted by previous authors "$C_{10}Cs$"[100,28]. Ellenson et al[101] noted changes in stacking order leading to a similar liquid phase for C_8Rb at 747K. Variable stoichiometries have also been found in stage I and stage II potassium intercalates at 390°C [102].

There is some evidence that C_6Li, which shows αα stacking at room temperature[52], changes to αβγ stacking below 200K [27] with accompanying resistivity[30] and specific heat[103] anomalies. The stage II lithium intercalate appears to exist in two stoichiometries $C_{12}Li$ and $C_{18}Li$ with radically different graphite stacking orders and temperature dependence of the metal layer structures[104].

1.4.3 Pressure Dependence of Intercalate Structures

In addition to the temperature induced changes, there are also pressure induced changes. At pressures around 3 Kbar, all the stage II compounds $C_{24}M$ change to a stage III (2×2) structure without changing their stoichiometry[105,106]. For higher stage compounds, the situation is less clear-cut; there is some evidence for $C_{36}Cs$ (stage III) developing patches of (2×2) stage IV under pressure[68], and for $C_{48}Rb$ (stage IV) changing to (2×2) stage VI [106].

The stage I compound C_8K changes to a mixture of stage I and stage $\frac{3}{2}$ compounds at 15 Kbar, followed by a change to a mixture of stage I and stage II compounds at 19 Kbar[107]. The stage $\frac{3}{2}$ is clearly indicated by

the 00ℓ lines in the neutron diffraction pattern, somewhat broadened by stacking faults, and it has a repeat distance of 13.61Å and a stacking order CMCCM... The in-plane structure of the stage $\frac{3}{2}$ and stage II phases has yet to be determined, but it could be the $(\sqrt{3}\times\sqrt{3})R30°$ C_6M structure. A similar transition to stage $\frac{3}{2}$ also occurs for C_8Rb at 20 Kbar.

1.5 REACTIONS OF INTERCALATES WITH GASES

Intercalates show four characteristic reactions with gases: chemisorption, physisorption, de-intercalation and catalysis. The first two are of particular interest because they show strong resemblance to surface chemisorption and physisorption, but occur throughout the sample to produce compounds with a well defined stoichiometry. Hydrogen can be both chemisorbed and physisorbed by intercalates.

1.5.1 Chemisorption of Hydrogen

C_8K will chemisorb hydrogen, slowly at room temperature and atmospheric pressure, faster at 120°C to a limiting composition $C_8KH_{\frac{2}{3}}$ [108,109]. The reaction is reversible and both absorption and desorption isotherms have been plotted, although desorption is very slow with a lot of hysteresis so that a single isotherm takes weeks to measure. The dark blue product is a stage II intercalate as characterized by X-ray[108,47] and neutron[48] diffraction with a sandwich structure similar to mixed potassium/mercury intercalates and a stacking sequence CCKHKCC... The stage II nature of the compound is further shown by the fact that $C_8KH_{\frac{2}{3}}$ will intercalate more K,Rb,Cs to form $C_8KH_{\frac{2}{3}}.\frac{1}{2}M$; these are single compounds with a coppery colour and a c axis repeat distance consistent with the intercalation of M^+ [110,47]. Furthermore, $C_8KH_{0.6}$ (but not $C_8KH_{\frac{2}{3}}$) will physisorb small quantities of hydrogen in a manner similar to $C_{24}K$ to give $\approx C_8KH_{0.6}(H_2)_{0.08}$[47].

Other intercalates will also chemisorb hydrogen, but less readily. Thus C_8Rb will only form $C_8RbH_{0.05}$ at atmospheric pressure, requiring

170 atm to form $C_8RbH_{\frac{2}{3}}$. C_8Cs will not absorb hydrogen even at 200 atm [109]. $C_{24}K$ absorbs hydrogen to give $C_{24}KH_{0.36}$ at atmospheric pressure, $C_{24}KH_{0.54}$ at 130 atm [109]. The product is almost black and has been characterized as stage III by X-ray diffraction[47]. The amount of hydrogen physisorbed by $C_{24}KH_x$ decreases linearly with x with an intercept of zero physisorption at x = 0.66 [47]. The compounds will also chemisorb deuterium, but there is considerable isotopic dependence; deuterium has a desorption pressure six times higher than hydrogen[109].

There has been a considerable amount of research into the chemical state of the absorbed hydrogen. ESR spectra[111,112] show a Dysonian lineshape typical of metals. Conard et al[111] noted a large ^{13}C NMR Knight shift which was attributed to the negative charge in the hydrogen layer, and the lack of a proton NMR line (later weakly observed) was attributed to the presence of paramagnetic H_2^- ions. (In the gas phase, H_2^- undergoes pre-ionization in 10^{-14}sec - See Appendix I.) Enoki et al [112] studied the ESR spectrum of C_8K during hydrogen uptake (without measuring the composition) as a function of time and found a signal which increased then decreased, which was attributed to the dissociation of H_2 to $H^\cdot$ followed by ionization to H^-. Beaufils et al[113], studying the neutron diffraction pattern of $C_8K \rightarrow C_8KD_{\frac{2}{3}}$ in situ postulated a similar two step mechanism. Finally, Trewern et al[114] examined the inelastic neutron spectrum of $C_8KH_{\frac{2}{3}}$ and $C_8KD_{\frac{2}{3}}$ in both the μeV and meV regions. Although librational lines were seen, the absence of a tunnelling spectrum, in contrast to the case of physisorbed hydrogen, (Chapter 7) is further evidence against the species H_2^-.

1.5.2 Physisorption of Hydrogen and other Gases

In 1971/3 Watanabe et al[115,116] reported that the stage II intercalates $C_{24}M$ would physisorb hydrogen at temperatures below 90-100K to form compounds of stoichiometry $\approx C_{24}M(H_2)_2$. The reaction was fast and

reversible, and also occurred for $C_{36}K$ but not the stage I compounds C_8M. Deuterium was absorbed more easily than hydrogen, in contrast to chemisorption. Other gases, nitrogen, argon and methane were also absorbed to a greater or lesser extent by $C_{24}Rb$ and $C_{24}Cs$ only. Helium and neon were not absorbed at 63K. Mixtures of deuterium and argon over $C_{24}K$ at 77K resulted in the absorption only of the deuterium, the argon remaining wholly in the gas phase. Mixtures of deuterium and nitrogen at 77K gave a less marked separation, and more nitrogen was absorbed from the N_2/D_2 mixture than would have been absorbed from N_2 alone at that temperature. H_2/D_2 mixtures over $C_{36}K$ at 90K also concentrated the deuterium in the absorbed phase, regardless of whether the H_2 or D_2 was absorbed first, or whether a mixture of both gases was introduced.

The intercalates, therefore, had a molecular sieve type action, similar to zeolites[117]. This was reflected in the heats of absorption (10-30 KJ/mol) and the equilibrium pressures, $C_{24}Cs$ being the best absorbant, and nitrogen having the greatest heat of absorption. Measurement of the 00ℓ lines of $C_{24}K(D_2)_2$ by neutron powder diffraction indicated a slight c axis expansion from 8.67 to 8.96Å, showing that the intercalate was still stage II with the absorbed deuterium in the plane of the metal ions.[##] This also explained the absorption and desorption isotherms: the combination of small metal ions and large gas molecules, if absorption occurred at all, was most likely to produce an isotherm in the form of an "all or none" step function, whereas the reverse gave a smooth increase in absorption with increasing pressure. The $C_{24}K/H_2$ and $C_{24}Cs/CH_4$ systems showed no hysteresis on gas absorption and desorption; slight hysteresis was observed for $C_{24}Rb/Ar$. Absorption data and molecular diameters are listed in Table 1.1.

This contrasts with the zeolites, where the aluminosilicate framework is completely rigid[116,117].

Table 1.1 Watanabe's Physisorption data for Intercalate/Gas Systems[116]

	H_2, D_2	N_2	Ar	CH_4
Molecular diameter (A):	2.40	3.00	3.80	4.00

Absorptive Capacity of Alkali Graphites (mol)

	He,Ne	H_2, D_2	N_2	Ar	CH_4
$C_{24}K$	-	2.10	0.7	-	-
$C_{24}Rb$	-	2.05	1.0	1.2	0.9
$C_{24}Cs$	-	2.00	1.3	1.4	1.2
C_8M	-	-	-	-	-

A dash indicates no absorption. Temperature range 196 to 63K.

Equilibrium Pressure/KPa at Half Coverage at 90K

	H_2	D_2	N_2	Ar	CH_4
$C_{24}K$	12.0	2.5	-	-	-
$C_{24}Rb$	0.49	0.12	(1.0×10^{-5})	9.7	0.35
$C_{24}Cs$	0.17	0.055	(1.3×10^{-7})	0.01	(7.3×10^{-5})

A value in brackets is extrapolated from one at a higher temperature using the Clausius-Clapeyron equation.

Isosteric Heat of Absorption $-\Delta H/KJmol^{-1}$ at Half Coverage

	H_2	D_2	N_2	Ar	CH_4
$C_{24}K$	9	11	-	-	-
$C_{24}Rb$	11	12	23	11	13
$C_{24}Cs$	12	13	26	15	20

Partition of a 1:1 H_2/D_2 mixture over $C_{36}K$ at 90K

		H_2	D_2
gas phase	volume %	81	41
	P/KPa	2.8	1.4
absorbed phase	volume %	19	59
	mol. absorbed	0.23	0.70

Kondow's data for in-plane Resistivity at 77K ($\mu\Omega$.cm) [ref 118]

$C_{24}K$ 7.42±0.3 $C_{24}K(H_2)_2$ 8.53±0.2 $C_{24}K(D_2)_2$ 12.04±0.1

Watanabe[116] also attempted to establish the structure of the absorbed molecules, but with only a powder sample and an unknown in-plane structure for the metal ions in the intercalate, he could not determine whether the deuterium molecules lined up parallel or perpendicular to the graphite c axis.

More recently, Kondow et al[118] measured the electrical resistivity of $C_{24}K$, $C_{24}K(H_2)_2$ and $C_{24}K(D_2)_2$ as a function of temperature, and found that the in-plane resistivity increased somewhat on gas absorption, the effect being much greater for D_2 than H_2 (Table 1.1). They also found that the resistive anomaly seen at 98K for $C_{24}K$ and associated with T_L disappeared on gas absorption.

Beyond these reports, this phenomenon has been little researched. $C_{36}K$ [116] and $C_8KH_{0.6}$ (stage II) (but not $C_8KH_{\frac{2}{3}}$)[47] will also physisorb hydrogen, as will $ZrS_2Cs_{0.37}$[119]. An un-named dark blue caesium intercalate, probably $C_{24}Cs$, was reported to catalyze both ortho-para conversion in hydrogen and H_2/D_2 equilibration at 195-300K with an activation energy of 0.6 Kcal/mol [120].+ Watanabe et al[122] further studied the H_2/D_2 equilibration with potassium intercalates at 0°C and found that the order of catalytic activity was $C_{24}K > C_{36}K \geq C_8KH_{\frac{2}{3}} >> C_8K \approx 0$. The first order rate constant for $C_{24}K$ at 0°C was 1.23/hour. However, 0°C is well above the temperature range for physisorption, and Watanabe did not report the presence of HD in his later hydrogen/deuterium partition experiments over $C_{36}K$ [116].

The physisorption appears to resemble the incorporation of liquid solvent molecules with species such as $C_{24}K(DMSO)_3$, $C_{24}K(C_6H_6)_3$ [123], $C_{24}K(THF)_2$ [124], $C_{24}K(toluene)_{1.2}$, $C_{24}K(xylene)_2$ [125], and also absorption by liquid ammonia, hexamethylphosphoramide, ethylenediamine,

---

+ Ortho/para conversion rate for H_2 = 1.90%/hr and for D_2 = 0.06%/hr in the pure solid. In the gas phase at STP, the conversion is much slower[121].

pyridine and oxolan[28] having been reported. Absorption of the larger molecules causes considerable c axis expansion; $C_{24}K(DMSO)_3$ has a c axis of 15.0A [123].

1.5.3 De-intercalation Reactions

The decomposition reactions of the alkali metal graphite intercalates have been studied by Daumas and Hérold[58]. Oxygen and water both react very rapidly with C_8K at room temperature to give graphite + KO_2 and graphite + KOH + $\frac{1}{2}H_2$ respectively. Other oxidizing gases react similarly: NO and NO_2 react at room temperature to produce complex products, N_2O gives KO_2 + $2N_2$ above 120°C, SO_2 gives K_2SO_4 + S (or possibly $K_2S_2O_3$) at 300°C, CO_2 gives the oxalate at 220°C, the carbonate at 350°C. CO gives a slow de-intercalation at 200°C so that pure higher stages can be isolated.

Reaction with halogens is superficially similar, resulting in a black product with stoichiometry C_8MX or $C_{24}MX$ (X = Cl,I; M = K,Cs). The black product, however, does not appear simply to be a mixture of the alkali metal halide and graphite and undergoes distinctive intercalation reactions with alkali metals, alkali metal halides and mercury(II) chloride[126].

1.5.4 Catalysis

Alkali metal graphite intercalates catalyze a large number of reactions such as H_2/D_2 exchange, methane/deuterium exchange, hydrogenation of alkenes, Fischer-Tropsch synthesis of hydrocarbons from hydrogen and carbon monoxide, double bond isomerization, dimerization of alkenes and polymerizations. However, their great sensitivity to air and water limits their usefulness. Metal halide intercalates will also catalyze brominations, ammonia synthesis and graphite to diamond interconversion. The catalytic properties of the alkali metal graphite intercalates are summarized by Boersma[29] and those of the metal halide intercalates by Novikov and Vol'pin[127].

APPENDIX I : THE SPECIES H_2^- IN THE GAS PHASE

In its ground state H_2^- is $^2\Sigma_u^+$ with electron configuration $1\sigma^2 1\sigma^*$ and is thus paramagnetic. The ground state has energy +3.75 eV for the process $H_2 + e^- \rightarrow H_2^-$, and there are also several excited states around 11 eV [128]. The $1\sigma^*$ orbital has no orbital angular momentum, but the unpaired electron spin would be expected to couple with the molecular rotational levels, possibly causing Λ doubling as in Hund's case (b) [129].

The bond length of H_2^- has been calculated by Sharp[130] to be the same as that for H_2, but with a smaller bond energy. Any charge transfer in the physisorbed hydrogen should thus be expressed as a shift in the H-H stretching frequency, enabling the amount of charge transfer to be measured.

It was on these premises that H_2 was proposed as the absorbed species in $C_8KH_{\frac{2}{3}}$[111]. On closer examination, however, it emerges that Sharp[130] was concerned mainly with H_2 and H_2^+, and merely sketched in a guessed potential curve for H_2^- on an otherwise accurately calculated diagram. Furthermore, the $^2\Sigma_u^+$ ground state of H_2^- is highly unstable in the gas phase, undergoing pre-ionization to $H^- + H^\cdot$ in 10^{-14} sec, less than one vibrational period; this is reviewed by Schulz[128]. Various low energy electron scattering experiments[131] have been carried out and agree that while there is some evidence for a minimum in the potential curve, the $v = 0 \rightarrow 1$ frequency of the the $^2\Sigma_u^+$ state cannot be determined. By contrast, the excited states of H_2^- are stable enough to show a well developed vibrational structure in electron scattering experiments, with the $v=0 \rightarrow 1$ transition at around 280 meV [132]. Potential curves for these states have been calculated by Eliezer et al [133].

CHAPTER 2

THE CHEMISTRY OF POLYACETYLENE

INTRODUCTION

A very large number of papers and conference proceedings have been published about polyacetylene, but a good and thorough general account is given in Chien's book[2], published in 1984, while Nehmé's thesis [134] provides more material on the Luttinger synthesis.

2.1 SYNTHESIS

Acetylene is polymerized chemically, unlike polypyrrole which is usually produced electrochemically. A variety of methods has been used, of which only the most important are listed here.

2.1.1 Ziegler-Natta catalyst

This method, also known as Shirakawa's method[135], is used by the vast majority of researchers, including Chien[2]. The catalyst consists of titanium tetrabutoxide dissolved in toluene at -78°C to which triethylaluminium is added. The mixture is allowed to warm to room temperature for half an hour. It is then cooled again and shaken so that the walls of the vessel are wetted. Acetylene is admitted and immediately polymerizes on the wetted section of wall to form a thin film of cis-polyacetylene. To form trans-polyacetylene, the reaction can either be carried out at 70°C or the cis isomer can be isomerized by heating at 180°C for half an hour. This method is also suitable for bulk preparations.

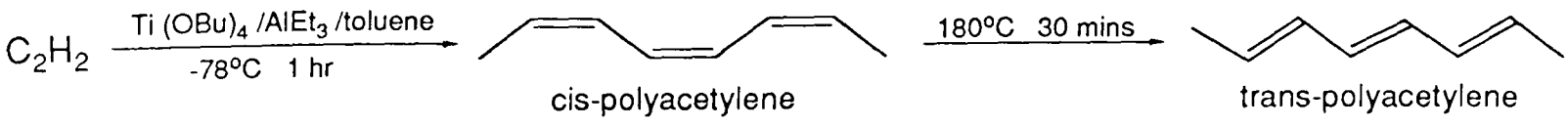

The problem with this method is that the catalyst is extremely air-sensitive and all work has to be done in a high vacuum or a good dry box. The mechanism of polymerization is complex and not fully understood, but probably involves steps such as:

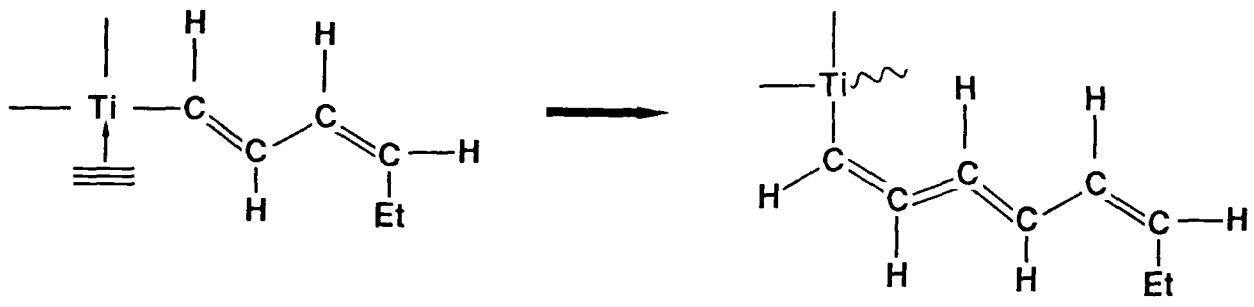

Where the other ligands on the Ti atom are not specified.

2.1.2 Luttinger Catalyst

This method, originated by Luttinger in 1960[136,137] can involve a variety of transition metals. The present study followed the version used by Nehmé[134,138]. Sodium borohydride and cobalt(II) nitrate are dissolved in ethanol and cooled to -78°C. When the two solutions are mixed, a carmine coloured cobalt complex forms. Acetylene is added, and cis-polyacetylene forms as a gel. (See also Section 4.1.) This method has the advantage that the catalyst is not air sensitive (although cis-polyacetylene is). The disadvantages are that the catalyst decomposes above -35°C and that special methods have to be used for thin films[134,139].

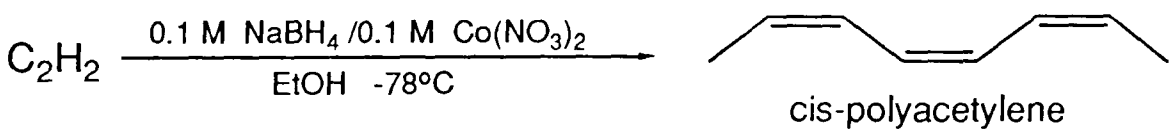

The mechanism of the polymerization and the nature of the complex are discussed by Nehmé.

2.1.3 Durham Polyacetylene

A new form of polyacetylene can be formed by thermal elimination[140,141]:

e.g.

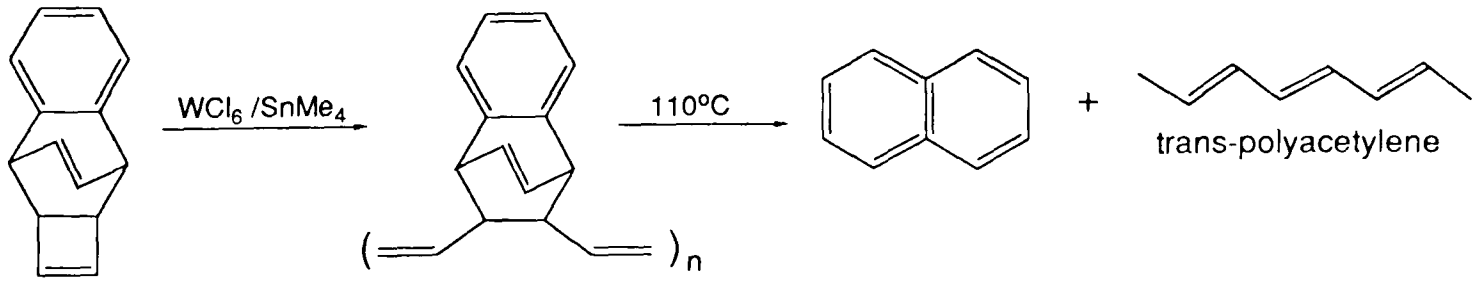

This method has the advantage that the intermediate polymer is soluble in common solvents. The final product is normally amorphous and more difficult to dope than trans-polyacetylene produced by the

Ziegler-Natta or Luttinger methods. The degree of order can, however, be greatly increased by uniaxial stress on the intermediate polymer, and the resultant has an anisotropic conductivity[142].

2.2 STRUCTURE AND MORPHOLOGY

Polyacetylene occurs in cis and trans forms:-

cis-polyacetylene

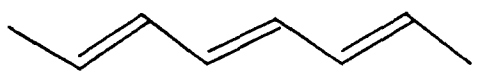

trans-polyacetylene

Both of these are greyish, insoluble powders, shiny as films. To transmitted light, cis-polyacetylene is red and trans-polyacetylene is blue. The cis form is produced in low temperature syntheses, but is metastable and readily isomerizes to the trans form on heating[143] or doping[144]. This process also takes place slowly at room temperature and is speeded up by exposure to air[139]. The cis:trans ratio of a sample can be determined from the infra-red spectrum[145,139], since the peaks at 770 and 446 cm^{-1} only occur in the cis isomer, while the peak at 1015 cm^{-1} only occurs in the trans isomer[143]. It might be expected that all the C-C bonds in trans-polyacetylene would be the same length. This is not in fact the case since both cis- and trans-polyacetylene are semiconducting rather than metallic. The bond alternation is confirmed by X-ray[146], NMR[147], and theoretical[148,149] studies and is an example of a Peierls distortion[1].

A crystal structure for cis-polyacetylene has been proposed by Baughman et al[150] and for trans-polyacetylene by Fincher et al[146] on the basis of X-ray and other data. Powder neutron diffraction patterns have also been measured by Riekel et al[151] and are in broad agreement. Cis-polyacetylene has an orthorhombic unit cell with a Pnma space group and eight carbon atoms per unit cell. Trans-polyacetylene has a monoclinic unit cell with a P21/n space group and four carbon atoms per unit cell. The monoclinic angle in trans-polyacetylene is estimated at

91.5°, making the structure very nearly orthorhombic, and it repeats along the chain axis every two CH groups instead of four. Confusion is caused by the axis labelling convention: the chain axis is denoted by b in cis-polyacetylene and by c in trans-polyacetylene. The structures and unit cell parameters are given in Figs 2.1 and 2.2. It should be stressed that the X-ray patterns themselves are not of sufficient quality to determine all the parameters and other data have also had to be used.

Recently, a greatly improved diffraction pattern has been obtained from trans-polyacetylene prepared by the Durham method, with the intermediate polymer subjected to uniaxial stress prior to heating. The values of the cell parameters obtained are close to those of Fincher et al[146], who used the Ziegler-Natta catalyst, but no full X-ray intensity analysis was carried out[142]. Nehmé also made a close study of Luttinger polyacetylene using X-ray, neutron and electron diffraction, and infra-red and ultraviolet spectroscopy, concluding that while there were differences in the amount of crosslinking and chain length, the overall crystal structure was the same[134].

The mass of a polyacetylene chain varies with reaction conditions, but a typical number average is 7000 with a mass average of 15000. [2,152] In Durham polyacetylene, the chains are longer (M_n = 100000, M_w = 300000) [153], but with the Luttinger method considerable quantities of oligomers are also produced. It is believed that the polymer chains are not appreciably crosslinked when formed, but that they may become crosslinked over time[134].

The bulk density of polyacetylene is about 0.4 g/cm^3 compared with a value of 1.18 g/cm^3 as obtained from floatation techniques[154,155]. The reason is that polyacetylene consists of a mass of randomly oriented fibrils about 200Å in diameter, which only occupy about a third of the

Fig 2.1 Baughman's Structure for Cis-polyacetylene[150]

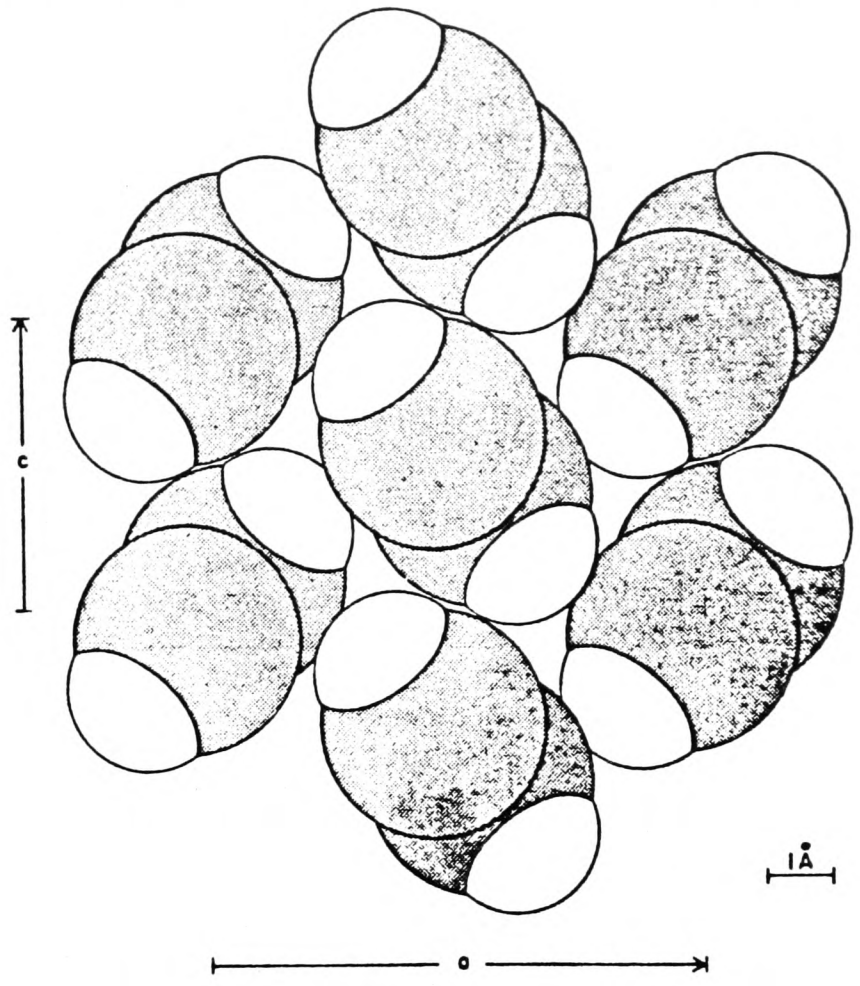

Chain axis projection of the structure of cis-polyacetylene.

Hydrogen atoms are white and carbon atoms are grey.

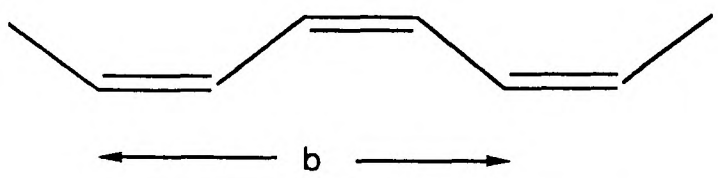

Unit cell data: Orthorhombic space group Pnma

a = 7.61 Å, b = 4.47 Å, c = 4.39 Å

Eight CH groups per unit cell gives theoretical density 1.16 g/cm^3

Molecular data used in peak intensity calculations:

C-C bond length 1.46 Å

C=C bond length 1.35 Å

C-H bond length 1.09 Å

C-C-H bond angle 120°

C-C-C bond angle 127.3°

ϕ angle between polymer backbone and ab plane 50.8°

Riekel's neutron data[151]: a = 7.45 Å, b = 4.40 Å, c = 4.30 Å

Fig 2.2 Fincher's Structure for Trans-polyacetylene[146]

(Made by Shirakawa's method and oriented by stretching)

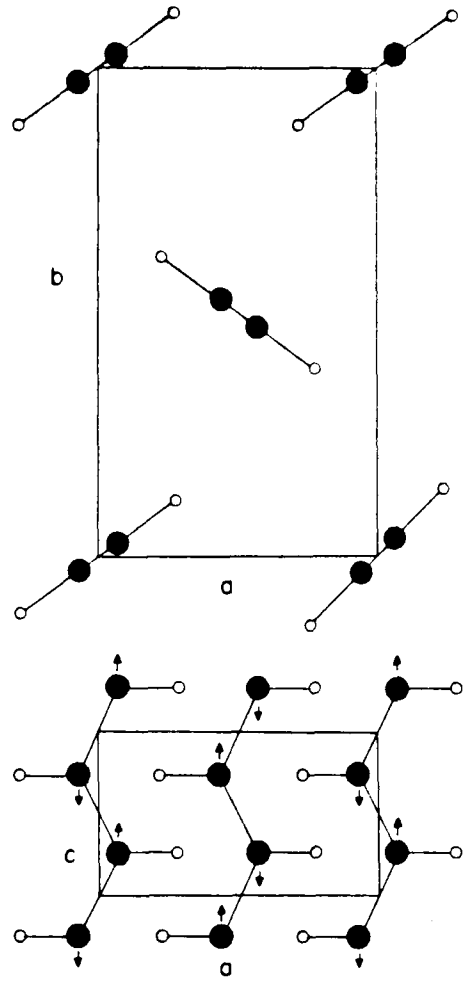

Two schematic projections of the structure of trans-polyacetylene

Unit cell data: Monoclinic space group P21/n

a = 4.24 Å, b = 7.32 Å, c = 2.46 Å, β = 91.5°

Molecular data: Setting angle ϕ = 55° from 010 plane

Bond alternation 0.03 Å and out of phase

i.e.

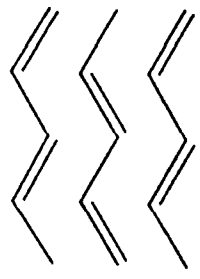

Riekel's neutron data measured at 4K [151]:

Orthorhombic unit cell

a = 3.99 Å, b = 7.29 Å, c = 2.51 Å

Oriented Durham polyacetylene[142]: a = 4.18 Å, b = 7.34 Å, c = 2.43 Å,

β = 90.5°

total space. This fibrillar structure has been demonstrated in many electron micrographs and appears to be the same for both Ziegler-Natta[2] and Luttinger[134,138] preparations. These fibrils can be partially aligned by mechanical stretching with an improvement in the quality of the diffraction pattern[134,154].

2.3 THE CHEMISTRY OF DOPING

Doping was first achieved in 1977 by Shirakawa et al[156] when they found that when trans-polyacetylene was exposed to bromine or iodine vapour (and later arsenic pentafluoride[157] or sodium naphthalide), [158] it ceased to transmit infra-red light and its conductivity increased from 10^{-5} S/cm to 10^{2} S/cm. Since this time, a large number of dopants have been used, but most work has been done with these ones. Cis-polyacetylene can also be doped, partially isomerizing in the process[144,159]. Furthermore, it was found that conducting sodium doped polyacetylene could be undoped or compensated by exposure to arsenic pentafluoride or iodine vapour[160], and that the conductivity of trans-polyacetylene could be **lowered** by more than four orders of magnitude by exposure to ammonia without detectable increase in mass[158]. Conductivities and compositions vary widely and can be misleading since the time taken for the dopant ions to diffuse through the fibrils was not originally appreciated[161]. The conductivity would be expected to be highly anisotropic, but sample crystallinities are generally not good enough to quote separate values for measurements parallel and perpendicular to the chain direction, in contrast to the graphite intercalates (See Introduction - Table 2). A comprehensive list of dopants and conductivities is given in Chien's book[2] of which a selection is shown in Table 2.1.

The usual method of p-doping is by direct combination; oddly enough, this is not popular for n-doping. (The only literature mention of

Table 2.1 Conductivities of some Polyacetylenes (after Chien[2])

	undoped[160]	S/cm at 298K
trans	$(CH)_x$	10^{-5}
cis	$(CH)_x$	10^{-9}
trans	$[CH(NH_3)_y]_x$	$<10^{-9}$
	p-dopants	
trans	$[CH(HBr)_{0.04}]_x$	7×10^{-4}
cis	$[CHI_{0.3}]_x$	550
trans	$[CHI_{0.2}]_x$	160
trans	$[CH(AsF_5)_{0.10}]_x$	400
cis	$[CH(ClO_4)_{0.0645}]_x$	970
cis	$[CH(CF_3SO_3H)_y]_x$	-
	n- dopants	
cis	$[Li_{0.3}(CH)]_x$	200
cis	$[Na_{0.21}(CH)]_x$	25
cis	$[K_{0.16}(CH)]_x$	50
trans	$[Na_{0.28}(CH)]_x$	80
cis	$[(Bu_4N)_{0.08}(CH)]_x$	-

n-doping by direct combination is by Baughman et al[162] who used a sodium/potassium eutectic.) Mention has already been made of sodium naphthalide; a gentler alternative is sodium in benzophenone[163]. Both n- and p-type doping have been carried out electrochemically and this has formed the basis of the polyacetylene battery[164-166] and allowed measurement of the electrode potentials of polyacetylene for both p- and n-type doping[167,168,289].

In n-doped polyacetylene, the dopant exists as M^+ ions[162]. In p-doped polyacetylene, however, the situation is less clear-cut. Raman [155,160,169-171], photoelectron[152,172] and Mössbauer[173,174] spectra of iodine doped polyacetylene demonstrate that most of the dopant exists as I_3^- with some I_5^- present at high doping levels. AsF_5 is thought to

disproportionate to AsF_6^- and the inert AsF_3[159,175].[+] The conductivity σ increases with temperature in both the doped and undoped material. This contrasts with normal metals and the graphite intercalates[8] whose conductivities **decrease** with temperature, and suggests an activated conduction mechanism, similar to a semiconductor. However, the temperature dependence is weak, a plot of $\ln\sigma$ versus $T^{-\frac{1}{4}}$ (not 1/T) giving a straight line[157]. A number of studies have been made to determine the conductivity and ESR spectrum as a function of dopant concentration. The most careful one was by Chien et al[159], who also took electron micrographs to ensure that the dopant was evenly distributed throughout the sample. The doping caused the fibrils to swell.

For doped polyacetylene of composition $[CH(AsF_5)_y]_x$ or $[CH(I_3)_y]_x$, the semiconductor to metal transition was originally thought to occur at $y = 0.01-0.03$ [157]. Chien's study[159] showed this to be incorrect, and when log scales were used, the midpoint of the transition was 7×10^{-4}. The thermopower shows a similar variation. By contrast, the Pauli magnetic susceptibility only shows an increase at $y = 0.06-0.10$ [161], suggesting that the conduction does not take place via free carriers. Furthermore, ESR studies[159] on cis-polyacetylene show that at low doping levels ($y = 10^{-4}$), a narrow line appears on top of the broad line due to the undoped polymer, and it is only at high doping levels ($y > 0.02$) that the signal acquires an asymmetric Dysonian lineshape typical of metals. It is thus clear that the mechanism of conduction in polyacetylene corresponds neither to the electron-hole formalism of inorganic semiconductors nor to the free electron model in a metal. This mechanism has been rationalized in terms of the soliton model. (See Appendix II)

+ In AsF_5 intercalated graphite there is evidence for this by XPS[42].

2.3.1 Structure of p-doped polyacetylene

Diffraction patterns from doped polyacetylene have up to now been relatively poor. This may be a consequence of uneven doping, but nevertheless, polyacetylene heavily doped with either arsenic pentafluoride[151,176] or iodine[155,177] clearly shows a low angle line corresponding to a d spacing of approximately 8Å, together with various other higher angle lines indicating a new structure.

By analogy with the graphite intercalates, two structures have been proposed for p-doped polyacetylene. There is the stage I model, where each layer of polyacetylene chains is separated by a layer of dopant ions (Fig 2.3). This has been proposed for all levels of arsenic pentafluoride doping[176] and for heavy iodine doping[155,177]. Given a spacing between dopant ions of 9.4-9.7Å, the value observed for chains of I_3^- in conducting radical cation salts and tetra-(n-butyl)ammonium iodide[20,178,179], Baughman et al[180], calculated the maximum dopant concentration as $[CH(I_3)_{0.13}]_x$. For less heavy iodine doping, a stage III model has been proposed with limiting composition $(CHI_{0.13})_x$ where sheets of I_3^- are separated by three layers of polyacetylene chains[180]. At still lower doping levels, half the positions occupied by I_3^- can be replaced by polyacetylene chains (Fig 2.3). There is no evidence for this structure with AsF_5 dopant[176] nor for any stage II type compound[180].

2.3.2 Structure of n-doped polyacetylene

The diffraction pattern of n-doped polyacetylene is quite different from that of p-doped polyacetylene and Baughman[162,287] has proposed a tetragonal structure with the dopant ions lying in channels between the polyacetylene chains (Fig 2.4). In his X-ray analysis of partially oriented polyacetylene doped with alkali metals, Baughman observed equatorial lines at 6.0-6.43 Å, depending on the alkali metal, with the

Fig 2.3 Structural Models for p-doped Polyacetylene

(projected along chain axis)

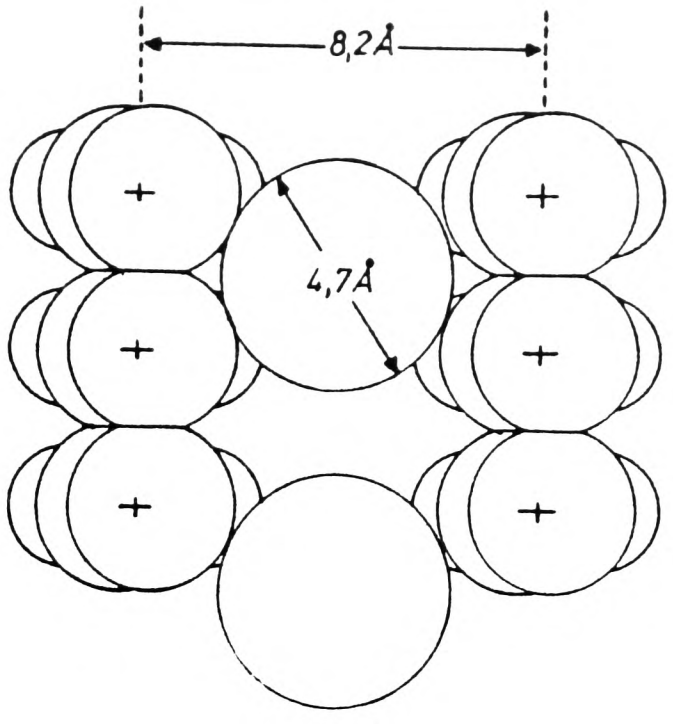

Stage I model proposed for AsF_5 doping and heavy iodine doping[176] (Diagram illustrates doping with AsF_5) The distance of 8.2A corresponds to the low angle diffraction peak not seen in undoped polyacetylene[176].

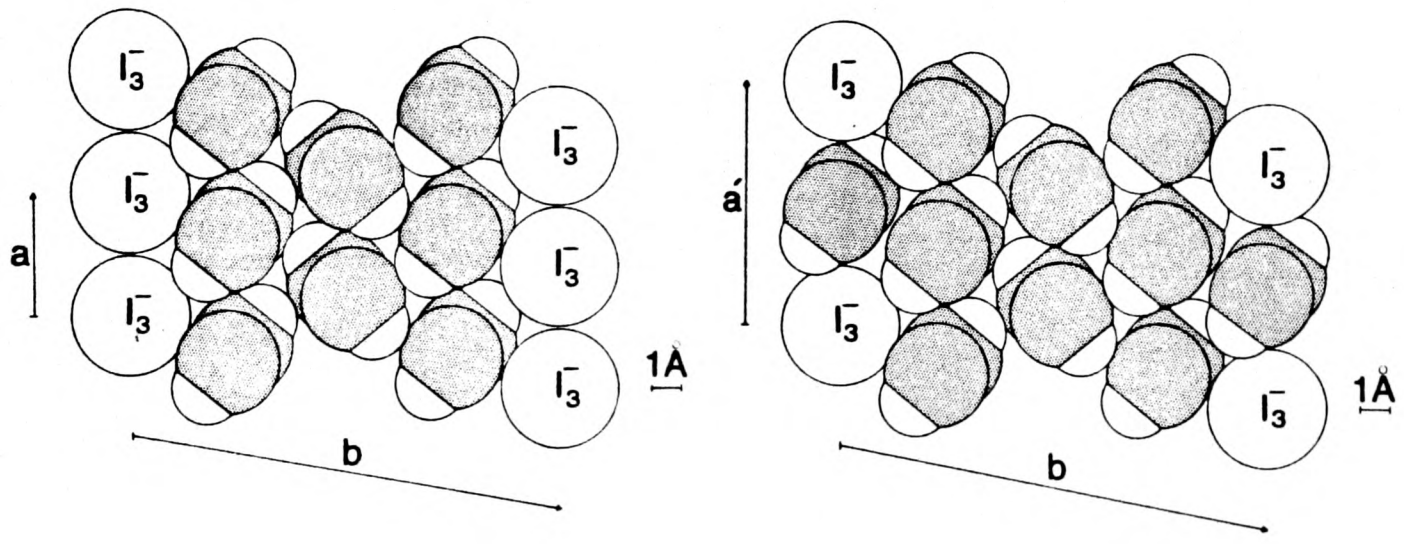

Baughman's stage III models for moderate iodine doping[180].
Compositions are $(CHI_{0.13})_x$ and $(CHI_{0.056})$ respectively.
a = 4.08 Å, b = 14.5 Å, γ = 100.5°
a'= 2a, data otherwise similar.

exception of the lithium doped sample which was disordered. From these data, he postulated that this corresponded to the interchannel spacing. For small dopant ions (Na^+, K^+), the polyacetylene chains touch and the interchannel distance is limited to 6Å. For larger ions (Rb^+, Cs^+), the lattice expands and the interchannel distance depends on the size of the dopant ion. These metal-metal distances are largely confirmed by Flandrois et al[288], but these authors propose a layer model, similar to p-doped polyacetylene.

Baughman[162] also observed meridional lines at 3.5-3.8Å and 4.4Å in the potassium and rubidium doped samples respectively. However, undoped polyacetylene has an intense line at 3.8Å, and Baughman's equatorial 110 line at d spacing 6.19Å in the rubidium doped sample predicts a 200 line at 4.38Å. The meridional lines may, therefore, be suspect.

In this structure, the a and b cell parameters are $\sqrt{2}$ times the interchain distance in a body centred structure. Hence, the line at 6.0 to 6.43Å is properly indexed as 110 with the 100 line absent. The space group is either I4cm or I4/mcm depending on whether or not the bond alternation in undoped polyacetylene is maintained in the doped compound.

Indirect structural information has recently been obtained by Shacklette and Toth[289], who measured the reduction potential of sodium and potassium doped polyacetylene as a function of dopant concentration, and obtained plateaux at distinct compositions eg $(C_4H_4)_4K$, $(C_4H_4)_3K$, $(C_4H_4)_2K$, $(C_3H_3)_2K$. They suggest that for composition $(C_nH_n)_mM$ n is the number of carbon atoms between each metal ion along the chain axis and m the number of polymer chains per channel of metal ions in the ab plane. (In Baughman's model shown in Fig 2.4, m is two with n unspecified.) When n is four, the metal-metal distance along the chain axis is 4.96Å. This is **exactly** the same as the in-plane metal-metal distance in the

Fig 2.4 Baughman's Structural Model for n-doped Polyacetylene[162]
(projected along chain axis)

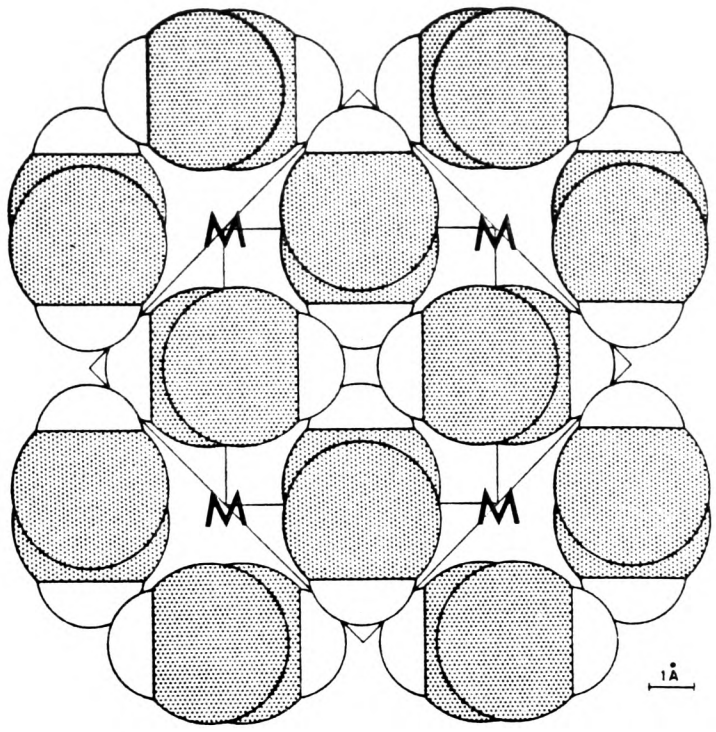

Carbon atoms are grey, hydrogen atoms are white. The metal ions, denoted by M, lie in the channels. The small square, side a', is the unit cell of the projection, the probable 3D unit cell being given by the larger square.

Variation of unit cell parameters a' with metal ion

Metal	a' calc A	a' obs A[162]	a' obs A[288]
Li	(4.45)*	amorphous	4.5 ±0.1
Na	(5.22)*	5.98±0.1	5.98±0.05
K	5.94	6.0 ±0.1	6.15±0.05
Rb	6.16	6.19±0.07	
Cs	6.43	6.43±0.07	6.42±0.05

* Minimum calculated parameter for polyacetylene chains not to overlap is 6.04±0.36Å.

Meridional lines:

Metal	d spacing A
K	3.5-3.8
Rb	4.4

Space group: Tetragonal I4cm or I4/mcm

(2×2)R0° structure in C_8K (Fig 1.5), and a trans-polyacetylene chain will correspond exactly with a zig-zag line of carbon atoms in the graphite structure, with the dopant ions in the same positions as the metal ions in the intercalate. (The distance between adjacent polymer chains, however, is more than the C-C bond length in graphite.) Similar correspondence to the $(\sqrt{3}\times\sqrt{3})R30°$ structure in C_6Li is obtained when n is three, but this time the dopant ions are on alternate sides of the polymer chain. These facts suggest that a reason for the poor diffraction patterns from doped polyacetylene samples to date has been the arbitrary levels of doping, resulting in mixtures of several stages.

2.4 REACTIONS OF POLYACETYLENE

Discussion of the chemistry of polyacetylene has so far centred on the reversible doping and compensation reactions. Polyacetylene is, however, also a conjugated linear polyene and can undergo the irreversible reactions characteristic of such compounds.

Undoped polyacetylene becomes doped on exposure to oxygen with a large increase in conductivity[181-183]. This reaction is partially reversible in its early stages, but on prolonged exposure it becomes degraded with a decrease in conductivity. Doped polyacetylene tends to lose conductivity on exposure to air, the value falling by an order of magnitude in a week[183,184]. It is also highly unstable to water, where the conductivity was observed to fall by four orders of magnitude in a single day[184,185]. In highly acidic aqueous solution, however, it maintains conductivity[185]. (This does not necessarily mean that the dopant remains unchanged - the final product was not analysed chemically.) For the above reasons, most polyacetylene chemistry is done in vacuo or a dry box with non-aqueous solvents such as propylene carbonate. Air exposure of the undoped material for no more than a few minutes is, however, usually tolerated.

In addition to being air and water sensitive, polyacetylene shows some tendency to undergo irreversible reaction with dopants. While bromine can act as an effective dopant, excess bromine or heating the doped material cause it to go yellow/white and the conductivity to drop to 10^{-6} S/cm with evolution of HBr [2,186]. Long term, samples doped with arsenic pentafluoride, iodine and iron(III) chloride tended to lose conductivity even in a dry box. However, when kept at -30°C in an argon dry box, the conductivity stabilized after a few days[184].

A further example of substitution is the reaction of alkali metal doped polyacetylene with hydrogen. Whereas undoped and p-doped polyacetylene are inert to hydrogen, n-doped polyacetylene shows several distinct reactions. First, hydrogen and deuterium gas will exchange over n-doped polyacetylene at room temperature in a manner similar to the graphite intercalates (Section 1.5.2). Second, deuterium gas can exchange with hydrogen atoms in the polyacetylene chain. This takes place at 150 to 200°C with low pressures of deuterium. (NB n-doped polyacetylene on its own is stable to 230°C.) All the hydrogen atoms in the polyacetylene were found to be accessible and equilibrium was reached after 250 hours with 85 torr deuterium at 200°C [2,187].

If more hydrogen is used, an addition reaction takes place and the product is transparent and soluble in hot tetralin[152,187]. When methanol is added, hydrogen is evolved suggesting the presence of a metal hydride[188]. (Methanol[189] or ethanol[190] vapour will also react directly with the n-doped polyacetylene.) Visible, infra-red and Raman spectra all indicate that the hydrogen adds in a random fashion, introducing CH_2 groups and interrupting the conjugation of the polymer backbone[189-191]. On taking the reaction to completion, the final product is polyethylene[188]. Hydrogenated samples redoped with iodine, show poor electrical conductivity. The solubility in hot tetralin has

been used for determining the molecular weight of the fully hydrogenated polymer and hence the original polyacetylene [152]; these are not necessarily the same since crosslinking and/or scission may have occurred during doping and hydrogenation.

Undoped polyacetylene is relatively stable to heat. Ito et al[143] measured loss of mass and phase transition enthalpies on heating and found that below 200°C no change occurred other than cis-trans isomerization. Above about 350°C, the sample started to lose mass and thermal transitions were observed at 325°C and 420°C; these were attributed to crosslinking and decomposition respectively. n-doped polyacetylene also appears to undergo no visible changes up to 230°C, but p-doped polyacetylene is less thermally stable, iodine doped polyacetylene being only stable to 80°C and AsF_5 doped polyacetylene to 130°C [187].

In a further study by Chien et al[2,192], polyacetylene and p-doped polyacetylene were pyrolyzed at temperatures between 500 and 1000°C. The products were then separated by gas chromatography and analysed in a mass spectrometer. The main product was found to be benzene with smaller amounts of methane, ethane, propene, ethane, butadiene, toluene and xylene. Doping greatly enhanced the yield of saturated hydrocarbons, the effect being greater for iodine than arsenic pentafluoride doping. (See Table 2.2.)

Table 2.2 Products of Pyrolysis of Polyacetylene at 650°C in order of increasing Boiling Point (after Chien[2])

		Mass yield relative to benzene from:		
Product	rmm	$(CH)_x$	$(CH(AsF_5)_{0.14})_x$	$(CHI_{0.06})_x$
methane	16	11.5	70.7	156.7
ethene	28	9.8	26.0	48.4
ethane	30	9.5	27.8	109.3
propene	42	9.3	19.5	56.2
			C4	34.7
butadiene	54	12.4	13.7	45.5
			C4	9.3
			CH_3I	41.4
cyclopentadiene	66	8.0	7.7	-
pentadiene	68	6.2	5.7	18.2
benzene	78	(100)	(100)	(100)
toluene	92	21.9	32.6	59.5

and many other high boiling point compounds.

CHAPTER 3

THE CHEMISTRY OF POLYPYRROLE

3.1 SYNTHETIC METHODS

Polypyrrole can be synthesized by a variety of methods, most of them involving oxidative coupling of pyrrole molecules in dilute solution with simultaneous doping. Conducting films form under a wide range of conditions but are liable to include atmospheric oxygen unless careful precautions are taken. In spite of the large number of recent papers on polypyrrole, no comprehensive review has been published, although the electrochemical synthesis and the redox properties of thin films are covered by Diaz and Kanazawa[193].

3.1.1 Electrochemical syntheses

(a) In Acetonitrile

These can be further subdivided depending on the counter-electrode reaction:-

(a i) H^+ reacts at counter electrode

(Electrolyte $R_4N^+BF_4^-$, $LiClO_4$ etc)[194,195]

This is the original method and remains by far the most popular. A 0.05M solution of pyrrole with 0.1M of a suitable salt are electrolyzed in acetonitrile with 1% water added. A variety of salts has been used such as R_4N^+ (R = Me, Et, Bu [196]) BF_4^-, PF_6^-, AsF_6^-, ClO_4^-, HSO_4^-, FSO_3^-, $CF_3SO_3^-$, $BrC_6H_4SO_3^-$, $C_7H_7SO_3^-$, $CF_3CO_2^-$ [197] and also $LiClO_4$ [19]. The chief requirements of the salt are that it should be non-nucleophilic and provide a suitable dopant. Thus Et_4NBr failed to produce a film [194]. Pyrrole turns brown on prolonged exposure to air and light and is best purified by drying quickly over solid potassium hydroxide followed by distillation, preferably under nitrogen[198]. The film forms on the anode, which can be made of any inert material, usually platinum, either as a solid electrode[199], or evaporated onto a microscope slide[196].

Transparent indium tin oxide electrodes[200] can also be used[19].+ The counter electrode is best made of gold wire, rather than platinum to allow the discharge of hydrogen gas at the electrode without the buildup of overpotential. The choice of a reference electrode suitable for acetonitrile presents a problem[202]; many workers have either used an aqueous calomel electrode or none at all[194]. Preparations have been carried out in both one compartment[196] and two compartment cells[201], with the reference electrode near the working electrode. The 1% of water added to the acetonitrile provides hydrogen ions for the counter electrode reaction[201] and improves film texture[203]. Films do not form at all if thoroughly dried acetonitrile is used[18], although ordinary acetonitrile contains considerable quantities of water[204]. This limits the chemical purity of the films produced. THF and dichloromethane have also been used as solvents[197].

Before starting, the cell is purged with nitrogen or helium for six minutes to exclude oxygen. A low voltage is always used for electrolysis, and the film forms on the anode, the thickness being controlled by the charge passed, each pyrrole ring incorporated corresponding to $2.3e^-$ [205,206]. Typical conditions for a 0.1 μm film suitable for studying by cyclic voltammetry are a potential of +810 mV versus calomel and a current density of 160 $\mu A/cm^2$, with a charge passed of 40 mC/cm^2 on a 0.5 cm^2 platinized microscope slide[196]. Such a film forms in a few minutes. Thick films (20 μm) suitable for chemical analysis can also be made using a current density of 500 $\mu A/cm^2$ on a 7 cm^2 electrode[196]. After manufacture, films should be washed with fresh 1% aqueous acetonitrile to remove traces of electrolyte. This is often done in a soxhlet extractor[206].

+ The electrode must withstand strongly oxidizing conditions, thus gold and palladium are usable but silver, indium, iron, and aluminium dissolve. Chromium, titanium and nickel form the polymer over a protective oxide layer[201].

(a ii) Ag^+ reacts at counter electrode[18]

The electrolyte consists of the silver salt of one of the anions described previously. $AgClO_4$ is the most common but $AgBF_4$, $AgPF_6$ [207], and $AgCF_3CO_2$ [204] have also been used. The working electrode is platinum or indium tin oxide, but the counter electrode is a silver wire onto which silver plates out during the electrolysis. The solvent is pure acetonitrile with no added water, and for this reason films produced by this method are reckoned to have the highest purity, particularly if the solvents are outgassed by freeze pump thaw cycles before use. However, the silver ions consumed during electrolysis are replaced by hydrogen ions from the pyrrole and the solution slowly becomes acid - this point is generally not appreciated (See Section 5.3). The reference electrode, if used, is another silver wire[204]. Electrolysis proceeds similarly at about 0.5V applied with a current of 1mA.

(b) In Aqueous Solution

Polypyrrole has also more recently been grown in water, but films produced this way tend to incorporate more oxygen and show somewhat less good conductivity[208]. Parallels to both acetonitrile syntheses exist.

(b i) H^+ reacts at counter electrode

Electrolyte salts used include Et_4NBF_4, $LiClO_4$, Na_2SO_4 [209], Na CF_3CO_2 [210] and $NaNO_3$ [211] as well as Dall' Olio's original preparation of conducting pyrrole black in dilute H_2SO_4 [212]. Platinum electrodes are normally used with concentrations similar to the acetonitrile preparations.

(b ii) Cu^{++} reacts at counter electrode[208]

Aqueous solutions of $CuSO_4$, $Cu(NO_3)_2$, $Cu(ClO_4)_2$ and $Cu_3(PO_4)_2$ have been used with copper plating out on the counter electrode. The solution becomes acidic during electrolysis, and film quality is poor with a conductivity of only about 8 S/cm and large amounts of excess oxygen.

3.1.2 Chemical preparations

(a) By oxidation of pyrrole monomer

Whereas red and black tars derived from the oxidation of pyrrole have been known for a long time[213-215], chemically prepared polypyrrole has been recognised only recently. The two are not necessarily the same thing: anhydrous pyrrole black is an insulator and is only electrically conducting when made in the presence of water[216].

(a i) In dilute H_2SO_4 [217]

This is the only widely recognised chemical preparation of polypyrrole. 2 ml of pyrrole in 10 ml ethanol is added to 20 ml of 1.9M H_2SO_4 in a petri dish, and allowed to stand in air overnight. A thin orange film forms on the surface as the solvent evaporates. This synthesis is distinctive in that it appears to form polypyrrole in its undoped, electrically insulating state (See Section 3.4.2). However, chemical analysis gave the formula $C_{4.0}H_{6.5}N_{0.8}O_{0.8}(SO_4)_{0.16}$. Various possibilities exist for the excess material: incorporation of water into the film, doping by bisulphate or sulphate ions and/or oxygen, incorporation of hydrogen and/or carbonyl groups into the polymer chain.#

The film proved to be conducting on oxidation with bromine or iodine and became blackened after a few days in air. It was further characterized by infra-red spectroscopy[217,18], where C=O and $SO_4^{=}$ vibrations could be seen as well as the pyrrole bands. It would be interesting to see whether films can be produced by this method with oxygen rigorously excluded.

(a ii) With Iron(III) Chloride Solution

Polypyrrole doped with $FeCl_3$ can be prepared by allowing pyrrole vapour to come into contact with $FeCl_3$ solution[218]. A variation on

---

See Hyodo and MacDiarmid[209] for the effect of sulphate ions on the electrochemical synthesis in aqueous solution of poly-N-methylpyrrole.

this is to use filter paper dipped in $FeCl_3$ solution, so that the polypyrrole covers the cellulose fibres in the paper. A conductivity of 2 S/cm was obtained by this method[216].

(b) From Halogenated pyrroles

In a series of carefully researched papers published in 1963 but since largely ignored, Mc Neill et al[219-221] describe the pyrolysis of tetraiodopyrrole at 120-700°C to produce a black, infusible, amorphous polymer with a conductivity of 0.005 to 1 S/cm. They found that removal of iodine caused loss of conductivity and did extensive research into the redox chemistry, as well as the temperature dependence of the conductivity and an ESR spectrum.

This work is to some extent paralleled by Audebert and Bidan[222] who discovered that the substituted pyrroles

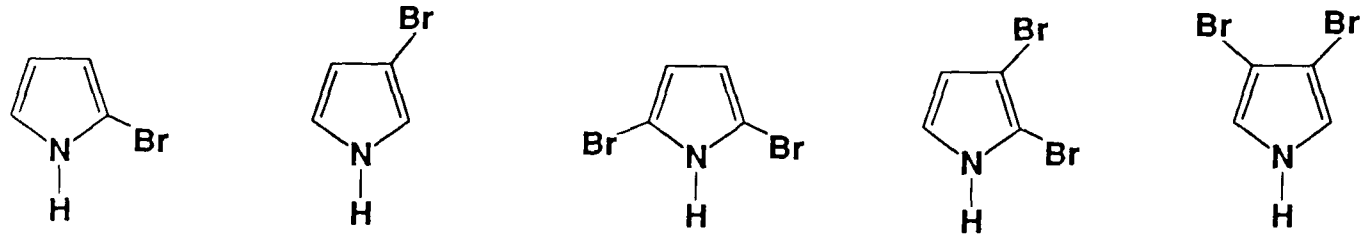

were only stable in dilute solution and showed a tendency to polymerize spontaneously with elimination of HBr to form doped polypyrroles with a conductivity of up to 10 S/cm. In addition, the pyrroles

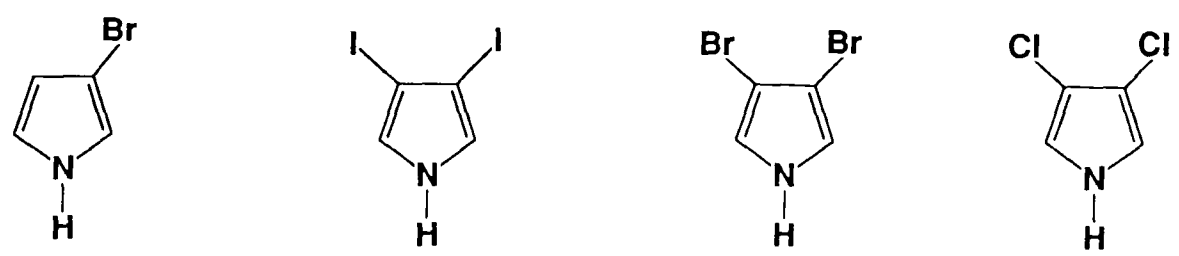

could be polymerized electrochemically, but with relatively poor conductivity (10^{-2} to 10^{-3} S/cm) owing to steric hindrance. There appears to be room for further development in this field.

3.2 MECHANISM AND CHEMISTRY OF THE SYNTHESIS

The various studies undertaken[210,223] have proved inconclusive and the commonly proposed mechanism is based on the nature of the product[204]:

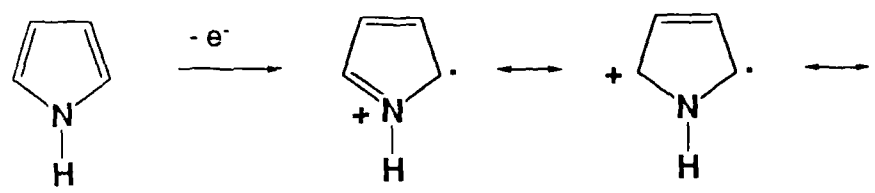

Radical cation formed by oxidation
(can be attacked by nucleophiles)

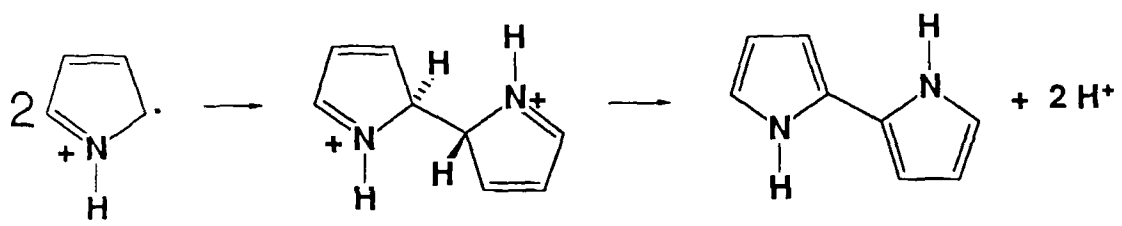

Radicals couple to form a dimer
(rate determining step)

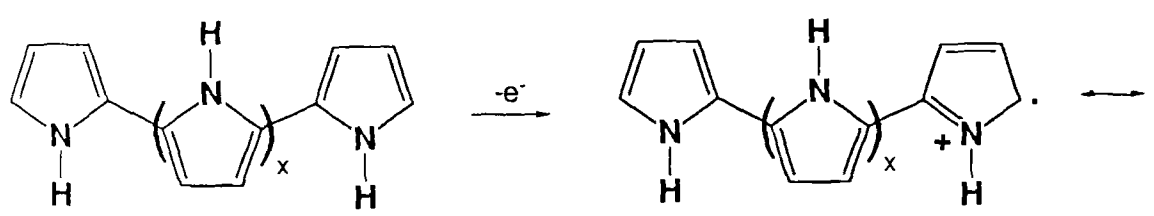

Oxidation of oligomer

The chain grows

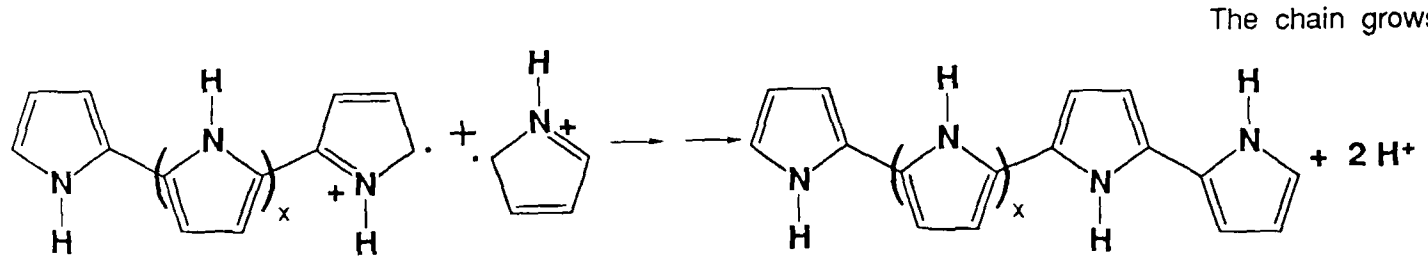

Reaction rate is first order with respect to electrolyte, zeroeth order with respect to pyrrole [201].

Oxidation of a pyrrole molecule produces a radical cation, followed by the slow coupling of two radicals. The dimer is in its turn oxidized and couples to another radical and, since the oxidation potentials of pyrrole oligomers are lower than that of the monomer[224], the chain grows. Eventually, the oxidized chain becomes insoluble and the negative ions which surround it are incorporated into the film as dopant. Two further points: the radical cation is susceptible to nucleophilic attack, and H^+ ions are released into the solution, which therefore becomes acidic unless hydrogen is discharged at the counter electrode.

The charge passed per pyrrole ring is 2.2 to 2.4e^- [205,206], two electrons being used in the oxidation and the remainder being used in

doping. Chemical analysis of a perchlorate doped film[18], gave the empirical formula $C_{3.94}N_{1.0}H_{3.37}(ClO_4)_{0.33}$ suggesting that the pyrrole rings remain intact with linkage at the α position and three pyrrole rings per dopant ion, as shown below:-

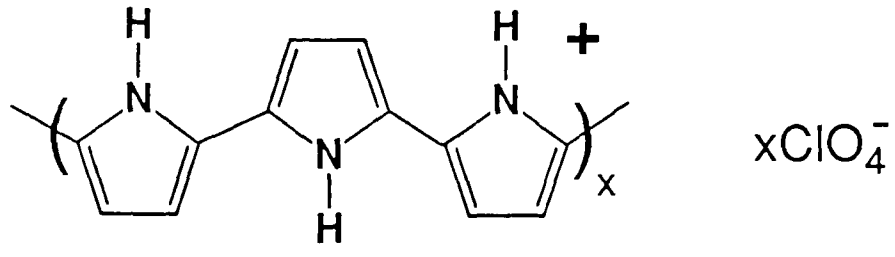

In borofluoride doped films, there are usually reckoned to be four pyrrole rings per dopant ion[195], but these figures are only approximate.

Further evidence for the retention of the pyrrole ring with linkage at the α position includes the fact that α-substituted pyrroles do not form a comparable polymer[225] and studies on the tritiated monomer indicating retention of β-hydrogen[226], together with the similarity of XPS [207], ^{13}C NMR [204] and IR [226] spectra to those of the pyrrole monomer. However, the presence of excess hydrogen, disorder in the XPS spectrum[207] and the amorphous nature of the substance compared with poly-β-dimethylpyrrole[208] show that this may be something of an oversimplification.

Film thicknesses are generally estimated from the charge passed. The figure of 2.2 to $2.4e^-$ appears to have been derived from weighing bulk preparations rather than direct measurements of thin films. It is also, therefore, an average over the entire area of the film, neglecting uneven growth patterns. More recently, direct measurements of the thickness have been made with conflicting results. Ellipsometry of polypyrrole films gave a thickness of 0.1 μm to a 60 mC/cm^2 film instead of the predicted 24 mC/cm^2 [227]. On the other hand, measurements of 0.21 μm films of poly-β-dimethylpyrrole using an Alpha step profiler

show no such disagreement[228]. The film initially deposited may, therefore, differ to some extent from the bulk film.

A molecular weight determination of poly-β-dimethylpyrrole[229] was made using the α-tritiated compound, the residual tritium corresponding to the chain ends. By this method, the chain length was fixed at 750 pyrrole rings, corresponding to a molecular weight of 100,000 for the perchlorate, with a value of 50,000 for the borofluoride. Values from 10,000 to 125,000 were obtained by varying the conditions. This must be considered a minimum since excess hydrogen and crosslinking will depress the figure. If all the excess hydrogen from the chemical analysis were incorporated at chain ends, the chains would only consist of six or eight pyrrole rings, which seems far too short.

3.3 PHYSICAL PROPERTIES

3.3.1 Morphology and mechanical properties

The floatation density of polypyrrole is 1.48 g/cm^3 [195] and electron microscopy shows that, unlike polyacetylene, it exists not as fibres but as a continuous rough film[196]. (This is the usual morphology although "crystalline" and "Swiss cheese" structures have also been reported[201].) The degree of roughness is highly structure dependent and depends on the anion[197]. Poly-N-substituted pyrrole films are rougher[230] and polythiophene films are smoother[19] than polypyrrole.

The mechanical properties of polypyrrole films are poor with a tendency to brittleness[226]. They can be enhanced by the use of p-toluenesulphonate as the counter ion[226], by synthesis at -20°C [231], by graft copolymerization and polymerization in an inert swellable polymer matrix, and by the use of vitreous carbon electrodes[226] (See Section 3.8). When damp, however, polypyrrole films swell with solvent and are highly flexible[231].

Table 3.1 Room temperature Conductivities of Pyrrole based Polymers

Variation with dopant for polypyrrole[193]

Dopant	doping level*	σ S/cm
BF_4^-	0.26-0.30	30-100
PF_6^-	0.24	100
AsF_6^-	0.33	100
ClO_4^-	0.30	100-200
HSO_4^-	0.30	0.3
$CF_3SO_3^-$	0.31	0.3
$CH_3C_6H_4SO_3^-$	0.32	20-100
$CF_3CO_3^-$	0.33	12
$HC_2O_4^-$	0.40	10^{-3}-10^{-2}

Variation with substituent for borofluoride doping [193,208]

Substituent	doping level*	σ S/cm
H	0.25-0.29	30-100
N-methyl	0.23-0.29	10^{-3}
N-phenyl	0.15	10^{-3}
β-methyl	-	4
ββ'-dimethyl	-	10
ββ'-diphenyl	-	10^{-3}
polythiophene	0.1	10^{-3}-10^{-1}

* Defined as number of dopant ions per pyrrole ring in fully doped polymer.

3.3.2 Electrical Conductivity

The conductivity of a polypyrrole film depends more on the anion and conditions of synthesis than its subsequent treatment, excluding the doping/undoping and acid/base transitions discussed in Sections 3.4 and 3.8. Carefully synthesized polypyrroles with various dopants have conductivities ranging from 10^{-2} to 200 S/cm, with perchlorate giving the best conduction. Both N- and β-substituted polypyrroles have lower conductivities than polypyrrole itself (Table 3.1). (This variation is independent of conductivity changes associated with the redox chemistry of polypyrrole.) It has also recently been found that improved conductivities of up to 1000 S/cm can be obtained by synthesis at -20°C followed by stretching in hot solvent vapour[231].

The conductivity σ of polypyrrole decreases by a factor of three on cooling from room temperature to 80K, with a thermopower coefficient of

7 μV/K. This suggests an activated process with p-type carriers[195]. More exactly, a plot of log σ versus $T^{-\frac{1}{4}}$ gives a straight line[232]. This is the same temperature dependence as polyacetylene (Section 2.3) and fits a three dimensional variable range hopping mechanism for conduction, originally proposed in a different context by Mott[233].

When measuring conductivities, care has to be taken not to apply high voltages as these cause chemical changes. Thus a simple Avometer is liable to give an erroneous answer (eg Prejza et al[201]) and it is necessary to use four probe methods (See Section 5.4).

3.3.3 Air Stability

Polypyrrole has traditionally been reckoned to be much more stable to air than polyacetylene on the grounds that the conductivity only falls by 20% after a year's exposure to air[208,234], and that no apparent changes take place on heating to 250°C in air[195]. More recently, however, XPS has demonstrated a constant conductivity is no guarantee of chemical purity, and that polypyrrole shows a strong tendency both to scavenge oxygen during synthesis and to absorb oxygen in place of the dopant ion over the course of time. These effects would be expected to be most severe in the very thin films used for electrochemical doping/undoping and optical spectroscopy.

Early XPS studies showed no dopant at all in films which were under 1000A thick[235], or which had been electrochemically cycled[236]! Later studies using better experimental techniques contradict this[207]. The chemical synthesis in dilute H_2SO_4, as well as revealing the presence of oxygen in the chemical analysis, showed a C=O stretch. Worst of all, XPS analysis of borofluoride doped films stored under various conditions showed that the BF_4^- ion had a strong tendency to leave the film spontaneously without loss of conductivity. This effect was diminished, but by no means eliminated by storage in an inert atmosphere. Thus

polypyrrole exposed to air for a year with a 20% loss of conductivity had **no** detectable fluoride in it, and even after 500 hrs storage under argon there was an 8% **gain** in conductivity with only 30% of the original fluoride present[234]. The combination of oxygen and water causes greater degradation than either of these on their own. Polythiophene and especially poly-β-methylthiophene show much greater stability towards air[237].

3.3.4 Structure

Structural work on polypyrrole has long been hampered by its disordered nature and electron diffraction patterns have traditionally only given a single maximum at 3.41Å [195], close to the graphite 002 line at 3.34Å. Geiss et al[238] have remeasured the electron diffraction pattern of undoped polypyrrole to obtain about five lines, and by analogy with graphite, poly-β-dimethylpyrrole and di- and terpyrrole, have proposed a monoclinic layer structure[208,235] (Fig 3.1). This should at best be regarded as extremely tentative, bearing in mind that such important work has not been published in a major journal. Recent work by Ogasawara et al[231] on stretched polypyrrole has produced X-ray diffraction patterns which are somewhat clearer, but these have yet to be analysed.

3.4 REDOX CHEMISTRY

3.4.1 The Transition [196]

Thin films of polypyrrole, initially in the doped state, can be electrochemically undoped and redoped in the appropriate salt solution eg $R_4N^+BF_4^-$, $R_4N^+ClO_4^-$ (See Fig 3.2). Cyclic voltammograms show broad oxidation and reduction peaks at -0.3 and -0.1V respectively versus calomel, the peak corresponding to 9% of the charge required to produce the film, and the height proportional to the scan speed[205,196]. (This is now commonly used as a characterization test of polypyrrole films.)

Fig 3.1 Tentatively Proposed Structure for Polypyrrole[238]

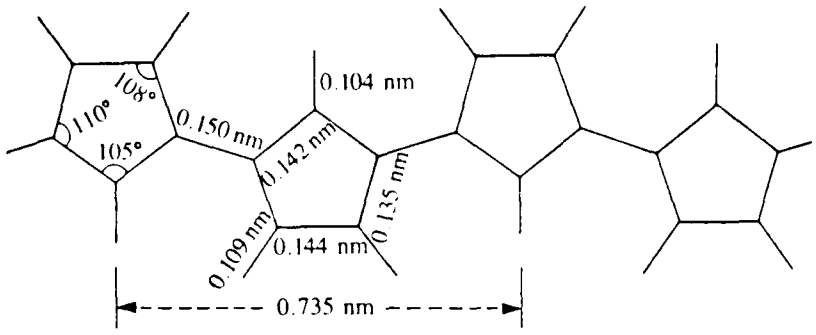

Linear chain structure for neutral polypyrrole

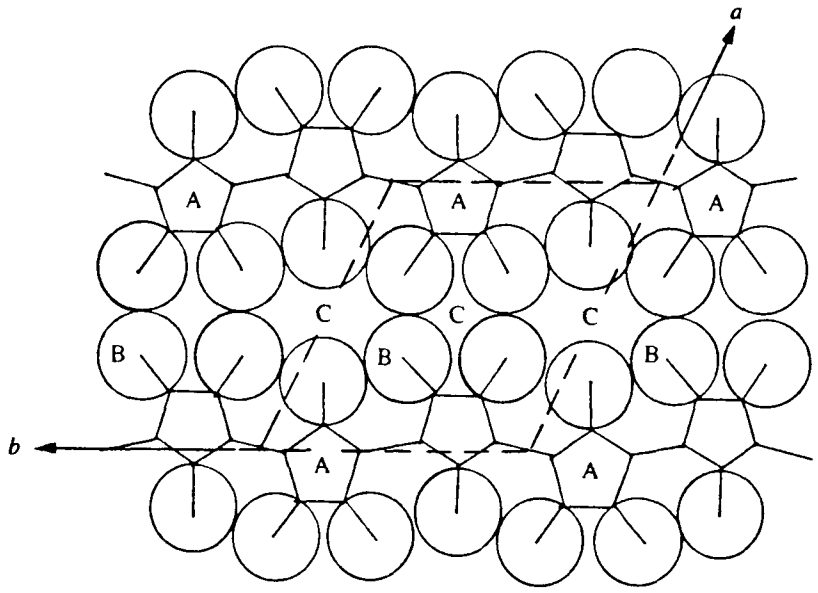

Proposed arrangement of the chains in the first layer of neutral polypyrrole. The circles represent the van de Waals diameters of the hydrogen atoms. The locations marked B represent the locations of pyrrole rings, A, in the second layer of the ABAB stacking. Positions marked C are probable locations for anion intercalation. The a and b axes of the proposed monoclinic unit cell are indicated. The c axis is normal to the plane of the figure.

Space group:	Monoclinic P21/a
Lattice constants:	a = 8.2 A, b = 7.35 A, c = 6.82 A, γ = 117°
Calculated density:	1.47 g/cm^3
Volume of unit cell:	366 A^3

The voltammogram in Fig 3.2 was made with iR compensation, which subtracts out a background current in the anodic region, not seen with a blank platinum electrode. On extending the range of potential sweep in Et_4NBF_4, no transitions were seen in the cathodic (reducing) region up to -2.3V, while in the anodic region, a large irreversible transition occurred at between +1 and +2V. Thus there are no reports of electrochemical n-doping of polypyrrole. This doping/undoping transition is also seen in poly-N-substituted pyrroles[196] and polythiophene[239], but with differences in the switching potentials and waveforms. Polypyrrole films can be cycled repeatedly[196], but are reported to degrade eventually after 10^3 to 10^4 cycles. By contrast, a film of poly-β-methylthiophene was unchanged after 10^5 cycles[240].

The process is limited by the diffusion of dopant ions in and out of the film and the peak shapes do not correspond to a single transition[241]. As the film thickness is increased from 0.2 to 0.5 μm, the transition becomes slower and finally impossible[196]. The chemistry is more complex than originally thought; recent in situ measurements in lithium perchlorate show a mass **increase** on reduction, suggesting that Li^+ ions diffuse into the film. This does not occur if the p-toluene-sulphonate counter ion is used[242]. The measurements are confirmed by two step chronoamperometry, where the reduction process occurs faster than oxidation, as the latter process requires ClO_4^- ions to move into the film[243]. Where the two methods disagree, however, is whether the Li^+ ions are incorporated into the film permanently or only temporarily. The large surface area of the film also raises the question of a capacitative contribution reducing the true oxidation state of the bulk film. This contribution cannot easily be determined[241].

These complications, together with the tendency of the films to scavenge oxygen in the initial stages of synthesis may account for the

Fig 3.2 Redox Chemistry of Polypyrrole[196]

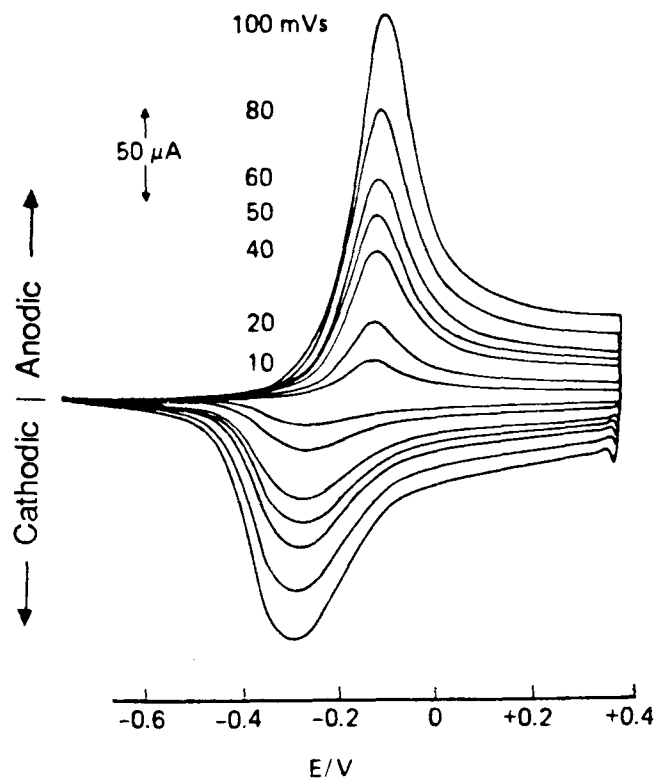

Cyclic voltammograms of [Pt] polypyrrole borofluoride in Et_4NBF_4/CH_3CN solution showing oxidation and reduction waves. The potential is measured relative to a sodium chloride calomel electrode. The peak height is proportional to the sweep rate. The film was made with a charge passed of 8 mC/cm^2, corresponding to a thickness of 0.02 μm. [ref 196]

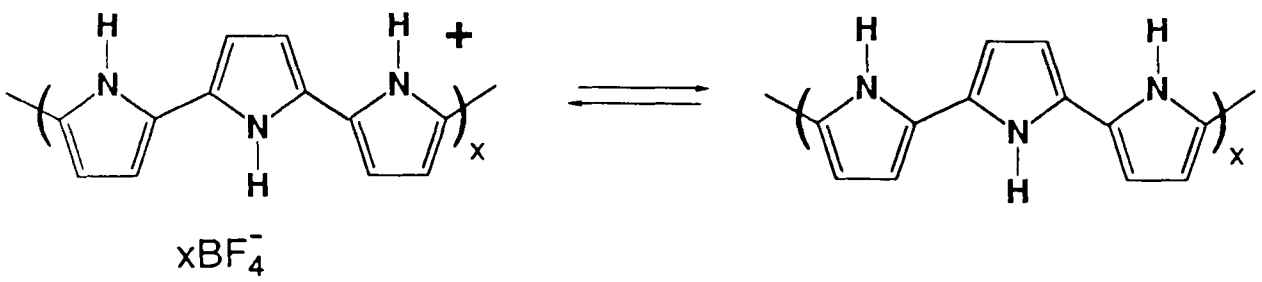

Representation of polypyrrole redox chemistry. In the oxidized form, the anion resides in the film, whereas in the reduced form, it is in solution. The number of pyrrole rings per anion lies between 3 and 4.

reports of distinct stages of oxidation[236] and different morphologies of the various types of polypyrrole[201].

3.4.2 Neutral Polypyrrole [18]

Neutral polypyrrole is yellow-green in colour and an electrical insulator. It can be redoped either electrochemically as described previously, or chemically by direct reaction with the dopant. Conductivities by chemical redoping can be higher than the original value, 600 S/cm having been obtained for bromine. Neutral polypyrrole, unlike doped polypyrrole, is very susceptible to doping by atmospheric oxygen and darkens after only fifteen minutes exposure to air. This oxygen doping is irreversible, as is shown by the decay in response to electrochemical cycling of a 20 nm film of neutral polypyrrole exposed to air for five minutes[196]. The morphology[196] of neutral polypyrrole films appear to be indistinguishable from doped polypyrrole, in spite of a theoretical 30% reduction in mass on undoping in the case of borofluoride. Measurements of poly-β-dimethylpyrrole films using an Alpha step profiler gave ambiguous results, suggesting that the reduced films were thicker than the as-grown films, but were highly porous and could easily be squashed thinner than the as-grown films[228].

3.5 OPTICAL AND MAGNETIC SPECTROSCOPY AS A FUNCTION OF DOPING

The change in colour on undoping is reflected in the visible/UV spectrum. Doped polypyrrole has strong absorptions at 1.0 and 2.7 eV, whereas undoped polypyrrole has a single absorption at 3.2 eV (Fig 3.3) [244,283,284]. This change is also observed in chemical doping with iodine[236]. The ESR spectrum of polypyrrole was measured as a function of oxygen uptake and showed an increase in peak intensity, followed by a decrease[236,245]. This, together with the UV spectrum, is taken as evidence for the polaron/bipolaron model (See Appendix II). The ESR spectrum could, however, also be explained in terms of partial irreversible addition to the polymer backbone, breaking the conjugation.

Fig 3.3 UV spectrum of Polypyrrole as a Function of Doping Level[244]

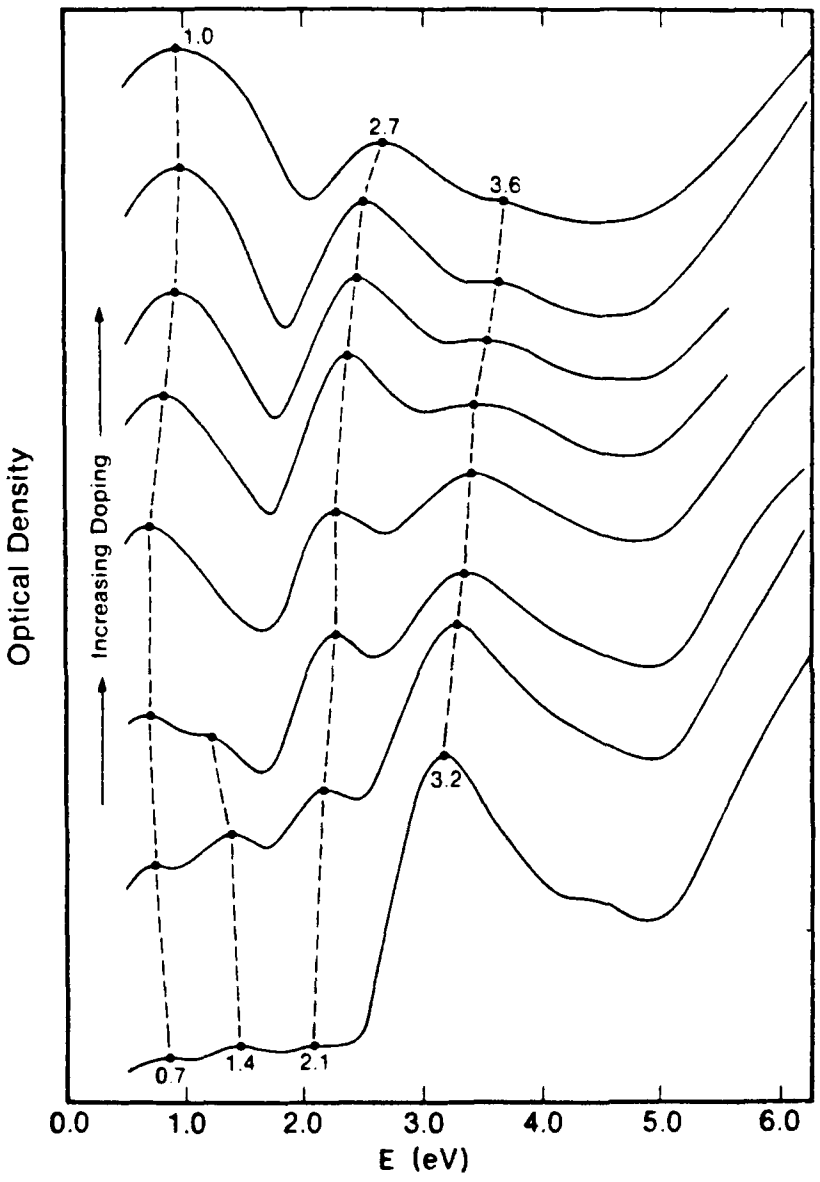

Evolution of the optical absorption spectrum of polypyrrole as a function of doping level. The concentration of perchlorate ions increases from bottom curve (almost neutral polypyrrole) to top curve (33 mol% level doping).

Fig 3.4 Infra-red Spectrum of doped and undoped Polypyrrole[ref 18]

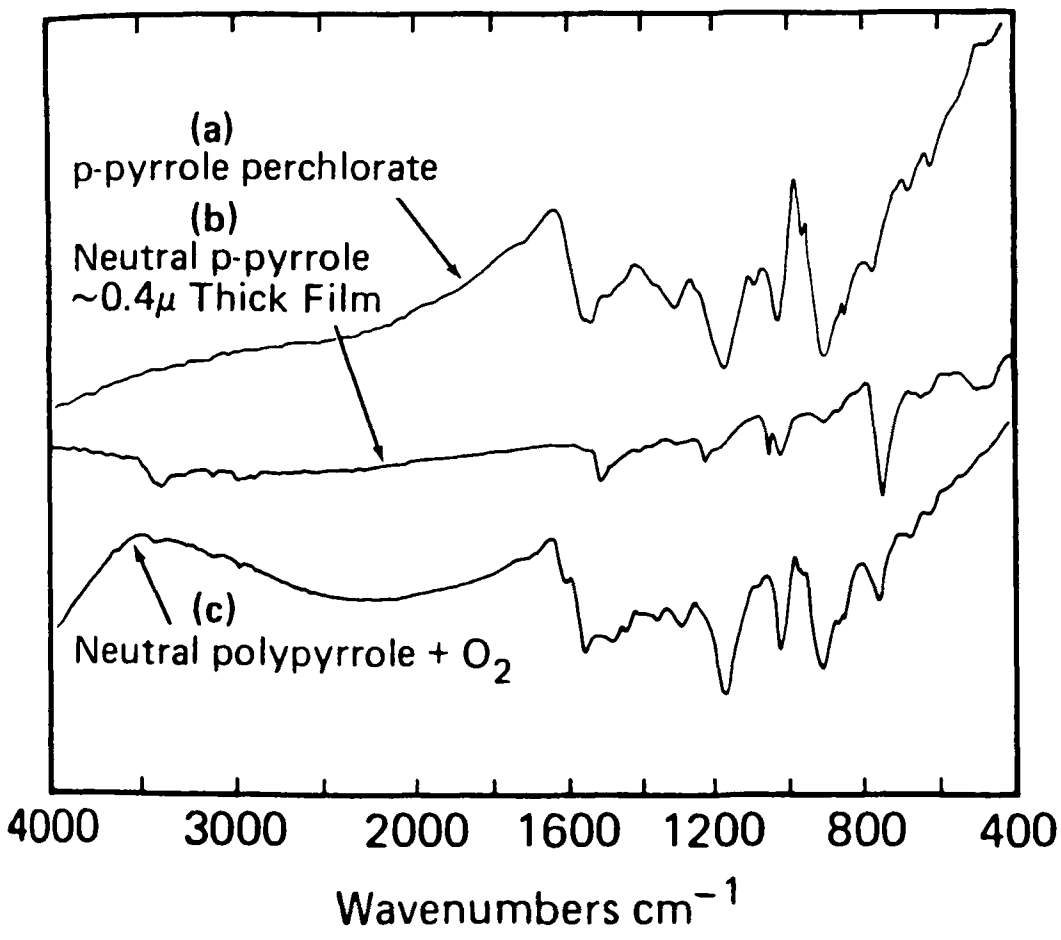

The infra-red spectrum of polypyrrole does not show the same dramatic changes on doping as the visible/UV spectrum. The spectra are dominated by pyrrole bands,++ the spectrum of neutral polypyrrole resembling those of dipyrrole and terpyrrole[226]. On doping, the bands sharpen and mask the dopant bands without any great qualitative change. (In AsF_6^- doped polypyrrole, however, As-F bands show at 780 and 400 cm^{-1} in a region where polypyrrole itself is transparent.) Street et al [18,226] show infra-red spectra for polypyrrole synthesized in dry acetonitrile without giving exact band positions (Fig 3.4); figures have only been published for polypyrrole synthesized in aqueous solution[209].

The ^{13}C NMR spectrum of neutral polypyrrole shows two main peaks at 123 and 105 ppm downfield from TMS, consistent with α-α' linkage in a linear chain. A third smaller peak at 135 ppm may be due to non α-α' linkage or terminal carbon atoms. On doping, a single very broad asymmetric peak forms, shifted downfield from neutral polypyrrole. This is consistent with the transfer of charge to the polymer backbone[18].

3.6 PHOTOELECTRON SPECTROSCOPY AS A FUNCTION OF DOPING

3.6.1 XPS Core Spectra[207,236]

XPS is a particularly valuable technique in this case since it gives direct information on the chemical content of thin films and does not rely on long range order in the sample. The role of XPS in identifying oxygen contamination has already been described. The most complete analysis to date on carefully synthesized films was carried out by Pfluger and Street[207], who managed to obtain semi-quantitative data. They found that the N1s line in polypyrrole perchlorate was asymmetric and could be split into three components with intensity ratio 1:2:2. These were assigned to three types of nitrogen atoms at different

---

++ Infra-red data on pyrrole monomer are given by R.A. Jones[246].

distances form the dopant ion. The C1s line was very broad, and as well as having components from α and β carbon atoms, a third broad component was found. This was attributed to disorder such as cross-linking, chain termination etc. The large area of this component, corresponding to one third of all carbon atoms, calls into question the accepted linear picture of polypyrrole. In poly-β-dimethylpyrrole, the line width was reduced, indicating a higher degree of order. The C1s line also had shake-up satellites at intervals of 3.5 eV corresponding to π-π* transitions. The anion core levels confirmed the presence of perchlorate and borofluoride ions, with doping levels of 35% and 26% respectively. By contrast, the P:F ratio was not 1:6, and the PF_6^- ion appears to have undergone chemical reaction.

3.6.2 Valence Band Spectra

The valence bands of oxidized and neutral polypyrrole and poly-β-dimethylpyrrole have been investigated by ultraviolet[247] and X-ray photoelectron spectroscopy[207] with band structure calculations by Ford et al[248] in broad agreement with the observed data. No detectable density of states was observed at the Fermi edge; this does not necessarily preclude semi-metallic behaviour, however, since in graphite the density of states is too low to be detected except in intercalation compounds.

3.7 ACID-BASE CHEMISTRY OF POLYPYRROLE

In addition to the redox chemistry already described, the conductivity of polypyrrole in aqueous solution can also be modified by a parallel protonation/deprotonation transition. Addition of 2M NaOH solution to polypyrrole causes the conductivity to decrease by three to four orders of magnitude. This is partially reversed by exposure to 6M HCl [227]. A similar, though less marked reversible reduction in conductivity is achieved by exposing the dry film to ammonia[195]. It is

Fig 3.5 The Acid - Base Transition in Polypyrrole [after ref 227]

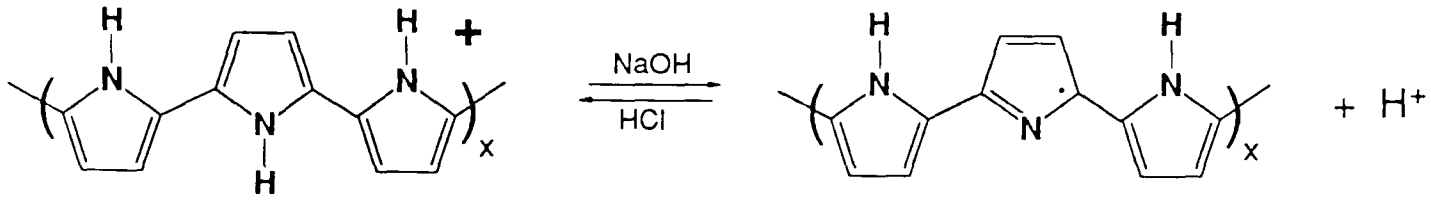

Protonated, charged, conjugated

Deprotonated, uncharged, conjugation interrupted

Could also form a soliton/ antisoliton pair in the neutral form:

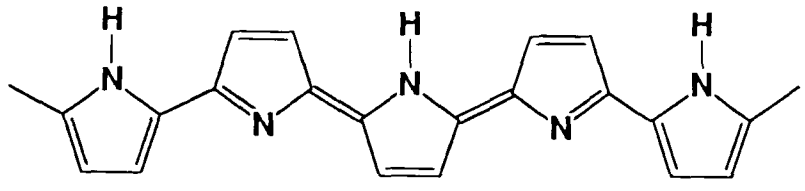

believed that the base deprotonates the nitrogen, neutralizing the positive charge on the polymer backbone, and interrupting the conjugation. On acidification, this is reversed [227] (Fig 3.5).

Treatment with NaOH also caused loss of mass and thickness, suggesting removal of the dopant ions[249]. A change in pH caused the potential of the doping/undoping transition to decrease by 60 mV per pH unit[250].

In the longer term, polypyrrole is only stable in aqueous solution between pH 1 and pH 7; at pH 12 it is only stable for an hour [250]. However, it is claimed that **brief** treatment with NaOH tends to slow further degradation[249].

3.8 UNUSUAL FORMS OF POLYPYRROLE: COMPOSITES

3.8.1 Polypyrrole n-alkyl Sulphates and Sulphonates[218,251,252]

An interesting form of polypyrrole can be prepared by electrolyzing pyrrole in an aqueous solution of the sodium salt of a long chain n-alkyl sulphate or sulphonate. Compounds used were $H(CH_2)_n\text{-}SO_3^- Na^+$ with n between 4 and 18, and also the difunctional compound $Na^+ {}^-SO_3\text{-}(CH_2)_{10}\text{-}SO_3^- Na^+$. Optimum growing conditions were temperature 20°C, pH 2 to 5 and current 2 mA/cm². The samples had good mechanical properties, and the conductivities varied from 1 to 160 S/cm. The temperature dependence of conductivity was much weaker than in normal

Fig 3.6 Idealized Proposal for the Short Range Order in Polypyrrole n-alkyl Sulphates and Sulphonates[ref 218]

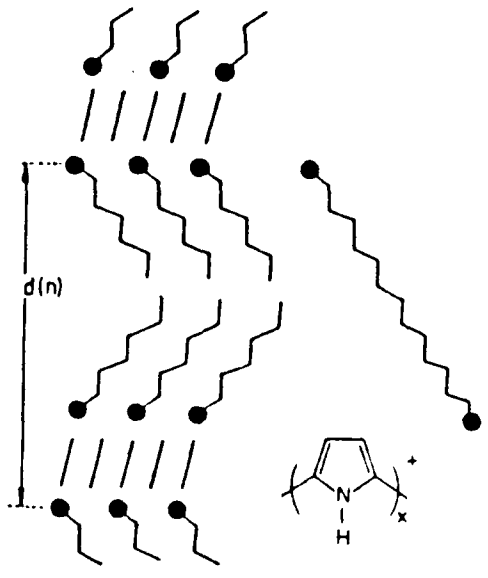

View along polypyrrole chain axis. The simple black lines represent the polypyrrole chains, the zigzag lines the n-alkyl chains, and the black dots the terminal sulphate or sulphonate groups.

polypyrrole. The stoichiometry gave three or four pyrrole rings per dopant ion. The samples were analysed by X-ray diffraction, and the patterns contained a low angle line corresponding to a distance of (1.9n + 12) A where n is the alkyl chain length. This was attributed to a bilayer structure with layers of pyrrole rings intercalated between n-alkyl chains (Fig 3.6). By contrast, the difunctional compound produced a single layered compound. This method has obvious potential since it uses cheap and non-toxic materials and gives a more ordered product than conventional preparations.

3.8.2 A Polyacetylene/Polypyrrole Composite[253,254]

It has recently been reported that pyrrole can be polymerized onto a polyacetylene electrode. Conditions used were otherwise usual for polypyrrole preparation (0.1M Bu_4NBF_4 or Bu_4NClO_4, 0.1M pyrrole in acetonitrile, +1.0V versus calomel, room temperature). During polymerization, a red colour develops in the solution near the anode. If undoped polyacetylene is used, polymerization starts near the current supporting wire and a film slowly spreads over the surface of the

electrode. The resulting structure is a sandwich with polyacetylene in the middle and polypyrrole on the outside. The polyacetylene becomes doped during the polymerization, the concentration of dopant falling off towards the centre of the sandwich. If doped polyacetylene is used, polymerization starts immediately throughout the sample and individual fibrils become coated with polypyrrole. Both types of composite have conductivity 20-40 S/cm and show better stability to air and water than ordinary polyacetylene. Cyclic voltammetry shows that both polymer components are electroactive.

3.8.3 Other forms of Polypyrrole

A form of polypyrrole with improved mechanical properties has been made by growing it in a matrix of an inert, swellable polymer, usually PVC [255,256] or polyvinyl alcohol[225]. The conductivity and electroactivity are, however, slightly reduced. Pyrrole rings have also been chemically introduced into soluble polystyrene to act as nucleation sites for a polystyrene/polypyrrole copolymer, but this produced little improvement in the mechanical properties[225]. A similar approach was used to bond pyrrole rings chemically to an n-doped silicon photoanode to prevent peeling of the protective polypyrrole coating[257]. Thin films of poly-N-(p-nitrophenyl)pyrrole show redox chemistry in both the nitro group and the polymer backbone. This is the nearest to n-doping so far achieved[258]. The polymer has also been prepared on the gram scale in air on a vitreous carbon electrode[226].

3.9 APPLICATIONS OF POLYPYRROLE AND SIMILAR POLYMERS

The colour change on doping/undoping electroactive conducting polymers has led to proposals for using as liquid crystal type display devices. Low voltages are used, and no current at all is needed to maintain them in the selected state. Poly-N-methylpyrrole has been used[259], but in general polythiophene and poly-β-methylthiophene are

favoured, owing to the greater air stability of the undoped form. On undoping, polythiophene changes from blue to red[235,240,260]. Other uses of the doping/undoping transition include pH control of aqueous solutions[261] and gas detection[262]. Polypyrrole has also been tested for use as a conducting but chemically inert protective coating in photovoltaic devices[263-266], and as an information storage medium[267].

APPENDIX II : THE SOLITON MODEL

1. The Soliton

The soliton or π phase kink was proposed to explain magnetic anomalies in polyacetylene. The increase in conductivity at lower doping levels than the increase in magnetic susceptibility has already been mentioned (Section 2.3). Furthermore, trans-polyacetylene has a very high concentration of free spins, 1 spin per 1000 to 3000 carbon atoms, and the ESR spectrum broadens at low temperatures, suggesting that they are very mobile[268,269].

Trans-polyacetylene is unique among the conducting polymers in having two equivalent structures separated simply by an interchange of double and single bonds (Fig 1). The transition state between the two structures is simply the hypothetical non-alternant "metallic" form, calculated by Karpfen and Höller[148] to be less stable than the normal structure by 30 KJ/mol of C_2H_2 units. In cis-polyacetylene and polypyrrole, the two structures are non-degenerate and the model does not apply.

The soliton as introduced by Su, Schrieffer and Heeger[270,271] is a free radical at a break in conjugation in the chain with spin $\frac{1}{2}$ and zero charge. This concept was extended by Rice[272] to include charged solitons, which are carbonium ions or carbanions at a break in

Fig 1. Degeneracy in trans - polyacetylene

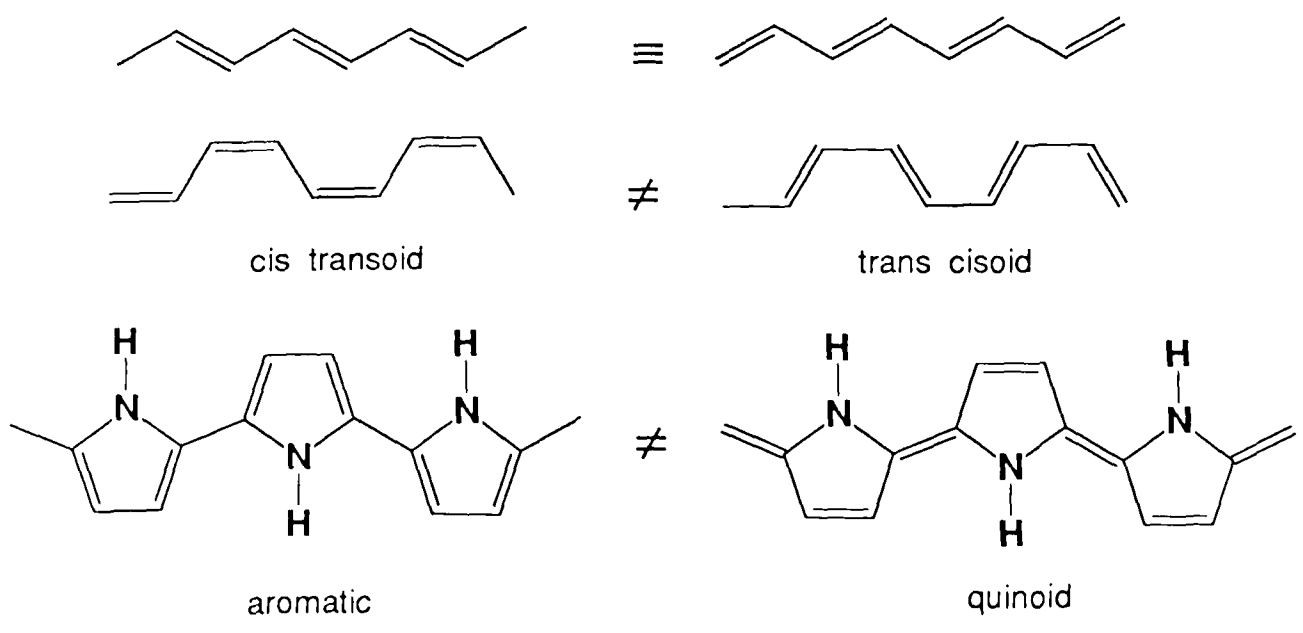

Fig 2. Positive, neutral and negatively charged solitons and their effect on the band structure of polyacetylene

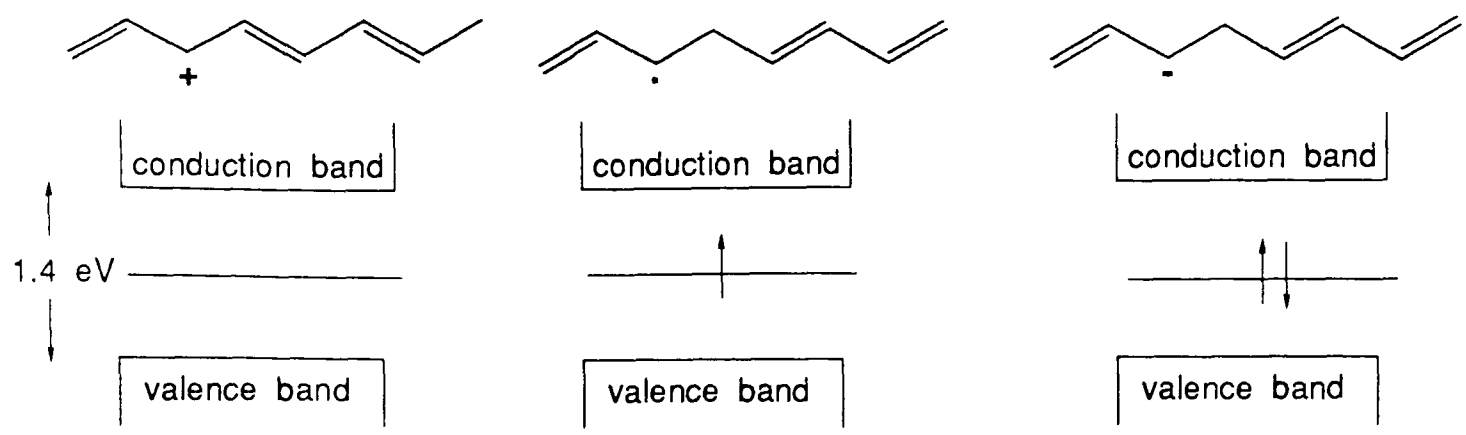

A soliton spread over 14 carbon atoms

conjugation and have zero spin but are charged. On doping, the solitons cluster round the dopant ions, picking up charge and are "pinned", the number of free spins being reduced in this process[273].

Su, Schrieffer and Heeger[271] calculated the energy of a neutral soliton, and found that it was most stable when spread out over about 14 carbon atoms. This means that at the phase change (soliton), the bond alternation is reduced. The length of a charged soliton is a little more[273].

An important consequence of the soliton is that the unpaired electron is in a non-bonding molecular orbital, or in band theory a mid-gap state. Trans-polyacetylene shows a peak in the visible region with the absorption edge at 1.4 eV, assigned to the interband transition.[+] On light doping, a new absorption appears at 0.7 eV regardless of dopant[274,275], with infra-red bands at 1370 and 900 cm^{-1}[276]. Similar behaviour on strong laser illumination is attributed to photoinduced pairs of positively and negatively charged solitons[277]. Solitons have also been proposed as a mechanism for the cis-trans isomerization of polyacetylene[278].

+ The absorption maximum, however, is at 1.9 eV.

2. Polarons and Bipolarons

The polaron was originally proposed for polyacetylene by Campbell and Bishop[279] who used relativistic field theory. Chemically, however, it merely consists of a charged defect in the polymer chain accompanied by local distortion, and has charge $\pm e$ and spin $\frac{1}{2}$ (Fig 3).# There is no change in the phase of the double and single bonds and hence the model can be, and usually is, applied to systems such as cis-polyacetylene and polypyrrole where the two states are non-degenerate and the soliton model does not apply. A bipolaron consists of two associated defects with the same charge but paired spins. Thus the effect of a bipolaron, similar to a charged soliton, is to transfer charge from the dopant to the polymer backbone without increasing the number of free spins.

The band structure of a polymer chain incorporating such defects has been calculated by Brédas et al [280,281], who considered the **hypothetical** n-doped polypyrrole. Unlike the soliton, which causes a single state to appear in the middle of the band gap, the polaron or bipolaron causes two states to appear. In the case of a single polaron, one state is singly occupied, but for a bipolaron the states are either doubly occupied or empty, depending on whether there is n- or p- type doping. The repulsion between the positive charges in the two polarons is more than compensated for by the more favorable electronic states created by the formation of the bipolaron (Fig 3).

The bipolaron was calculated to extend over about four pyrrole rings. When the concentration of bipolarons is increased so that they interact, the bands broaden, but even at 33% doping, the maximum observed for polypyrrole, they still keep their identity. Finally, at a hypothetical 100% doping, the bipolaron bands simply become part of the

---

The definition of a polaron in an ionic solid is given by Kittel[1].

Fig 3. Polarons and bipolarons in Polypyrrole[after refs 280,281]
(The data are shown for the hypothetical n-doped polypyrrole, but a similar picture could be envisaged for p-doped polypyrrole and for p- or n-doped polyacetylene. For clarity the states are shown localized, but a bipolaron has been calculated to extend over about four pyrrole rings. Energies are only approximate and depend on the calculation.)

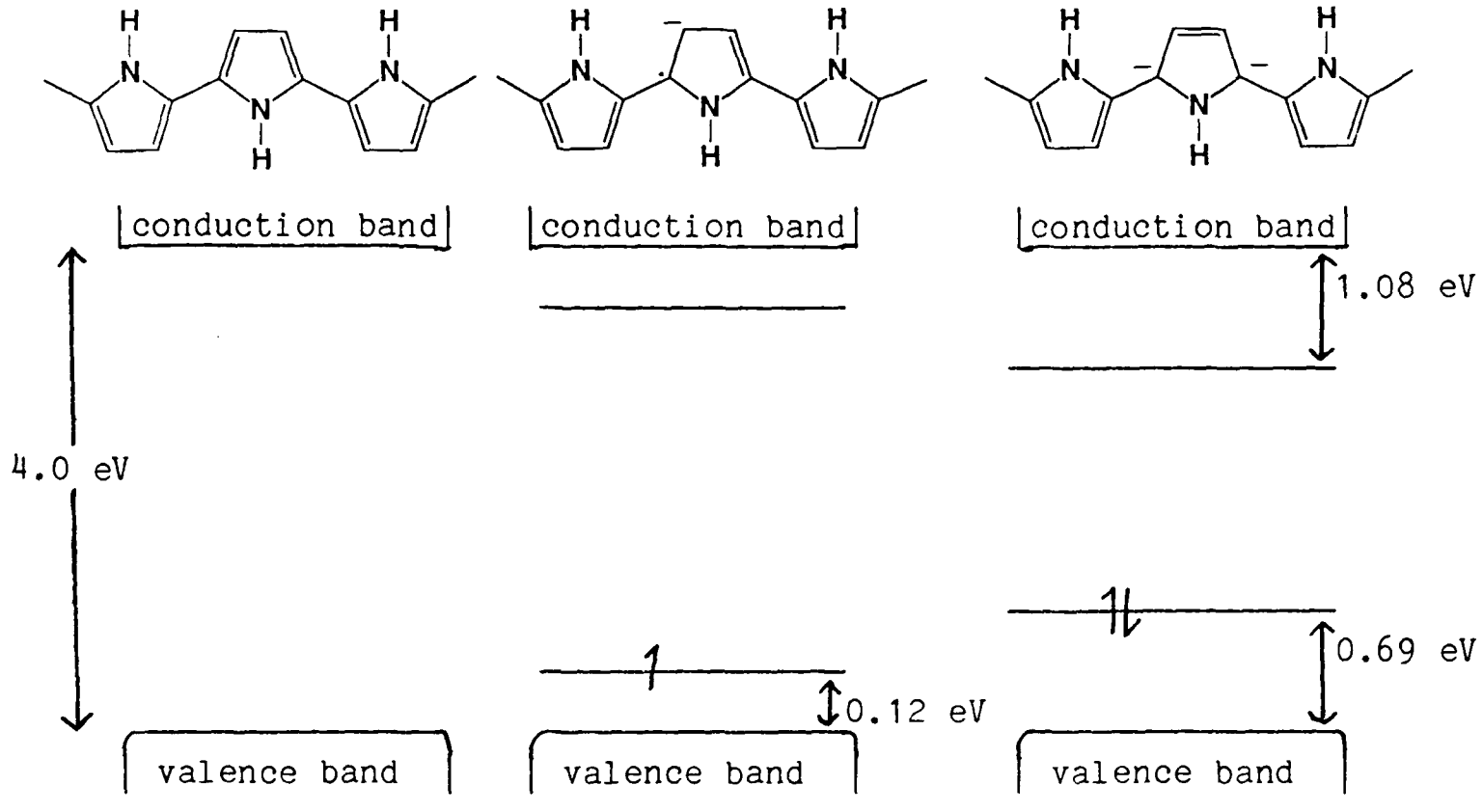

Undoped polypyrrole
1 transition possible

Lightly doped polypyrrole showing a polaron.
Charge = -e, spin = 1/2
4 transitions possible

On increasing the doping or simply waiting, the polarons coalesce to form bipolarons
Charge = -2e, spin = 0
3 transitions possible

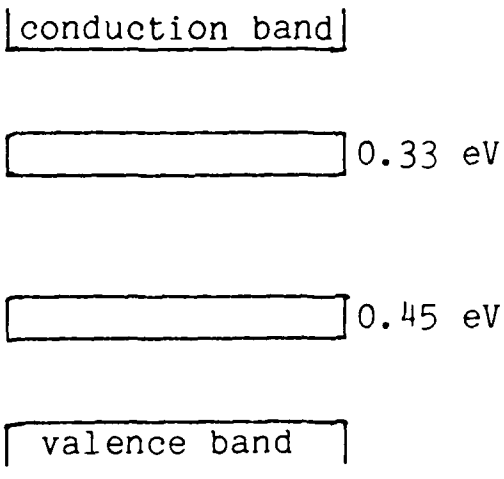

Fully doped polypyrrole
(33% doping)
On heavy doping, the bipolarons overlap and the bands broaden.

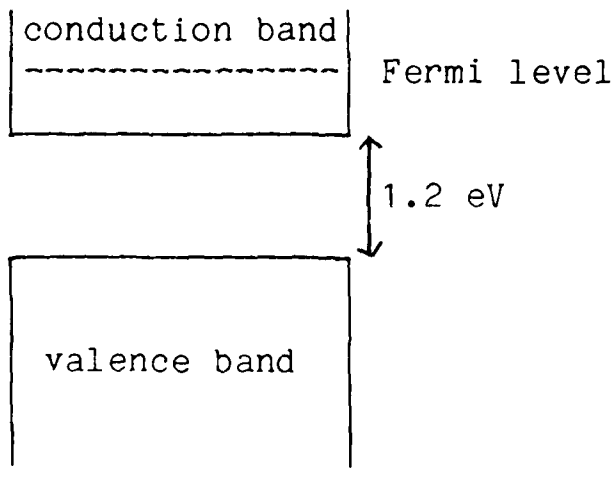

Hypothetical 100% doped polypyrrole is metallic, the polaron bands becoming part of the conduction and valence bands.

conduction and valence bands, and the bandgap narrows but does not disappear[280,281]. It is in this context, therefore, that fully doped polypyrrole is sometimes referred to as not being fully metallic, in contrast to heavily doped polyacetylene[247].

Evidence for polarons and bipolarons stems from ESR and optical experiments on polypyrrole[282]. ESR experiments on polypyrrole doped with oxygen[236,245] showed a signal which increased, reached a maximum, and then decreased as the concentration of oxygen was raised. This was taken as evidence that at low doping levels polarons formed, but that on increased doping, they merged to form spinless bipolarons. Optical spectra show broad transitions with energies less than the band gap; whether all the proposed transitions can be resolved is, however, more doubtful (See Fig 3.3).

3. Limitations of the Soliton Model

The soliton model was devised to explain why the increase in conductivity in polyacetylene occurred at much lower levels of doping than the increase in magnetic susceptibility. In doing so, it relies on the degeneracy of the phases of the double and single bonds. The data on polypyrrole are broadly similar, but because the ground states are not degenerate, the soliton model cannot apply and the data have had to be explained in terms of a different model involving polarons.

Second, much is made of the mid-band optical absorption as evidence for solitons and/or polarons. When first observed in iodine doped polyacetylene[170], it was explained in terms of a charge transfer spectrum. This possibility cannot be dismissed entirely.

Third, and most important, experiments have been carried out on a copolymer of acetylene and carbon monoxide[285,286]. Incorporation of carbon monoxide interrupts the conjugation of the polymer chain and should prevent the migration of solitons (Fig 4). In spite of this,

however, the copolymer can be doped with arsenic pentafluoride or iodine and has magnetic, conductivity and ESR properties similar to trans-polyacetylene. This occurred even at composition $[(C_2H_2)_1(CO)_{0.15}]_x$ where the occurrence of C=O groups is the same as the soliton width. In normal doped polyacetylene, the conductivity is supposed to be accounted for by the soliton mobility, which is not possible here. This must, therefore, cast doubts on the validity of the soliton model.

Fig 4. Proposed chain structure for acetylene / carbon monoxide copolymer showing break in conjugation

CHAPTER 4

EXPERIMENTAL STUDIES OF POLYACETYLENE AND DERIVATIVES

INTRODUCTION

Some aspects of the physics and chemistry of polyacetylene were studied in the search for a link between the very crystalline graphite intercalates and the very non-crystalline polypyrrole. Undoped, n-doped and partially hydrogenated trans-poly-(acetylene-d_2) were studied by neutron diffraction to extend the X-ray work, and in addition, it was found that acetylene was irreversibly absorbed by the stage I and stage II caesium graphite intercalates to produce compounds $C_8Cs(C_2H_2)_{0.5}$ and $C_{24}Cs(C_2H_2)_{1.7}$.

4.1 PREPARATION OF POLYACETYLENE AND POLY-(ACETYLENE-D_2)

Polyacetylene for these experiments was synthesized by the Luttinger method (Section 2.1.2) as developed by Nehmé[134]. 25 cm^3 of an 0.1M cobalt(II) nitrate solution in ethanol was put into a Rotorvapour flask attached to a vacuum line and cooled to -79°C in an ethanol/ solid carbon dioxide slush bath.[+] To this, 25 cm^3 of precooled 0.1M sodium borohydride solution in ethanol was added, the motor switched on, and the whole system pumped to 0.2 torr. On mixing, the solution changed colour from pink to carmine, indicating the presence of the cobalt complex which catalyzes the reaction. (If it stayed pink, more sodium borohydride was added.) The temperature after mixing had to be kept below -35°C, otherwise the complex decomposed to black cobalt boride[134].

After pumping, acetylene gas was added. C_2H_2 was obtained from a cylinder, and added at atmospheric pressure via a rubber helium balloon;

+ The function of the Rotorvapour device was to rotate the flask so as to provide a wet surface on which the acetylene could polymerize, and to provide a gas pumping line. The condenser was unused.

C_2D_2 was made when required from calcium carbide and D_2O, and dried by passing through a column of calcium chloride. Acetylene is fairly soluble in ethanol at this temperature and was added until the pressure was close to atmospheric; too low a pressure caused a red soup of low molecular weight oligomers to form instead of a polymer. Keeping the flask rotating, the solution was allowed to warm to about -55°C (but no warmer) to allow polymerization to occur. The solution then turned into a dark purple gelatinous mass, and the pressure rose as excess acetylene was driven out of solution; this acetylene had to be pumped away.

The crude polyacetylene was filtered in a large Buchner funnel, rinsed with cold ethanol in a nitrogen-enriched atmosphere, and dried under vacuum. 90% of crude polyacetylene is solvent, and solvent removal from cis samples without isomerization caused problems; a solvent with a lower boiling point, as in Nehmé's preparation in ether[134], would make this easier. Samples of cis-polyacetylene were stored in a flask of liquid nitrogen to prevent isomerization, whereas trans-polyacetylene samples were isomerized at 180°C under vacuum for half an hour and stored under nitrogen gas. A typical preparation as described gave 0.5g of the dry polymer.

4.2 CHARACTERIZATION OF POLYACETYLENE

A sample of perdeuterated trans-polyacetylene was characterized by neutron diffraction. This is a particularly suitable technique in this instance, since both carbon and deuterium have large coherent neutron scattering lengths, whereas hydrogen contributes very weakly to X-ray diffraction patterns.# The pattern was recorded on the CURRAN powder diffractometer at AERE Harwell. The sample had been made a few days previously and stored at 77K. The day before the experiment, it was

---

A general introduction to neutron scattering methods is given in books by Bacon[290,291] and Willis[292].

isomerized by heating under dynamic vacuum at 210°C for one hour, then 190°C overnight, and transferred under nitrogen to a vacuum-tight cylindrical 8 mm diameter vanadium sample can. The sample mass before heating was 2.9g, but a small proportion of this was outside the beam. The scan was recorded at room temperature with a wavelength of 1.3679Å and lasted 48 hours. Owing to the the relatively large degree of disorder in the sample, high resolution was not attempted and 2θ was stepped in units of 0.5°. A background scan of the empty can was also measured, but the counts were under 1% of the sample counts and it was not considered worthwhile doing the subtraction.

The measured pattern, shown in Fig 4.1 and Table 4.1, compares to advantage with the published X-ray data. The counts have not been scaled and the mean error is 300, with many of the smaller peaks statistically significant. Values of the cell parameters obtained were a = 4.13 Å, b = 7.33 Å, c = 2.46 Å, β = 91.5°. (cf Oriented Durham polyacetylene [142] a = 4.18 Å, b = 7.34 Å, c = 2.43 Å, β = 90.5°) A theoretical pattern based on Fischer's monoclinic structure[146] with refined values of a, b and c was calculated using programs TRANSPAX (adapted from Nehmé's program P21N [293]) and PLOTPAX run on a VAX 11/780. The method of calculation of neutron powder diffraction intensities is given in Appendix III. At low angles, the agreement between calculated and measured patterns is good, but at higher angles some of the peaks (eg 002) do not correspond. Attempts were made to refine the unit cell parameters one at a time, but it was found that the scope for improvement was limited without a proper fitting program.

4.3 DOPING WITH CAESIUM METAL

This was done by direct combination in a manner analogous to the preparation of the graphite intercalates. Samples were made using 1 g caesium to 0.78 g cis-polyacetylene so as to give a composition

Fig 4.1 Observed and Calculated Diffraction Patterns of Trans-polyacetylene

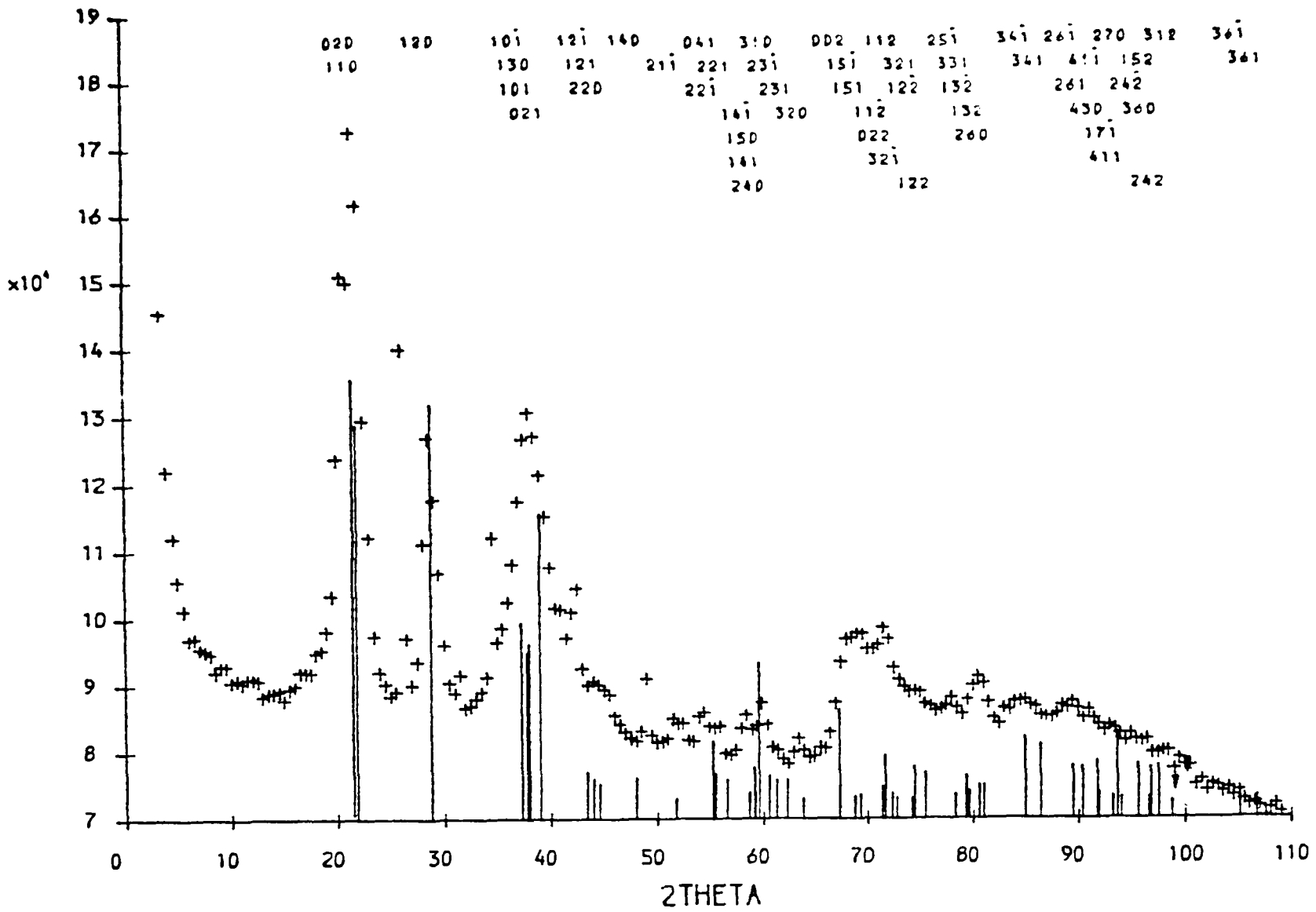

Parameters used in the calculated pattern (Structure shown in Fig 2.2)

Space group: P21/n (monoclinic)

Molecular data[146] (a, b and c slightly modified to give best fit):

a = 4.13 Å; b = 7.33 Å; c = 2.46 Å; β = 91.5°

ϕ (angle of polymer chain to 100 plane) = 55°

C-C-C bond angle = 127.3°

C=C bond length = 1.35 Å

C-D bond length = 1.09 Å

Additional data:

λ = 1.3679 Å

b_{coh} for C = 0.665×10^{-12} cm

b_{coh} for D = 0.667×10^{-12} cm [290,294]

u^2 in the Debye-Waller factor = 0.02 Å^2 [empirical]

Sample shape cylindrical, absorption and factors independent of θ ignored, minimum intensity listed = 10, maximum intensity = 259.

Published data:

Fischer et al[146]: a = 4.24Å; b = 7.32Å; c = 2.46Å; β = 91.5°

Durham polyacetylene[142]: a = 4.18Å; b = 7.34Å; c = 2.51Å; β = 90.5°

Table 4.1 Trans-poly-(acetylene-d_2) Neutron Diffraction data

	2θ	sinθ /λ	d Å	Index	2θ calc
s	20.5	0.1301	3.84	020	21.5
vvs	21.5	0.1364	3.67	110	21.9
s	28.4	0.1793	2.79	120	28.9
				$10\bar{1}$	37.4
vs	38.0	0.2380	2.10	130	37.9
				101	38.2
				021	39.1
w	42.5	0.2650	1.89	$12\bar{1}$	43.5
				121	44.2
w	44.8	0.2786	1.80	220	44.7
w	48.9	0.3026	1.65	140	48.2
vw	52.3	0.3222	1.55	$21\bar{1}$	51.9
vw	54.6	0.3353	1.49	041	55.4
				$22\bar{1}$	55.6
w	58.5	0.3572	1.40	$?14\bar{1}$	58.9
w	60.0	0.3655	1.37	240	59.9
vw	63.3	0.3836	1.30	231	62.6
m	68.0	0.4088	1.22	002	67.6
m	71.5	0.4271	1.17	022	71.8
vw	74.6	0.4430	1.13	$12\bar{2}$	74.6
vvw	77.9	0.4596	1.09	?	
				$13\bar{2}$	79.7
w	80.5	0.4723	1.06	132	80.7
				260	81.2
vw	84.5	0.4915	1.02	$34\bar{1}$	85.1
vvw	89.6	0.5151	0.97	$26\bar{1}$	89.6

s = strong; m = medium; w = weak; v = very.

NB This indexing only takes account of the **nearest** intense line and hence looks somewhat better than it is.

$(CHCs_{0.125})_x$ or $(CH)_8Cs$. The partially dried polymer was ground roughly in a pestle and mortar, then dried and isomerized under dynamic vacuum (10^{-3} torr) at 180°C for a couple of hours in a glass sample tube. (Polyacetylene is very mobile and must be evacuated slowly.) The heat also caused oligomers to distill out; these were collected in a solid carbon dioxide trap.

After cooling to room temperature, the apparatus was let up to nitrogen and a 1g glass ampoule of caesium precooled in solid carbon dioxide was broken and inserted with care. The apparatus was then pumped to 10^{-4} torr and the tube sealed off under vacuum. The sealed tube was heated, so that the caesium could run over the polyacetylene, and left at 180°C for a couple of days, at the end of which, all the caesium had intercalated, leaving no trace of white oxides. Unlike the graphite intercalates, caesium doping of polyacetylene causes no change in colour.

4.4 NEUTRON DIFFRACTION FROM CAESIUM DOPED POLY-(ACETYLENE-D_2)

A sample of caesium doped poly-(acetylene-d_2) was examined by neutron diffraction to complement to Baughman's X-ray work (Section 2.3.2) where the largest contributions to the structure factors arise from the dopant ions; in neutron diffraction, the polymer backbone scatters most strongly.

The sample was made from 1.05g deuterated polyacetylene and 1g caesium to give a nominal composition $(CDCs_{0.10})_x$. This scan was also recorded on the CURRAN powder diffractometer at the same time as the polyacetylene pattern and with similar scan conditions. (8 mm vanadium sample can, room temperature, λ = 1.3679Å, 2θ step = 0.5°, 48 hour scan, no background subtraction needed.)

The observed pattern is shown in Fig 4.2 and Table 4.2. The undoped polyacetylene lines appear quite strongly, but with increased widths,

suggesting that the sample was poorly intercalated and that the partial caesium doping has increased the degree of disorder. There are, however, also lines at low angles which index on a d spacing of 6.48Å, close to Baughman's value of 6.43±0.07Å [162]. (The line at 17.3° could also be a meridional line corresponding to Baughman's line at 4.4Å in the rubidium doped sample.)

A theoretical pattern based on Baughman's channel structure (Fig 2.4) was calculated using program CHXCS. For this purpose, the scattering from the caesium atoms was assumed negligible, and the bond alternation in the chain, 0.03Å in trans-polyacetylene[146], was assumed to have disappeared on doping. c was taken to be 2.46Å, the value in trans-polyacetylene.

The theoretical and measured patterns are compared in Fig 4.2. The line positions agree well, but there is a profound mismatch in the intensities; the 200 reflection, observed at moderate intensity, is predicted to be very intense indeed. This occurs because all the polyacetylene chain axes run along the fractional unit cell co-ordinates $(\pm\frac{1}{4},\pm\frac{1}{4},z)$, making every carbon atom in the unit cell scatter in phase, further reinforced by the deuterium atoms. (This line would be predicted to be much weaker in an X-ray pattern.) It is not possible to match the observed and calculated intensities by realistic adjustments to the molecular parameters, and this pattern must, therefore, cast doubt on Baughman's channel structure. However, without a better sample, it is difficult to refine on another structural model.

4.5 ABSORPTION OF HYDROGEN BY N-DOPED POLYACETYLENE

A sample of caesium doped polyacetylene of composition $(CH)_8Cs$ was exposed to an atmosphere of hydrogen at room temperature. No absorption was noted. It was then cooled to -196°C to see if any hydrogen was physisorbed in the manner of the stage II graphite intercalates

Fig 4.2 Neutron Powder Diffraction Pattern of Caesium Doped Polyacetylene

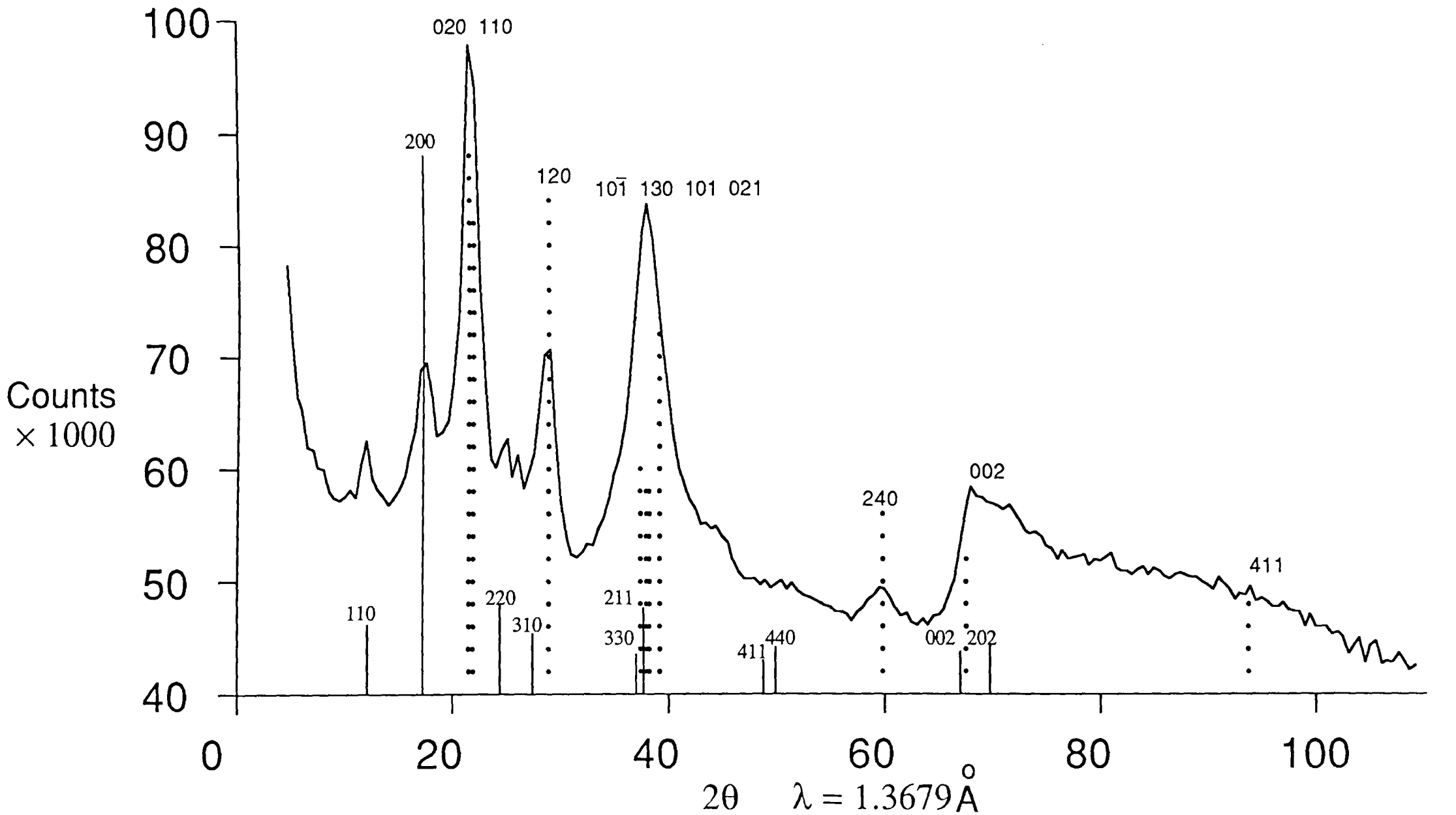

Lines assigned to doped polyacetylene are marked by solid lines and are indexed 110 (Parameters in Table 4.2). Undoped polyacetylene lines are marked by dotted lines and are indexed 020.

Table 4.2 $(CDCs_{0.1})_x$ Neutron Diffraction data

	2θ	sinθ /λ	d Å	Substance	Index	sinθ/λcalc	2θcalc
w	12.0	0.0764	6.54	$(CDCs_y)_x$	110	0.0772	12.1
m	17.3	0.1099	4.55	$(CDCs_y)_x$	200	0.1092	17.2
vs	21.4	0.1357	3.68	$(CD)_x$			
vw	25.0	0.1582	3.16	$(CDCs_y)_x$	220	0.1544	24.4
m	28.9	0.1824	2.74	$(CD)_x$			
vvw	32.3	0.2033	2.46	?			
vs	37.9	0.2374	2.11	$(CD)_x$			
vw	44.2	0.2750	2.82	$(CD)_x$			
vw	51.0	0.3147	1.59	$(CD)_x$			
w	59.5						
m	68.1	0.4093	1.22	$(CD)_x$			
m	71.0	0.4245	1.18	$(CD)_x$			
vvw	78.3	0.4615	1.08	$(CD)_x$			

Parameters used in the calculated pattern (Structure shown in Fig 2.4)

Space group: I4/mcm (tetragonal)

Molecular data (a=b adjusted from Baughman[162] to give best fit):

a = b = 9.16 Å = √2 × 6.48 Å; c = 2.46 Å

C-C-C bond angle = 127.5°

C-D bond length = 1.09 Å

Additional data:

λ = 1.3679 Å

b_{coh} for C = 0.665×10^{-12} cm

b_{coh} for D = 0.667×10^{-12} cm

b_{coh} for Cs assumed zero. (Actual value 0.55×10^{-12} cm [287,290])

u^2 in the Debye-Waller factor = 0.02 $Å^2$ [empirical]

Sample shape was cylindrical.

Absorption and factors independent of θ ignored.

Lines less than 0.1° apart were added.

Minimum intensity listed = 50, Maximum intensity = 1698

Published data: Baughman X-ray[162]: a = b = √2 × 6.43 Å

(See Section 1.5.2), but no detectable amount of hydrogen was absorbed under these conditions. On heating to 180°C, however, the pressure in the system dropped as the doped polyacetylene absorbed the hydrogen gas, and more hydrogen was admitted as necessary. After several days, a limiting composition of $(CH)_8CsH_{1.68}$ or $[CHCs_{0.125}H_{0.21}]_x$ was reached. After this, the sample was allowed to cool and excess hydrogen pumped away. The sample was heated under vacuum to 180°C, but little desorption occurred, and the temperature was raised to 240°C, at which temperature gas was given off, the volume being half the absorbed volume. On prolonged heating at 300°C, more gas was given off so that the total volume desorbed was slightly more than what had been absorbed. The final composition was not limiting, and gas was still being desorbed when the oven was switched off. The gas was collected in a demountable glass bulb and analysed by mass spectroscopy (Section 4.9).

The hydrogenation of n-doped polyacetylene to polyethylene has previously been reported, as has the mass spectrum analysis of the gases evolved from the pyrolysis of polyacetylene (Section 2.4), but the thermal degradation of partially hydrogenated polyacetylene is new work.

A perdeuterated sample was similarly hydrogenated to give a composition $(CD)_8CsH_{0.52}$ or $[CDCs_{0.125}H_{0.0625}]_x$. This sample was examined by neutron diffraction and then heated to 300°C so that the gas evolved could also be analysed by mass spectroscopy.

4.6 NEUTRON DIFFRACTION FROM CAESIUM DOPED POLY-(ACETYLENE-D_2) WITH ABSORBED HYDROGEN

The sample of $(CD)_8CsH_{0.52}$ was studied by neutron diffraction. While fully hydrogenated samples have been identified as polyethylene (Section 2.4), it is not clear whether the hydrogen initially adds to the polymer chain, forms a metal hydride with simultaneous undoping of the polyacetylene, or forms an intercalated metal hydride similar to the graphite intercalate $C_8KH_{\frac{2}{3}}$ (Section 1.5.1).

The two separate neutron diffraction experiments used the same sample which had total mass 3.72g and composition $(CD)_8CsH_{0.52}$. This was freshly made for the first experiment, kept in a sealed silica tube for the second experiment three months later, and always handled under nitrogen.

A trial diffraction pattern was recorded on D2 at the ILL with λ = 1.22Å at room temperature in an aluminium sample can, which regrettably superimposed a series of sharp background lines on the pattern, but which was needed for parallel experiments attempting to detect inelastic scattering from the absorbed hydrogen. The step in 2θ was 0.2° and the scan time was 1 hour and 8 minutes.[++] Unfortunately, time did not permit a background run of the empty can. The definitive pattern was measured on the CURRAN with λ = 1.3679Å at room temperature using a silica sample tube; this gives a gently sloping background with a few broad peaks. The 2θ step was 0.1°, but the points have been grouped to a 0.5° step to improve the statistics. The scan lasted three days, with a separate $2\frac{1}{2}$ day scan to record the empty silica tube. All the CURRAN patterns are plotted with the background subtracted. The D2 diffraction pattern is plotted in Fig 4.3 with the aluminium lines marked in the picture and excluded from the accompanying table. The CURRAN pattern is shown in Fig 4.4 and Table 4.3.

Three structural models have been studied to interpret the patterns. First, the $[CDCs_y]_x$ structure could be largely unchanged by the presence of absorbed hydrogen; second, there could be patches of polyethylene, and third, there could be patches of caesium hydride or deuteride. A neutron diffraction pattern of polyethylene has been measured by J. Twisleton[295] (Table 4.4), and caesium hydride has a sodium chloride

---

++ The fact that any worthwhile results at all can be recorded in this time illustrates the high flux available at the ILL.

Fig 4.3 Neutron Diffraction data from Caesium Doped Polyacetylene with Absorbed Hydrogen using Instrument D2

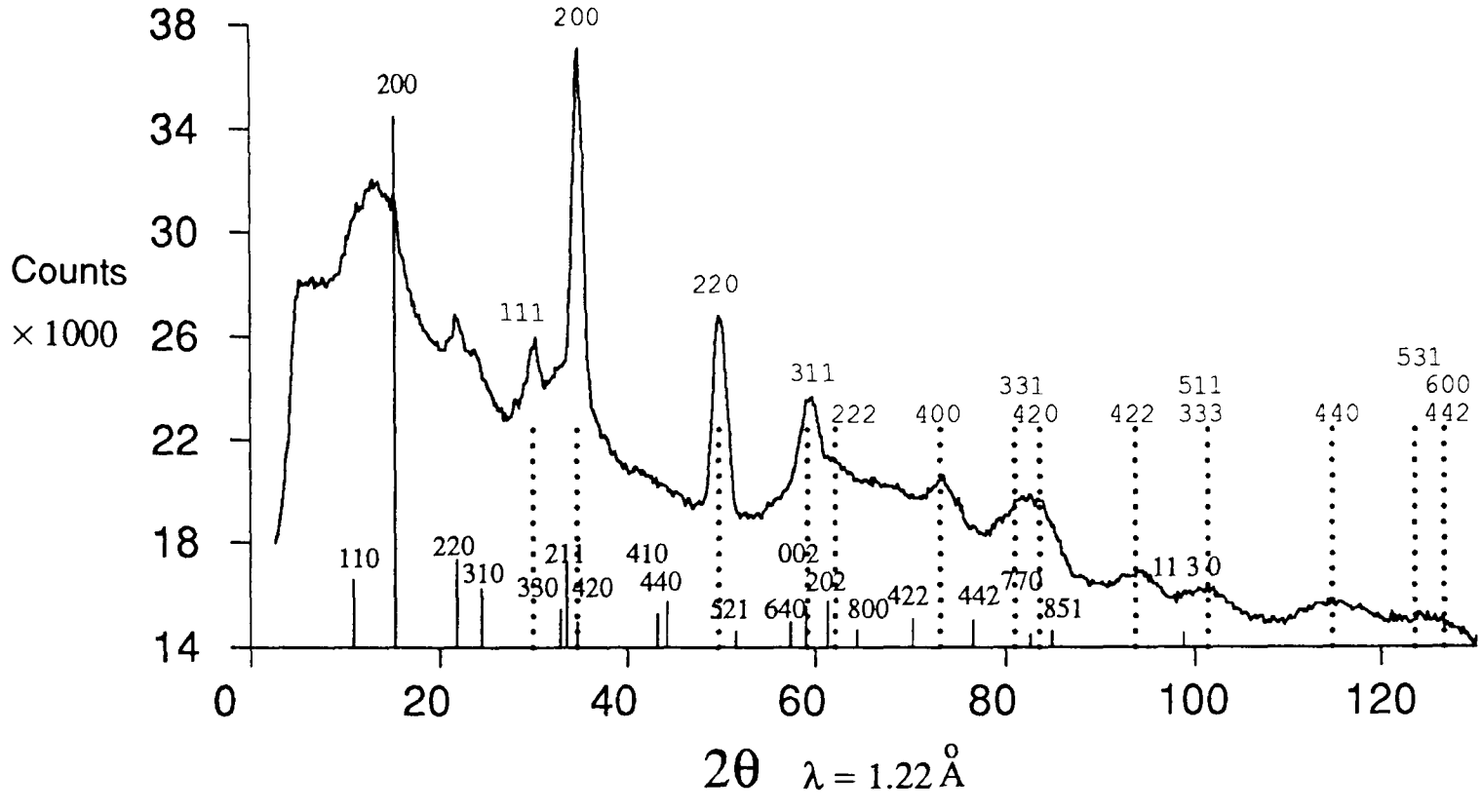

Solid lines with scaled intensities show indexing on Baughman's model for caesium doped polyacetylene (Data given in Table 4.2). Lines from the aluminium sample container are marked by dotted lines of arbitrary intensity, index on a fcc unit cell with dimension 4.098A (cf 4.04A in Wells[295]) and are excluded from the table below.

	2θ	sinθ /λ	d A	Substance	Index	2θcalc
sh	11.3	0.0807	6.196	$(CD)_xCs$	110	10.8
vs	13.2	5.307				
sh	15.2	0.1084	4.612	$(CD)_xCs$	200	15.3
w	21.9	0.1557	3.211	$(CD)_xCs$	220	21.7
vvw	23.8	0.1690	2.958	$(CD)_xCs$	310	24.3
				$(CD)_xCs$	330	32.8
sh	32.7	0.2307	2.167	$(CD)_xCs$	211	33.4
				$(CD)_xCs$	420	34.6
sh	36.8	0.2587	1.933	?		
vvw	66.2	0.4476	1.117			
vvw	68.6	0.4619	1.082			

Fig 4.4 Neutron Diffraction Data from Caesium Doped Polyacetylene with Absorbed Hydrogen using CURRAN

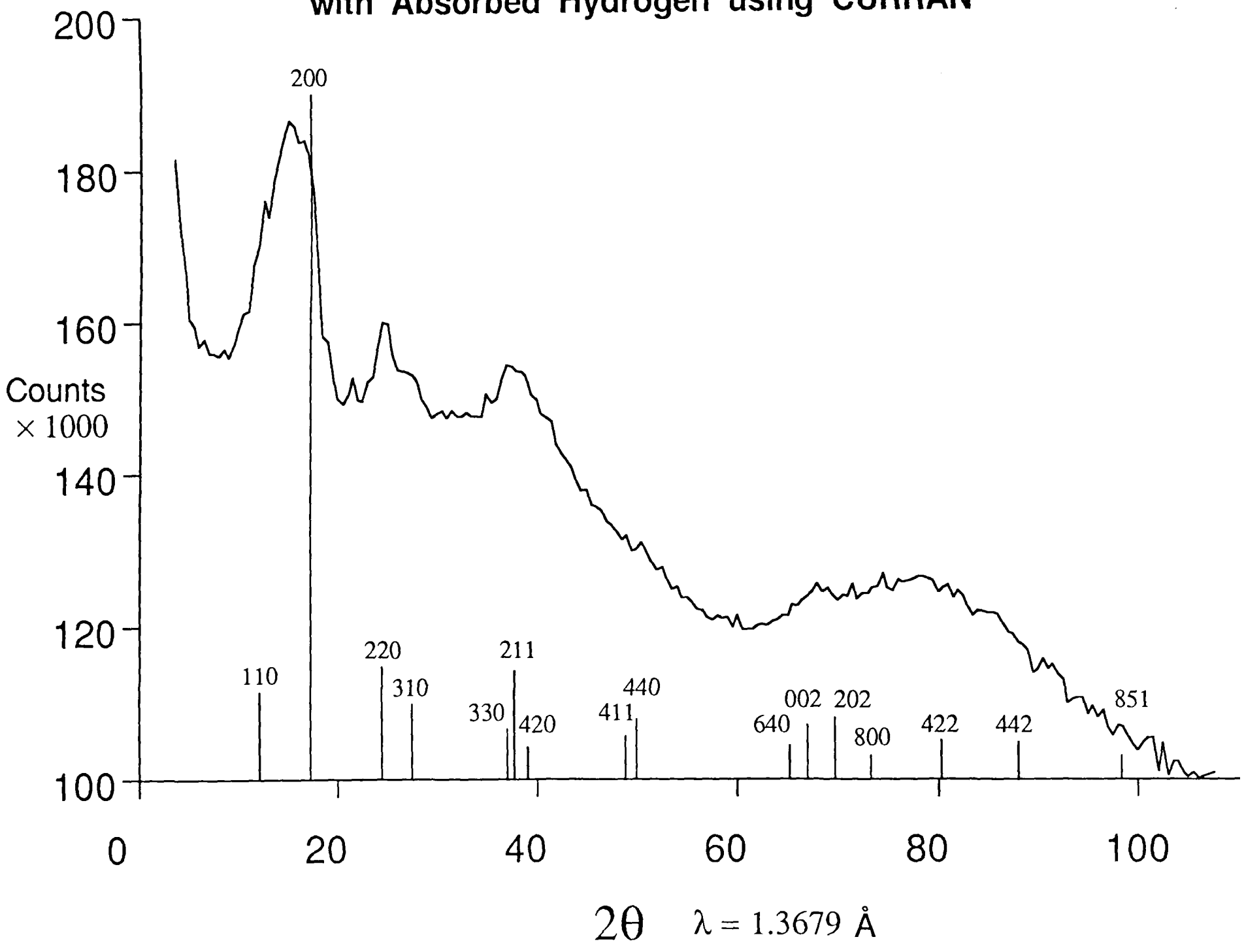

Table 4.3 Neutron Diffraction data from Caesium Doped Polyacetylene with Absorbed Hydrogen: Lines observed on CURRAN

	2θ	sinθ /λ	d Å	Substance	Index	sinθ/λcalc	2θcalc
vvs	14.9	0.0948	5.27	$(CD)_xCs$	110	0.0772	12.1
vvs	16.6	0.1055	4.74	$(CD)_xCs$	200	0.1092	17.2
vvw	19.0	0.1207	4.14	?			
w	21.5	0.1364	3.67	$?(CD)_x$	110		22.0
vvw	23.2	0.1470	3.40	?			
s	24.7	0.1564	3.20	$(CD)_xCs$	220	0.1544	24.4
m	27.0	0.1707	2.93	$(CD)_xCs$	310	0.1725	27.3
				$(CD)_xCs$	330	0.2316	36.9
s	37.8	0.2368	2.11	$(CD)_xCs$	211	0.2357	37.6
vvw	50.6	0.3124	1.60	$(CD)_xCs$	440	0.3083	50.0
vvw	58.7	0.3583	1.39	$(CD)_xCs$	521	0.3564	58.4
w	68.2	0.4099	1.22	$(CD)_xCs$	002	0.4032	67.0
vvw	74.0	0.4400	1.14				
vvw	78.5	0.4625	1.08		Definite assignments not		
vvw	81.6	0.4777	1.05		really possible in this		
vvw	85.6	0.4967	1.01		region.		
vvw	101.1	0.5645	0.89				

λ = 1.3679 Å

Doped polyacetylene indexed as before with a = b = 9.16 Å; c = 2.48 Å.

Table 4.4 Twisleton's Neutron Diffraction Data from Polyethylene[296]

	2θ	sinθ /λ	d Å	Impurity?	Index
vvs	15.0	0.1297	3.85		200
m	16.7	0.1444	3.46		
w	21.0	0.1811	2.76		
m	27.5	0.2363	2.12		201
w	28.6	0.2455	2.04	Al	200
w	29.5	0.2531	1.98		
m	32.2	0.2757	1.81		
vw	39.0	0.3318	1.51	Al	220

λ = 1.006Å

structure with unit cell dimension 4.51A [297]. Neither of these produces a diffraction pattern resembling the observed, although caesium hydride is difficult to rule out owing to its weak structure factors. The most reasonable indexing is thus that for unaltered caesium doped polyacetylene, and Figs 4.3 and 4.4 show the effect of indexing the patterns on Baughman's model. However, the 111 and 200 lines appear to have moved closer together, and there is considerable diffuse scattering, falling off smoothly with increasing 2θ.

4.7 THE REACTION OF GRAPHITE INTERCALATES $C_{26}Cs$ AND C_8Cs WITH ACETYLENE

Having all the materials to hand, it was decided to test whether acetylene could be absorbed or even polymerized by the graphite intercalates, possibly to make a new material with intermediate properties. The stage II compound $C_{24}Cs$ was chosen because it has the largest lattice spacing and physisorbs nitrogen most easily (Section 1.5.2).

A sample tube containing 3.5g of $C_{26}Cs$ was attached to a high vacuum system with a mercury manometer. First, the system volume and sample purity were checked with hydrogen. A calibrated bulb was filled with hydrogen and the rest of the system evacuated. The bulb was opened to the system and the pressure noted. The sample was then cooled in a Dewar of liquid nitrogen to form $C_{26}Cs(H_2)_2$; 226 torr litres were absorbed compared with a calculated 256 torr litres. The sample was then warmed to room temperature and the hydrogen pumped away.

Next, the liquid nitrogen traps were all replaced with solid carbon dioxide slush baths and the sample was exposed to a known volume of acetylene gas. The sample went black, became hot and swelled in the tube with a drop in pressure. On cooling the sample to -79°C, the reaction rate increased. The reaction reached completion after a few hours and the final absorption was 192 torr litres, giving a composition based on the hydrogen absorption of $C_{26}Cs(C_2H_2)_{1.70}$.

After this, the sample was warmed to room temperature and a slight rise in pressure (≈10 torr) was noted. The following day, it was cooled in a solid carbon dioxide slush bath again, then rewarmed. No significant amount of gas came off. The sample was then heated to 180°C and 5.2 torr litres of gas were desorbed. These were collected for analysis by mass spectroscopy (Section 4.9). The sample was then allowed to cool overnight. The following day, the sample was pumped to 10^{-3} torr and hydrogen was admitted. The sample was then cooled in a Dewar of liquid nitrogen, but no hydrogen was absorbed. Another sample of $C_{26}Cs$ was exposed to C_2D_2 and absorbed it to a composition of $C_{26}Cs(C_2D_2)_{1.27}$. Both samples were kept for study by neutron diffraction.

Following the successful absorption of acetylene gas by $C_{24}Cs$, it was decided to see whether C_8Cs would also absorb acetylene. C_2D_2 was used because the vacuum line was already set up to prepare the sample of $C_{26}Cs(C_2D_2)_{1.27}$ for the neutron diffraction experiment. The sample tube contained a sample of C_8Cs made with 2g Cs metal, having total mass 3.44g. The sample was cooled to -79°C and exposed to dried C_2D_2. No uptake was observed over a period of minutes, so the sample was allowed to warm to room temperature. The pressure started to fall very slowly from an initial value of 378 torr and after six days finally stabilized at 278 torr, indicating a limiting composition of $C_8Cs(C_2D_2)_{0.50}$. The product was brown in appearance, with flecks of unreacted golden C_8Cs, indicating that more acetylene might have been absorbed under harsher conditions. The reaction is much slower than both the reaction of C_8Cs with air and the reaction of $C_{24}Cs$ with acetylene.

After completion, the sample was taken off the vacuum line and transferred in a glove bag into a sealed container for analysis by neutron diffraction. It was thought safest not to try to seal it off under vacuum with acetylene present.

4.8 NEUTRON DIFFRACTION FROM ACETYLENE/ INTERCALATE SAMPLES

The neutron diffraction patterns of the samples of $C_{26}Cs(C_2D_2)_{1.27}$, $C_{26}Cs(C_2H_2)_{1.70}$ and $C_8Cs(C_2D_2)_{0.50}$ described above were measured on the CURRAN, together with a 3.5g sample of $C_{26}Cs$ and a 4g sample of outgassed graphite for reference. (The graphite diffraction pattern is well-known and not reproduced here. The $C_{26}Cs$ diffraction pattern measured in this experiment has already been shown in Fig 1.1) The wavelength was 1.3739 Å, and the samples were run at room temperature in a 12 mm diameter vacuum tight vanadium can. The step size was originally 0.1°, although the points have been grouped to a 0.3° step. The scan on $C_{26}Cs(C_2D_2)_{1.27}$ lasted two days, the other samples being run for 24 hours. The very low instrument background made the running of the empty can unnecessary.

The quality of the diffraction patterns reflects the much greater order in the intercalates compared with the conducting polymers. The diffraction patterns of $C_{26}Cs(C_2D_2)_{1.27}$ and $C_{26}Cs(C_2H_2)_{1.70}$ show the disappearance of the $C_{24}Cs$ 00ℓ lines and the appearance of large quantities of graphite together with other weak lines (Figs 4.5, 4.6). The question thus arises as to the fate of the caesium ions. The most obvious possibility is that caesium acetylide, $Cs^+ (HC{\equiv}C)^-$, has been formed. Although sodium and potassium acetylides have had their diffraction patterns measured and have been shown to have the tetragonal face-centred calcium carbide structure (Space group I4/mmm, cell parameters a = 5.40, 6.05 Å; c = 8.17, 8.42 Å respectively [298,299]), there appears to be no structural determination of caesium acetylide and no easy way to calculate the cell parameters.

The weak lines in the diffraction patterns unaccounted for by graphite are the same in both $C_{26}Cs(C_2D_2)_{1.27}$ and $C_{26}Cs(C_2H_2)_{1.70}$ and appear to index on a hexagonal unit cell with a = b = 11.47 Å and c = 7.95 Å. This corresponds to no known structure and does not appear

Fig 4.5 Neutron Diffraction Pattern from $C_{26}Cs(C_2D_2)_{1.27}$

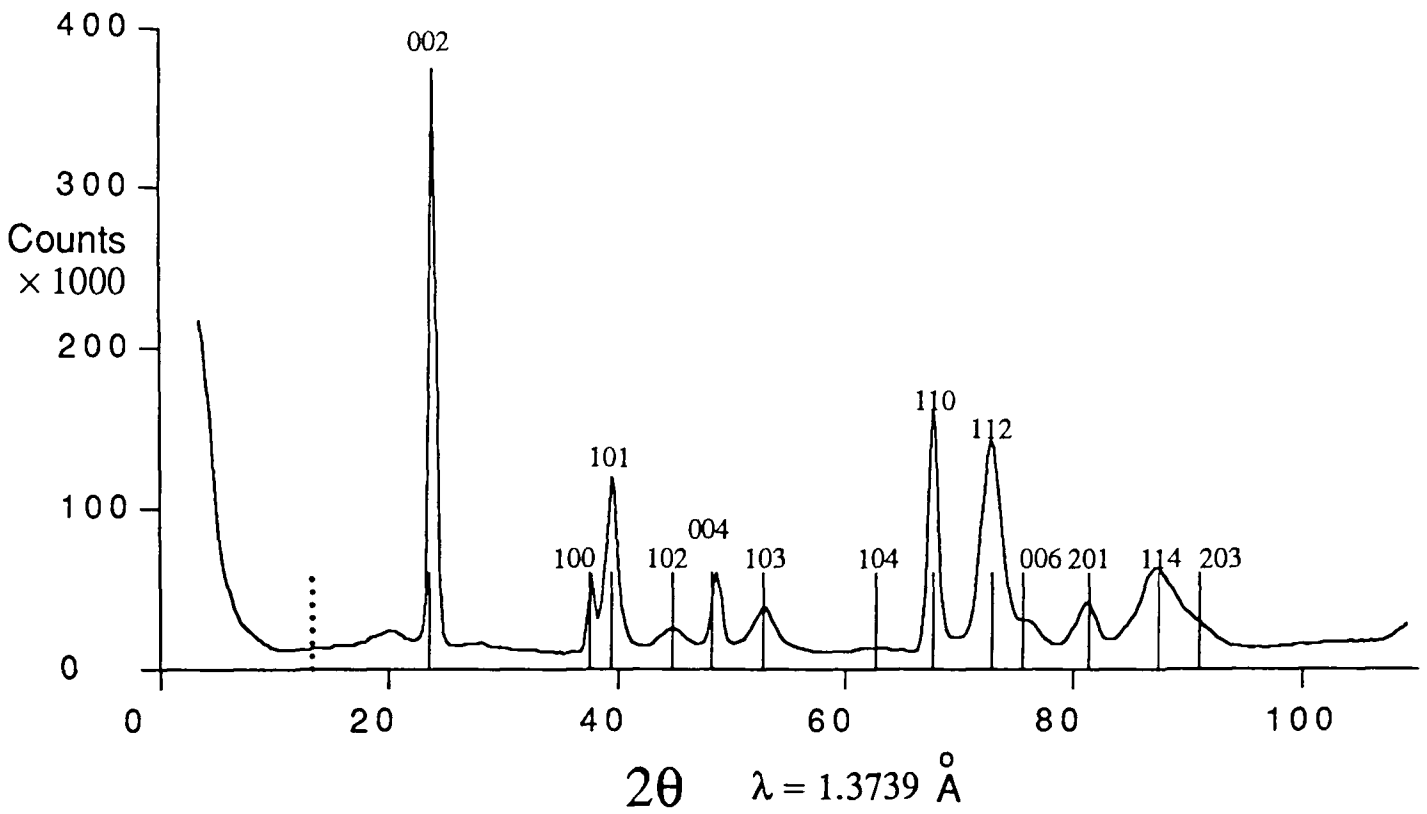

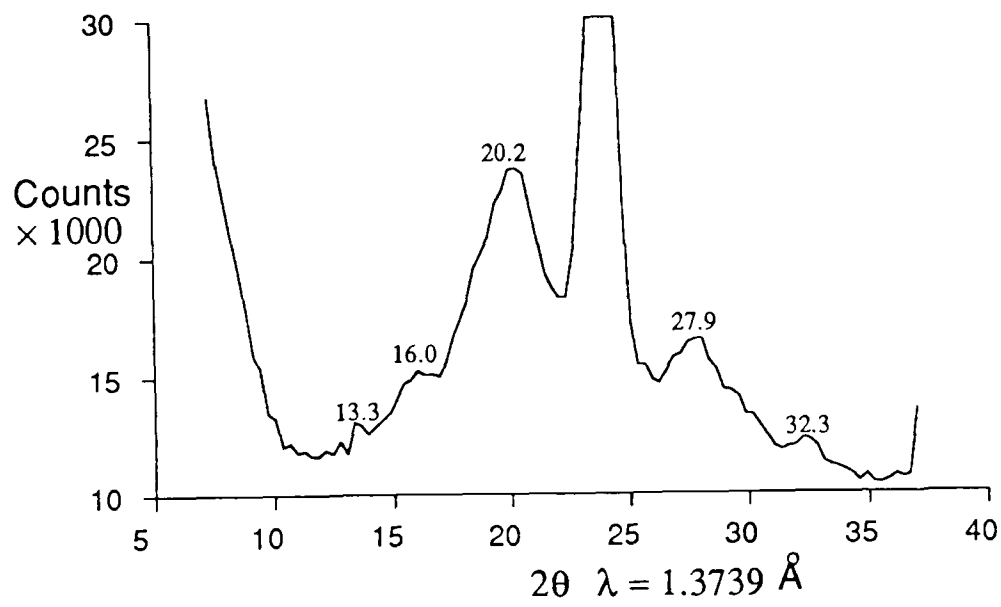

The top picture shows the full pattern, and the bottom picture an enlargement. Solid lines of arbitrary height mark the graphite peaks indexed on a hexagonal unit cell with a = 2.463A, c = 6.725A, the values obtained from the graphite pattern. (Published values a = 2.456A, c = 6.696A [295].) The 00ℓ lines show a small shift from these values. The dotted line at 13.3° is the C_8Cs 001 line.

Lines not accounted for by Graphite or C_8Cs

	2θ	sinθ /λ	d Å	Index	sinθ/λcalc	2θcalc
vw	16.0	0.1013	4.936	200	0.1013	16.0
s	20.2	0.1276	3.917	002		
m	27.9	0.1755	2.850	220	0.1754	27.9
w	32.3	0.2025	2.470	400	(0.2026)	(32.3)

ab lines index on hexagonal unit cell with in-plane d spacing 9.88 Å.

(Indexed from 400) a = b = $2d/\sqrt{3}$ = 11.41 Å; c = 7.83 Å.

Fig 4.6 Neutron Diffraction Pattern from $C_{26}Cs(C_2H_2)_{1.7}$

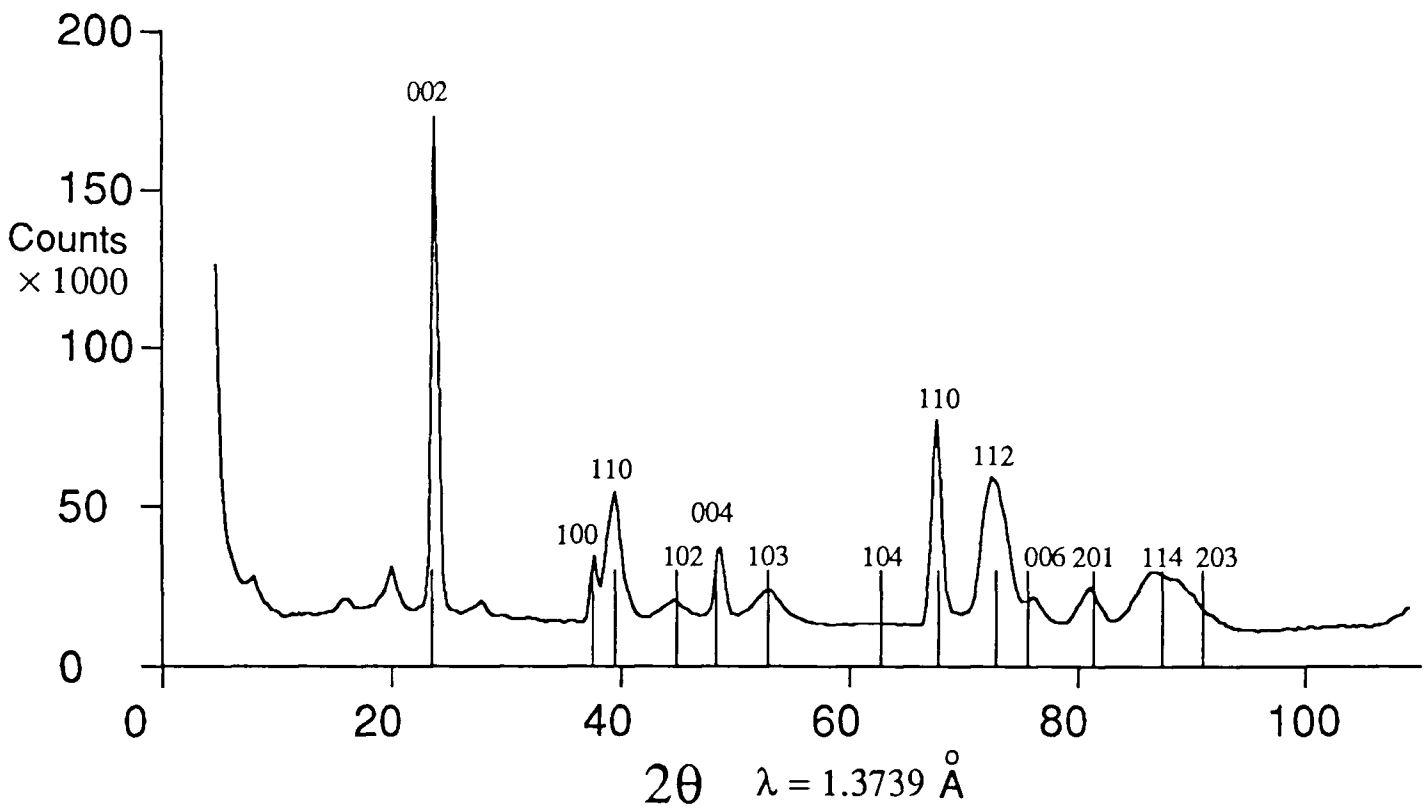

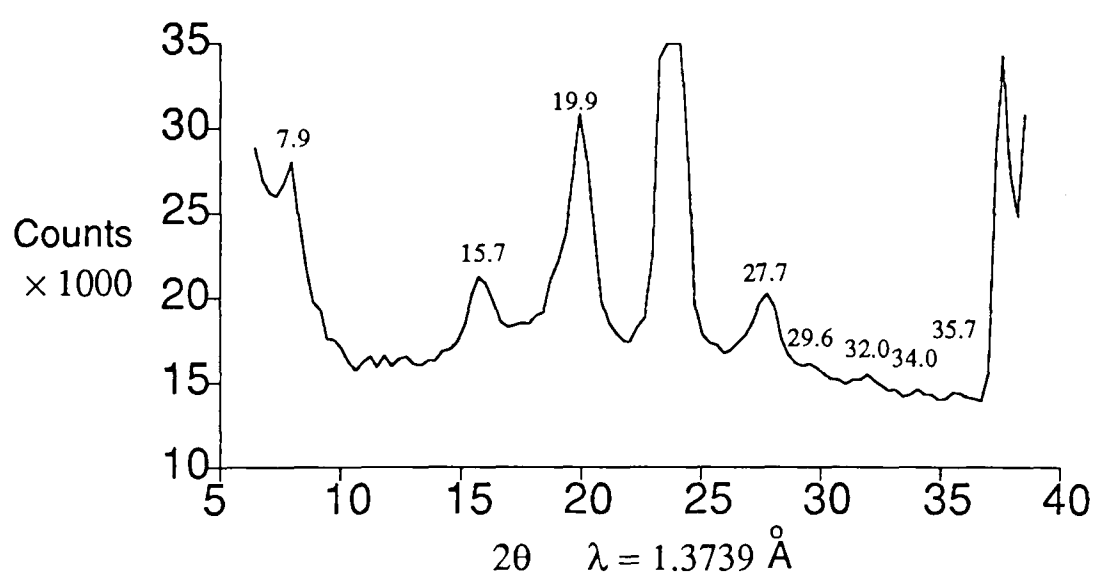

The top picture shows the full pattern, and the bottom picture an enlargement. Solid lines of arbitrary height indicate graphite peaks. (See Fig 4.5 for indexing details.)

Lines not accounted for by Graphite

	2θ	sinθ /λ	d Å	Index	sinθ/λcalc	2calc
vw	7.9	0.0501	9.972	100	0.0503	7.9
w	15.7	0.0994	5.030	200	0.1006	15.9
m	19.9	0.1258	3.976	002	(0.1258)	(19.9)
w	27.7	0.1742	2.870	220	(0.1742)	(27.7)
vvw	29.6	0.1859	2.689	003	0.1887	30.0
vw	32.0	0.2006	2.492	400	0.2012	32.0
vvw	35.7	0.2231	2.241	113	0.2230	35.7

The lines are almost identical to $C_{26}Cs(C_2D_2)_{1.27}$

Hexagonal unit cell with d = 9.94Å so a = b = 11.47 Å(Indexed from 220)

c = 7.95 Å (Indexed from 002)

Fig 4.7 Neutron Powder Diffraction Pattern from $C_8Cs(C_2D_2)_{0.5}$

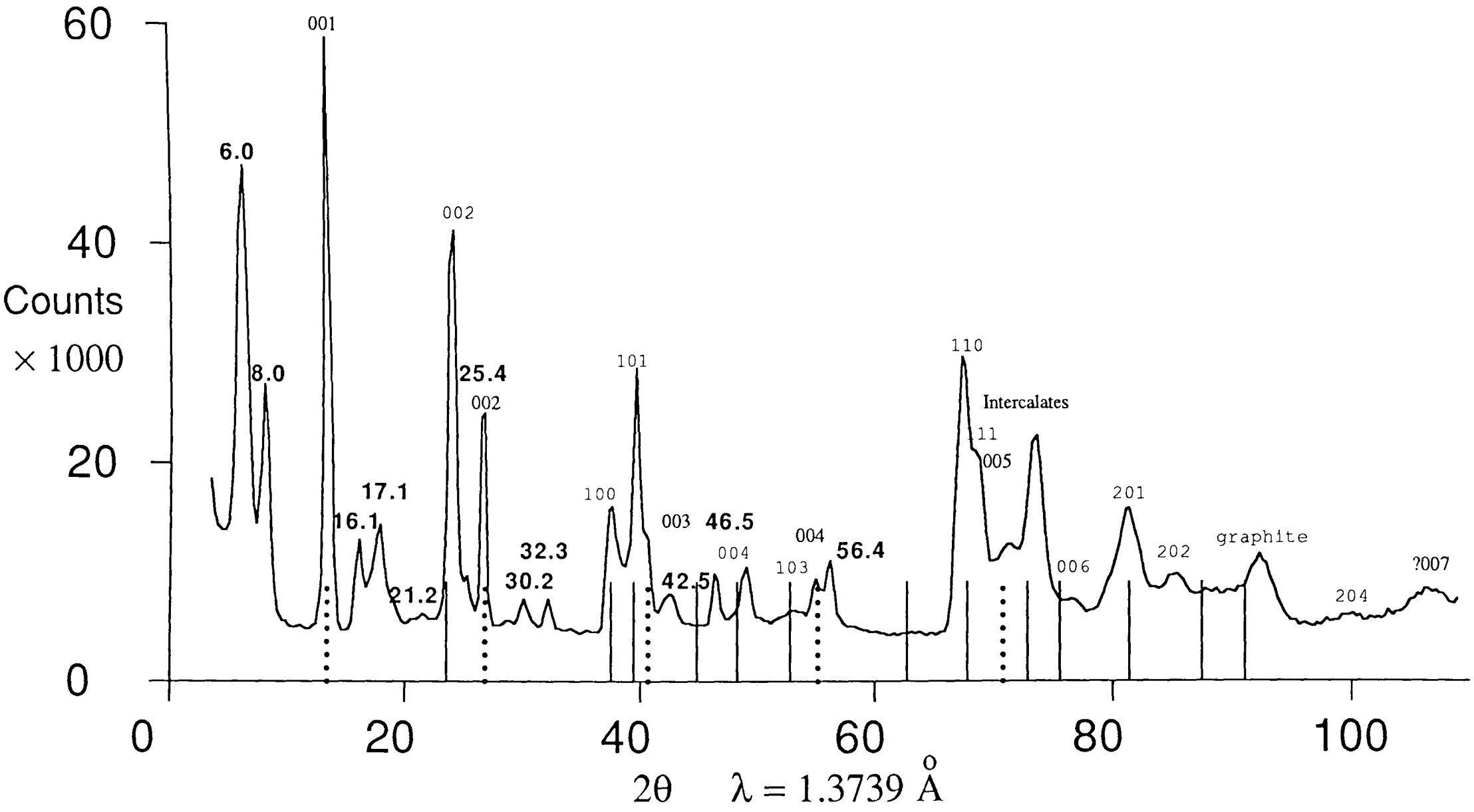

Lines from the graphite pattern are marked with solid lines and are indexed 002. Intercalate peaks are marked with dotted lines and indexed 001 Lines accounted for neither by graphite nor intercalate are indexed in Table 4.5 and have their positions marked **6.0.** (N.B. Graphite and intercalate calculated lines are taken from the diffraction patterns of the pure substances. Not all the lines are visible here. Similarly, some lines which could not be indexed appeared in the graphite and intercalate patterns; in these cases the substance responsible has been marked with no index.)

Table 4.5 $C_8Cs(C_2D_2)_{0.5}$ Neutron Diffraction data

Lines not accounted for by Graphite or C_8Cs

	2θ	sinθ /λ	d Å	Index	sinθ/λcalc	2θcalc
vs	6.0	0.0381	13.126	0 0 3	0.0381	6.0
s	8.0	0.0508	9.848	0 0 4	(0.0508)	8.0
w	16.1	0.1019	4.905	0 0 8	0.1016	16.0
w	17.7	0.1120	4.465	0 0 9	0.1143	18.1
vw	21.2	0.1339	3.734	1 0 0	0.1319	
vvw	25.4	0.1600	3.125	009×√2	0.1583	
w	30.2	0.1896	2.637	1 1 0	0.1893	
				0 0 15	0.1905	30.3
w	32.3	0.2025	2.470	0 0 16	0.2032	32.4
w	42.5	0.2638	1.895	2 0 0	(0.2638)	(42.5)
w	46.5	0.2873	1.740	2 0 9	0.2865	46.4
w	56.4	0.3439	1.454	0 0 27	0.3429	56.2

Orthorhombic structure a = 3.79 Å (from 200); c = 39.4 Å (from 004)
The only 00ℓ lines visible are 0 0 3n and 0 0 4n but not 0 0 6n

to tie in with the caesium acetylide theory, although calcium carbide does have four structural modifications. Furthermore, the formation of caesium acetylide would account for the absorption of only one mole of acetylene. On the other hand, the lines do not correspond to doped or undoped cis- or trans-polyacetylene and the 100 d spacing is **exactly** four times the graphite in-plane cell parameter.

The $C_8Cs(C_2D_2)_{0.5}$ diffraction pattern is still more mysterious (Fig 4.7). As well as residual C_8Cs and graphite peaks, there are two intense low angle lines at 2θ = 6.0 and 8.0 degrees, corresponding to repeat distances of 13.1 and 9.85 Å. Both of these lines have several higher order multiples. These **could** correspond to stage II and stage III components with the c axis expanded by the acetylene absorption.

Alternatively, they index as 003 and 004 respectively on a single parameter of 39.4A, which is 16 times both the c axis in trans-polyacetylene and the a axis in graphite.

4.9 Mass Spectrum Analysis of the Gases evolved from the Pyrolysis of $(CH)_8CsH_{1.67}$, $(CD)_8H_{0.52}$ and $C_{26}Cs(C_2H_2)_{1.70}$

The gases evolved from the pyrolysis of $(CH)_8CsH_{1.67}$ were analysed by mass spectroscopy (Fig 4.8). In contrast to what had been expected, the main component was found to be methane, with smaller quantities of higher alkanes (assumed to be n-alkanes); also large quantities of either N_2 or CO (both mass 28), and a small amount of water, air and trichloroethylene solvent. (The most likely cause of the N_2 or CO is air leakage during hydrogen uptake.) A small amount of hydrogen was seen, but little if any unsaturated compounds were present, in contrast to the results for polyacetylene alone (Table 2.2).

In the case of $(CD)_8CsH_{0.52}$, the main component was CH_2D_2, with smaller quantities of CHD_3 and CD_4 and partially deuterated higher alkanes. In the hydrogen peaks, the quantity of D_2 was greater than that of HD, and much greater than that of H_2. CH_3D and CH_4 were notable by their absence, as was C_2D_6 and the impurities N_2, CO and O_2.

The proportions of each component identified are given in Table 4.6, with experimental details and the method of calculation of proportions of each component in Appendix IV. Without the aid of a gas chromatograph to separate components, as used by Chien in his pyrolysis of polyacetylene[2,192], identification of higher weight molecular compounds proved difficult, particularly as the higher alkanes undergo extensive fragmentation with relatively small parent peaks. Because of the large number of possible isomers and the ambiguity in the mass of the parent peaks, the identification of deuterated compounds containing more than one carbon atom has not been attempted, although they are undoubtedly present in considerable quantities.

Fig 4.8 Some Mass Spectra of gases obtained from Pyrolysis of Polyacetylene derivatives

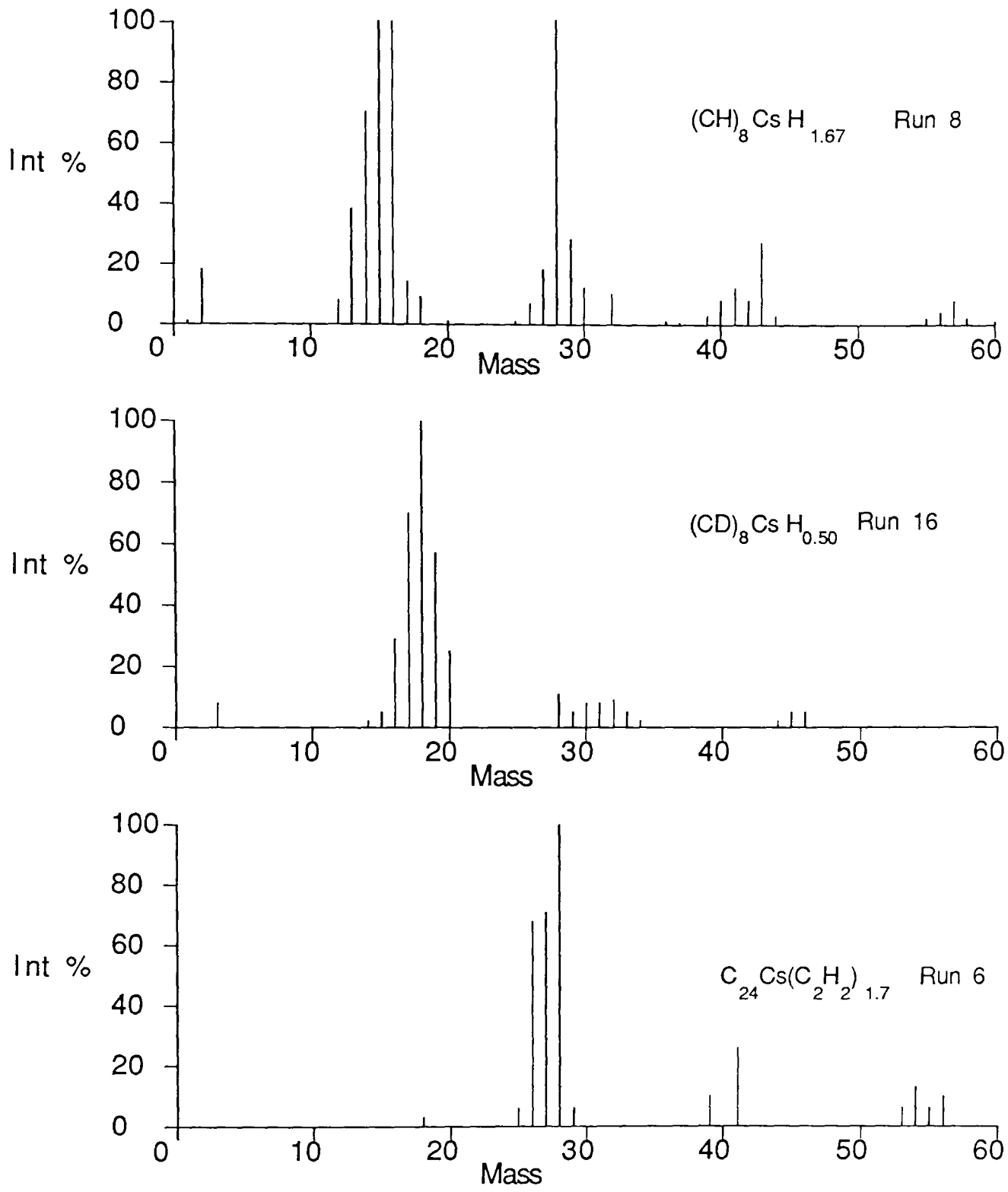

Peaks normalized to give most intense peak intensity 100. Peaks which ran off scale also given intensity 100.

The preponderance of methane in the mass spectrum confirms the irreversible nature of the hydrogenation reaction, and the fact that partially hydrogenated doped polyacetylene is less thermally stable than the unhydrogenated compound suggests that methane elimination takes place at the CH_2 groups introduced during the hydrogenation, probably resulting in a polydiacetylene.## (A series of ring closure reactions to

---

The photopolymerization of substituted diacetylenes in the solid state to produce conjugated polymers with triple bonds is discussed by Wegner[309].

Table 4.6 Gases evolved on Pyrolysis of Polyacetylene Derivatives

	$(CH)_8CsH_{1.67}$		
Compound	rmm	Mole fraction %	Mass fraction %
methane	16	72	60
N_2 (or CO)	28	21	30
air	28.5	2.1	3.0
hydrogen	2	1.8	0.18
ethane	30	1.5	2.4
butane (as n-butane)	58	0.4	1.3
water	18	0.4	0.4
propane (from mass 44)	44	0.3	0.6
hexane (as n-hexane)	86	0.2	1.0
argon	40	0.21	0.4
trichloroethylene	131	0.1	0.7

Proportions of Hydrogen and Methane Isotopes in $(CD)_8CsH_{0.52}$

Compound	rmm	Relative Mole fraction %
CH_2D_2	18	100
CD_3H	19	78
CD_4	20	22
D_2	4	19
HD	3	14
H_2 (from mass 2)	2	2-3

give a graphite intercalate, although more difficult kinetically, would result in a more thermodynamically stable product.) Elimination of heavier molecules would be most likely to occur at the chain ends.

In the case of $C_{26}Cs(C_2H_2)_{1.67}$, the amount of gas evolved was much smaller than from the polyacetylene compounds. Analysis of the mass spectrum shows that the main product is ethylene with substantial quantities of butene, butadiene, acetylene, ethane, hexadiene and hexatriene (Table 4.7). The number of possible butene and hexene isomers is large, so guesses have had to be made, but apart from a disagreement

Table 4.7 Gases evolved on Pyrolysis of $C_{26}Cs(C_2H_2)_{1.7}$

Compound	rmm	Mole fraction %	Mass fraction %
ethylene	28	57	46
butene (as trans-but-2-ene)	56	11	18
butadiene (from mass 54)	54	8.9	14
acetylene	26	8.0	6.0
water	18	4.8	2.5
ethane	30	3.1	2.7
1,3-hexadiene (from mass 82)	82	1.3	3.0
trans-1,3,5-hexatriene (from mass 80)	80	1.3	3.0
hydrogen	2	1.2	0.07
propene (from mass 42)	42	1.1	1.4
propyne (from mass 40)	40	0.6	0.7
butane (as n-butane)	58	0.5	0.9
methane	16	0.3	0.14
propane	44	0.2	0.3
trans-1,3-pentadiene (from mass 68)	68	0.14	0.3
benzene	78	0.07	0.16

NB Reasonable uncertainty as to the identity of each component is expressed in (brackets). The figures given are maxima and do not imply that all components not mentioned have a mole fraction <0.7%.

at mass 39, the calculated and observed spectra compare well. (Method in Appendix IV) Methane, benzene and molecules with odd numbers of carbon atoms generally are notable by their scarcity, and N_2, O_2 and CO appear to be absent. The results clearly indicate the polymerization of acetylene to an unsaturated chain compound. However, the relatively large quantity of hydrogen in the gases evolved, compared with the original acetylene, suggests that some of the acetylene has formed graphite, as suggested by the neutron diffraction data.

APPENDIX III : CALCULATION OF NEUTRON POWDER DIFFRACTION INTENSITIES

The theory of neutron diffraction by crystals is well documented and good accounts are given by Windsor[300] and Bacon[290]. Bacon on p. 112 gives the following expression for the absolute intensity of neutron diffraction peaks from a powder sample in a cylindrical container normal to the incident beam:-

$$\frac{P}{I_0} = \frac{\lambda^3 l_s}{8\pi r} \frac{V\rho'}{\rho} \frac{j N_c^2 F^2}{\sin\theta \sin 2\theta} e^{-2W} A_{hk\ell} \qquad (A3.1)$$

where

P is the number of neutrons diffracted per minute into the counter.

I_0 is the number of neutrons per unit beam area hitting the specimen.

* λ is the neutron wavelength (Å).

* l_s is the height of the counter slit.

* r is the distance of the specimen from the counter.

* ρ' is the theoretical density of the specimen.

* ρ is the measured density of the specimen.

j is the number of co-operating planes for the particular reflection being measured.

* N_c is the number of unit cells per cm^3.

F is the structure amplitude factor (see below).

θ is the angle of diffraction.

e^{-2W} is the Debye-Waller factor (see below).

$A_{hk\ell}$ is the neutron absorption factor with $hk\ell$ as Miller indices.

The terms marked * in the above expression do not vary with either $hk\ell$ or θ and are only important if absolute intensities are to be calculated. Neutron absorption can also be neglected for the

polyacetylene samples, since they only give ≈10% scattering, and the neutron absorption cross-sections for carbon and deuterium are much less than their scattering cross-sections[294]. If planes with the same d spacing are each considered individually (eg 100 and 010 in a cubic crystal), j can also be eliminated.

Defining $I_{hk\ell}$ as the relative intensity of the hkℓ reflection:-

$$I_{hk\ell} = \frac{F^2_{hk\ell}\, e^{-2W}}{\sin\theta \sin 2\theta} \qquad (A3.2)$$

In the centrosymmetric case (the space groups used in the calculations, P21/n and I4/mcm, are both centrosymmetric[301]):-

$$F_{hk\ell} = \sum_\rho b_\rho \cos 2\pi(hx + ky + \ell z) \qquad (A3.3)$$

where

$\sum_\rho$ denotes summation over all the atoms in the unit cell.

b_ρ is the coherent scattering length of atom ρ.

x y z are the fractional co-ordinates of atom ρ within the unit cell.

The Debye-Waller factor, e^{-2W} takes account of random thermal motions, and its effect is to diminish the intensities of high angle lines. A commonly used approximation is given by [302]:-

$$W = \tfrac{1}{2}Q^2\langle u^2\rangle \qquad (A3.4)$$

where Q is momentum transfer in the scattering event and $\langle u^2\rangle$ is the mean square thermal motion, averaged for all atoms in the unit cell.

For elastic scattering $$Q = \frac{4\pi}{\lambda}\sin\theta \qquad (A3.5)$$

$\langle u^2\rangle$ for polyacetylene at room temperature is, however unknown and had to be chosen empirically. A value of 0.02Å^2 seemed to match the observed results.

APPENDIX IV

IDENTIFICATION OF COMPOUNDS IN A MULTI-COMPONENT MASS SPECTRUM

1. The Experiments

The gases evolved from the pyrolysis at 300°C of $(CH)_8CsH_{1.67}$, $(CD)_8CsH_{0.52}$ and $C_{26}Cs(C_2H_2)_{1.7}$ were analysed using a Micromass 12 single deflection mass spectrometer. Mass calibration used samples of air, followed by a blank run to check impurity levels. Scans started at mass 1 instead of the more usual mass 12 to enable analysis of hydrogen. Problems with the system included lack of multiple recording so that scans had to repeated to register both major and minor components, and limitations on pen speed, making large peaks shrink on fast scans. Some representative spectra have already been shown in Fig 4.8 with partial intensity data in the Tables which follow. Intensities less than 100 are measured values; those greater than 100 been calculated by comparing two spectra at different sensitivities, and are only accurate to ±10%.

2. Compound Identification

The mass spectra indicated a complex mixture of hydrocarbons, and peaks which could be unambiguously assigned were used to construct a theoretical spectrum for each component using the "Eight Peak Index of Mass Spectra" [303]. The hydrogen, methane and n-alkane parent peaks were initially chosen, and after the spectra from these components had been calculated, excess intensity in the remaining peaks was attributed to alkenes (assumed alternant) and impurities such as air and water. The large number of possible isomers in the deuterated spectrum allowed analysis of the hydrogen and methane peaks only. The abundance of each component was calculated using molecular ionization cross-sections by Otvos and Stevenson[304]. In a few cases, a measured cross-section was not available; it was then obtained from related compounds, since molecular ionization cross-sections are approximately additive.

($\sigma \approx 4.16N_C + N_H$ where N_C and N_H are the number of carbon and hydrogen atoms in the molecule[304].) Thus the cross-section for butadiene was obtained from butene and hydrogen.

The abundance of each component was calculated as follows:

$$P_X = \frac{I_{obs} \times \sum I_{calc}}{I_{calc} \times \sigma_X}$$

P_X is the molar abundance of component X, and I_{calc} the listed[303] height of the chosen peak, normalized so that the most intense peak in the mass spectrum of component X has intensity 100. I_{obs} is the measured peak height after contributions from other components have been subtracted, and $\sum I_{calc}$ is the sum of the listed peak heights. σ_X is the molecular ionization cross-section[304], with calculated values in (brackets).

Components of the mass spectra and comparison of calculated and observed intensities are shown for $(CH)_8CsH_{1.67}$ and $(CD)_8CsH_{0.52}$. The method used for $C_{26}Cs(C_2H_2)_{1.7}$ (Table 4.7) was similar to $(CH)_8CsH_{1.67}$, and the large number of components identified precludes a full listing.

Components in the Mass Spectrum of $(CH)_8CsH_{1.67}$ in order of Calculation

Component:	H_2	CH_4	C_2H_6	C_3H_8	C_4H_{10}	C_6H_{14}	H_2O	Air	Ar	(N_2)	C_2Cl_3H
Peak:	2	13	30	44	58	57	18	32	40	28	130
σ_X:	2.56	7.90	15.2	22.2	27.2	39.5	(5.3)	*	10.9	7.15	(44)
P_X:	7.03	288	6.05	0.99	1.69	0.94	1.61	8.23	0.84	83.3	0.4

The N_2 peak could be CO (P = 90.1). σ for O_2 = 5.96.

Comparison of Calculated and Measured Peak Intensities in the Mass spectrum of $(CH)_8CsH_{1.67}$

Mass	Components										I_{calc}	I_{obs}
	H_2	CH_4	C_2H_6	C_3H_8	C_4H_{10}	C_6H_{14}	H_2O	Air	Ar	N_2	C_2HCl_3		
1	0											0	1
2	18											18	18
12		13										13	8
13		38										38	38
14		102						2		30		134	70
15		1007										1007	1116
16		1275										1275	1568
17		14					2					16	14
18							9					9	9
19													
20									1			1	1
25			1									1	1
26			8									8	7
27			13	2	5	3						23	18
28			44	5	5			43		631		728	728
29			10	7	7	4						28	28
30			12									12	12
31													
32								10				10	10
36												0	1
37												0	0.5
38													
39				1	2	1						4	3
40									8			8	8
41				1	5	7						13	12
42					2	3						5	8
43				3	18	6						27	27
44				3								3	3
55												0	2
56						4						4	4
57						8						8	8
58					2							2	2
59													
60											1	1	1
70												0	1
71												0	2
80												0	2
86						1						1	0
95											4	4	3
97											2	2	2
130											4	4	4
132											4	4	3
134											1	1	1

Comparison of Calculated and Measured Peak Intensities for Hydrogen and Methane Isotopes in the Mass Spectrum of $(CD)_8CsH_{0.52}$

Mass	D_2	HD	CD_4	CD_3H	CH_2D_2	H_2	I_{calc}	I_{obs}
1				3	16		19	0.5
2	1		3			6	10	10
3		39					39	39
4	52						52	52
12			2	6	8		16	3
13					12		12	3
14			6	19	23		48	13
15				22	39		61	26
16			12	41	121		173	158
17				162	242		404	387
18			73	89	391		554	554
19				317			317	317
20			89				89	89
21			1				1	0.5

Components identified left to right from parent peaks.
No CH_3D or CH_4 was identified.

CHAPTER 5

EXPERIMENTAL STUDIES OF POLYPYRROLE

INTRODUCTION

Most work on polypyrrole has used the films ≈0.1 μm thick which show electroactive properties. The present study, however, was directed towards obtaining neutron data for comparison with polyacetylene, and for this purpose a 1 g sample was required. This corresponds to a charge of 2260 Coulombs passed or a thickness of 524μm on each side of a 1 inch square platinum electrode (1 inch (1") = 25.4 mm). Although a 1 g electrochemical synthesis was found to be possible for the perchlorate, its explosive properties prevented repetition of the synthesis, and when safer dopants such as the borofluoride were used, the most obtained in a single synthesis was 0.3 g. The synthesis of thick films was carried out under high vacuum because it was felt that insufficient attention had been paid to oxygen incorporation into the films. In view of more recent studies, this concern has been justified. Thin films were, however, also made for characterization by cyclic voltammetry.

5.1 SYNTHESIS AND CHARACTERIZATION OF THIN POLYPYRROLE FILMS

5.1.1 Preparation

The preparation followed the method of Diaz et al [194,195] whereby 0.1M Bu_4NBF_4/ 0.06M pyrrole were electrolyzed in acetonitrile with 1% added water. Commercially available pyrrole containing tarry impurities was purified by drying for a few hours over solid potassium hydroxide followed by distillation at atmospheric pressure under nitrogen (bp 130°C). It was kept in suba seal bottle and removed in a syringe. The other chemicals, analR acetonitrile and Aldrich 99% Bu_4NBF_4, were used as obtained. (Acetonitrile forms a minimum boiling point mixture with water. Bu_4NBF_4 is very soluble in acetonitrile, and is reported to be deliquescent, but few problems were encountered in handling.)

A double sided 1 cm × 1 cm platinum spade working electrode was used with a gold wire counter electrode and another gold wire to act like a reference electrode. (See Section 3.1.1.ai) The solution was purged with white spot nitrogen (99.98%) for at least six minutes and then the current was switched on, the working electrode being maintained at +1.1V relative to the reference electrode by a potentiostat (Fig 5.1). The current increased to a roughly constant 1 mA/cm^2 and the film formed in about twenty seconds. When very thin the film looked yellow, but on getting thicker, it turned tan and then brown/black. Bright colours could sometimes be seen under strong light, possibly due to interference between the front and back of the film.

Some difficulty was experienced in obtaining films which covered the electrode evenly. Polypyrrole itself is an efficient working electrode with a large surface area. Even thickness is, however, of critical importance for cyclic voltammetry. As well as varying the synthesis current, various methods of cleaning the working electrode were tried. These included rubbing with paper soaked in ethanol, polishing with jeweller's rouge, scouring powder, roughening the surface with Scotchbrite, concentrated nitric acid, and heating to white heat in a flame. None of these was wholly satisfactory, and the voltammograms shown were obtained from films made with up to 250 mC/cm^2, compared with literature values of 8-32 mC/cm^2 [196].

Films were also prepared using Et_4NBF_4 and $AgClO_4$. In the latter case, silver wire counter and reference electrodes were used and the working electrode was maintained at +0.7V relative to Ag/Ag^+. The current was 2 mA/cm^2 and the film formed in twelve seconds; they had a similar appearance to the borofluoride doped films. Syntheses with tetraälkylammonium perchlorates were not attempted for safety reasons.

Fig 5.1 Circuit Diagram for Polypyrrole Synthesis

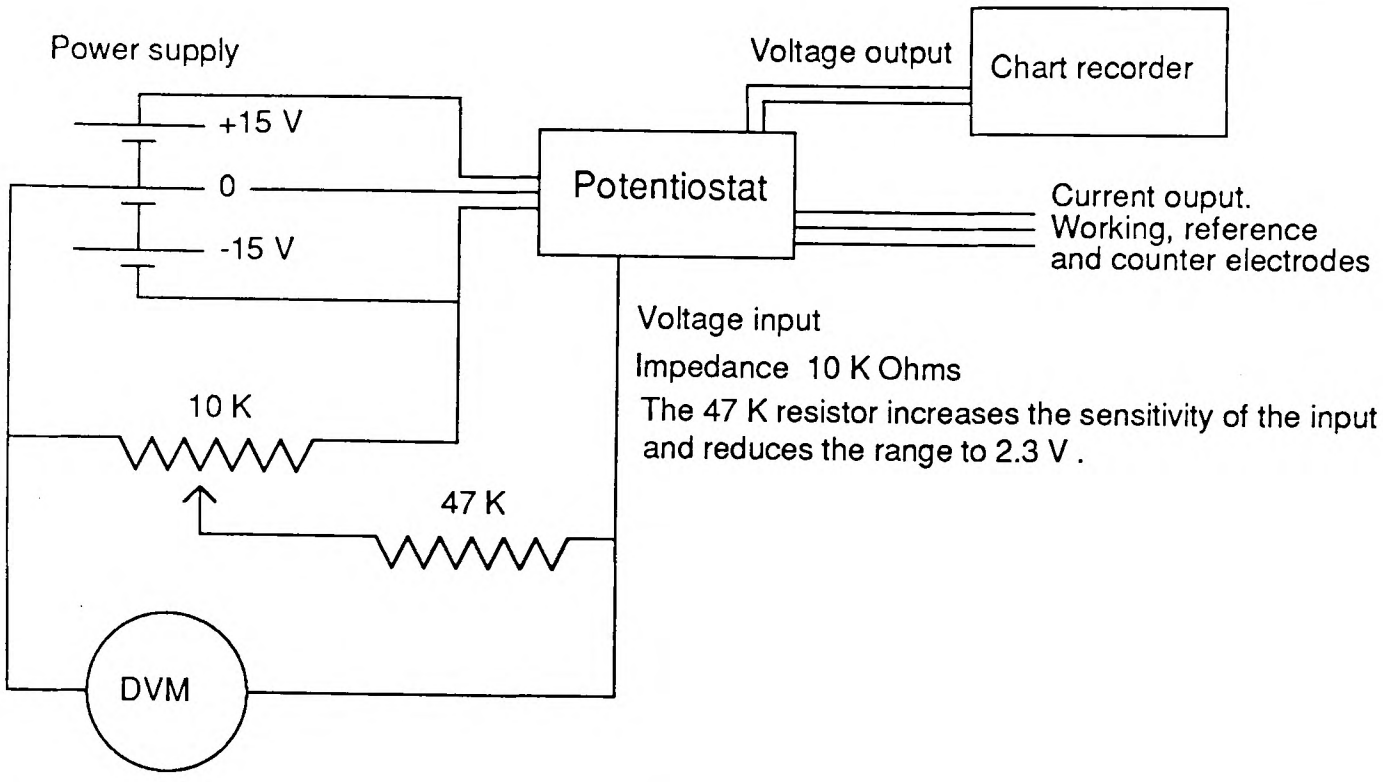

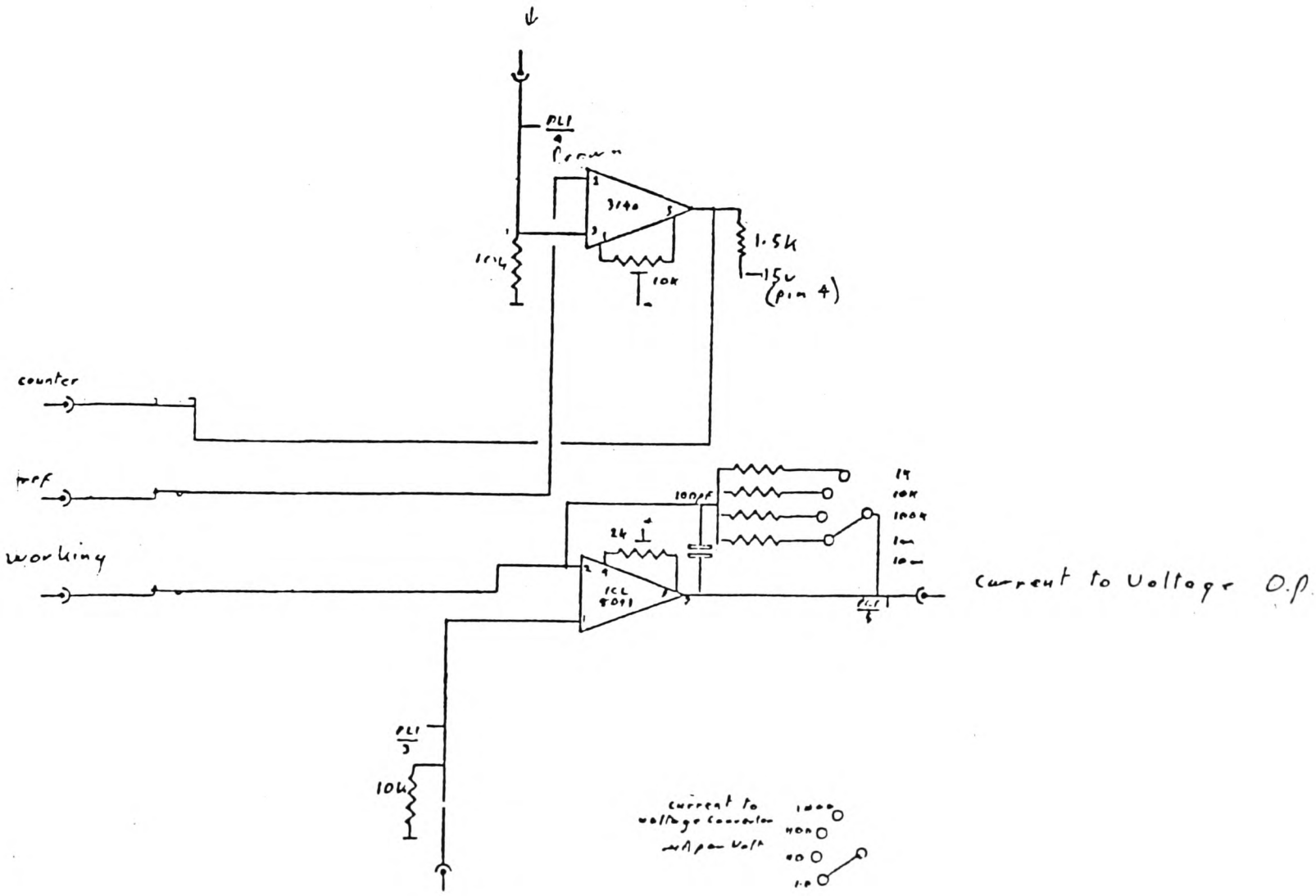

Circuit diagram of the potentiostat, built by the PCL electronics workshop to a design modified from a ring-disk electrode system of Prof W.J. Albery. The maximum current was 10 mA, another design being used for higher currents.

5.1.2 Cyclic Voltammetry

Linear sweep polarography and its extension into cyclic voltammetry is a powerful technique for investigating redox processes at electrodes. The application to the polypyrrole system is somewhat specialized, and hence a brief outline only is attempted here. Fuller descriptions are given by Ebersen & Schäfer[305] and Adams[202].

At its simplest, linear sweep polarography involves placing two electrodes into a solution of a suitable electrolyte, together with a small quantity of the substrate. The potential between the two electrodes is varied linearly with time and the current which flows is plotted against potential. In practice a reference electrode is often used as well. The extension to cyclic voltammetry merely consists of taking a linear polarogram and then immediately reversing the direction of sweep so that back reactions can be studied. In cyclic voltammetry, the sweep speeds are usually faster than in linear polarography.

Consider an electrolyte solution in which only ohmic processes are taking place. This will act like a simple resistor and the current-voltage curve will be a straight line with the gradient given by the resistance. Departures from this straight line may be due either to the capacitance of the solution or redox changes in its chemistry. These redox changes usually involve ions in solution; in this case, however, the redox system is the polypyrrole film on the working electrode which is undoped and redoped.

Imagine, for the sake of simplicity, a cell as described above. The working electrode is platinum coated with a thin polypyrrole film and the counter electrode is any inert metal. A potential is then applied, the working electrode being at say +1V relative to the calomel reference electrode, and an ohmic current flows through the solution. If the potential difference is now reduced linearly with time, the ohmic

current will also fall linearly, neglecting capacitance effects. As the potential is reduced, the environment round the working electrode, having been strongly oxidizing, becomes more reducing, and the polypyrrole film is reduced. This shift in equilibrium superimposes a peak on top of the ohmic current. It appears as a peak because there is a limited amount of film to be reduced, and once it has all been reduced, the current reverts to the ohmic value. (NB This is different from redox processes on ions in solution where diffusion is important.)

When the potential has reached a suitably reducing value, the direction of sweep is reversed. This allows investigation as to whether the redox process is reversible. If an oxidation wave is also seen, the process is reversible and vice-versa. This process can be continued for several cycles, the first often being different from subsequent cycles. The polypyrrole system clearly shows both oxidation and reduction waves over several cycles, showing that the process is reversible.

5.1.3 The Voltammograms (Fig 5.2a-e)

The newly synthesized borofluoride films were rinsed in outgassed acetonitrile, then in 0.1M electrolyte in acetonitrile with 1% water added. The voltammograms were measured without a reference electrode on a PO4g Polariter polarography machine with sweep speeds of 0.8 and 0.4 V/min and no iR compensation, and show the characteristic polypyrrole switching behaviour (a,b). For the perchlorate films, a 0.1M solution of $LiClO_4$ was used to avoid reduction of the Ag^+ ions. The voltammograms show a good oxidation wave, but a poor reduction wave (c). (The potential range of the instrument was later extended by insertion of a NiCd rechargeable battery into the circuit; this still failed to locate a reduction wave.) Controls of the solvent alone and of the electrolyte solutions on a blank platinum electrode confirm that the redox chemistry is caused by the presence of polypyrrole (d,e).

Fig 5.2 Cyclic Voltammograms of Thin Polypyrrole Films on a 1 cm × 1 cm Platinum Spade Electrode

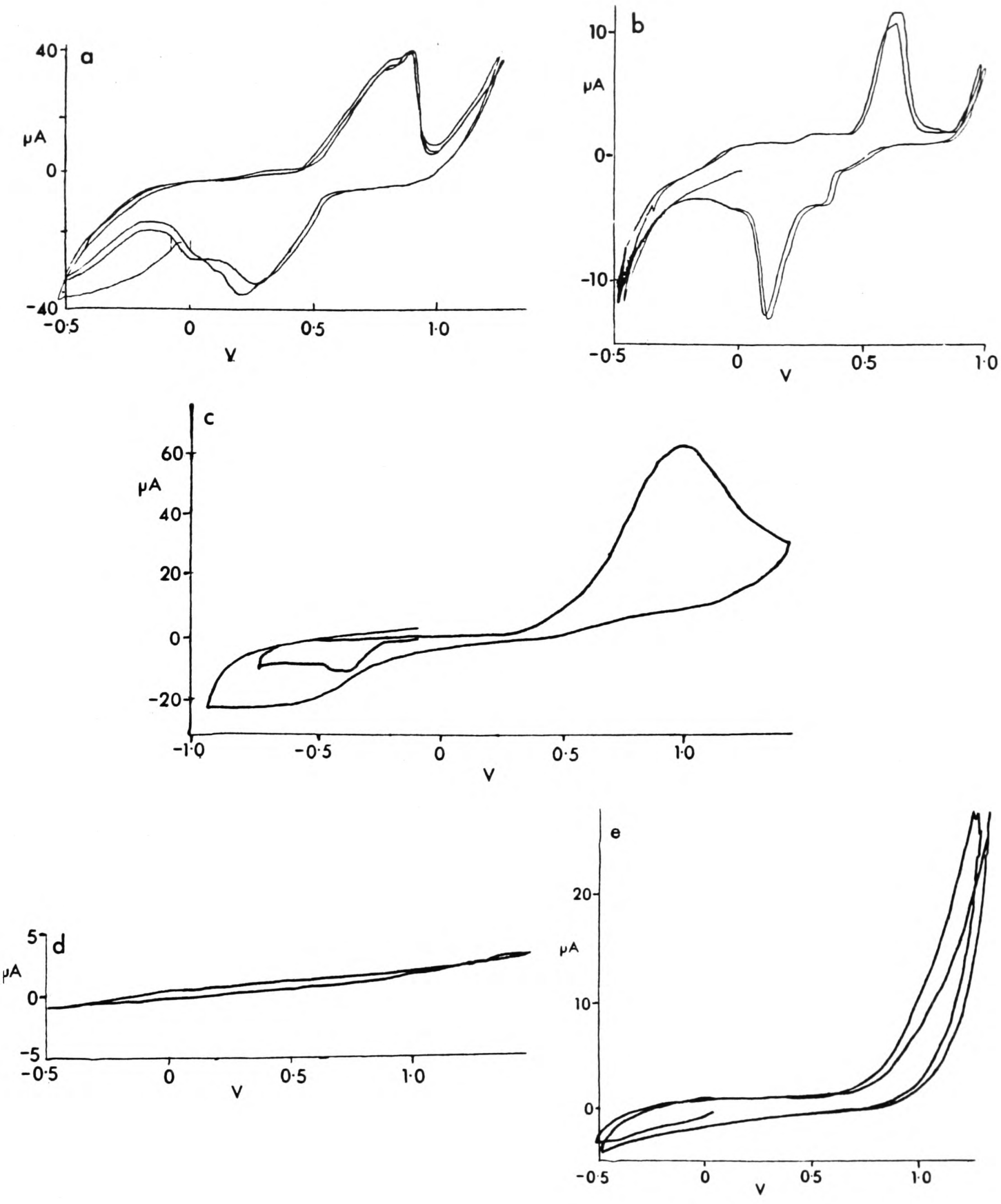

No iR compensation used on these scans.

a. 455 mC film in 0.1M Et_4NBF_4/MeCN showing 3 complete voltage scans. Sweep speed 0.8V/min.

b. 512 mC film in 0.1M Bu_4NBF_4 showing 2 scans. Sweep speed 0.4V/min.

c. 100 mC film synthesized in $AgClO_4$, scanned in 0.01M $LiClO_4$. Sweep speed 0.8V/min. Note the poor reduction wave.

d,e. Control scans of clean Pt electrode in pure MeCN and 0.1M Bu_4NBF_4.

5.2 ELECTROCHEMICAL PREPARATION OF POLYPYRROLE IN GRAM QUANTITIES

The silver perchlorate synthesis (Section 3.1.1aii) was used in a specially constructed demountable high vacuum glass apparatus, which was made in two halves round a B55 conical joint (Fig 5.3). In the top half, three thick tungsten wires were set into the glass to provide attachments for the electrodes, while the solutions were placed in the bottom half, together with a pumping line and a tap. The tungsten wires were joined to the electrodes by small brass cable connectors. Problems with the apparatus included jamming of the B55 joint after prolonged evacuation during synthesis, corrosion of the cable connectors in the highly acidic and oxidizing environment, and electrodes being dragged out of the connectors by lumps of frozen acetonitrile.

Before the synthesis, the working electrode was assembled; this comprised a 1" × 1" × 0.001" (1" = 25.4 mm) platinum foil glued to a thin platinum wire with RS conducting epoxy resin and cleaned with Vim then jeweller's rouge and rinsed repeatedly in distilled water before use. The counter electrode was a 1" × 1" piece of silver foil similarly glued to a thick silver wire. (A large surface area is needed to prevent the growth of dendrites which, while they look very attractive, eventually cause a short circuit.) These electrodes, together with a silver wire reference electrode were attached to the top half of the electrochemical cell. They were arranged so as to be the correct length, so as not to touch, so that the working and counter electrodes were facing each other, and so as to be as far apart as possible.

After this, roughly 3g of silver perchlorate (BDH 98%) was weighed out quickly into a weighing bottle with a snap on top. (Silver perchlorate is highly deliquescent and is reasonably soluble in acetonitrile. It was not considered safe to try to dry it.) The silver perchlorate was then placed in the bottom half of the apparatus and the

Fig 5.3 The electrochemical cell used for making thick polypyrrole films

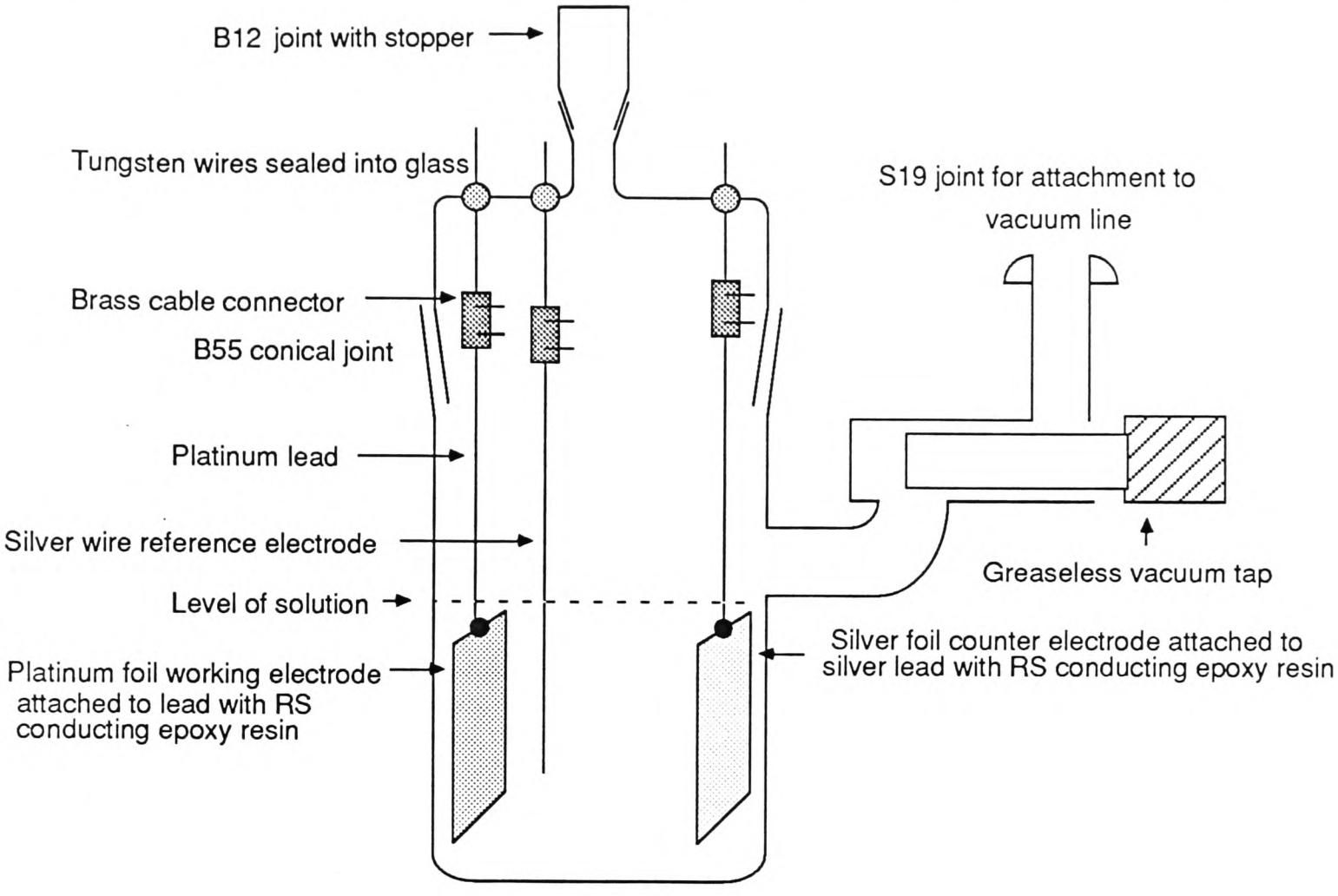

Fig 5.4 The apparatus used to measure conductivities

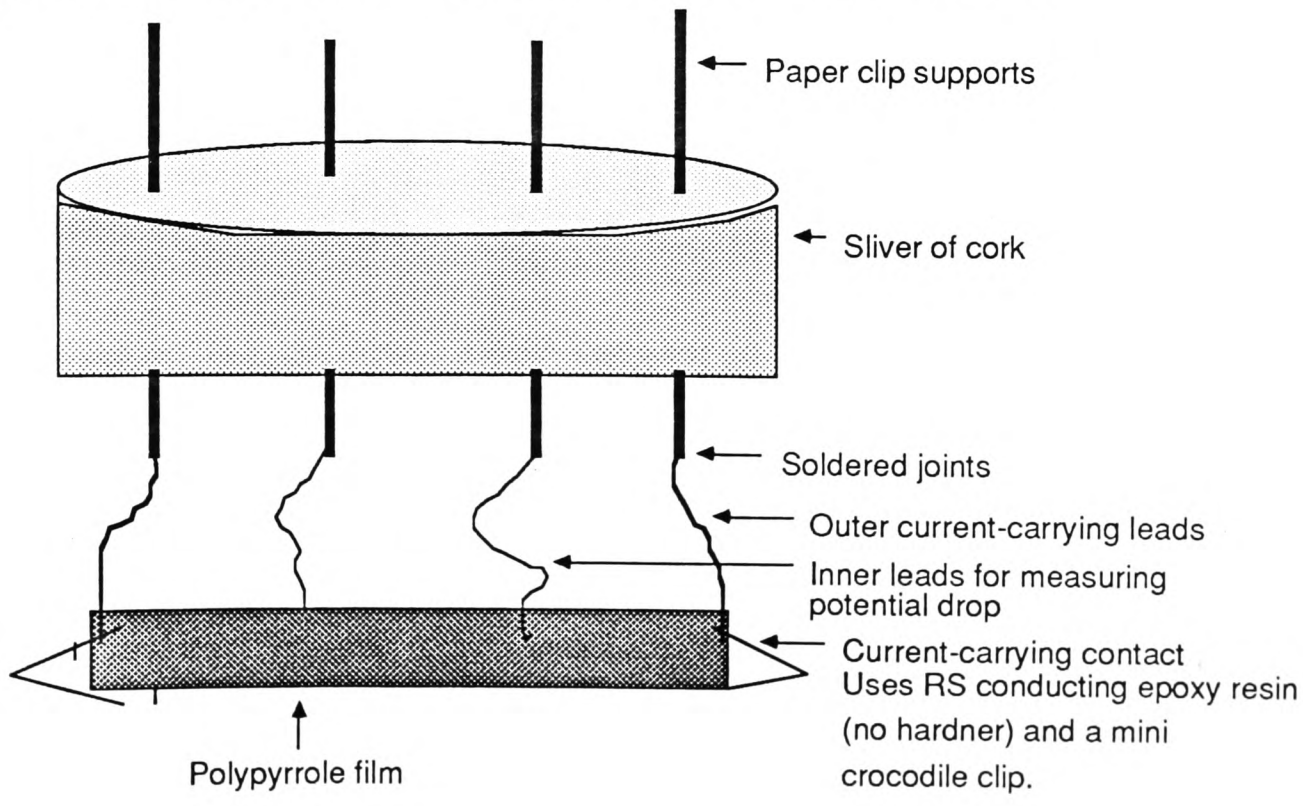

correct volume of acetonitrile (≈150 cm^3) was immediately added to make a 0.1M solution.+ The amount of silver perchlorate needed to get the correct solution volume required careful judgement. After this, enough pyrrole to make a 0.06M solution (≈0.6 cm^3) was injected in. The top was then put on, the tap closed, and the solution frozen in a dewar of liquid nitrogen. (Acetonitrile freezes at -43°C.) When fully cold, it was pumped to 10^{-4} torr, then the tap was shut and the apparatus was warmed to room temperature in a beaker of ethanol. Three or four such freeze-pump-thaw cycles were used to remove all traces of air.

After this, the potentiostat was set up so the working electrode was +0.55 to 0.65V relative to Ag/Ag^+. The initial current was about 10mA, falling off as Ag^+ ions and pyrrole were removed from solution, although the current sometimes took time to build up as the polypyrrole slowly spread across the electrode. The current was recorded on a chart recorder and integrated on a PET microcomputer. A typical current profile is shown in Fig 5.5. A large scale synthesis involving several hundred Coulombs took several days.

Although the easiest synthesis involved silver perchlorate, satisfactory results were also obtained with silver borofluoride. This substance is sensitive to air, moisture and light, and a glove bag was used to transfer it into the weighing bottle. Current densities were slightly lower than with silver perchlorate, and the chemical itself looked less pure. The solution was also more susceptible to degradation and it was impossible to use silver(I) oxide to improve matters (Section 5.3). A synthesis was also attempted with silver trifluoro-acetate; a polypyrrole film did eventually form, but the initial current was only 1 mA and fell to 0.2 mA after only a couple of hours.

+ Really accurate work would also dry the acetonitrile over calcium hydride since analR acetonitrile contains up to 0.1% water.

After synthesis, the films were rinsed in clean acetonitrile, then dried in an evacuated dessicator until constant mass was reached. They were then peeled off the electrode and stored under nitrogen for future use. The polypyrrole films were found to show a strong tendency to absorb acetonitrile, which caused them to swell and become flexible. From mass measurements, assuming 25% doping in the borofluoride films and 33% doping in the perchlorate films, it was found that polypyrrole samples which were apparently dry but had not been dried under vacuum had excess mass equivalent to ≈0.2 acetonitrile molecules per pyrrole ring. Part of this mass increase could, however, also be due to atmospheric oxygen. Unfortunately, the design of the electrolytic cell precluded dismantling it in a glove bag.

5.3 CHEMISTRY OF THE SYNTHESIS: DEGRADATION AND SILVER(I) OXIDE

During large scale syntheses, it was noticed that as well as current fall-off, there was also a tendency for the solution to turn black over time. This was attributed to the silver ions which plate out on the counter electrode being replaced by H^+ ions from the pyrrole monomer. This acidification was confirmed by a potentiometric titration with sodium hydroxide solution on the residue from a polypyrrole perchlorate synthesis, which indicated a one to one correspondence between charge passed and H^+ ions in solution (Fig 5.6). It was found to be possible to counteract the acidification by the addition of insoluble silver(I) oxide to the solution which both neutralized the acid and replenished the silver ions. This halted both degradation of the solution and current fall-off, making a 1g synthesis possible, provided extra pyrrole monomer was added (Fig 5.5). (It also added a little water to the solution. However, the amount was less than that already in the analR acetonitrile.) Unfortunately, to be fully effective, the silver oxide had to be kept in suspension, which led to its incorporation into the

Fig 5.5 Current-Time profile plots of Polypyrrole Perchlorate synthesis showing the improvement brought about by using silver(I) oxide

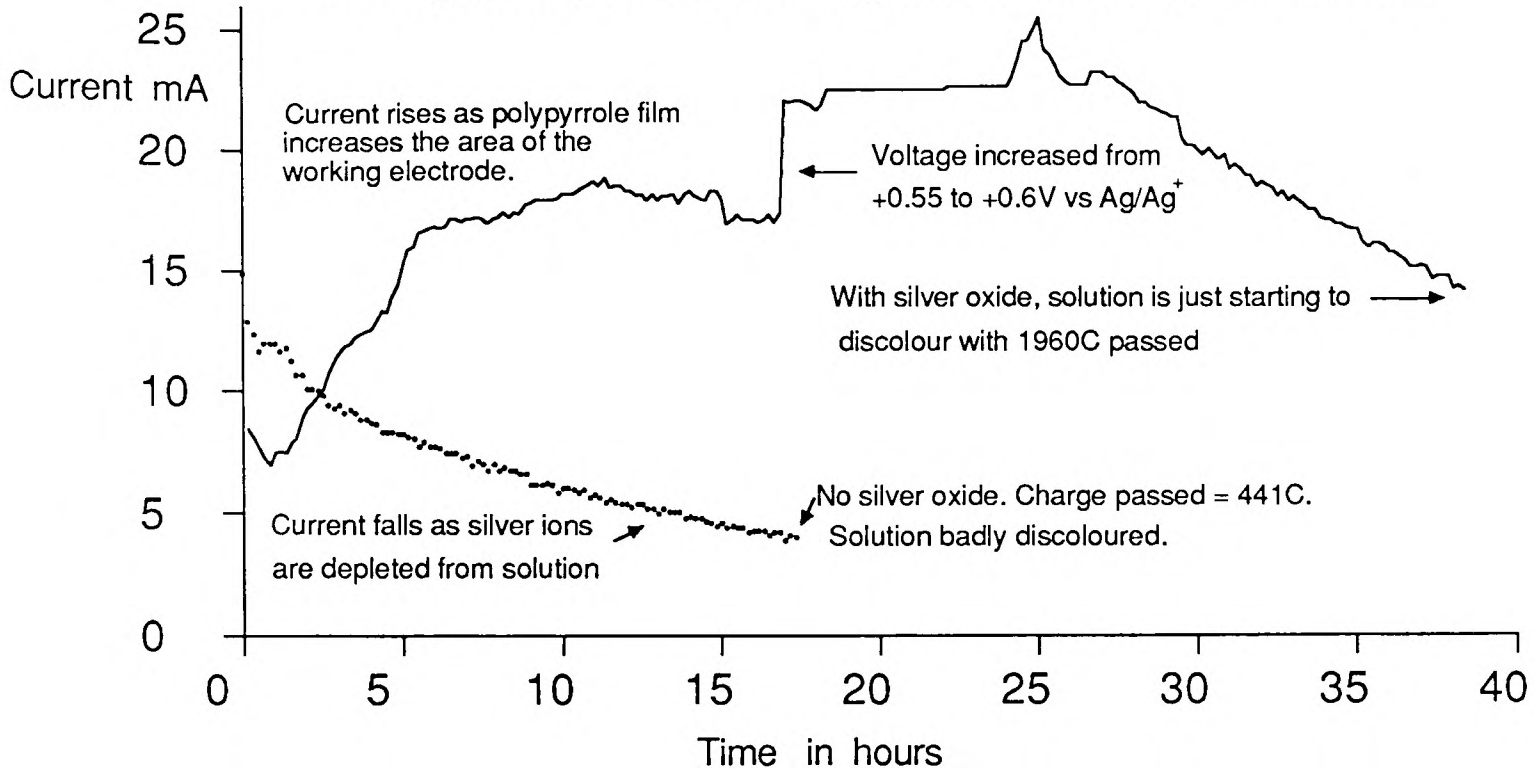

Fig 5.6 Potentiometric Titration of residue from Polypyrrole

(pH values initially distorted by MeCN solvent.)

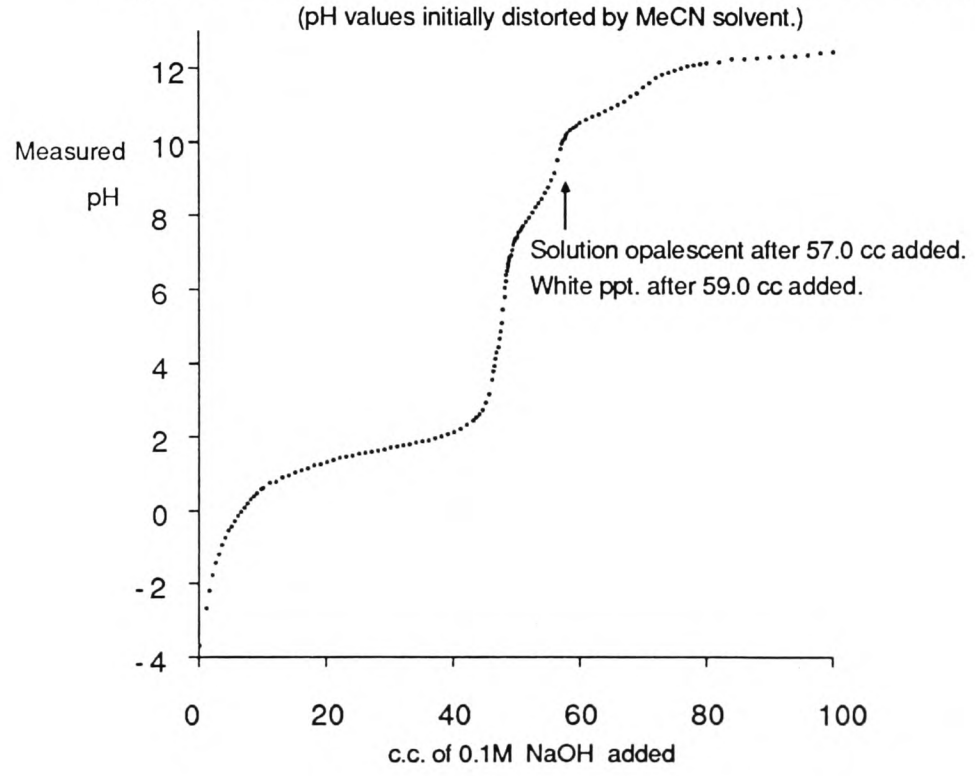

c.c. of 0.1M NaOH added

Synthesis used $AgClO_4$ (no Ag_2O) and was run mainly at 0.55V for 27 hrs.
The solution was golden yellow in colour before titration.
Measured charge passed = 652C.
Mass Ag deposited = 0.7729g, corresponding to 691C.
Mass polypyrrole deposited = 0.343g after 24 hrs in air.
(Gives 20.8% by mass acetonitrile contamination.)
Of the 652C passed, 567C would be used in polymerization and would release H^+, the rest in doping.
This corresponds to 0.00587 mol H^+ or 58.7 cm^3 0.1M NaOH solution.

film. Furthermore, it was only effective for the perchlorate synthesis; attempts to add it to the borofluoride synthesis resulted in the solution going black in minutes and very low currents being passed.

5.4 CONDUCTIVITY MEASUREMENTS

Some preliminary conductivity measurements were carried out on thick pieces of polypyrrole film. A four probe technique was used since the resistance of the current carrying contacts is then unimportant[306]. (Fig 5.4) The dimensions across the middle wires were approximately 12 mm long × 6 mm wide × 0.2 mm thick. Measurement of two pieces gave conductivities of 55 S/cm and 29 S/cm; these are a little lower than the literature values (Table 3.1). It was found that the films were very susceptible to polarization. If voltages above 2V were used, the apparent resistance increased markedly. This effect could be reversed by changing the direction of current or by using AC. A normal ohmmeter would be totally unsuited to these measurements. A single piece of polypyrrole also had its conductivity measured at room temperature, -79°C and -196°C, the value at -196°C being roughly half that at room temperature.

5.5 EXPLOSIVE PROPERTIES OF POLYPYRROLE PERCHLORATE

Although the bulk synthesis of polypyrrole perchlorate is technically easier than that of the borofluoride, one very undesirable property was discovered literally by accident: **polypyrrole perchlorate is a powerful explosive which is liable to detonate without warning.** A 1.6g sample of polypyrrole perchlorate was rinsed thoroughly in clean acetonitrile and dried overnight in a vacuum dessicator. The following day, it was let up to air, weighed, and put back to dry. When, a few hours later, it was let up to air again so that it could be reweighed, the polypyrrole perchlorate detonated violently, causing the lid of the dessicator to smash on the ceiling.

While it is unsurprising that an organic perchlorate should be explosive, there is no mention of this all the published work on polypyrrole, although Chien notes in his book that perchlorate doped polyacetylene explodes on heating[2]. This lack of warning seems surprising in view of the fact that much of the recent work has been done with the perchlorate. Possible reasons for the discrepancy are as follows: first, the common electrochemical doping/undoping studies use only microgram quantities of polypyrrole. Second, high vacuum techniques in polypyrrole synthesis, first reported in 1984 [207], have become common only relatively recently; previous bulk samples may have included some atmospheric oxygen. Third, the film in this case had been carefully dried; it is probable that it had been stabilized by the incorporation of solvent.

As a result of this explosion, preparation of bulk samples of polypyrrole perchlorate had to be abandoned. Thin films, such as used in cyclic voltammetry burn normally when the electrode is heated in a flame. Thick films of polypyrrole borofluoride only burn with difficulty under such circumstances, and it can safely be assumed that they are not explosive.

Some controlled detonations of milligram quantities of polypyrrole perchlorate were also carried out. It was found that detonation could be caused by the heat from a bunsen burner or prolonged contact with a soldering iron. More interestingly, it was found that the samples used for conductivity measurements could be detonated electrically by passing a current of 0.5A through the films with a potential of 2V across them. This was quite difficult to achieve, since it demanded good electrical contact between the wires and the films, and voltages above 2V caused them to stop conducting. Electrical detonation was much less violent than thermal detonation and usually destroyed only part of the films. It is just possible that this might find application in a detonator.

5.6 CHEMICAL SYNTHESIS OF POLYPYRROLE

The chemically prepared film was made by oxidizing 10 cm^3 distilled pyrrole in 50 cm^3 ethanol with 100 cm^3 of 1.8 M aqueous sulphuric acid (Section 3.1.2ai), but in a closed vessel with white spot nitrogen (99.98%) bubbling through so as to minimize oxygen incorporation. The red-brown solid took about 24 hours to form. The sample was rinsed in ethanol/water mixture and kept under nitrogen before use.

Some chemically prepared polypyrrole was kept under air in a screw-cap bottle. Over a matter of months it turned black, indicating doping by atmospheric oxygen.

CONCLUSION TO PART A : DOPING AND INTERCALATION

Comparison has often been made between the doping process in polyacetylene and the intercalation process in the graphite intercalates. (See for example Flandrois[307] and Billaud & Begin[308].) This is particularly applicable to the structural models for doped polyacetylene where sample disorder has until recently forced analogy and intuition to make up for the lack of quality of the diffraction patterns.+ Current models for p-type doping of polyacetylene are layer structures (Fig 2.3), whereas Baughman's model for n-type doping is a channel structure (Fig 2.4).

In his researches, Baughman measured X-ray diffraction patterns from polyacetylene doped with the alkali metals sodium, potassium, rubidium and caesium (Section 2.3.2); this results in strong scattering from the metal ions with weak and negligibly small scattering respectively from the carbon and hydrogen atoms. In the current study using neutron diffraction however, the carbon and deuterium atoms scatter strongly, with relatively weak structure factors from the metal ions[290,294].

The neutron diffraction pattern of ($CDCs_{0.10}$) has line positions consistent with Baughman's tetragonal structure, but there is a serious mismatch in the relative intensities of the 110 and 200 peaks compared with the calculated pattern based on Baughman's structure (Fig 4.2). The sample of caesium doped polyacetylene also contained undoped polyacetylene whereas the diffraction pattern of trans-polyacetylene

---

+The published diffraction patterns of cis[150,151] and trans-polyacetylene[142,146,151], some of them from oriented samples, show four to eight lines. Baughman observed four or five lines from oriented samples of polyacetylene doped with alkali metals[162], and a maximum of five lines from iodine doped samples[180]. The layer structure for polyacetylene doped with AsF_5 was originally proposed on the basis of a single diffraction line[176]. Better patterns of p- and n-doped polyacetylene have since been published but not yet fully analysed[151,288].

used to characterize the sample (Fig 4.1) compared to advantage with previous X-ray data from the material. Further study with a better sample is needed to see whether a channel structure as favoured by Baughman [150,287] or a layer structure as proposed by Flandrois[288] best fits the observed data.

The analogy with the graphite intercalates was explored further in the study of hydrogen absorption by caesium doped polyacetylene (Sections 4.5, 4.6, 4.9). Here, however, the neutron diffraction data (Figs 4.3, 4.4; Table 4.3) give no evidence for a polyacetylene analogue of $C_8KH_{\frac{2}{3}}$ (See Section 1.5.1). By contrast, the presence of methane and other alkanes in the desorbed gas (Section 4.9) indicates the irreversible nature of the reaction, and supports the hypothesis of an addition to an unsaturated polymer chain (Section 2.4). The random nature of the addition is confirmed by the lack of polyethylene lines in the diffraction pattern and the broadening of the lines from the doped polymer. By contrast, the final product which would occur on taking the pyrolysis to completion is unknown; although a polydiacetylene is structurally easier to achieve, it is possible that ring closure reactions could take place to produce a thermodynamically more stable graphite intercalation compound. This could easily be checked by measuring the neutron diffraction pattern.

The search for an ordered form of doped polyacetylene was continued by the absorption of acetylene gas into the graphite intercalates $C_{26}Cs$ and C_8Cs, to give products $C_{26}Cs(C_2H_2)_{1.70}$, $C_{26}Cs(C_2D_2)_{1.27}$ and $C_8Cs(C_2H_2)_{0.50}$ (Section 4.7). The neutron diffraction patterns of the products, besides indicating the presence of large quantities of graphite, also show lines accounted for neither by polyacetylene nor caesium doped polyacetylene (Figs 4.5 - 4.7; Table 4.5). The diffraction patterns from the products derived from C_8Cs and $C_{26}Cs$ are different

from each other, and the composition $C_{26}Cs(C_2H_2)_{1.70}$ is inconsistent with the formation of caesium acetylide, which would account for the absorption of only one mole of acetylene. The mass spectrum of the gases evolved on heating $C_{26}Cs(C_2H_2)_{1.70}$ show, besides ethylene, large quantities of butene, butadiene and other alkenes, with little if any methane or benzene (Table 4.7). This suggests that some form of acetylene polymerization has indeed occurred, but that new materials, as yet unidentified have been produced, rather than polyacetylene or doped polyacetylene. It would be interesting to measure the X-ray diffraction pattern of the materials, since in the X-ray pattern, the Cs^+ structure factors would show more strongly than the graphite.

Polypyrrole has been synthesized electrochemically in gram quantities in a non-aqueous solvent under high vacuum conditions, and has been characterized by cyclic voltammetry and conductivity measurements (Sections 5.1 to 5.4). Quantities of the perchlorate doped polymer obtainable in a single synthesis have been increased from 0.3g to over 1g, and problems of acidification and oxidation of the solution have been overcome as a result of adding insoluble silver(I) oxide to the solution (but see below). Unfortunately, this proved inappropriate for the synthesis of the borofluoride doped polymer. It would be interesting to try the effect of silver(I) oxide with some other counter ions such as trifluoroacetate and p-toluenesulphonate.

While the quantities of electrochemically synthesized polypyrrole now obtainable are just enough for neutron work, a marked tendency to absorb acetonitrile solvent was noted; the strong neutron scattering from the solvent will make it essential to remove all traces of solvent from the polypyrrole before any neutron work is attempted. (See Section 6.5 for the neutron spectrum of acetonitrile.) Alternatively, the polypyrrole could be soaked in excess CD_3CN before being partially

dried. A tendency to absorb solvent is also seen in the graphite intercalation compounds (Section 1.5.2) and polyacetylene (Section 4.1) and presumably relates to the solvation of the dopant ions by the polarizable acetonitrile molecules.

Finally, the danger posed by perchlorate doped conducting polymers, especially when synthesized in oxygen-free conditions and when dry has been grossly underestimated (Section 5.5), and the perchlorate ion is still widely used for electrochemical doping of polypyrrole and in rechargeable polyacetylene batteries[2,165].

PART B PHYSICAL ASPECTS OF INTERCALATION

(Structural Aspects of the Intercalation Site Determined by the Dynamics of Absorbed Hydrogen using Inelastic Neutron Scattering)

CHAPTER 6

THE THEORY OF INELASTIC NEUTRON SCATTERING INTENSITIES AND HINDERED ROTATION

INTRODUCTION

We are now going to consider in detail the expected neutron scattering cross-sections for the various possible types of motion of hydrogen molecules physisorbed by the stage II graphite intercalates: harmonic oscillation, free rotation and hindered rotation. The scattering laws for the harmonic oscillator and the freely rotating homonuclear diatomic molecule have been developed by Zemach & Glauber[310] and Sears[311] respectively, and application to beryllium filter spectroscopy is given in succeeding sections. The case of the hindered rotor, however, is far from simple, and the problem here can be broken down into two halves: first, the calculation of the energy levels of the hindered rotor as a function of the number of degrees of rotational freedom, and the strength and symmetry of the hindering potential, and second, calculation of neutron scattering cross-sections for transitions between the energy levels. While the problem of energy level calculation has been solved for many cases by expansion in terms of the free rotor wavefunctions[312-314], there have been no corresponding neutron scattering intensity calculations to date, except for the classical rotation of heavy molecules[315] and tunnelling intensities[316]. One is thus reduced to the limiting cases of the harmonic oscillator and the free rotor.

6.1 INELASTIC NEUTRON SCATTERING FROM A HARMONIC OSCILLATOR

6.1.1 The Scattering Law

Zemach and Glauber's[310] original expression for the partial differential scattering cross-section of an oriented assembly of harmonic oscillators is both very general in application and uses

notation which has become non-standard, leading to unnecessary complexity. Howard and Waddington's[317] rendering of the expression is:

$$\left(\frac{\partial^2\sigma}{\partial\Omega\partial E}\right)_{inc} = \frac{k_f}{k_i} \times \frac{1}{8\pi^2\hbar} \sum_L \sigma_{inc}^L \prod_a \left\{ \exp\left[-(\mathbf{Q}.\mathbf{C}_L^a(q))^2 \frac{\hbar}{2\bar{\nu}_a c m_L} \coth\left(\frac{c\hbar\bar{\nu}_a}{2kT}\right)\right] \times \exp\left(\frac{-n_a c\hbar\bar{\nu}_a}{2kT}\right) \times I_{n_a}\left[\frac{(\mathbf{Q}.\mathbf{C}_L^a(q))^2\,\hbar}{2m_L c\bar{\nu}_a \sinh(c\hbar\bar{\nu}_a/2kT)}\right] \delta(\hbar\bar{\nu}_a - \hbar\textstyle\sum_a |n_a|\bar{\nu}_a \right\} \quad (6.1)$$

It may be of help to point out in advance that for many purposes the expression can be simplified to[318]

$$\left(\frac{\partial^2\sigma}{\partial\Omega\partial E}\right)_{inc} \propto Q^2u^2 \exp(-Q^2u^2) \quad (6.2)$$

provided that the temperature is low enough not to lead to appreciable population of excited states, the sample is polycrystalline, the vibration of only one fundamental mode is being considered, scattering from atoms other than hydrogen is negligible and that Q^2u^2 is less than about 0.8 .

To explain terms and symbols:-

$\left(\frac{\partial^2\sigma}{\partial\Omega\partial E}\right)_{inc}$ is the partial differential cross-section. ie the scattering cross-section as a function of both scattering angle Ω, and energy transfer E. The suffix $_{inc}$ means that only incoherent scattering is being considered. In the case of hydrogen, this is dominant.

Q is the momentum transfer associated with the transition ($Å^{-1}$) and u is the mean amplitude of vibration (Å).(Strictly, the mean displacement from equilibrium)

k_i and k_f are the magnitudes of the initial and final neutron wave-vectors ($Å^{-1}$) defined by $k=2\pi/\lambda$.

$$\mathbf{Q} = \mathbf{k}_f - \mathbf{k}_i \quad (6.3)$$

(The factor of k_f/k_i is eliminated from all beryllium filter spectra by counting at constant monitor.)

$\sum_L$ sums over all types of atoms with σ_L^{inc} as the incoherent scattering cross-section for each atom. In most cases, scattering from all atoms except hydrogen is negligible so that $\sigma = \sigma_H^{inc}$ and the sum can be dispensed with. (In most calculations, σ_H^{inc} is assumed to have a value of ≈80 barns (1 barn = 10^{-24} cm²) and to be independent of the incident neutron energy. In fact, this is only approximately true, and in a beryllium filter spectrum, where the incident energy is scanned, the correction becomes significant. For E_{inc} = 3, 10 and 120 meV, $\sigma_H^{tot} \approx \sigma_H^{inc}$ = 81.5, 48 and 27 barns [294]. In common with usual practice, however, this correction has been ignored in the calculations which follow.)

$\prod_a$ sums over all normal modes. If the internal modes of a polyatomic molecule were being considered, this would be important, but in this case the torsional mode under consideration has a much lower frequency than the internal modes and can be considered in isolation, dispensing with the product.

$\mathbf{c}_L^a$ are the normalized polarization vectors for each atom of type L in mode a (See also Equation 6.5).

$\bar{\nu}_a$ is the frequency of normal mode a in cm^{-1}, hence c is expressed in cm/sec.

n_a is the number of quanta of energy transferred in mode a. For a fundamental excitation, n = ±1.

m_L is the mass of the scattering atom.

k is Boltzmann's constant.

$I_{n_a}(x)$ is a modified (ie hyperbolic) Bessel function of order n_a with argument x.

The delta function $\delta(\hbar\bar{\nu}_a - \hbar\sum_a |n|\bar{\nu}_a)$ means that excitation only takes place at multiples of the normal mode frequencies $\bar{\nu}_a$.

Various other simplifications can be made to this expression. First, the initial constants can be eliminated by expressing the scattering cross-section in terms of the scattering law $S(\mathbf{Q},\omega)$ defined by:

$$\left(\frac{\partial^2\sigma}{\partial\Omega\partial E}\right)_{inc} = \frac{1}{8\pi^2\hbar}\,\sigma_H^{inc}\,S(\mathbf{Q},\omega) \qquad (6.4)$$

Second, it is simpler to use the vibrational amplitude **u** instead of the polarization vector $\mathbf{C}_L^a$. These are related in the harmonic approximation by the formula[317]:

$$|\mathbf{u}_L^a| = \left(\frac{\hbar}{2m_L c\bar{\nu}_a}\coth\left(\frac{ch\bar{\nu}_a}{2kT}\right)\right)^{\frac{1}{2}} |\mathbf{C}_L^a(q)| \qquad (6.5)$$

Introducing these simplifications, one obtains for inelastic incoherent scattering from one normal mode of frequency $\bar{\nu}_a$:

$$S(\mathbf{Q},\omega) = \exp\{-(\mathbf{Q}.\mathbf{u})^2\} \times \exp\left(-n\,\frac{ch\bar{\nu}}{2kT}\right) \times I_n\left[(\mathbf{Q}.\mathbf{u})^2\,\mathrm{sech}\left(\frac{ch\bar{\nu}}{2kT}\right)\right]$$
$$\times\ \delta(\hbar\bar{\nu} - n\hbar\bar{\nu}_a) \qquad (6.6)$$

One further simplification can be introduced: all the samples were cooled so that the proportion of excited states was negligible. This allows temperature factors to be eliminated:-

$$S(\mathbf{Q},\omega) = \exp\{-(\mathbf{Q}.\mathbf{u})^2\} \times I_n(\mathbf{Q}.\mathbf{u})^2 \times \delta(\hbar\bar{\nu} - n\hbar\bar{\nu}_a) \qquad (6.7)$$

For polycrystalline samples, the polarization vectors need to be replaced by spherical averages. The normal method is to replace $(\mathbf{Q}.\mathbf{u})^2$ with $Q^2\langle u_Q^2\rangle$ where $\langle u_Q^2\rangle$ is the mean square displacement in the direction of polarization.

$$\langle u^2\rangle = \frac{1}{3}|\mathbf{u}|^2 \qquad (6.8)$$

This is strictly true only for a cubic unit cell[319], but no other formula appears to be in use. Hence:

$$S(\mathbf{Q},\omega) = \exp\{-Q^2\langle u_Q^2\rangle\} \times I_n(Q^2\langle u_Q^2\rangle) \times \delta(\hbar\bar{\nu} - n\hbar\bar{\nu}_a) \qquad (6.9)$$

The Bessel function is often replaced by the first term in the power series expansion, valid at low argument[310,317]:-

$$I_n(x) = \frac{|\tfrac{1}{2}x|^{|n|}}{n!} \qquad (6.10)$$

This gives the final expression

$$S(\mathbf{Q},\omega) = \tfrac{1}{2}Q^2\langle u_Q^2\rangle \times \exp\{-Q^2\langle u_Q^2\rangle\} \times \delta(\hbar\bar{\nu} - n\hbar\bar{\nu}_a) \qquad (6.11)$$

with everything except Q and u constant.

6.1.2 Shortcomings of the Usual Formulation

Equation (6.11), while possessing the virtue of simplicity, contains some assumptions which need to be examined in more detail. It predicts that as Q^2u^2 is increased, the scattered intensity rises, reaches a maximum, and then falls. However, Jobic et al[318] measured the neutron spectrum of hexamethylenetetramine on the unrebuilt IN1 beryllium filter spectrometer at the ILL at energy transfers up to 3600 cm^{-1}, where Q^2u^2 should have been large enough for the exponential factor to make the lines very weak. The C-H stretch was observed as a broad intense peak near 3000 cm^{-1} both at low temperatures and at 300K, and the overtone and combination bands were also strong.

The first assumption is the approximation to the Bessel function, originally suggested by Zemach and Glauber[310], which appears to be generally accepted without question. To test its range of validity, the functions $\frac{1}{2}Q^2u^2\exp(-Q^2u^2)$ and $\exp(-Q^2u^2)I_1(Q^2u^2)$, representing two approximations of the fundamental intensity, were plotted as a function of Q^2u^2. Higher order Bessel functions $\exp(-Q^2u^2)I_n(Q^2u^2)$ were also plotted to represent overtone intensities (Fig 6.1).[+] For $Q^2u^2 \leq 0.8$, the approximation holds good, but above this value, higher order terms

---

+ Values of $e^{-x}I_n(x)$ were taken from Abramowitz and Stegun[320].

Fig 6.1 Vibrational Neutron Scattering Intensities as a function of Q^2u^2

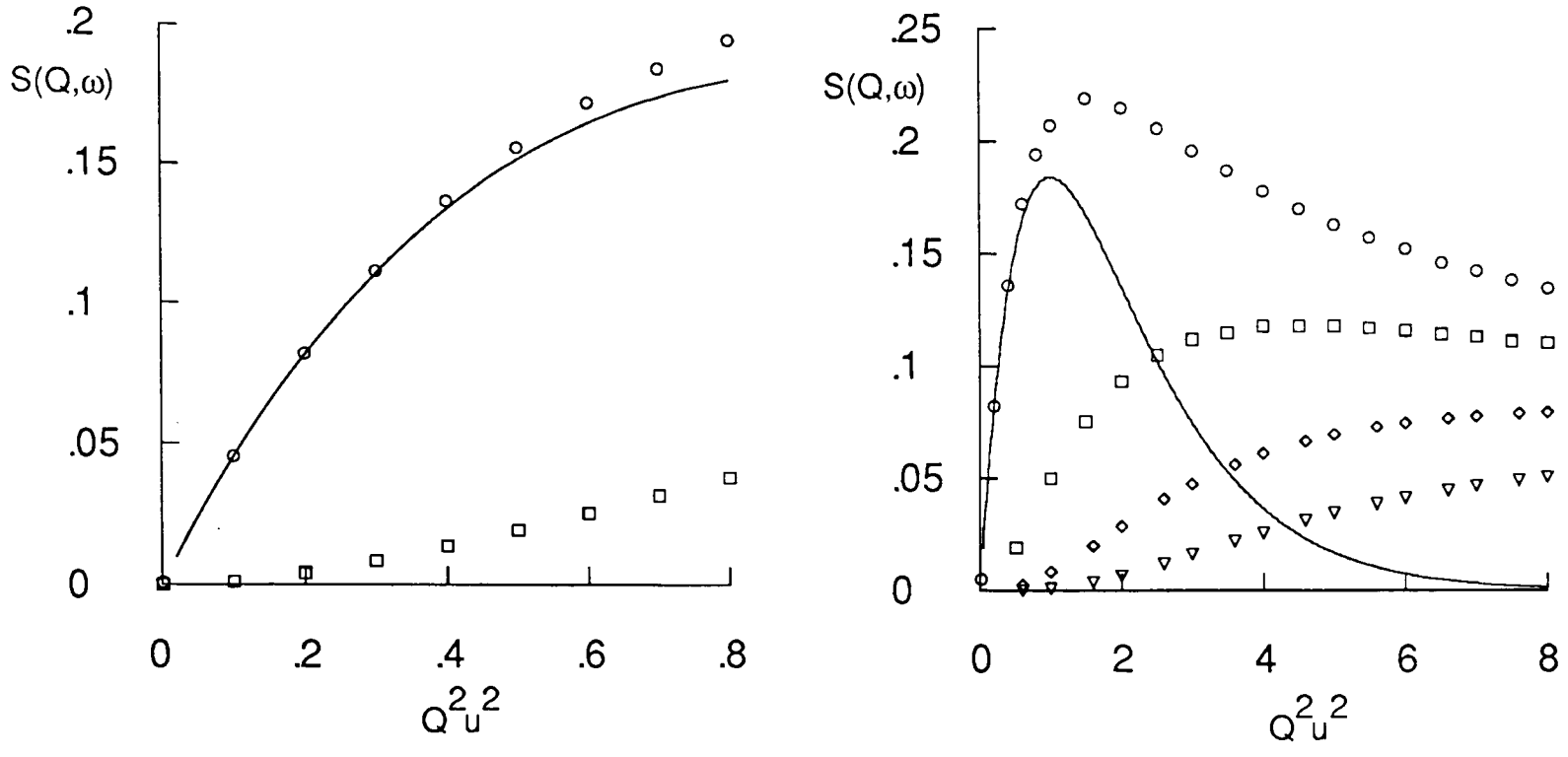

The circles show the intensity of the fundamental as given by $\exp(-Q^2u^2)\, I_1(Q^2u^2)$. The continuous line shows the same intensity plotted with the approximation $I_1(x) \approx \frac{1}{2}x$, only true for small arguments. The squares, diamonds and triangles are the intensities of successive overtones on the same scale.

in the power series become significant and the value of $I_1(x)$ increases sharply enough to offset the effect of the exponential so that the intensity does not fall off as expected. At the same time, the overtones change from being very weak to being quite intense; for these to be observed at all, Q^2u^2 must be large enough to be outside the range in which the approximation is valid.

A second assumption is more subtly hidden and more difficult to overcome. The expression which Zemach and Glauber[310] actually derived was:-

$$\langle\sigma[n_\lambda](\theta)\rangle_T = \frac{k}{k_0} \sum_{vv'} a_v a_{v'} \times \exp[i\mathbf{Q}.(\mathbf{b}_v - \mathbf{b}_{v'})]\, W_{vv'}$$

$$\text{where } W_{vv'} = \Pi_\lambda \exp\{-[(\mathbf{Q}.\mathbf{c}_v^{(\lambda)})^2 + (\mathbf{Q}.\mathbf{c}_{v'}^{(\lambda)})^2] \times (4\omega_\lambda)^{-1} \coth(\omega_\lambda/2T)\}$$

$$\times \exp(-n_\lambda\omega_\lambda/2T) \times I_{n\lambda}\left[\frac{(\mathbf{Q}.\mathbf{c}_v^{(\lambda)})(\mathbf{Q}.\mathbf{c}_{v'}^{(\lambda)})}{2\omega_\lambda \sinh(\omega_\lambda/2T)}\right] \qquad (6.12)$$

Symbols, where different from above, are as follows:-

Units are chosen with $\hbar$=1 throughout.

k_o and k are the initial and final neutron momenta.

$\sum_{vv'}$ sums over initial and final vibrational states.

Π_λ is the product over vibrational modes.

a is the bound neutron scattering length.

$(\mathbf{b}_v - \mathbf{b}_{v'})$ takes account of the change in mean bond length with vibrational state. This would only be significant if the vibration were very anharmonic.

ω_λ is the angular frequency of the vibration = $2\pi\nu$

T is measured in units of energy so that with $\hbar$=1, ω/T is dimensionless.

In particular, $\mathbf{c}_v^{(\lambda)}$ and $\mathbf{c}_{v'}^{(\lambda)}$, the vibrational amplitudes in the initial and final states are used, whereas even Howard and Waddington's initial expression (6.1) assumes that both of these values can be replaced with the thermally weighted crystallographic values derived from Debye-Waller factors measured for elastic scattering. In general, the vibrational amplitude of an excited state will not equal the the vibrational amplitude of the ground state, still less the vibrational amplitude of a higher overtone. Similarly, the polarization factor $\langle \mathbf{u}_Q^2 \rangle = \frac{1}{3}u^2$ is a spherical average of a tensor on the basis of a cubic unit cell.

Another reason for the appearance of the C-H stretch in hexamethylenetetramine has been suggested by Griffin and Jobic[321] and by Warner et al[322]. They have pointed out that in intensity calculations for polyatomic molecules in a solid, the same value of u^2 is used both for phonons at ~100 cm^{-1} and for molecular vibrations at up to 4000 cm^{-1}. If these are separated in the scattering law, similarly to molecular rotations and vibrations in the gas phase, the high energy bands have low u^2 and are predicted to be intense with phonon sidebands.

This explains the hexamethylenetetramine spectrum and in particular its temperature dependence, allowing for the fact that at typical resolutions now available, the phonon sidebands are smeared with the main peak into a single envelope. In the current study mutatis mutandis, this provides justification for ignoring the molecular modes when considering low frequency hindered rotations.

Finally, all the above treatments ignore recoil effects. For scattering from hydrogen molecules which are free to recoil[323]:-

$$E_{recoil} = \frac{h^2Q^2}{2m_{H_2}} \qquad (6.13)$$

In the context of a beryllium filter spectrum, the apparent energy transfer can be more than doubled (See Section 6.2.2). This may account for the broad, gently sloping background in the IN1B intercalate spectrum (Fig 7.7). However, Jobic[324] also using IN1 observed a similar background in the spectrum of solid ethylene (mass 28) which he attributed mainly to multiphonon excitations. Recoil effects reduce scattering cross-sections from the bound value by a factor of up to $(M/M+m)^2$ where M is the mass of the scattering atom and m the neutron mass[291]. For an unbound hydrogen **molecule**, this factor is $\frac{4}{9}$.

6.1.3 Application to a Beryllium Filter Spectrum

In this case Equation (6.9) was used to calculate scattering intensities:-

$$S(Q,\omega) = \exp(-Q^2\langle u_Q^2\rangle) \times I_n(Q^2\langle u_Q^2\rangle) \times \delta(\hbar\bar{\nu} - n\hbar\bar{\nu}_a) \qquad (6.9)$$

Q^2 was calculated as follows:

In a beryllium filter spectrum, the final neutron energy lies between 0 and 42 cm^{-1} with an average of about 25 cm^{-1} and the spectrum is measured by scanning the incident energy from say 12 to 120 meV. (See Section 7.3.1 and refs[317,325].) Thus $k_i >> k_f$ and $\mathbf{Q} \approx -\mathbf{k}_i$. More exactly, the scattering angle averages 90° so that:

$$Q^2 = k_i^2 + k_f^2 \tag{6.14}$$

$$\varepsilon = \frac{p^2}{2m} \quad \text{and} \quad k = \frac{2\pi}{\lambda} \quad \text{hence} \quad \varepsilon = \frac{h^2k^2}{8\pi^2m} \text{ Joules} \tag{6.15}$$

where ε is the neutron energy in J, m its mass in Kg, and k is in Å^{-1}. p is the neutron momentum in Kg m/sec, and λ its wavelength in Å.

Hence:

$$Q^2 = 0.05984(\bar{\nu}_{inc} + \bar{\nu}_f)\ \text{Å}^2 \quad \text{with } \bar{\nu}_{inc} \text{ the incident energy in cm}^{-1}$$

$$\bar{\nu}_f = 25\ \text{cm}^{-1} \quad \text{so} \quad k_f^2 = 1.45\ \text{Å}^{-2}$$

$$\text{Thus} \quad Q^2 = 0.4827\ E_{inc} + 1.45\ \text{Å}^{-2} \text{ with } E_{inc} \text{ in meV} \tag{6.16}$$

$$= 0.05984\ \bar{\nu}_{inc} + 1.45\ \text{Å}^{-2} \text{ with } \bar{\nu}_{inc} \text{ in cm}^{-1}$$

$$\text{and} \quad E_{inc} = E_{transition} + 3 \text{ meV} \qquad \bar{\nu}_{inc} = \bar{\nu}_{trans} + 25\ \text{cm}^{-1}$$

The formula for u^2 was that used by Cockbain et al[319] in calculating the crystallographic Debye-Waller factor for hexadiyne:

$$\langle u^2 \rangle = \frac{3\hbar}{4m_p\omega_D} \quad \text{where} \quad \langle u_Q^2 \rangle = \tfrac{1}{3}\langle u^2 \rangle \tag{6.17}$$

m_p is the mass of a proton and $\omega_D/2\pi$ the frequency of the fundamental vibration in Hz.

This formula was found to be convenient since it assumes that most of the vibrational motion is caused by a single torsional mode, contributions from internal modes being considered negligible. It does, however, approximate the torsion to a harmonic oscillation, which is not strictly true for moderate barriers to rotation.

6.2 NEUTRON SCATTERING FROM FREELY ROTATING HYDROGEN AND DEUTERIUM MOLECULES

6.2.1 The Scattering Law

Sears' expression[311] for the partial differential scattering cross-section from a freely rotating homonuclear diatomic molecule is very general and it is easier to use Young and Koppel's formula which is specific to hydrogen[326]. If only rotational transitions can take place (vibrational excitation occurs at 4162 cm^{-1} [121]):-

$$\left.\frac{d^2\sigma}{d\Omega d\varepsilon}\right|_{para} = 4\,\frac{k}{k_0}\left(\frac{M}{\pi Q^2 T}\right)^{\frac{1}{2}} \sum_{J=0,2,4} P_J \times \left[a_c^2 \sum_{J'=0,2,4} + a_i^2 \sum_{J'=1,3,5}\right](2J'+1) \tag{6.18}$$

$$\times \exp\left\{-\left(\varepsilon+\Delta E+\frac{Q^2}{4M}\right)^2 \Big/ \left(\frac{Q^2T}{M}\right)\right\} \times \sum_{l=|J'-J|}^{J'+J} j_l^2(Qd/2)\; C^2(JJ'l;00)$$

and

$$\left.\frac{d^2\sigma}{d\Omega d\varepsilon}\right|_{ortho} = \frac{4}{3}\;\frac{k}{k_0}\left(\frac{M}{\pi Q^2 T}\right)^{\frac{1}{2}} \sum_{J=1,3,5} P_J \times \left[a_i^2 \sum_{J'=0,2,4} + (3a_c^2+2a_i^2) \sum_{J'=1,3,5}\right] \tag{6.19}$$

$$\times (2J'+1)\exp\left\{-\left(\varepsilon+\Delta E+\frac{Q^2}{4M}\right)^2 \Big/ \left(\frac{Q^2T}{M}\right)\right\} \times \sum_{l=|J'-J|}^{J'+J} j_l^2(Qd/2)\; C^2(JJ'l;00)$$

To explain terms:

Units are chosen such that $\hbar$=1 throughout.

J and J' are the rotational quantum numbers of the initial and final states respectively. In para-hydrogen J is even and in ortho-hydrogen J is odd (see below).

$\frac{d^2\sigma}{d\Omega d\varepsilon}$ is the partial differential scattering cross-section.

k_0 and k are the initial and final neutron momenta. The k/k_0 dependence is eliminated in beryllium filter spectroscopy by scanning at constant monitor.

M is the mass of a proton.

Q is the neutron momentum transfer.

T is the temperature measured in eV. At 300K, T is 26 meV and at 10K it is 0.86 meV (see below).

$\sum_J P_J$ sums over initial rotational states with P_J as the statistical weight of state J.

a_c and a_i are the coherent and incoherent scattering lengths of hydrogen. (NB $a_i >> a_c$)

$\sum_{J'}$ sums over final states.

$\exp\left\{-\left(\varepsilon+\Delta\varepsilon+\frac{Q^2}{4M}\right)^2 \Big/ \left(\frac{Q^2T}{M}\right)\right\}$ takes account of recoil energy and temperature broadening. ε is the transition energy neglecting

recoil, $\Delta\varepsilon$ the observed energy and $Q^2/4M$ the recoil energy. The exponential function gives the temperature broadening (see below). $j_1^2(Qd/2)$ is the square of a spherical Bessel function of order 1 with argument $Qd/2$, where d is the H-H bond length.

$C^2(JJ'1;00)$ is a Clebsch-Gordan coefficient, and is concerned with the vector coupling of the initial and final angular momenta. The theory is given by Condon and Shortley[327], but Young and Koppel also list the values needed in this calculation.

The nuclear spin statistics are of critical importance. Hydrogen nuclei have spin $\frac{1}{2}$ and obey Fermi-Dirac statistics. This means that in para-hydrogen, the nuclear spins of the two hydrogen atoms are antiparallel and only rotational states with J even are allowed. In ortho-hydrogen, the nuclear spins are parallel and only states with J odd are allowed. This is summarized in Table 6.1; full accounts are given by Wheatley[328] and Silvera[121].

The sample temperature also has a profound effect on rotational state populations. At 300K, **k**T is 26 meV compared with 14.7 meV for the J=0→1 transition, so that excited states will be populated. At 10K, however, **k**T is 0.86 meV which means that on cooling from room temperature to 10K, thermal equilibrium dictates that all the molecules should be in the J=0 state. The J=1→0 transition is, however, spin forbidden and only takes place very slowly. This means that for a low temperature sample $\sum_J P_J$ can be dispensed with, but that both J=0 and J=1 have to be considered. Similarly for a momentum transfer $Q^2=50\text{Å}^{-2}$, the equivalent of a beryllium filter spectrum at 100 meV, $Q^2T=0.043$ at 10K, which allows the thermal broadening term

$$\exp\left\{-\left(\varepsilon+\Delta\varepsilon+\frac{Q^2}{4M}\right)^2\Big/\left(\frac{Q^2T}{M}\right)\right\}$$ to be replaced by a delta function $\delta(\Delta E-\varepsilon-E_r)$ where E_r is the recoil energy. (6.20)

Table 6.1 Summary of Nuclear Spin Statistics for H_2 and D_2

H_2 $I = \frac{1}{2}$ so nuclei obey Fermi-Dirac statistics so ψ_{tot} is **a**

para H_2 ψ_{nuc} is **a** so ψ_{rot} is **s** so J = 0,2,4...
$I_{mol} = 0$ so $g_I = (2I+1) = 1$

ortho H_2 ψ_{nuc} is **s** so ψ_{rot} is **a** so J = 1,3,5...
$I_{mol} = 1$ so $g_I = 3$

D_2 I = 1 so nuclei obey Bose-Einstein statistics so ψ_{tot} is **s**

ortho D_2 ψ_{nuc} is **s** so ψ_{rot} is **s** so J = 0,2,4...
$I_{mol} = 0,2$ so $g_I = 6$

para D_2 ψ_{nuc} is **a** so ψ_{rot} is **a** so J = 1,3,5...
$I_{mol} = 1$ so $g_I = 3$

HD is not a homonuclear diatomic molecule and has no spin statistics.

Under equilibrium conditions, H_2 is all **para** at low temperatures and 75% **ortho** at high temperatures. D_2 is all **ortho** at low temperatures and 67% **ortho** at high temperatures.

s = symmetric and **a** = antisymmetric

$\psi_{tot} = \psi_{nuc} \times \psi_{rot} \times \psi_{vib} \times \psi_{elec}$ with both ψ_{vib} and ψ_{elec} **s** throughout. g_I is the **nuclear** spin degeneracy and must be multiplied by (2J+1) to give the total degeneracy in rotational state J.

The hydrogen in the intercalate may or may not be translationally bound, so calculations are done with and without the recoil term.

By assuming low temperature and constant monitor counting, the expression for para-hydrogen can be simplified considerably:-

$$\left.\frac{d^2\sigma}{d\Omega d\varepsilon}\right|_{J=0} = 4\left[a_c^2 \sum_{J'\ \text{even}} + a_i^2 \sum_{J'\ \text{odd}}\right](2J'+1)\, j_{J'}^2\left(\frac{Qd}{2}\right) C^2(0J'J';00) \times \delta(\Delta E - \varepsilon - E_r) \qquad (6.21)$$

Young and Koppel[326] give the value of the Clebsch-Gordan coefficient:

$$(2J'+1)\, C^2(JJ'1;00) = 2J'+1 \qquad (6.22)$$

Thus:

$$\left.\frac{d^2\sigma}{d\Omega d\varepsilon}\right|_{J=0} = 4\left[a_c^2 \sum_{J'\text{even}} + a_i^2 \sum_{J'\text{odd}}\right](2J'+1)\, j_{J'}^2\left(\frac{Qd}{2}\right) \delta(\Delta\varepsilon-\varepsilon-E_r) \qquad (6.23)$$

Two points are immediately worthy of note: first, a **spherical** Bessel function is used in this case, whereas a hyperbolic Bessel function was used for the harmonic oscillator. Second, incoherent scattering is forbidden for J=even → even transitions, so that only J=0→1,3,5... will be observed with any reasonable intensity. It also predicts that para-hydrogen will give very little elastic scattering. These results may seem surprising, but are confirmed by experiment[323,329,330].

The expression for ortho-hydrogen can also be simplified:

$$\left.\frac{d^2\sigma}{d\Omega d\varepsilon}\right|_{J=1} = \frac{4}{3}\left[a_i^2 \sum_{J'\text{even}} + (3a_c^2 + 2a_i^2) \sum_{J'\text{odd}}\right](2J'+1) \times \sum_{l=J'-1}^{J'+1} j_l^2\left(\frac{Qd}{2}\right) C^2(1J'l;00)\, \delta(\Delta\varepsilon - \varepsilon - E_r) \qquad (6.24)$$

With J=1, the initial and final angular momenta can couple in two ways, each of which gives rise to a term in the scattering cross-section. Taking the Clebsch-Gordan coefficients from Young and Koppel:

$$(2J'+1)\, C^2(1J'J'+1;00) = J'+1 \qquad (6.25)$$

$$(2J'+1)\, C^2(1J'J'-1;00) = J \qquad (6.26)$$

Introducing these simplifications:

$$\left.\frac{d^2\sigma}{d\Omega d\varepsilon}\right|_{J=1} = \frac{4}{3}\left[a_i^2 \sum_{J'even} + (3a_c^2 + 2a_i^2) \sum_{J'odd}\right] \times (J'+1)\, j^2_{J'+1}\left(\frac{Qd}{2}\right) + J'\, j^2_{J'-1}\left(\frac{Qd}{2}\right) \times \delta(\Delta E - \varepsilon - E_r) \quad (6.27)$$

In this case, incoherent scattering to both even and odd rotational states is allowed, but the odd states are twice as intense.

Young and Koppel also calculated the scattering cross-sections for deuterium[326]. Apart from the different values for the rotational constant and the coherent and incoherent scattering cross-sections, the main difference lies in the nuclear spin statistics. For ortho-deuterium in the J=0 state, the simplified partial differential scattering cross-section is given by:-

$$\left.\frac{d^2\sigma}{d\Omega d\varepsilon}\right|_{J=0} = 4\left[(a_c^2 + \tfrac{5}{8}a_i^2) \sum_{J'even} + \tfrac{3}{8}a_i^2 \sum_{J'odd}\right](2J'+1)\, j^2_{J'}\left(\frac{Qd}{2}\right) \delta(\Delta\varepsilon - \varepsilon - E_r) \quad (6.28)$$

For para-deuterium in the J=1 state, the expression is:-

$$\left.\frac{d^2\sigma}{d\Omega d\varepsilon}\right|_{J=1} = \left[3a_i^2 \sum_{J'even} + (4a_c^2 + a_i^2) \sum_{J'odd}\right] \times (J'+1)\, j^2_{J'+1}\left(\frac{Qd}{2}\right) + J'\, j^2_{J'-1}\left(\frac{Qd}{2}\right) \times \delta(\Delta E - \varepsilon - E_r) \quad (6.29)$$

HD is not a homonuclear diatomic molecule, so the spin statistics do not apply and the nuclear cross-sections can be used.

6.2.2 The Calculated Beryllium Filter Spectra

Solid hydrogen is unique in being a quantum solid in which the molecules can rotate freely with J a good quantum number,# and this provides one possible model for the hydrogen absorbed by the intercalates: accordingly, the beryllium filter spectrum of para- and ortho-hydrogen were calculated using Equations 6.23 and 6.27 respectively.

The properties of solid hydrogen are reviewed by Silvera[121].

Two major uncertainties remain, however. The first is the ortho:para ratio; this will depend on the extent to which the intercalates catalyze the interconversion (See Section 1.5.2), the sample temperature and the time elapsed before measuring the spectrum. The second is the extent to which the recoil of the hydrogen molecules takes place. Scattering data from liquid hydrogen with 4Å (5 meV) incident neutrons show the J=0→1 peak at 15.2±0.5 meV independent of the scattering angle[329] (ie. no recoil). On the other hand, when 65 meV incident neutrons were scattered through 90°, the inelastic peaks were shifted as for a gas with relative molecular mass 2 [331], and recent experiments on solid and liquid hydrogen using 500 and 1900 meV incident neutrons offer further confirmation[323]. The current beryllium filter spectra, with the exception of the IN1 spectra, span the Q region between the first two experiments. Hydrogen would be expected to bind to the intercalate strongly and anisotropically compared with the binding to itself in liquid or solid hydrogen, and the anisotropy might cause a smearing out of the high energy peaks rather than a simple energy shift. The extent of recoil could be determined by examining the momentum dependence of the spectrum, but the design of a beryllium filter spectrometer permits little if any momentum resolution.

In the absence of firm answers, limiting cases have had to be used. The intensities of transitions from the J=0 and J=1 states have been plotted separately as a function of momentum transfer. Since beryllium filter spectroscopy has been used throughout, the momentum transfer has been translated into energy by Equation 6.16, and the position of each peak for the limiting cases of the molecule being tightly bound and free to recoil have been marked (Fig and Table 6.2).

The recoil correction was calculated as follows: if the neutron were completely stopped in the scattering process, then by conservation of momentum:

Fig 6.2 Calculated Beryllium Filter Intensities for the Rotational Transitions in Translationally Bound and Free para- and ortho-hydrogen

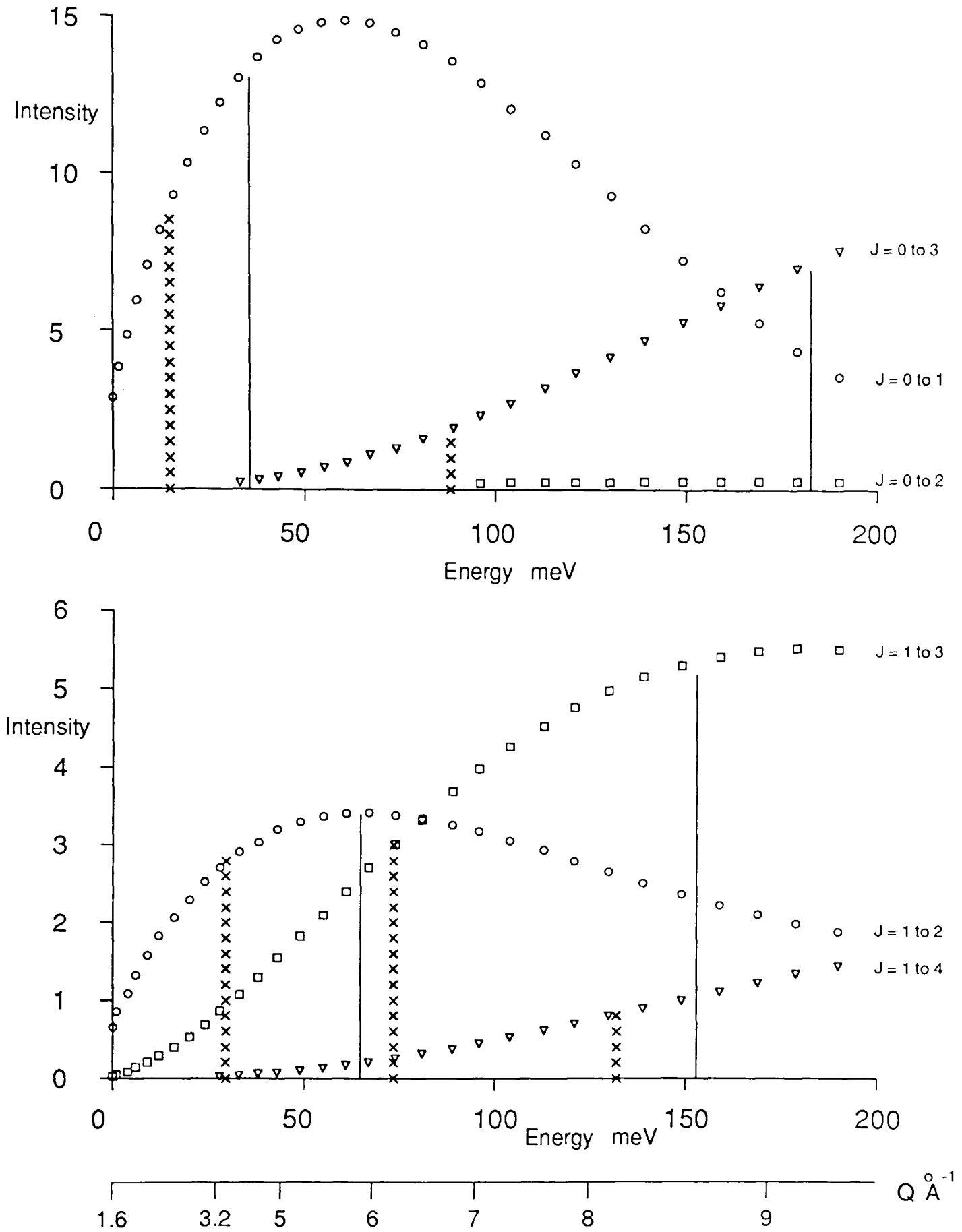

The plot shows the transition intensities as a function of Q^2 expressed as a beryllium filter transition energy. Note the difference in Y scale between the two plots. The actual transition energies for the bound molecule are marked by x , and those for the free molecule are marked by continuous lines. Absolute transition intensities for the free molecule should be multiplied by $\frac{4}{9}$.
Values of the parameters used are given in Table 6.2.

Table 6.2 Rotational Neutron Scattering Intensities for a Hydrogen Molecule: Momentum Transfer as in Beryllium Filter Spectroscopy

para-hydrogen J = 0

	Bound			Free	
transition	ε(meV)	$\frac{d^2\sigma}{d\Omega dE}$	E'_{tr}(meV)	Relative Intensity	Intensity reduced for recoil
0→1 2B	14.7	8.9	35	(13.7)	6.1
0→2 6B	44	0.084*	94	(0.20*)	0.089*
0→3 12B	88	1.9	182	(7.2)	3.2
0→4 20B	147	0.023*	300	(0.13*)	0.058*
0→5 30B	220	0.59	446	(5.0)	2.2

* Coherent scattering only.

ortho-hydrogen J = 1

	Bound			Free	
transition	ε(meV)	$\frac{d^2\sigma}{d\Omega dE}$	E'_{tr}(meV)	Relative Intensity	Intensity reduced for recoil
1→2 4B	29	2.77	64	(3.39)	1.51
1→3 10B	73	3.00	152	(5.36)	2.38
1→4 18B	132	0.83	270	(2.15)	0.96
1→5 28B	206	1.06	418	(3.84)	1.71

a_c bound coherent scattering length of H atom.

$\sigma_{coh} = 4\pi a_c^2 = 1.79\pm0.02$ barns [290,294]

Hence $a_c^2 = 0.142$ barns

a_i bound incoherent scattering length of H atom.

$\sigma_{tot} = 4\pi(a_c^2+a_i^2) = 81.5\pm0.5$ barns [290,294] (See Section 6.1.1)

Hence $a_i^2 = 6.48$ barns

For free molecules, these values are multiplied by $\frac{4}{9}$ giving

$a_c^2 = 0.063$ $a_i^2 = 2.88$ (Section 6.1.2)

Q neutron momentum transfer in a beryllium filter spectrum.

$Q^2 = 0.4827\ E_{inc} + 1.45\ A^{-2}$ (6.16) where $E_{inc} = E_{tr} + 3$ meV

d H-H bond length value 0.74A

$\varepsilon = BJ(J+1)$ where B = 7.35 meV [121]

Values of $j_1(x)$ obtained from Abramowitz and Stegun[320].

$$E_r = \varepsilon = \tfrac{1}{2}E_{inc} \qquad (6.30)$$

More exactly, the scattered neutron has an energy of 3 meV perpendicular to the incident direction. (Although it is **momentum** which is conserved in the scattering process, the 90° angle of scatter and simple mass ratio make it easier to use the square of the momentum and express it as an energy.) The hydrogen molecule will experience recoil both parallel and perpendicular to the incident direction:

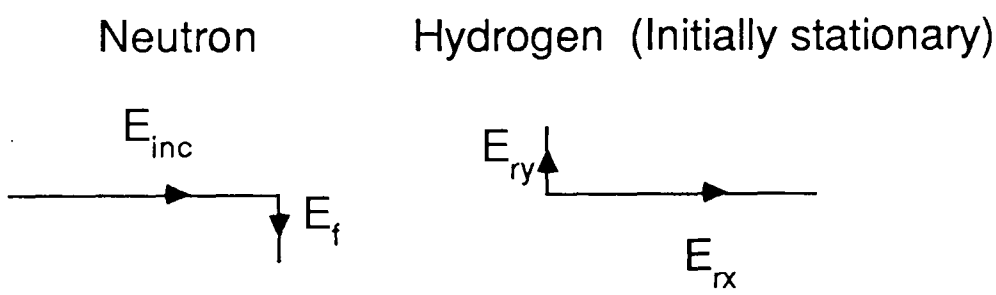

By conservation of momentum: $E_{rx} = \tfrac{1}{2}E_{inc}$

$E_{ry} = \tfrac{1}{2}E_f$

Conserving energy: $\varepsilon = E_{inc} - E_f - E_{rx} - E_{ry}$

From the filter properties: $E_f = 3$ meV

Hence $$E_{inc} = 2\varepsilon + 9 \text{ meV} \qquad (6.31)$$

The most useful quantity, however, is a notional transition energy where a nominal 3 meV filter correction has been applied:

$$E'_{tr} = 2\varepsilon + 6 \text{ meV} \qquad (6.32)$$

6.3 ENERGY LEVELS OF A HINDERED ROTOR

6.3.1 Types of Motion

The treatment of this large subject has of necessity to be brief and selective. Fuller account are given by Hüller and Press[312,332] with further examples by Thomas[333] and Howard & Waddington[317] in their reviews of inelastic neutron scattering.

Rotations of single particles in molecular crystals can be classified according to the number of degrees of rotational freedom (Fig 6.3). A well studied example with one degree of freedom is the methyl group. Systems with two degrees of rotational freedom are less

Fig 6.3 Single Particle Rotations with 1, 2 and 3 degrees of freedom

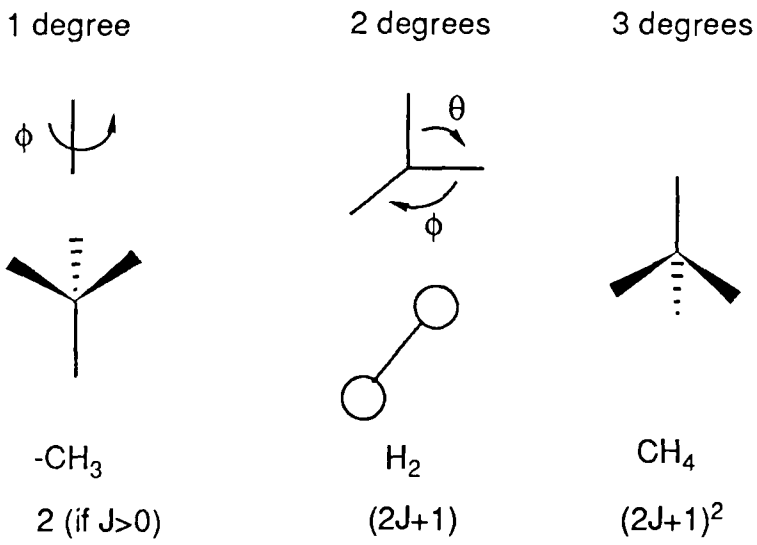

well studied, but include the hydrogen molecule and the cyanide ion. Systems with three degrees of rotational freedom include the methane molecule and the ammonium ion. The number of degrees of rotational freedom is also the number of angles on which the potential energy of the system depends. Thus for a methyl group, only a single angle ϕ is needed. For the hydrogen molecule, two angles θ and ϕ are needed, and for the three dimensional case, three angles, usually Euler angles or quaternions are used. Systems with one and two degrees of rotational freedom will be discussed individually. The case with three degrees of rotational freedom is more complex and will not be discussed further.

The hindering potential to which a single particle undergoing rotation is subject can be decomposed into a time independent (static) part $V(\phi)$ and a time dependent (fluctuating) part $V(\phi,t)$. The magnitude of the static part of the potential is determined by such factors as atom-atom potentials and charge distribution; it is largely temperature independent, although there is a weak pressure dependence. By contrast, the fluctuating part of the potential results from collective excitations (phonons), and its magnitude is determined by the temperature of the system. Depending on the magnitude of the static and fluctuating parts of the potential, various types of motion can occur (Table 6.3).

Table 6.3 The effects of Static and Fluctuating Potentials on Rotational Motion [refs 332,333]

$V(\phi)/B$	$V(\phi,t)/B$	Type of motion
High	-	Librational oscillation
Moderate	Low	Librational oscillation and Rotational tunnelling
Moderate	High	Jump diffusion
Low	Low	Quantized free rotation
Low	High	Rotational diffusion

$V(\phi)$ is a static potential, $V(\phi,t)$ a fluctuating potential, and B the rotational constant.

Since the magnitude of the fluctuating potential is determined by the temperature, a lowering of temperature is often accompanied by a transition from classical diffusive to quantized motion. The high temperature classical limit has been considered by various authors [312,333,334] and is outside the scope of this work which is concerned with the low temperature limit where low energy excitations are seen. Negligible coupling between rotating/librating molecules is assumed; if these interactions are introduced, the situation is greatly complicated.

6.3.2 Rotation with One Degree of Freedom: The Methyl Group

The methyl group is the best studied hindered rotor since B, the rotational constant, is 5.56 cm^{-1} (0.690 meV), large enough to resolve individual rotational states. Using the threefold rotational symmetry of the group, the hindering potential can be expressed in terms of multiples of $\cos 3\phi$:-

$$V(\phi) = \sum_{n=1}^{\infty} \frac{1}{2} V_{3n} \left[1 \pm \cos(3n\phi)\right] \qquad (6.33)$$

Substituting the expression for $V(\phi)$ into the Schrodinger equation, the Mathieu equation is obtained:-

$$B \frac{d^2\psi(\phi)}{d\phi^2} + \left[E - \sum_{n=1}^{\infty} \frac{1}{2} V_{3n} \left[1 \pm \cos(3n\phi)\right]\right] \psi(\phi) = 0 \qquad (6.34)$$

where $B = \hbar^2/2I$ with I the moment of inertia, E the total energy of the molecule and ϕ the angle of rotation. The solutions to the Mathieu equation are well-known and are expressed as an expansion in terms of the free rotor wavefunctions. Details of the solution, originally applied to a rotating methyl group by Stejskal & Gutowsky[335] are given by Roser[336]. The rotational energy levels for pure threefold and pure sixfold barriers have been calculated using Allen's program MATHIEU [336,337] on a VAX 11/780 with levels up to J = 25 as a basis set, and are plotted in Fig 6.4.

At low hindering potentials, $E_J = BJ^2$. For high $V(\phi)$, the energy levels approximate to those of a harmonic oscillator, but are split by an amount small in the ground state compared with the librational levels, but increasing sharply in excited librational states, until at high energy levels, the rotational wavefunctions are barely perturbed. The splitting can be viewed alternatively as tunnelling between librational states in adjacent potential wells caused by overlap of the librational wavefunctions in a manner reminiscent of the inversion of ammonia[338,339] (Fig 6.5).

The rotational wavefunctions, singly degenerate for J=0, doubly degenerate for $J \geq 1$ form librational levels with symmetries alternately (A+E) and (E+A). As the barrier height is increased, the first librational transition increases in energy, but the ground state tunnelling splitting decreases. The effect of symmetry, however, is totally different. In the sixfold case, the potential wells are both narrower and situated closer together than in the threefold case, so that both the tunnelling and the librational energies are increased for a given barrier height.

The dynamics of rotationally hindered methyl groups have been studied in many cases by inelastic neutron scattering. This technique is

Fig 6.4 Splitting Pattern for the Rotational Levels of a Methyl Group in 3- and 6-fold Potential Barriers

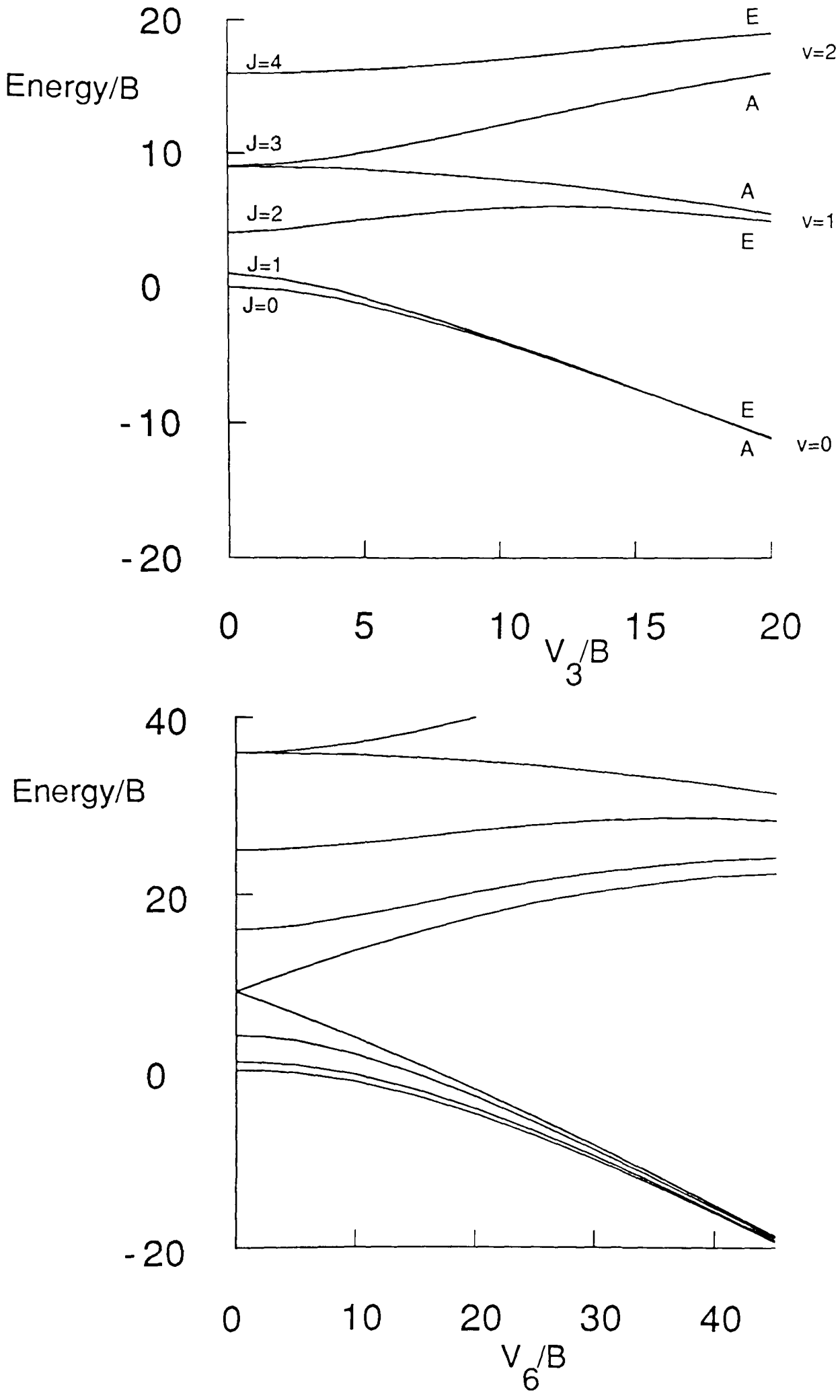

Note the change in scales between plots and the greatly increased tunnelling splitting in the case of the 6-fold barrier. The rotational levels split only where $J = 3n$.

Fig 6.5 Schematic Representation of Rotational Tunnelling

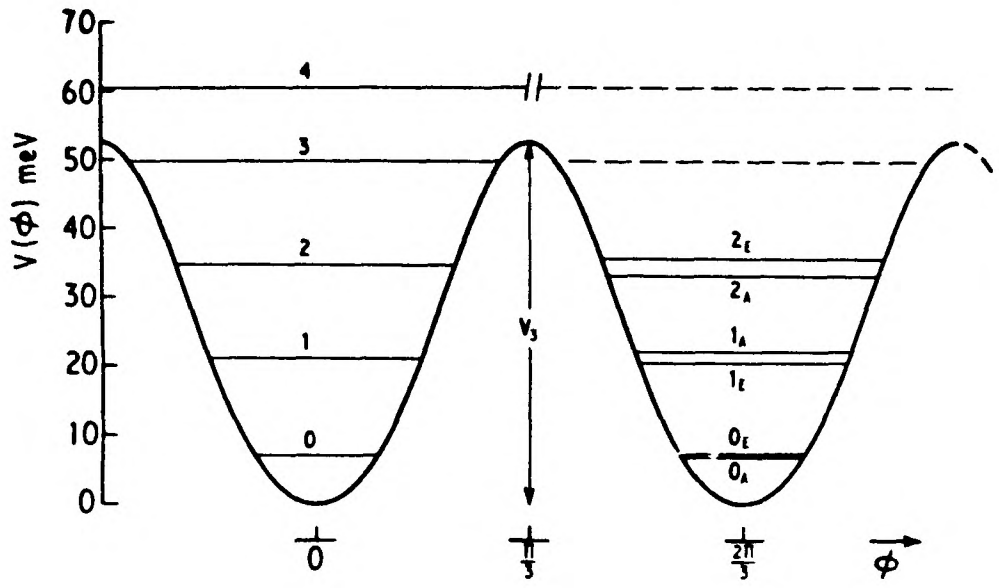

Energy levels for a methyl group in a threefold potential. The parameters are those for hexadiyne[340]. The tunnelling splitting in the ground state is exaggerated (after Thomas [ref 333]).

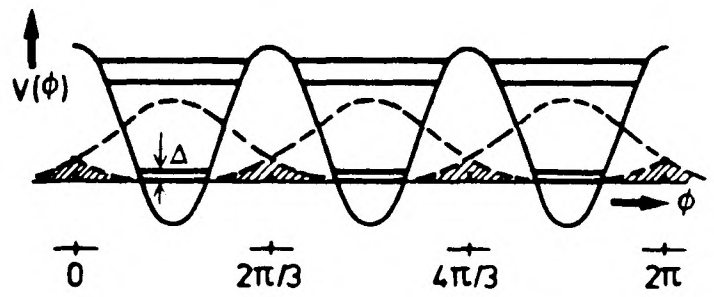

Schematic representation of rotational tunnelling splitting caused by overlap of wavefunctions in neighbouring potential wells [ref 312].

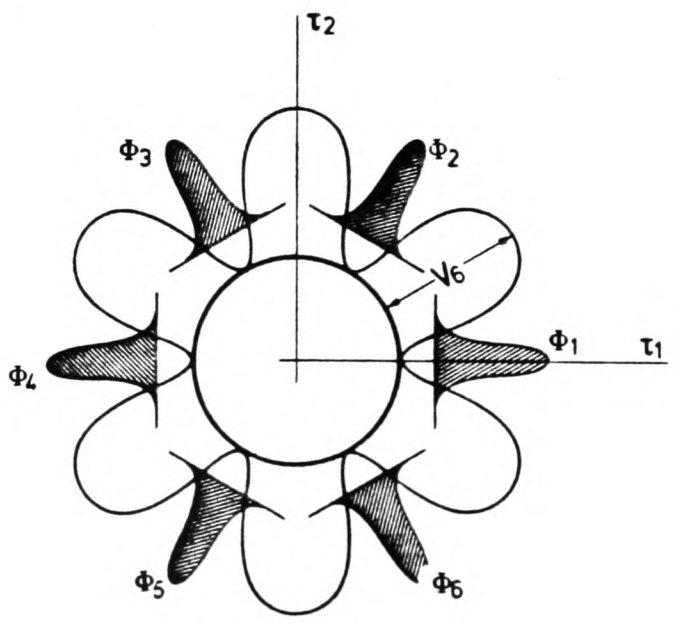

Schematic drawing of a one dimensional rotor in a sixfold barrier showing wavefunctions localized in each potential well [ref 312].

particularly suitable, since the torsional levels tend to lie in the far infra-red region and give weak optical spectra. By contrast, the region is easily accessible to neutron scattering, and the large amplitude motions of the hydrogen atoms give intense neutron peaks. The tunnelling transitions can be observed directly by inelastic neutron scattering on time of flight machines; alternatively they can be deduced from T_1 measurements in NMR [341].

A list of compounds studied is given by Thomas[333]. One well-studied system is hexadiyne ($H_3C-C\equiv C-C\equiv C-CH_3$) where both tunnelling and librational transitions have been observed directly and the barrier to rotation calculated as 432 cm^{-1} [340]. The transition from quantum to classical dynamics with increasing temperature can also be seen. As the temperature is raised from 4 to 50K, the tunnelling peaks slowly disappear into a broadened quasielastic peak typical of diffusive motion[319,340]. In all these cases, rotational barriers have been calculated from peak positions **only**; to test the quantitative applicability of the model, a study has been made of the dynamics of solid acetonitrile, CH_3-CN (Section 6.5).

6.4 THE ENERGY LEVELS OF A ROTATIONALLY HINDERED HYDROGEN MOLECULE

6.4.1 Axially Symmetric Field with a Twofold Barrier to Rotation

The rotational energy levels of a hydrogen molecule in an axially symmetric field with a twofold barrier to rotation were first calculated approximately by Stern in 1930 [342] using a mathematical procedure devised by Wilson[343]. Stern's paper, however, uses confusing notation and does not address the practical problems of machine calculation. We thus give some detail here.

The system under consideration is a dumbell shaped molecule which has a preferred orientation. The twofold barrier to rotation is independent of the path followed, and the system has cylindrical

symmetry. The energy can be expressed in terms of the positive barrier constant V_0 and the angle to the preferred orientation θ. The energy is independent of ϕ, the in-plane orientation. (For negative V_0, there is a preferred **plane** of orientation, and the treatment below does not apply.)

Fig 6.6 A Hydrogen Molecule in an Axially Symmetric Hindering Potential

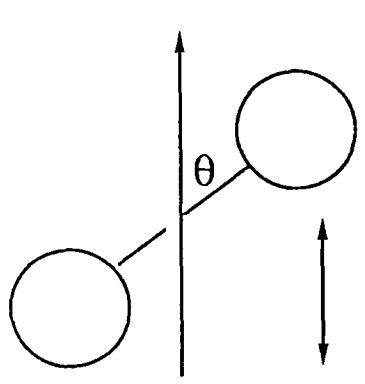

$V = V_0 (1 - \cos 2\theta)$
Barrier to rotation $= 2V_0$
(Excluding zero point energy)

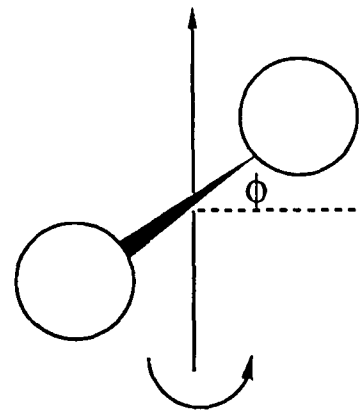

No change in energy
on rotation through ϕ

If the potential is assumed to be sinusoidal:

$$V = V_0 (1 - \cos 2\theta) \qquad (6.33)$$

and the Schrodinger equation has the form:

$$\nabla^2\psi + \frac{8\pi^2 I}{h^2} (E - V)\ \psi = 0 \qquad (6.34)$$

It is assumed that the solutions are separable in θ and ϕ so that:

$$\psi = F(\theta)\ e^{im\phi} \qquad (6.35)$$

If the following substitutions are made:

$$x = \cos\theta$$

$$\lambda = (E - 2V_0)\ \frac{8\pi^2 I}{h^2} = \frac{(E - 2V_0)}{B} \qquad (6.36)$$

$$K^2 = \frac{16\pi^2\ I\ V_0}{h^2} = \frac{2V_0}{B}$$

The equation now has the form:-

$$(1-x^2)F'' - 2xF' + \{\lambda + K^2x^2 - m^2(1-x^2)\}\ F = 0 \qquad (6.37)$$

λ is the eigenvalue and represents the total energy of the system measured from the top of the barrier (ie the sum of the potential and

the kinetic energy). Solutions with λ negative are mainly librational in character and those with λ positive are mainly rotational. K^2 is the energy difference between the top and bottom of the potential well in units of B, the rotational constant.

If a further substitution is made:

$$F = (1-x^2)^{M/2} y \quad \text{where } M = |m| \tag{6.38}$$

the equation has solutions in λ in the form of a continued fraction. The form of the fraction depends on whether M is even or odd.

For a solution based on a rotational level J, the allowed values of M are 0,1,2...J . Alternatively, each value of M gives a series of solutions in λ at different energies.

If M is even:

$$0 = \lambda - M(M+1) + \cfrac{1\times2\ K^2}{(M+2)(M+3) - \lambda - \cfrac{3\times4\ K^2}{(M+4)(M+5) - \lambda - \cfrac{5\times6\ K^2}{(M+6)(M+7) - \lambda - \ldots}}} \tag{6.39}$$

If M is odd:

$$0 = \lambda - (M+1)(M+2) + \cfrac{2\times3\ K^2}{(M+3)(M+4) - \lambda - \cfrac{4\times5\ K^2}{(M+5)(M+6) - \lambda - \ldots}} \tag{6.40}$$

The individual terms in each series converge very slowly, although the series as a whole converges more quickly. A 50 term expansion gave the same answers to precision 10^{-3} B up to K^2=40B as a 100 term expansion.

To find the eigenvalues λ, an iterative procedure is used. Each value of M gives a series of solutions of different energies, and for each solution, there is also a nearby singularity where the expression becomes undefined. Although each solution is associated with a value of J, J is not included in the equation. For each value of M, the residual

varies more and more rapidly as λ is increased, and it is thus easiest to find the low energy solutions. For high energy solutions with low M eg J=3, M=0 it is possible to converge on the wrong solution.

As a result of this, the method of calculation adopted was to calculate λ for each level starting with $K^2=0$, and slowly increasing K^2, keeping M fixed. This gave a known initial value for λ and a good initial guess for subsequent values by using a linear extrapolation.

For the lowest energy solution for each value of M (ie M = J, J-1), the residual is approximately equal to the error in λ. This gave very rapid convergence at low K^2, but for higher K^2, empirical corrections had to be added. The final expression used was:

$$\lambda_{n+1} = \lambda_n + R \div (1 + b/7 + b^2/70 + b^3/1000) \qquad (6.41)$$

where $b = K^2$, R is the residual and λ_n, λ_{n+1} represent successive guesses at λ. This method forms the basis of the calculation of the ground state energies.

For higher energy solutions (ie M < J-1), the above method does not converge on the correct solution, and it was necessary to take two values for λ, one each side of the solution, and take the average. This produced slow but reliable convergence provided that a singularity was not included in the range.

The energy levels in Fig 6.7 were calculated using ROTFIT with 100 terms in the expansion and a precision of 10^{-4}B ($\approx$1μeV). The entire diagram took about fifteen minutes interactively on a VAX 11/750 using two minutes of CPU time.

6.4.2 Tetrahedral and Octahedral Fields

The splitting patterns for the rotational energy levels of a hydrogen molecule in tetrahedral and octahedral fields have been calculated by Smith[344] and Sauer[345] (after Devonshire[346]) respectively, who list the energies of the ground and excited states for

Fig 6.7 Splitting Pattern for the Rotational Energy Levels of a Hydrogen Molecule in an Axially Symmetric $\cos 2\theta$ Potential

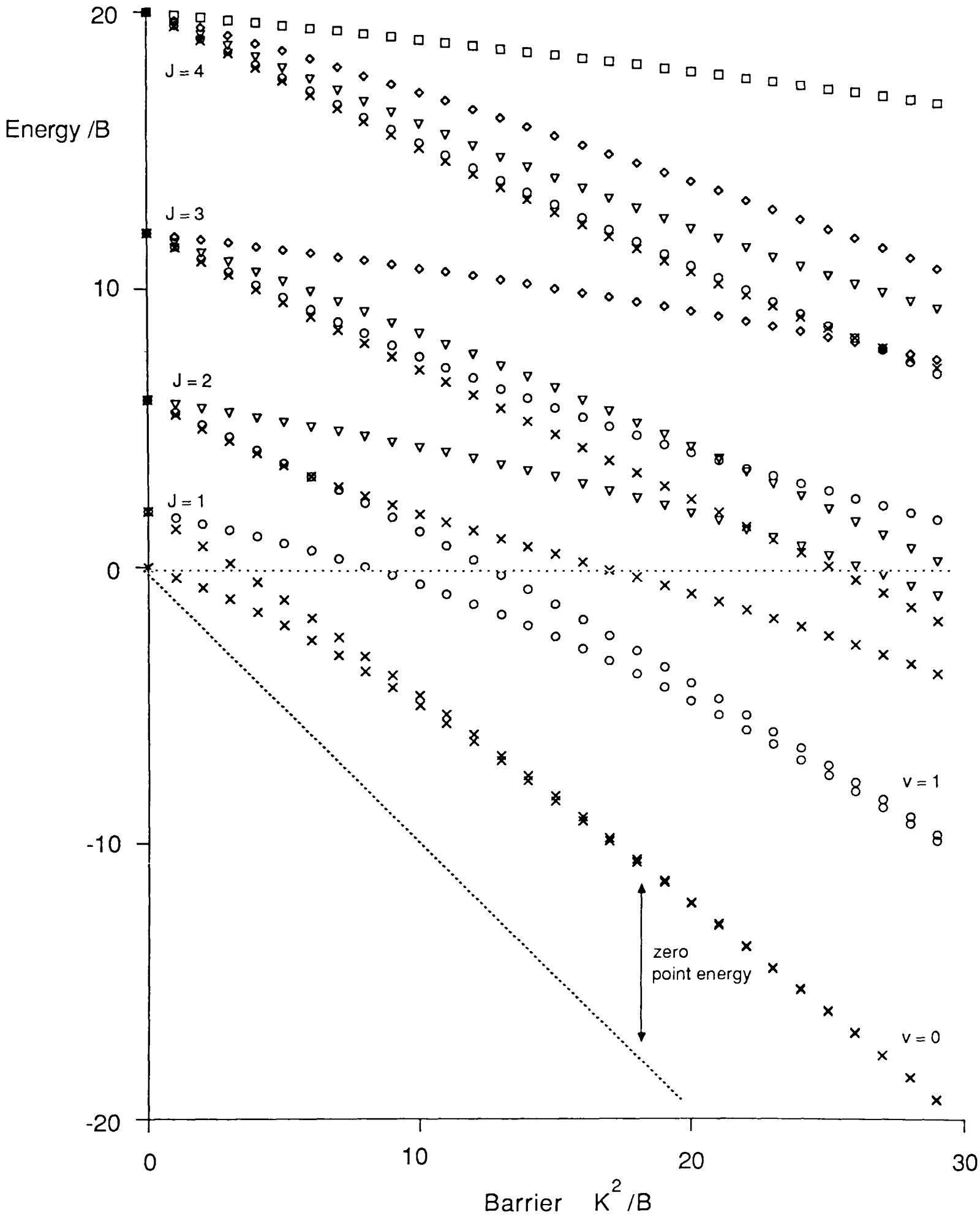

The diagram shows levels up to and including J = 4. Levels with M = 0, 1, 2, 3, 4 are represented by crosses, circles, triangles, diamonds and squares respectively. The top and bottom of the classical barrier are marked by dotted lines.

Fig 6.8 Splitting Pattern for the Rotational Energy Levels of a Hydrogen Molecule in Tetrahedral and Octahedral fields.

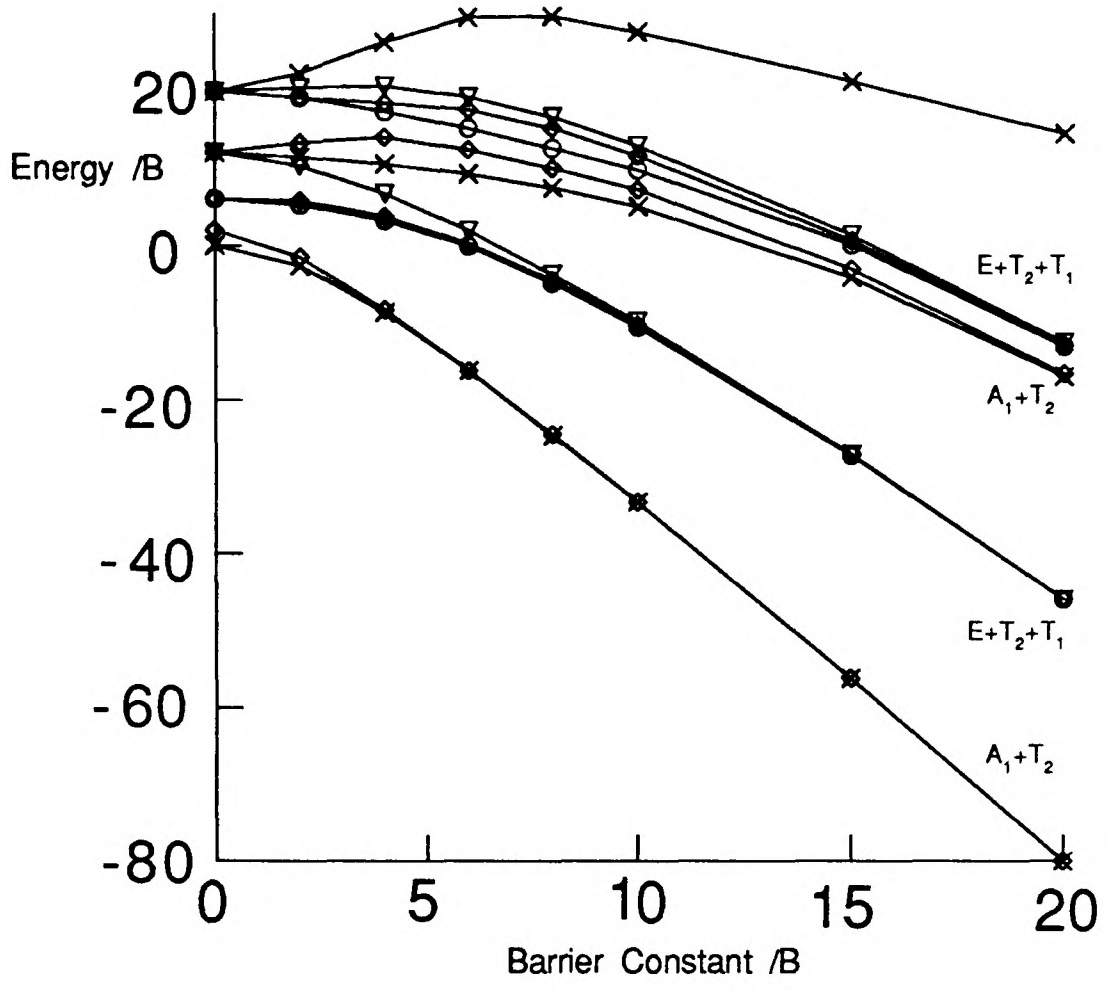

Tetrahedral field up to J = 4 plotted using Smith's figures[344]. Levels with symmetry A_1, E, T_1, and T_2 are marked respectively by crosses, circles, triangles and diamonds.

Sauer's plot for an Octahedral field [ref 345].

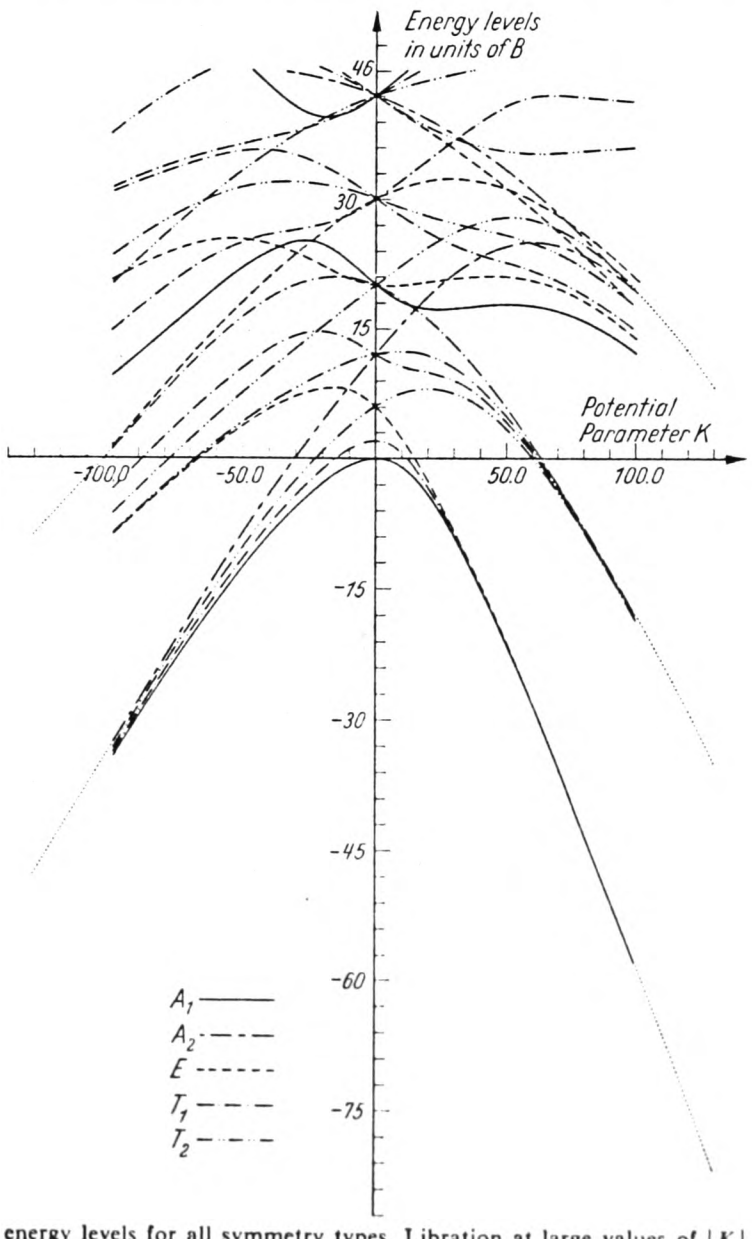

Lowest energy levels for all symmetry types. Libration at large values of $|K|$, free rotation at $K=0$. Dotted lines giving Devonshire's asyptmotic values for large $|K|$

convenient values of V_0. In an octahedral field, the sign of V_0 is important; if V_0 is +ve, the potential minima point toward the six corners of an octahedron, whereas if V_0 is -ve, they point towards the centres of the eight faces. In a tetrahedral field, the two configurations are equivalent. The splitting patterns are plotted in Fig 6.8.

6.5 SOLID ACETONITRILE: AN EXAMPLE OF NEUTRON SCATTERING FROM A ROTATIONALLY HINDERED METHYL GROUP

6.5.1 Introduction to Solid Acetonitrile

Acetonitrile, both liquid and crystalline, has attracted interest owing to its highly associated liquid structure and high symmetry, allowing molecular rotation in the crystal[347]. Solid acetonitrile exists in two phases, α-acetonitrile, stable below the transition temperature of 216.9K, and β-acetonitrile which is stable between this temperature and the melting point of 229K [347,348].++ The transformation between α- and β-acetonitrile has been followed by infra-red[349] and Raman[354] spectroscopy. Pure α-acetonitrile can be formed by annealing the solid at 210K for an hour. Metastable β-acetonitrile can be obtained pure at low temperatures either by vapour deposition onto a surface maintained at 77K, or by forming the solid at 222K and cooling in 15 minutes to 108K, the first 70K of cooling being accomplished in 5 minutes[349]. An X-ray powder diffraction pattern of α-acetonitrile indicated an orthorhombic structure with the molecules lined up antiparallel along the C-C≡N axis[347,349].

Both α- and β-acetonitrile have received extensive study by infra-red[349-352] and Raman[353,354] spectroscopy in the molecular vibration

---

++ The α and β phases are also confusingly referred to as Form II and Form I respectively. A high pressure γ form has been proposed from infra-red data[350], and there is a further change of slope in the heat capacity around 70K [348].

region. Whole molecule motions have been studied by Raman[354] and fourier transform infra-red[350,353] spectroscopy on the crystal and the matrix isolated molecule[355,356] at energies below 150 cm^{-1}. The deuterated molecule was also studied and modes were assigned as translational or librational, depending on the isotopic shift. The infra-red and Raman data on α- and β-acetonitrile for frequencies below 1000 cm^{-1} are listed in Table 6.4 .

6.5.2 Beryllium Filter Spectrum of Solid Acetonitrile

A beryllium filter spectrum of solid acetonitrile has been recorded by P.H. Gamlen[357]. The acetonitrile was supplied by BDH chemicals and was of GPR grade (98% pure by GLC, bp 80-82°C). The sample was cooled relatively quickly to 77K, and it is likely that a mixture of α- and β-acetonitrile was formed. The spectrum was run at AERE Harwell on the Pluto beryllium filter spectrometer[317,358], with a sampling step size

Fig 6.9 Beryllium Filter Spectrum of Solid Acetonitrile at 77K [ref 357]

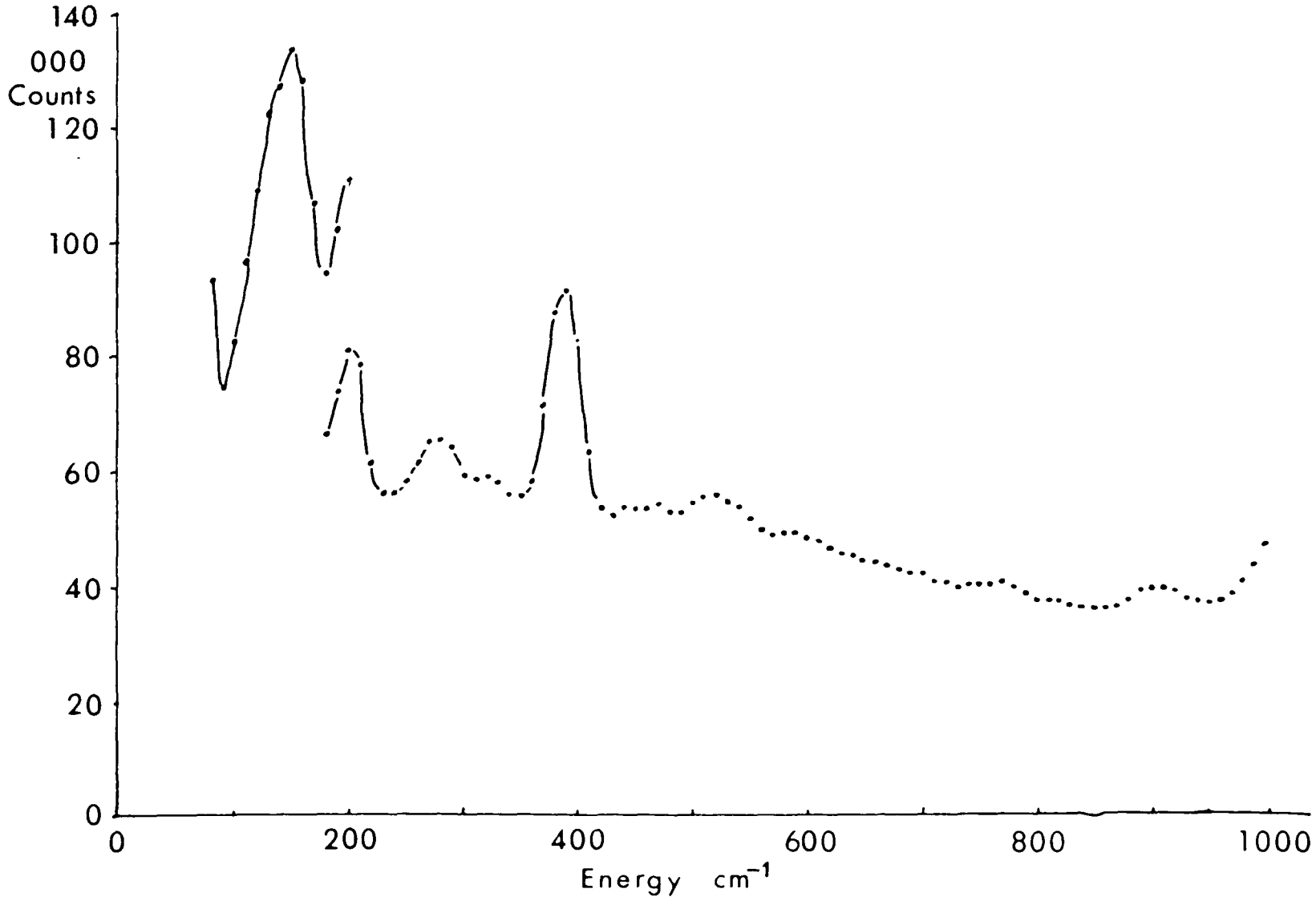

Table 6.4 Low frequency neutron, infra-red and Raman data on acetonitrile

(frequencies in cm^{-1})

Neutrons	Infra-red[350]		Raman[354]		Assignment
	α	β	α	β	
	50	50			T
				65 w	
			69 w	70 w	$T_{xy}(E)$
				75 vw	
			87 m	82 s	
			109 vs	80 sh	
?120 sh	87	73	117 vs	96 vs	$L_{xy}(E)$
			121 sh	103 m	
			131 m		
			134 sh		
?120 sh	119	116	145 vw	119 m	$T_z(A_1)$
			159 vs	137 vw	
140 vs	139	134		152 vw	L_z
190 s					L'_z
265 m					$2L_z$
310 w					
360 sh					$3L_z$, $2L'_z$
			383 vw	381 vw	
385 vs				386 m	$\nu_8(e)$
	392		391 s	392 sh	
	402		400 s	395 m	
430 vw					
460 vw					
517 w					$\nu_8 + L_z$
580 vvw					$\nu_8 + L'_z$
770 vw	780	769			$2\nu_8$
905 w	919	926	921 s	919 w	$\nu_4(A_1)$
				922 m	

w = weak, m = medium, s = strong, v = very, sh = shoulder

Intramolecular modes are represented by ν .

Whole molecule motions are represented by T for translational and L for librational modes. The subscipts xy and z refer to motion perpendicular and parallel to the C-C≡N axis. The coefficients eg $2L_z$ refer to the number of the excitation of that type. As the librations are considered as a hindered rotation, they are not harmonic.

of 10 cm^{-1} and a resolution of about 40 cm^{-1}. 25cm^{-1} has been subtracted from the incident neutron energies to correct for the beryllium filter. The cryostat background has been subtracted. The discontinuity at 180 cm^{-1} corresponds to a change in monochromator plane. The spectrum obtained is shown in Fig 6.9 with a list of observed peaks, together with assignments and infra-red and Raman data in Table 6.4.

6.5.3 Discussion: Peak Positions

In the molecular vibration region, the infra-red, Raman and neutron scattering results all correspond. The peaks at 385, 770, and 905 cm^{-1} can be assigned to ν_8(e) the C-C≡N bend, its first harmonic and ν_4 the C-C symmetric stretch respectively. Below 385 cm^{-1}, however, the infra-red, Raman and neutron scattering results are all different. This is not unexpected since the intensity of neutron peaks is governed by the amplitude of motion of the hydrogen atoms in the molecule, whereas the infra-red and Raman intensities are governed respectively by the molecular dipole moment and polarizability. Thus peaks which are weak in the infra-red and Raman spectra might be expected to show up strongly in the neutron spectrum. A secondary effect is that the momentum transfers vary widely between the methods, and dispersion may cause peak shifts between them.

One peak which might be expected to show up strongly in the neutron spectrum is the methyl group torsion L_z. This is best assigned to the peak at 140 cm^{-1}. The motion can be considered either as a harmonic oscillation or as a hindered rotation. Since the overtone occurs at 265 cm^{-1}, it is clear that there is considerable anharmonicity and the hindered rotor approach is better.## Assuming that V_3 dominates the

---

Gamlen[357] was concerned mainly with acetonitrile adsorbed on surfaces and merely considered the present system as a harmonic oscillator.

hindering potential, the splitting diagram can be replotted to show expected librational transition energies from the ground state directly in cm^{-1} as a function of V_3. This is done in Fig 6.10 which shows that L_z = 140 cm^{-1} gives V_3 = 42B. This site is called site A. The ground state is at -29B so the barrier to rotation is 72B or 400 cm^{-1}. Further transitions, mainly librational in character, are predicted at 264, 356 and 380 cm^{-1}. (Above this energy, the motion in the excited state is mainly rotational since the methyl group has enough energy to surmount the barrier.)

The line which is not predicted is the intense line at 190 cm^{-1}. This **could** be a harmonic of the L_{xy} libration observed at about 85 cm^{-1}, but this seems unlikely since the fundamental, which would be expected to be intense, is not observed. A possible explanation is that there is a second site with a different barrier to rotation, possibly in the other form of acetonitrile. These are called L_z' and site B respectively. A torsion at 190 cm^{-1} gives V_3 = 75B. The ground state is at -57B, giving a barrier to rotation of 132B or 734 cm^{-1} and predicting further librational lines at 364 and 524 cm^{-1}.

Using this two site model, the agreement between observed and theoretical data appears to be satisfactory. They are compared in Table 6.5 .

6.5.4 Neutron Line Intensities

As a further check on the assignment, the relative intensities of the torsional transitions were calculated. Since most of the motion in the two sites is librational, it was approximated to a harmonic oscillation and equations (6.9), (6.16) and (6.17) were used to calculate the intensities.

For a harmonic oscillation:

$$S(\mathbf{Q},\omega) = \exp\{-Q^2\langle u_Q^2\rangle\} \times I_n(Q^2\langle u_Q{}^2\rangle) \qquad (6.9)$$

Fig 6.10 **Expected Transition Energies from the Ground State as a function of Field Strength for a Methyl Group in 3-fold and 6-fold Hindering Potentials**

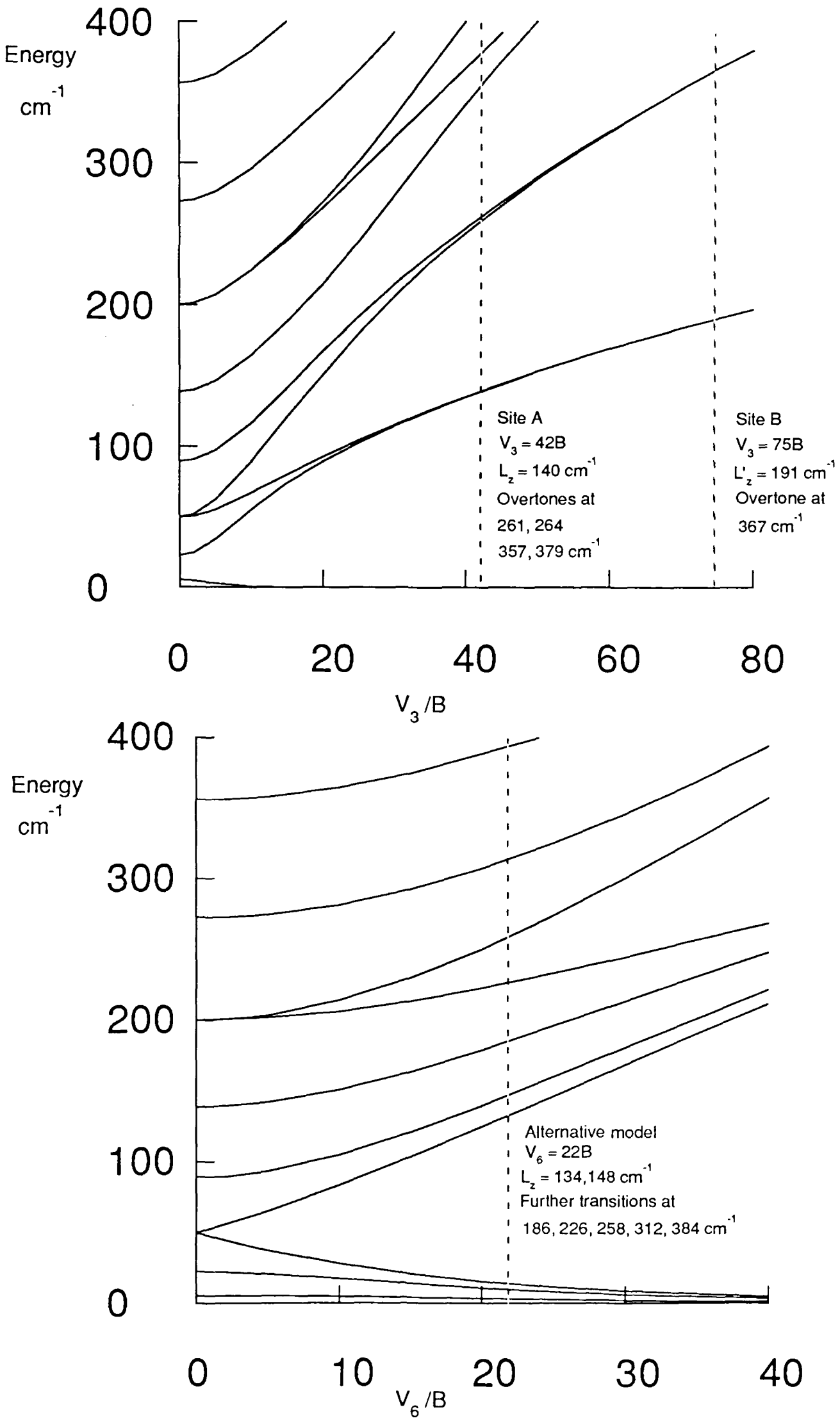

The dotted lines show the values of V_3 and V_6 required to give v = 0 to 1 transitions at 140 and 190 cm^{-1}

Table 6.5 Comparison of Observed and Calculated Torsional Frequencies

	Molecular modes		Site A torsions		Site B torsions	
$\bar{\nu}_{obs}$	mode	$\bar{\nu}_{calc}$	mode	$\bar{\nu}_{calc}$	mode	$\bar{\nu}_{calc}$
140 vs			L_z	140 (A+E)		
190 s					L'_z	191 (A+E)
265 m			$2L_z$	261 (A) 264 (E)		
310 m						
360 sh			3Lz	357 (E)	$2L'_z$	367 (A+E)
385 vs	ν_8		$3L_z$	379 (A)		
430 vw			$4L_z$	418 (A)		
460 vw			$4L_z$	463 (E)		
517 w	ν_8+L_z	525			$3L'_z$	523 (E) 526 (A)
580 vvw	$\nu_8+L'_z$	575				
					$4L'_z$	648 (A) 663 (E)
770 vw	$2\nu_8$	770				
905 w	ν_4					

Frequencies are in cm^{-1}.

ν_4 and ν_8 are molecular vibrations.

L_z and L'_z are the two proposed torsional fundamentals generated by threefold hindering potentials. For L_z, V_3 = 42B and the barrier to rotation is 72B or 400 cm^{-1}. For L'_z, V_3 = 75B and the barrier to rotation is 132B or 734 cm^{-1}. States near the top of the potential barrier have appreciable tunnelling splitting, and the symmetry species of each constituent line is shown.

Tunnelling:	Site A	0.000547 cm^{-1}	or 0.68 μeV
	Site B	0.000015 cm^{-1}	or 0.019 μeV

For site A $\langle u_Q^2 \rangle$ was calculated to be 0.05977 A^2 and for site B it was 0.04104 A^2. Values of $\langle u_Q^2 \rangle$ and $S(\mathbf{Q},\omega)$ were now calculated for all overtones of both torsions where $\bar{\nu}_{obs}$ was less than the barrier height. Allowance for the anharmonicity was made by taking $\bar{\nu}_{obs}$ and hence Q^2 from the mean peak position in the hindered rotor approximation, $\bar{\nu}_{av}$, rather than an exact multiple of the fundamental, $\bar{\nu}_{harm}$. In the calculation of $\bar{\nu}_{av}$, a statistical weight of 2 is given to E states and 1 to A states.

The calculated intensities were now normalized such that the peak at 140 cm^{-1} had intensity 1000. By Simpson's rule on the raw figures, it was found that the observed peak at 190 cm^{-1} had relative intensity 385 with $S(\mathbf{Q},\omega)$ nearly the same for the 140 cm^{-1} peak. The site B peaks were

Fig 6.11 Calculated and observed Beryllium Filter Spectrum of Solid Acetonitrile

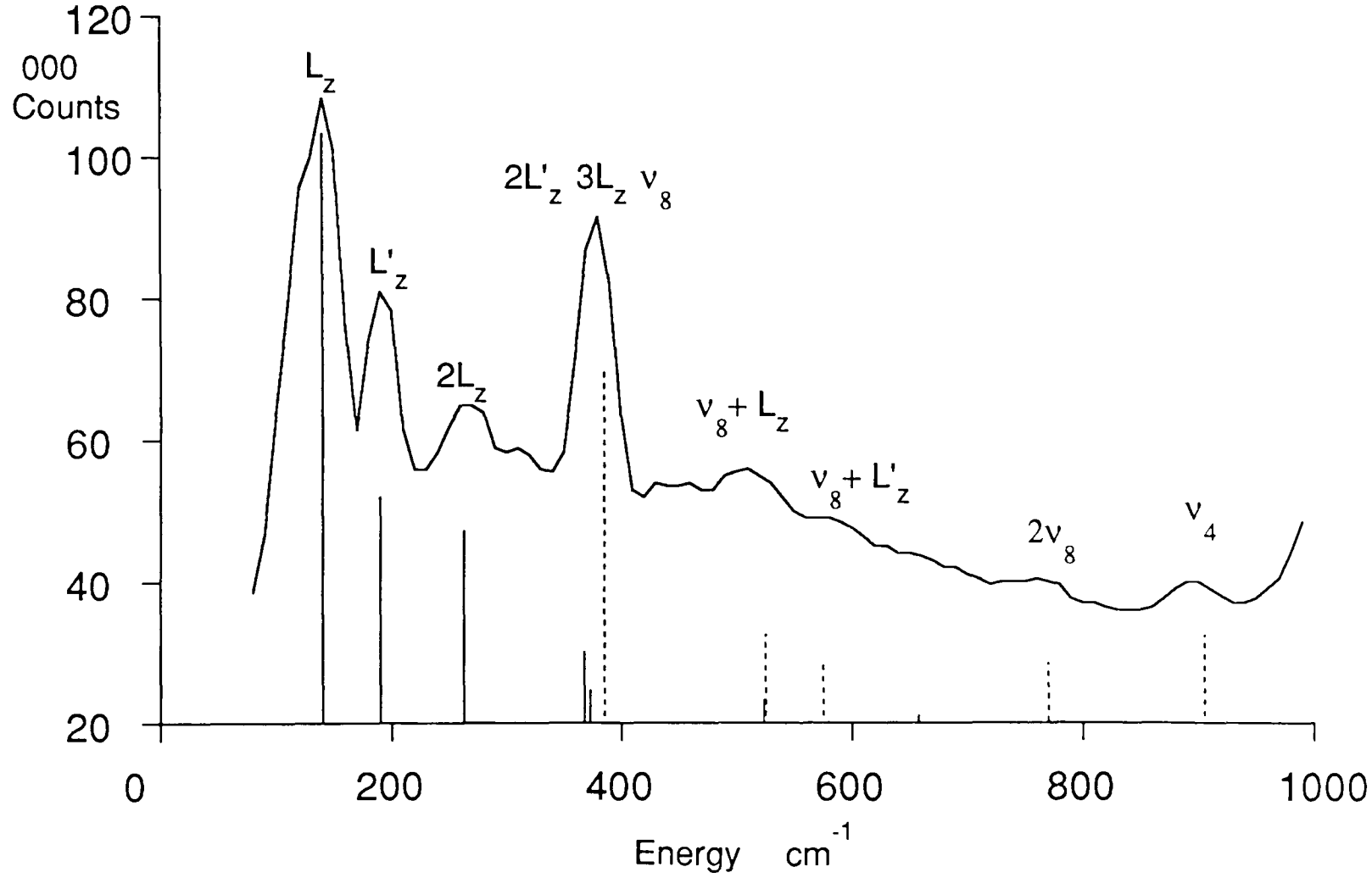

Methyl group torsions are shown in solid lines, with internal and combination modes represented by dotted lines of arbitrary intensity. The intensity ratio of the L_z to L'_z lines has been fixed empirically, and the change of monochromator plane in the observed spectrum has been scaled out.

Table 6.6 Neutron Scattering Intensities calculated for Acetonitrile on a Threefold Hindered Rotor Model

	Molecular transitions	Site A	Site B			Site A						Site B				
$\bar{\nu}_{obs}$		$\bar{\nu}_{rotor}$	$\bar{\nu}_{rotor}$	n	($\bar{\nu}_{harm}$)	$\bar{\nu}_{av}$	Q^2	$S(Q,\omega)$	Int	n	($\bar{\nu}_{harm}$)	$\bar{\nu}_{av}$	Q^2	$S(Q,\omega)$	Int
140 vs		140(E+A)		1	(140)	140	11.32	0.183	1000						
190 s			191(E+A)							1	(190)	190	14.3	0.183	385
265 m		261(A) 264(E)		2	(280)	263	18.7	0.0590	326						
310 w															
360 sh		357(E) 379(A)	367(A+E)	3	(420)	372	25.2	0.0101	56	2	(380)	367	24.9	0.0565	120
385 vs	ν_8		Onset of free rotation (400 cm^{-1})												
430 vw															
460 vw															
517 w	ν_8+L_z		523(E) 526(A)							3	(570)	524	34.3	0.0183	39
580 vvw	$\nu_8+L'_z$														
			648(A) 663(E)							4	(760)	658	42.3	0.00582	12
770 wv	$2\nu_8$										Onset of free rotation (735 cm^{-1})				
905 w	ν_4														

Frequencies in cm^{-1}. Scattering lengths not included in these calculations.

thus normalized with the 190 cm^{-1} peak having intensity 385. The results are shown in Table 6.6 and plotted in the form of a stick diagram against the observed frequency in Fig 6.11.

The calculated intensities are not inconsistent with the observed values. The value of the comparison is, however, limited by the fact that the internal modes were not included. To do this, a full **FG** matrix calculation of the force constants[377-379] would have to be undertaken.

The barriers to rotation calculated in this model of 400 and 734 cm^{-1} are comparable to, though somewhat lower than the value of 2.1 Kcal/mol (900 cm^{-1}) derived from T_1 measurements using NMR [359]. By contrast, in a more recent study of the liquid state, it was found to be only 0.8 Kcal/mol [360]. Further confirmation could be obtained from tunnelling data (see below).

6.5.5 An Alternative Model: the Sixfold Barrier

For comparison purposes, the energy levels of a sixfold hindered rotor were also replotted (Fig 6.10). It can be seen that for a fundamental at 140 cm^{-1}, V_6 must be lower at 22B or 122 cm^{-1}. The ground state is at -5.9B, giving a barrier to rotation of 27.9B or 155 cm^{-1}. In this model, therefore, the transitions are much closer to free rotations. The formula for a transition from a librational ground state to a more or less freely rotating excited state is unclear and intensity calculations were not attempted. The model could, however, be tested by examining the tunnelling neutron spectrum, since in the threefold model, a single tunnelling transition of 0.7 μeV is predicted, whereas the sixfold model predicts three tunnelling states 2.90, 9.61 and 13.61 cm^{-1} above the ground state (360, 1190 and 1690 μeV).

CHAPTER 7

INELASTIC NEUTRON SCATTERING FROM HYDROGEN IN $C_{24}Rb(H_2)_x$ and $C_{24}Cs(H_2)_x$

INTRODUCTION

In 1980 Beaufils et al[361] observed rotational tunnelling of hydrogen absorbed by the stage II graphite intercalates $C_{24}Rb$ and $C_{24}Cs$ in the energy region 0.5 to 1.3 meV. The rotational constant B for the hydrogen molecule is 7.36 meV [121] and it was decided to try to observe the librations corresponding to the tunnelling transitions, since these would be expected to be in the region 15 to 100 meV and hence accessible to beryllium filter spectroscopy. The inelastic incoherent neutron scattering studies complement earlier and continuing X-ray and neutron diffraction work since, unlike diffraction methods, they probe the short range order in the sample and give information about the dynamics of the hydrogen molecule. These experiments are unsuited to optical methods since the intercalates are metallic and the hydrogen molecule has no dipole moment. Conversely, the large incoherent neutron cross-section and the large vibrational amplitudes are ideally suited to neutron work.

7.1 SAMPLE PREPARATION

Powder samples of stage II caesium and rubidium intercalates were prepared by direct combination of stoichiometric quantities of the elements. The stoichiometries were generally taken as $C_{28}Cs$ and $C_{28}Rb$ so that 2.52 and 3.93g of graphite were used per gram of caesium and rubidium respectively. Other stoichiometries are noted on individual spectra; samples prepared $C_{26}M$ looked pure, but a stoichiometry of $C_{24}M$ gave visible flecks of golden stage I compound.

Natural graphite ground to 30 mesh was outgassed overnight at 250°C at 10^{-4} torr in a pyrex sample tube with a breakseal (Fig 7.1). After cooling, it was let up to white spot nitrogen (99.98%), and a 1g ampoule of caesium (99.98%) or rubidium (99.9%) was broken and immediately

Fig 7.1 Preparation of Intercalate Samples

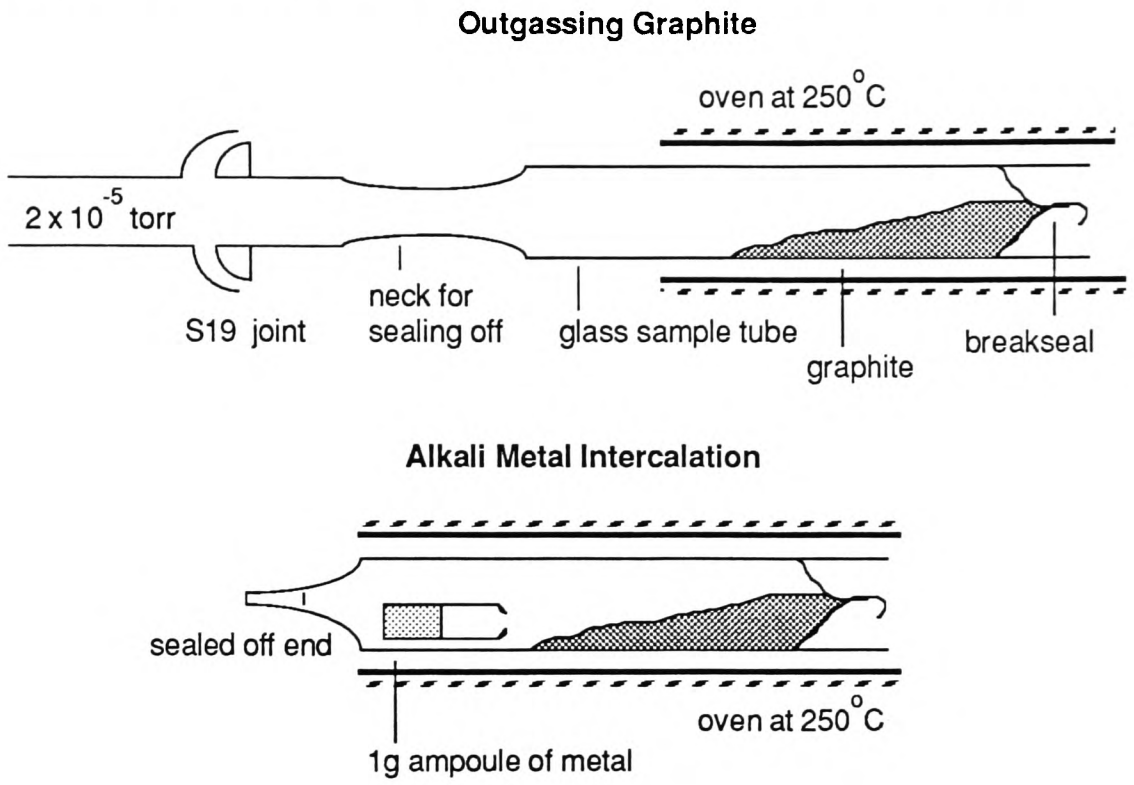

introduced into the tube.[+] This could be done either in a large glove bag or, given speed and confidence, in the air without excessive oxidation of the metal. Caesium melts at 29°C, so the ampoules were precooled over solid carbon dioxide. The sample with the ampoule was pumped again to 2×10^{-5} torr and sealed off from the pumping line under vacuum. When cool, the sealed-off end was reinforced with Araldite to avoid cracking. Next, the sample was intercalated at 250°C for 48 hours, keeping the Araldited tip cool. The graphite swelled on intercalation and needed to be spread out along the tube; it also helped to take the sample out and shake it occasionally. When the sample had a uniform dark blue colour, intercalation was assumed to be complete.

The intercalate samples were taken to the site of the experiment and transferred in a nitrogen filled glove bag into an evacuated 1cm internal diameter aluminium centre stick with a stainless steel top.

+ In earlier work[362], the ampoule was placed in an unheated part of the sample tube before outgassing and broken with a magnetic slug after sealing off. This is safer and avoids letting the outgassed graphite up to nitrogen and atmospheric oxidation of the metal, but mixes the slug and broken glass with the sample.

This was modified for gas handling by attaching a temperature sensor, Leybold vacuum fittings, a glass 1 litre gas storage bulb and a 0-1 bar digital pressure gauge (Fig 7.2). The system was pumped to 2×10^{-5} torr, then the bulb was filled with hydrogen to ≈400 torr, excess hydrogen in the stick being pumped away. Next, the centre stick volume was calculated by expansion of the hydrogen from the bulb into the stick and the sample purity was quickly checked by placing the intercalate sample in the end of the centre stick into a dewar of liquid nitrogen and noting the drop in pressure. (A stoichiometry of $C_{24}M(H_2)_2$ represents 256 or 398 torr litres of hydrogen at room temperature for a sample made with 1g Cs or Rb respectively. Typical quick absorptions were 80% of this, although samples would sometimes continue to absorb hydrogen slowly.) The sample was then warmed to room temperature and the stick evacuated, leaving enough hydrogen in the bulb to give the desired stoichiometry.

Most spectra were recorded in a liquid helium cryostat with single samples in 1 cm diameter sticks. This gave a sample 3.5-5 cm high with ≈20% scattering at full hydrogen absorption. Larger sticks have an indium seal at the sample can which is liable to leak, and gas absorption tends to be slow. A background intercalate spectrum was measured first and the gas absorbed in situ. This made it necessary to warm the sample to 100K before letting the gas onto the sample to ensure even absorption.

7.2 TUNNELLING EXPERIMENTS

The tunnelling experiments, originated by Beaufils et al[361], were continued by I.P. Jackson and W.J. Stead, and a full account will be given elsewhere[363]. Some representative spectra are shown here in reference to the predictions of tunnelling made from the librational assignments.

Fig 7.2 The Centre-stick for Neutron Scattering Experiments
(as used in Harwell Beryllium Filter experiments)

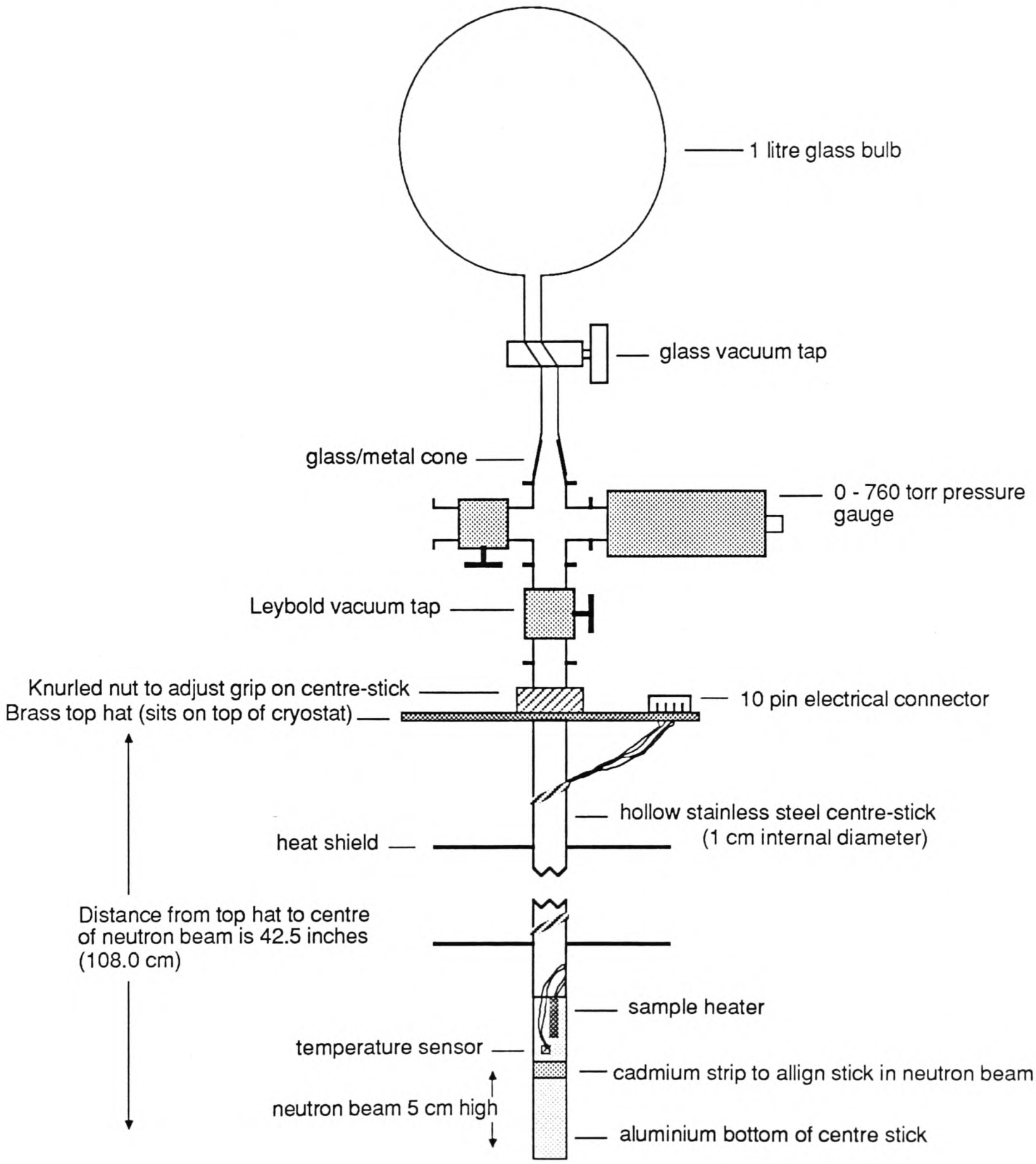

Transfer of a sample into the centre-stick using a glove bag

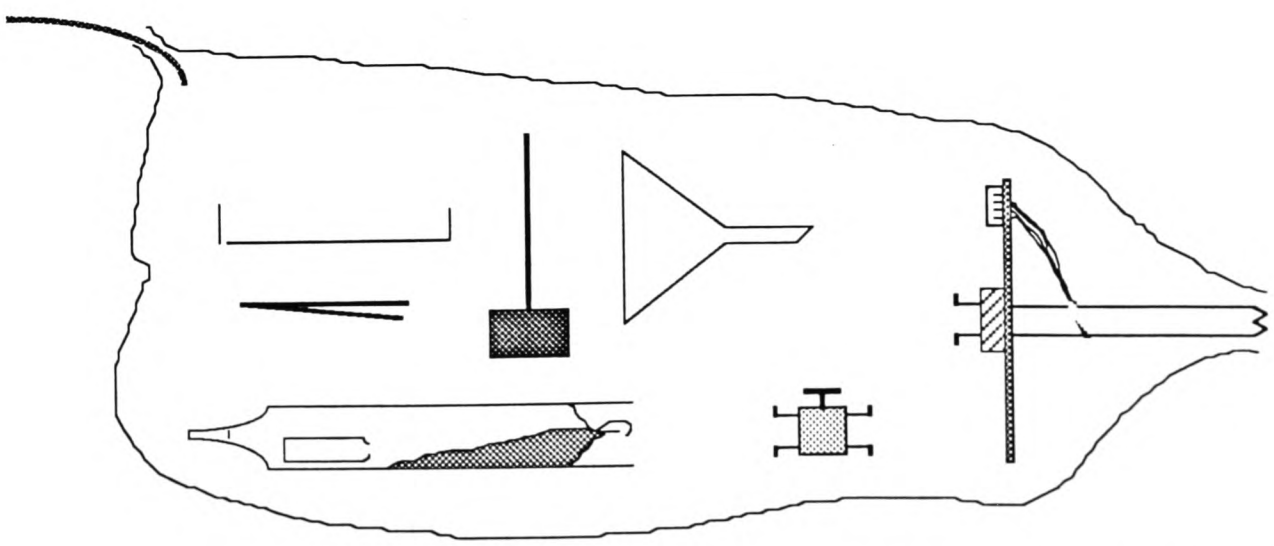

Also shown are various useful bits of equipment: a small funnel, a petri dish, a pair of tweezers and a heavy metal object

7.2.1 Instrumentation

The tunnelling spectra were measured on the multichopper time of flight spectrometers IN5 and IN6 at the ILL. These instruments have already been described[364,365], and the resulting spectra have a strong central elastic peak with weak peaks on either side, where the neutron has gained or lost energy. (Conversion from time of flight to energy transfer was done during the experiment by the PDP 11/34 minicomputer controlling the instrument.) The incident neutron wavelength used in the IN5 experiments was 8A giving a resolution of 40 μeV, and that on IN6 was 5.1A, giving a resolution of 80 μeV. The lower resolution on IN6 was, however, more than compensated for by the much higher neutron flux. On this type of instrument, large energy transfers are only seen on the neutron energy gain side and these are limited by the sample temperature, usually a nominal 4K, to around 4 meV. Experiments were started with a vanadium scan to check counter efficiencies. The intercalate background proved to be very low and flat under most conditions (Fig 7.3). This, coupled with difficulties in subtraction owing to slight shifts in the elastic peak from small movements of the centre stick in the cryostat, in spite of the use of spacers, have meant that unsubtracted spectra have sometimes had to be used. Intercalate backgrounds were, however, always measured. Runs on IN5 took 6-12 hours and those on IN6 took 2-6 hours, depending on the amount of hydrogen in the sample.

7.2.2 $C_{24}Rb(H_2)_x$

The tunnelling spectrum of $C_{24}Rb(H_2)_x$ was measured as a function of H_2 filling in a single set of experiments on IN5, the hydrogen being absorbed in situ (Fig 7.3). The wavelength used was 7.84A and the sample temperature during runs was 5K throughout. The flatness of the background is confirmed by the spectrum of $C_{24}Rb$. Hydrogen

stoichiometries are based on a saturation filling of $(H_2)_2$ in the cryostat; this is 85% of the value expected on the basis of the metal content. (In the laboratory at 77K, only 63% of the expected hydrogen was absorbed.)

At low fillings, a single peak at 1.4 meV grows in intensity without changing position. At composition $C_{24}Rb(H_2)_1$, a second peak at 0.7 meV appears and grows similarly. Both peaks are approximately Gaussian in shape and broad compared with the elastic peak. At fillings above $(H_2)_{1.2}$, the peaks become distorted and show a tendency to shift inwards with a suggestion of multiple unresolved peaks. Finally, at saturation filling, a totally new peak appears at 2.05 meV. Peak positions and intensities are listed in Table 7.1 and the intensities of the peaks at 1.2-1.4 and 0.6-0.7 meV are plotted as a function of filling in Fig 7.4.

Both peaks increase **linearly** with filling, with intercepts of zero intensity at fillings $(H_2)_{0.08}$ and $(H_2)_{0.81}$ respectively. Furthermore, the peak at ≈1.4 meV continues to grow after the peak at ≈0.7 meV has started to appear. These results are consistent with the two site model suggested by earlier results, but there appear to be complications at higher fillings. (Beaufils et al[361] named the site responsible for the excitation at ≈1.4 meV "Site A", and the one responsible for the ≈0.7 meV excitation "Site B". This convention is continued here.) Resolution of the overlapping peaks would require detailed peak shape analysis, which is currently in progress[363].

7.2.3 $C_{24}Rb(HD)_x$ and $C_{24}Rb(D_2)_2$

These spectra have only been measured for the half-filled and completely filled compounds. The spectrum of $C_{24}Rb(HD)_1$ shown in Fig 7.3 has already been published[361], and is included for the sake of completeness. The lack of peaks at 0.7 and 1.4 meV confirms that no significant equilibration to H_2 + D_2 has taken place. The subtracted

Fig 7.3 Tunnelling Spectrum of $C_{24}Rb(H_2)_x$ at 5K as a function of increasing Hydrogen concentration

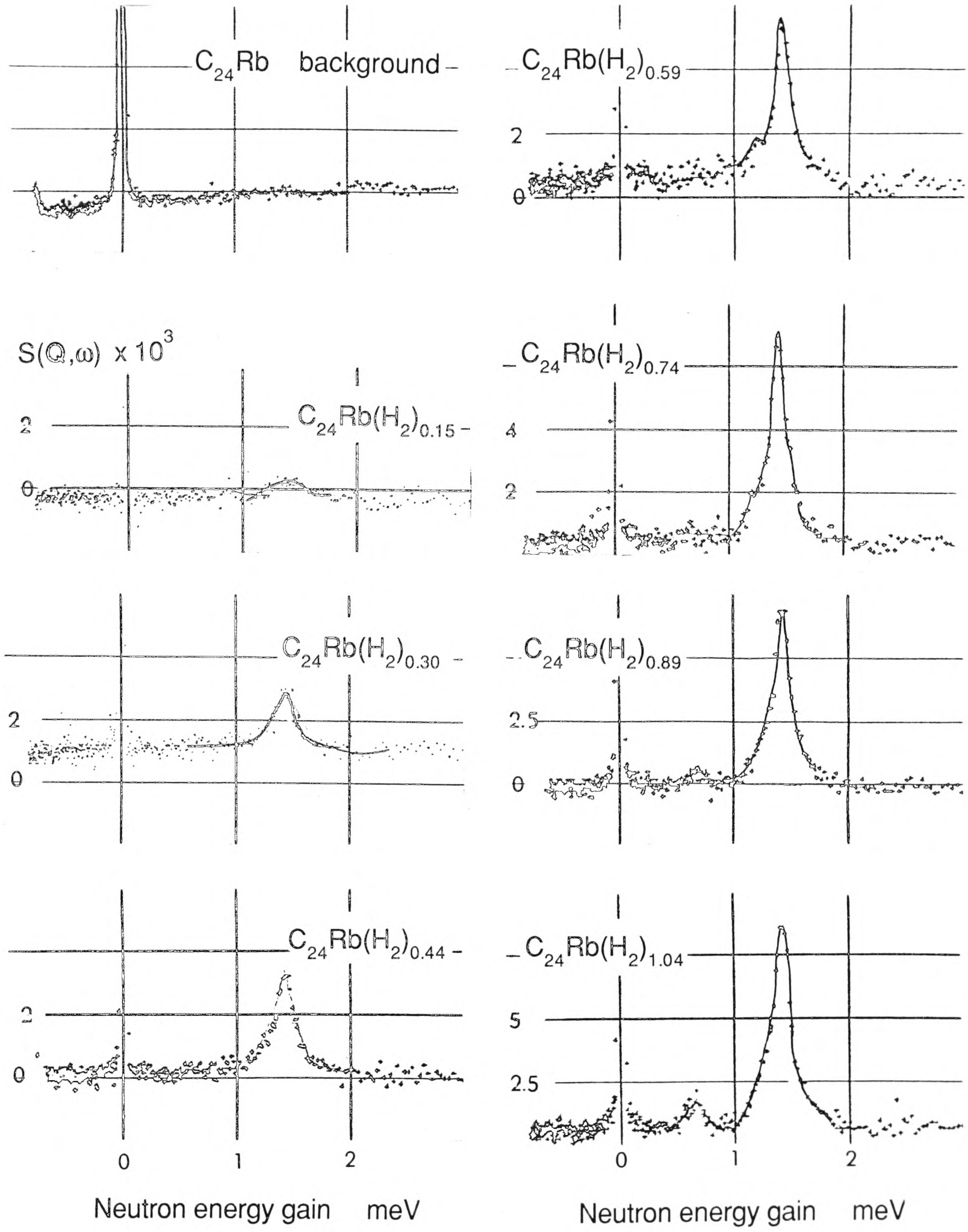

Note the changes in y scale. The lines are drawn as a guide to the eye only.

Fig 7.3(cont'd) Tunnelling Spectrum of $C_{24}Rb(H_2)_x$ at 5K as a function of increasing Hydrogen concentration

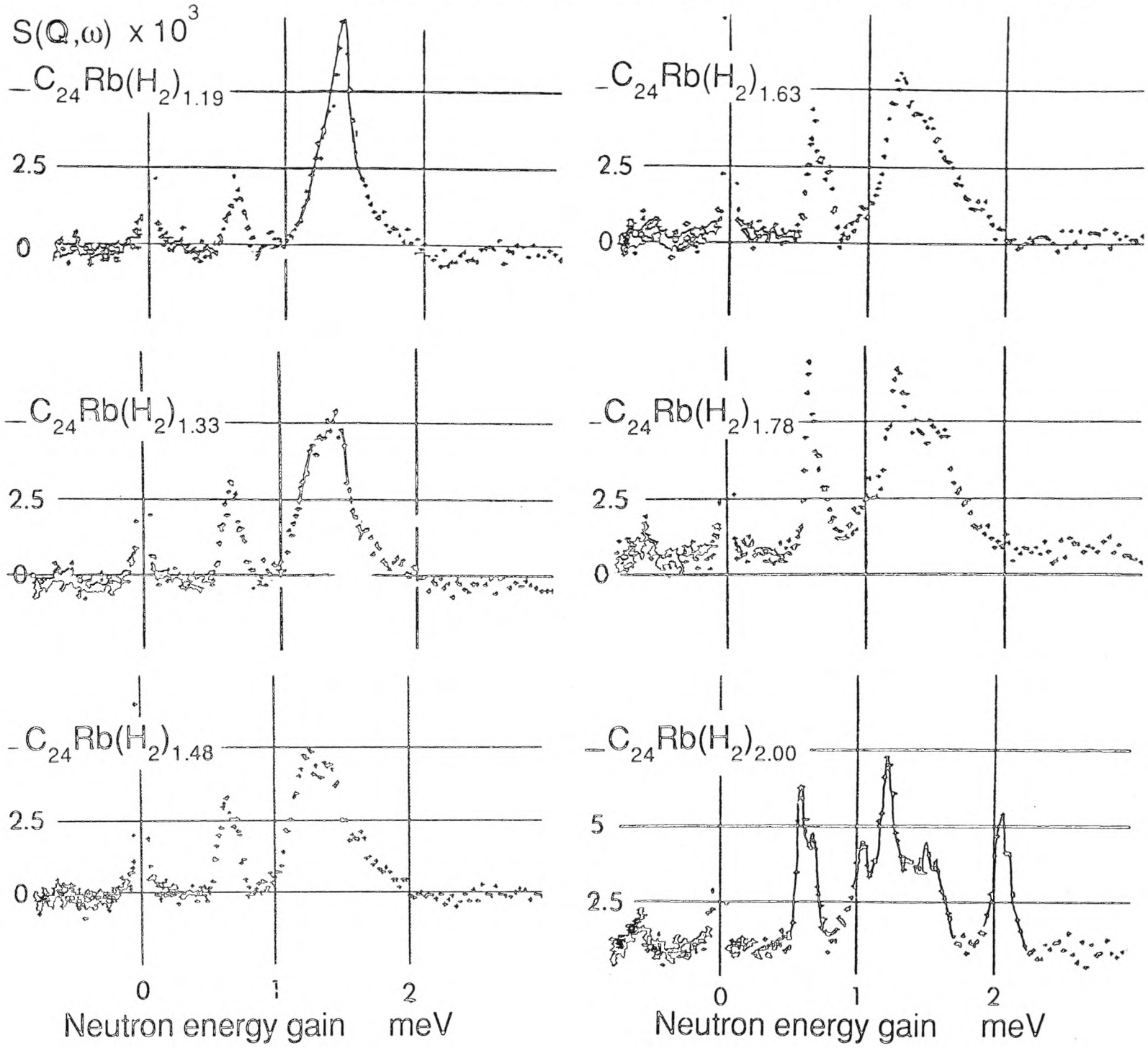

Tunnelling Spectra of $C_{24}Rb(HD)_1$ [ref 361] and $C_{24}Rb(D_2)_2$

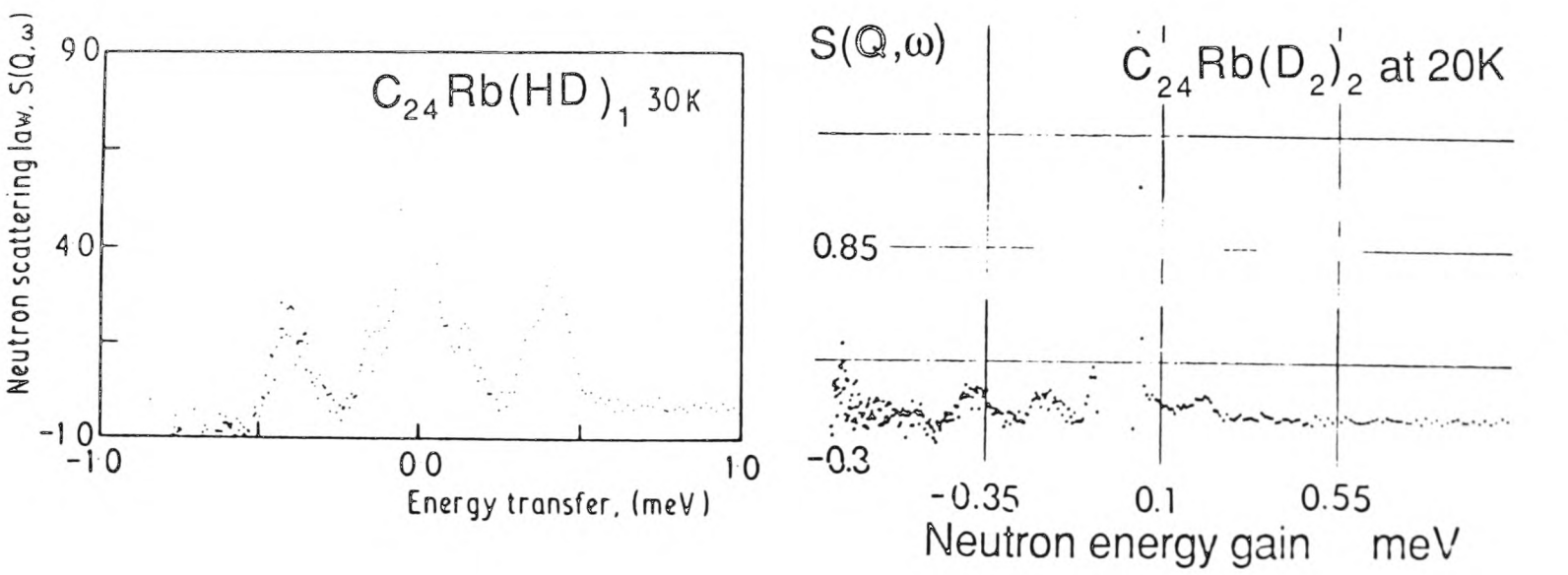

Both Stokes and anti-Stokes lines can be seen. The line at -0.35 meV in the spectrum of $C_{24}Rb(D_2)_2$ is an artifact. $S(\mathbf{Q},\omega)$ values in these plots are not comparable with previous spectra. Note the much weaker scattering from and the lower tunnelling energy of the deuterium atom.

Table 7.1 Tunnelling data for $C_{24}Rb(H_2)_x$: Approximate Peak Positions and Relative Areas

H_2 Filling	meV	Area	meV	Area	meV	Area
0.15			1.4	0.12		
0.30			1.42	0.36		
0.44			1.42	0.60		
0.59			1.42	0.86		
0.74			1.42	1.04		
0.89	0.67	0.07	1.42	1.31		
1.04	0.62	0.19	1.42	1.52		
1.19	0.63	0.32	1.42	1.65		
1.33	0.64	0.51	1.38	1.9		
1.48	w 0.63 s 0.71	0.61	s 1.23 s 1.4 w 1.6	1.95		
1.63	s 0.60 w 0.72	0.74	s 1.23 w 1.4	2.48		
1.78	vs 0.60 0.72	0.69	1.00 s 1.25 1.40 1.60	2.84		
2.00	0.60 0.70	0.50 0.39	1.05 1.22 1.50	0.54 1.07 0.67	2.05	0.64

Areas are FWHM in meV times height in $S(\mathbf{Q},\omega)$ units times 10^3. (These quantities were measured from printed spectra.) Multiple peaks at high fillings have been grouped with only qualitative evaluation of the area of each constituent peak.

Tunnelling data for $C_{24}Rb(HD)_x$ and $C_{24}Rb(D_2)_2$

Sample	Peak positions meV		
$C_{24}Rb(HD)_1$ 30K [361]			0.418
$C_{24}Rb(HD)_2$ 30K [361]	0.138	0.218	0.345
$C_{26}Rb(D_2)_2$ 20K	0.21		

Fig 7.4 Intensities of $C_{24}Rb(H_2)_x$ tunnelling peaks as a function of x

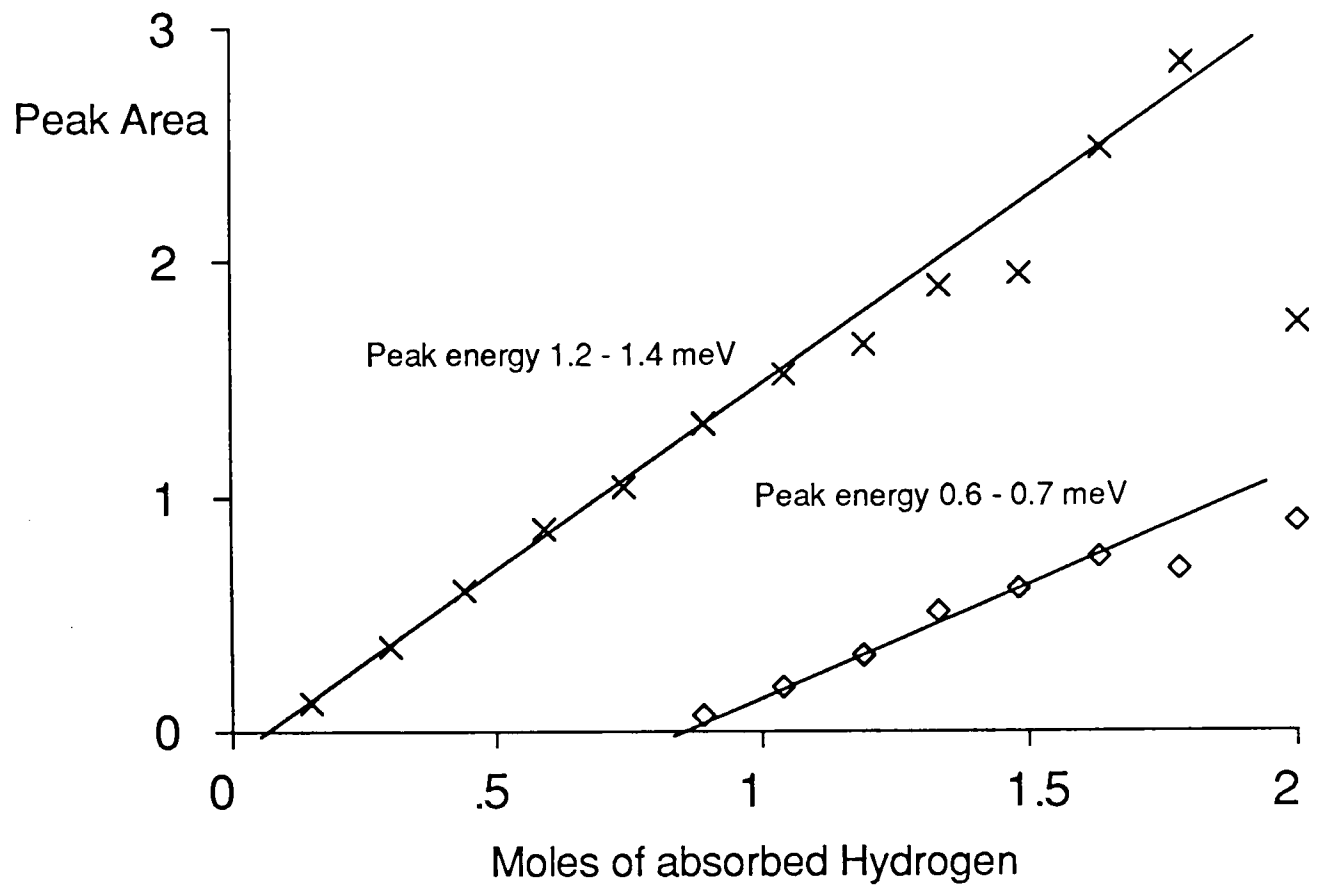

Both peaks increase linearly with hydrogen absorption with intercepts at x = 0.08 and 0.81 respectively. The peak at ≈1.4 meV continues to increase after the second peak at ≈0.7 meV has appeared.

spectrum of $C_{26}Rb(D_2)_2$ was measured on IN5 in 1982, using an extra large sample containing 6.3g Rb metal and a 6 litre gas bulb, to allow for the much weaker scattering by the deuterium atoms. Tunnelling energies are, as expected, lower than for hydrogen containing samples, and are listed in Table 7.1.

7.2.4 $C_{24}Cs(H_2)_1$, $C_{24}Cs(H_2)_2$ and $C_{24}Cs(N_2)_1(H_2)_1$

These spectra have been measured on IN6 between 1980 and 1984. The spectrum of $C_{24}Cs(H_2)_1$ at 100K shows a strong line at 1.2 meV, with a further weak excitation at 2.15 meV. $C_{26}Cs(H_2)_2$ at 4K shows lines at 0.67 and 1.0 meV. In the case of $C_{28}Cs(N_2)_1(H_2)_1$ at 1.5K, the nitrogen was absorbed first, then the hydrogen was absorbed to saturation; this shows peaks at 0.64 and 0.86 meV, with a further possible weak excitation at 0.37 meV. With the exception of the 2.15 meV peak, which is believed to be a hot band[366], this is consistent with the two site model, the excitation at 1.0-1.2 meV corresponding to the A site peak at

1.2-1.4 meV in $C_{24}Rb(H_2)_x$ and the B site peak constant at 0.67 meV. The tendency for the A site peak to decrease in energy with increasing hydrogen concentration, seen in $C_{24}Rb(H_2)_x$ is also seen with $C_{24}Cs(H_2)_x$. This tendency appears to be increased if a mixture of hydrogen and nitrogen is used. (Spectra of $C_{24}Cs(H_2)_x$ over the full range of partial fillings have been measured by Jackson[363].)

Fig 7.5 Tunnelling data for Caesium Intercalates

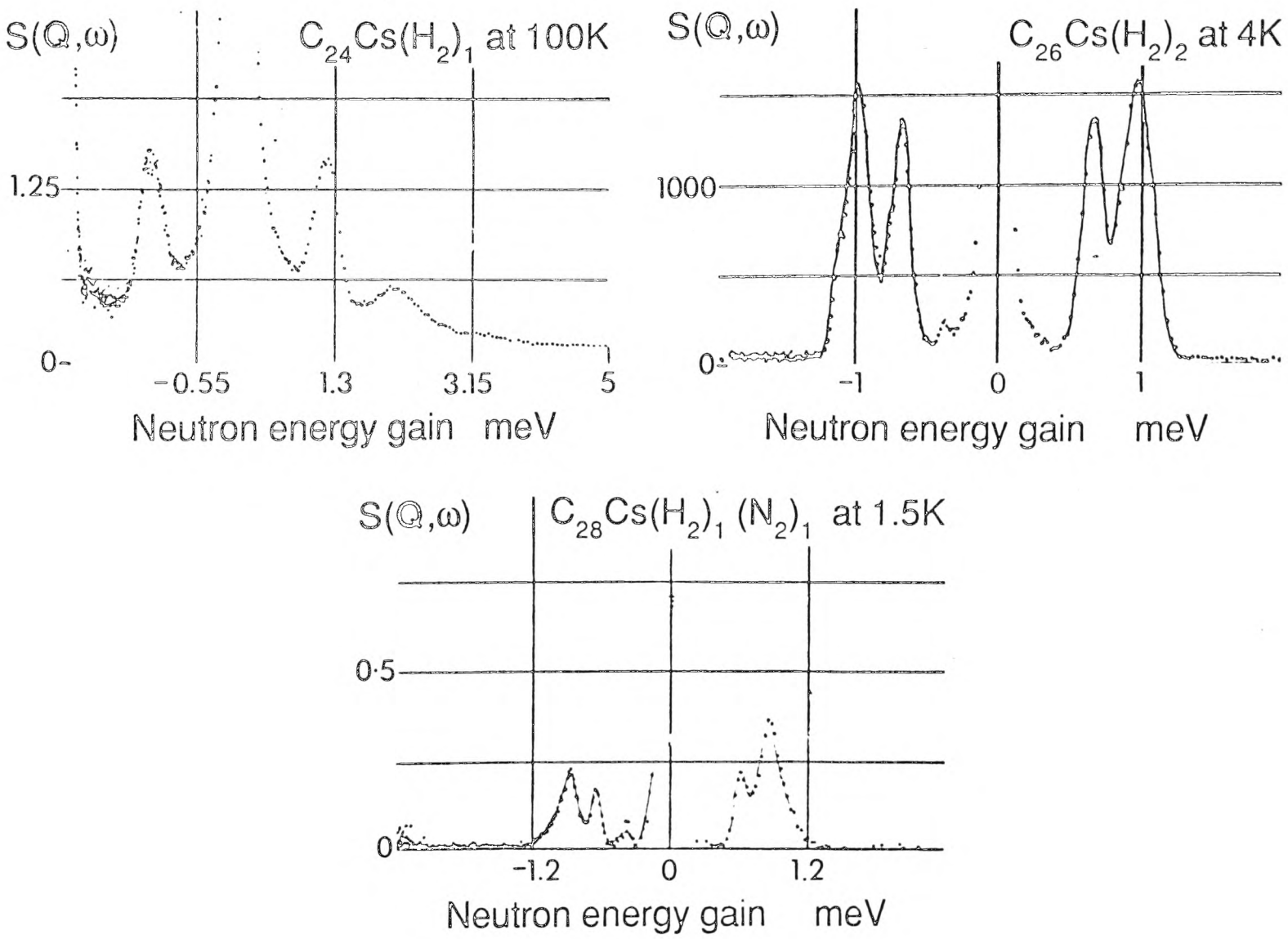

S(**Q**,ω) values are not comparable between spectra.

Sample	Peak positions meV			
$C_{24}Cs(H_2)_1$ 100K			s 1.20	w 2.14
$C_{24}Cs(H_2)_2$ 4K		m 0.67	s 0.99	
$C_{24}Cs(N_2)_1(H_2)_1$ 1.5K	vw 0.37	m 0.62	s 0.88	

7.3 LIBRATIONAL EXPERIMENTS

7.3.1 Instrumentation

Most of the librational spectra were recorded on the DIDO beryllium filter spectrometer at AERE Harwell[317,358]. The incident neutron beam from a thermal source is monochromated by diffraction from a single crystal of aluminium at 77K, and scattered by the sample. The scattered neutrons are filtered by a block of polycrystalline beryllium at 77K in front of the $^{10}BF_3$ detectors which are situated at right angles to the incident beam. The beryllium filter only allows through neutrons with energies less than 5 meV; the only neutrons with this energy are those which have been inelastically scattered with energy transfer slightly less than the incident energy. The incident energy is scanned by varying the angle of diffraction from the monochromator, and the result is a low resolution energy spectrum. Momentum resolution is not possible in this type of machine because the scattered neutrons have very low momentum, and hence the momentum transfer is nearly independent of scattering angle.

On the Harwell machine, the operating range for the Al 111 plane is 12-120 meV incident energy, with maximum flux at 42 meV and a resolution FWHM of 6 meV. Energy transfers average to 3 meV less than the incident energy[357]. Higher order planes can be used to reach 200 meV, but the flux falls off sharply with increasing energy. Spectra were recorded from 12 to 120 meV incident energy in 1 meV steps at constant monitor (ie constant total incident neutron flux) at sample temperatures between 10 and 80K. The machine background is high with small peaks, and the constant monitor scan, with its uneven scanning speed, causes it to rise at high energies. Raw data from a single $C_{28}Cs$ sample with and without absorbed hydrogen are shown in Fig 7.6, and it can be seen that while the hydrogen peaks are large compared with the background peaks, a good

Fig 7.6 Unsubtracted Intercalate and background spectra measured on the Harwell machine

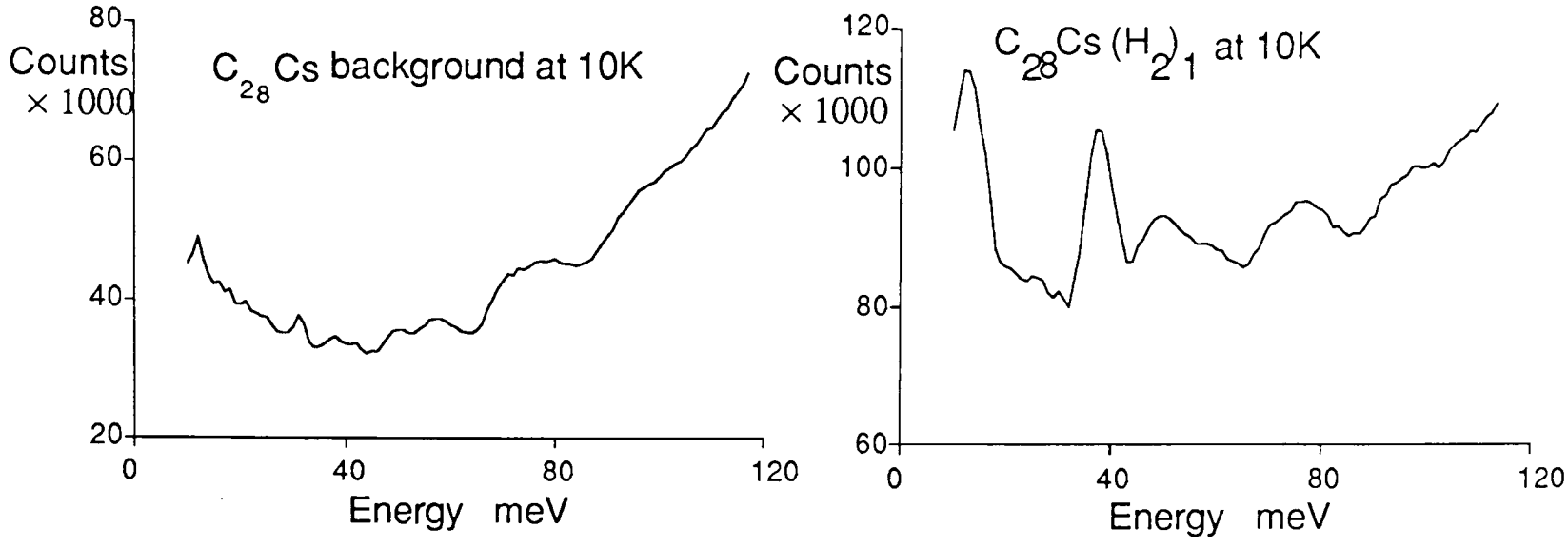

See Fig 7.7 for subtracted spectrum from same data. 3 meV filter correction was applied.

background subtraction is essential for accurate work. For this reason, all subsequent spectra have had the intercalate background and the 3 meV filter correction subtracted. A single scan over the entire energy range took 24 to 48 hours.

The spectrum of $C_{24}Cs(H_2)_2$ was also recorded on the rebuilt IN1B beryllium filter spectrometer at the ILL. This machine uses a hot neutron source, which allows higher incident energies to be used; the best energy range is 6.8 to 50 THz with a maximum flux at 20 THz (1THz is 4.14 meV). The monochromator is a series of copper plates formed into a block, which can be curved so as to focus the incident beam on the sample; in this experiment the 220 plane was used. IN1B uses a single beryllium filter and a single ^3He detector at right angles to the incident beam. This may appear inefficient compared with the Harwell machine which has two filters and 16 detectors, but the source is much more intense and counting times were 90 seconds or less per point, compared with six minutes at Harwell. The scans were recorded from 6.8 to 50 THz in 0.2/0.3 THz steps. The machine background is very low so that good statistics are obtained with fewer neutrons counted than on the Harwell machine. The intercalate background was measured and subtracted from the spectra and the filter correction applied.

As this was the first non-ILL experiment on the rebuilt machine, some problems were experienced with its operation: monochromator planes besides Cu 220 had not been calibrated, the computing was rudimentary, and at high energies the controlling motors had to be driven manually. In addition, only two days were available to study both the hydrogen librations and the high energy molecular vibration. While the preliminary results are promising, it is expected that future experiments will be able to make better use of the instrument.

7.3.2 $C_{24}Cs(H_2)_1$ and $C_{24}Cs(H_2)_2$

The spectra of $C_{24}Cs(H_2)_1$ and $C_{24}Cs(H_2)_2$ at 4-10K and 77-80K are shown in Fig 7.7, with peak positions in Table 7.2. The high temperature spectrum of $C_{24}Cs(H_2)_1$ shows two intense lines at 13 and 37 meV, whereas the low temperature spectrum is more complex with lines at higher energies. It is believed that the difference between the two spectra is a result of contamination of the low temperature sample by $C_{24}Cs(H_2)_2$ owing to non-equilibration of the sample in the cryostat, rather than a genuine temperature effect. There are several reasons for this: first, the sample at 80K would be able to equilibrate during the scan, whereas the hydrogen absorbed by the sample would be immobile at 10K. Second, the low temperature spectrum resembles the spectra of $C_{24}Cs(H_2)_2$, which is easier to prepare. Third, the high temperature spectrum agrees with the $C_{24}Cs(H_2)_1(N_2)_x$ results and fourth, the hydrogen for the low temperature scan was admitted at 60K, followed by immediate cooling.

In $C_{24}Cs(H_2)_2$, the peaks have been shifted to 18 and 35 meV, with new excitations at 51 and 71 meV. The IN1B spectrum of $C_{24}Cs(H_2)_2$ at 4K shows a similar pattern to the high temperature spectrum, but with considerable enhancement, although it shows a tendency to "fade out" at high energies, as expected from the recoil calculations. The spectrum also shows an interesting sharpening with time; this might be caused by ortho to para conversion.

Fig 7.7 Beryllium Filter Spectra of $C_{24}Cs(H_2)_1$ and $C_{24}Cs(H_2)_2$

(Intercalate background and 3 meV filter correction subtracted throughout.)

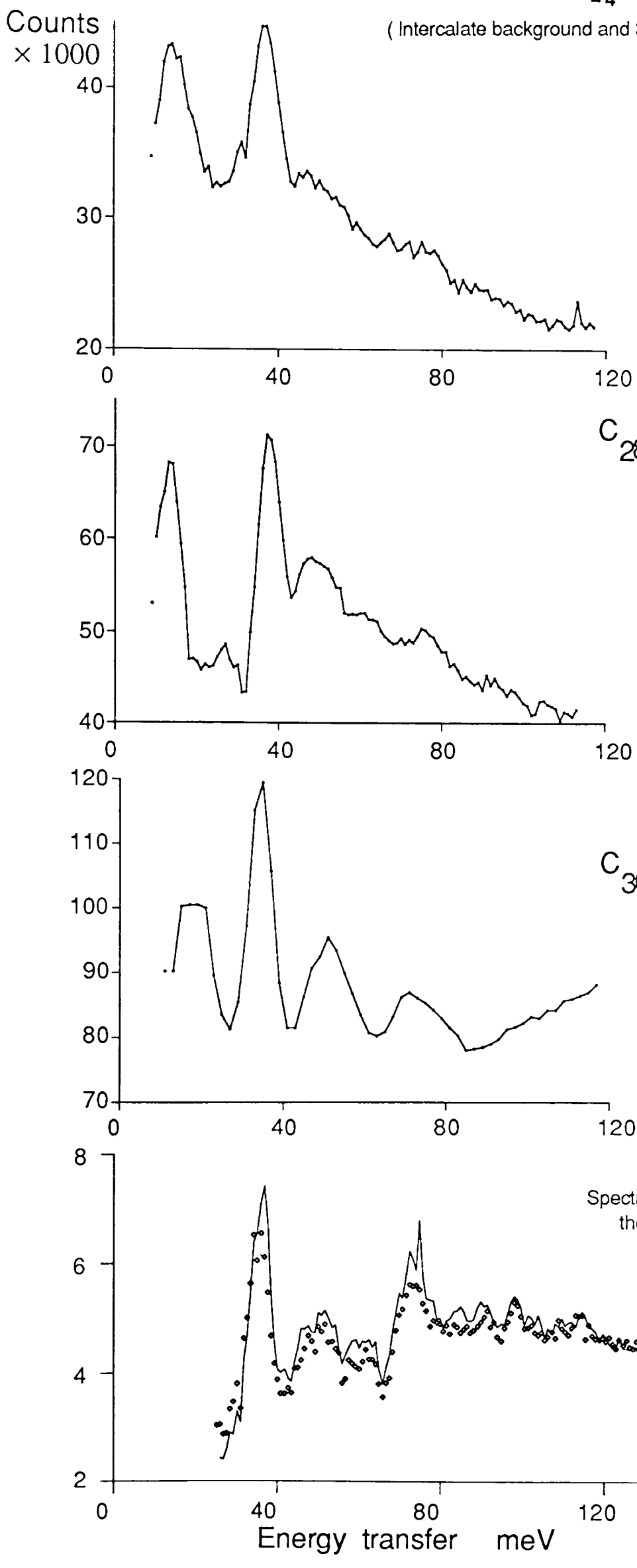

$C_{24}Cs(H_2)_1$ at 80K

(definitive spectrum)

$C_{28}Cs(H_2)_1$ at 10K [ref 362]

(Hydrogen unevenly distributed)

$C_{30}Cs(H_2)_2$ at 77K [ref 367]

(Run at Harwell by J. McCaffrey)

$C_{26}Cs(H_2)_2$ at 4K

Spectrum measured on IN1. The diamonds and the solid line are successive scans, showing the evolution of the spectrum with time.

It will be noticed that the peaks at ≈13 and 37 meV occur in the spectra of both $C_{24}Cs(H_2)_1$ and $C_{24}Cs(H_2)_2$, whereas the peaks at ≈51 and 71 meV only occur in the $C_{24}Cs(H_2)_2$ spectrum. Tentatively, therefore, the peaks at 13 and 37 meV can be associated with A sites, and those at 51 and 71 meV with B sites.

7.3.3 $C_{24}Cs(H_2)_1(N_2)_x$

In this experiment nitrogen was added to the sample of $C_{24}Cs(H_2)_1$ at 80K used previously, and the spectrum was recorded after each addition. As nitrogen was added, lines at 48 and 71 meV appeared, characteristic of $C_{24}Cs(H_2)_2$. One explanation is that the nitrogen molecules, with their larger heat of absorption, partially displaced the hydrogen molecules from the A site and moved them to the B site. The presence of nitrogen also caused a general sharpening of the lines, suggestive of a damping down of recoil effects. It did not, however, cause a significant shift in the A site fundamental at ≈37 meV in contrast to the tunnelling spectrum (Fig 7.5), nor did it cause the high energy lines to move down in energy, as would be expected from a damping down of recoil effects. The data are shown in Fig 7.8 and Table 7.2.

7.3.4 $C_{24}Cs(HD)_1$, $C_{24}Cs(HD)_2$, $C_{24}Cs(D_2)_1$ and $C_{24}Cs(D_2)_2$

The beryllium filter spectra of $C_{24}Cs(HD)_1$, $C_{24}Cs(HD)_2$, $C_{24}Cs(D_2)_1$ and $C_{24}Cs(D_2)_2$ were also measured to study the isotopic dependence of the librational peaks. This would be expected to show itself in three ways: first there is the mass effect,# second there is the difference in scattering cross-sections and third there is the difference in nuclear spin statistics. The spectra are shown in Fig 7.9 and Table 7.2 and show

---

The mass difference causes a reduction in frequency from H_2 by a factor of $\frac{4}{3}$ for an HD molecule rotating about its centre of mass, $\frac{3}{2}$ for an HD molecule rotating about its bond centre, and 2 for a D_2 molecule. For harmonic oscillations, the factors for HD and D_2 are $\sqrt{\frac{3}{2}}$ and $\sqrt{2}$ respectively. See Section 8.2 for the intermediate region.

Fig 7.8 Beryllium Filter Spectra of $C_{24}Cs(H_2)(N_2)_x$ at 80K

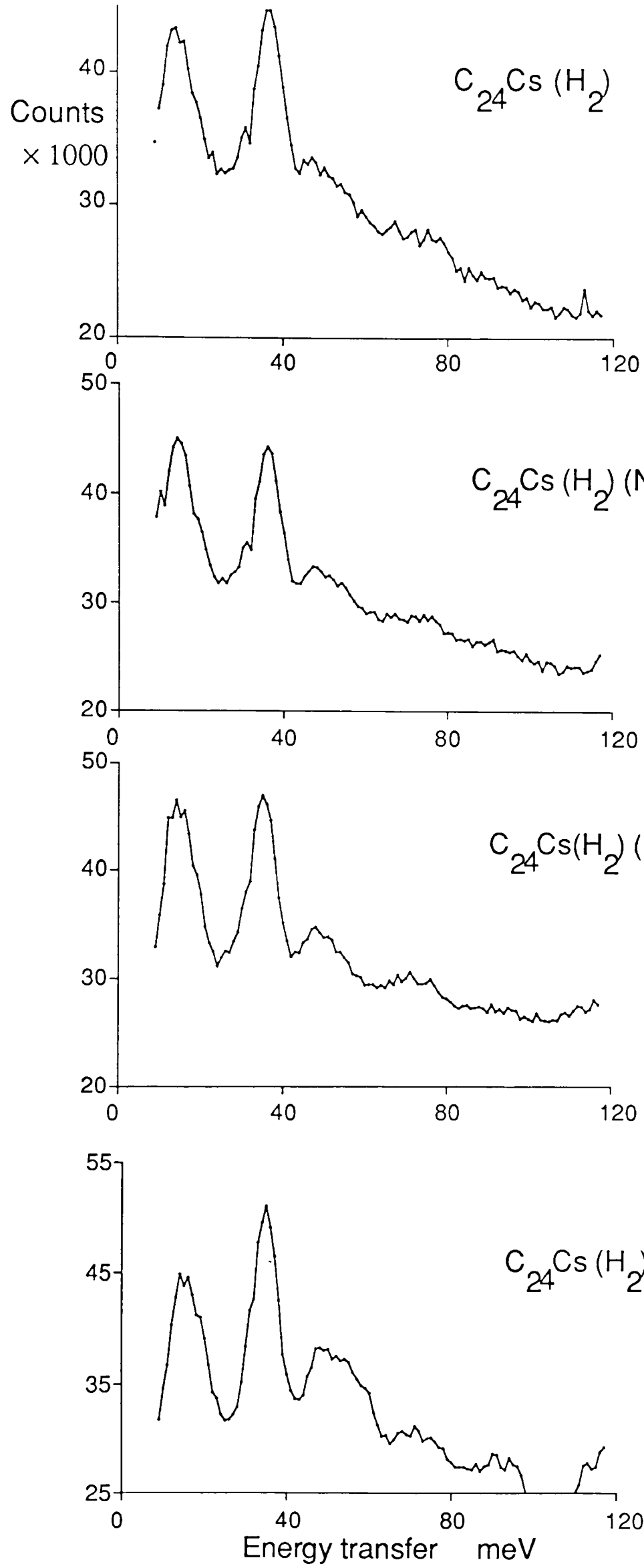

The addition of nitrogen to $C_{24}Cs(H_2)_1$ causes peaks to appear at 48 and 71 meV (c.f. $C_{24}Cs(H_2)_2$) and the spectrum to sharpen up generally. No shift in line positions is observed.

Fig 7.9 Beryllium Filter Spectra of $C_{28}Cs(HD)_x$ and $C_{28}Cs(D_2)_x$

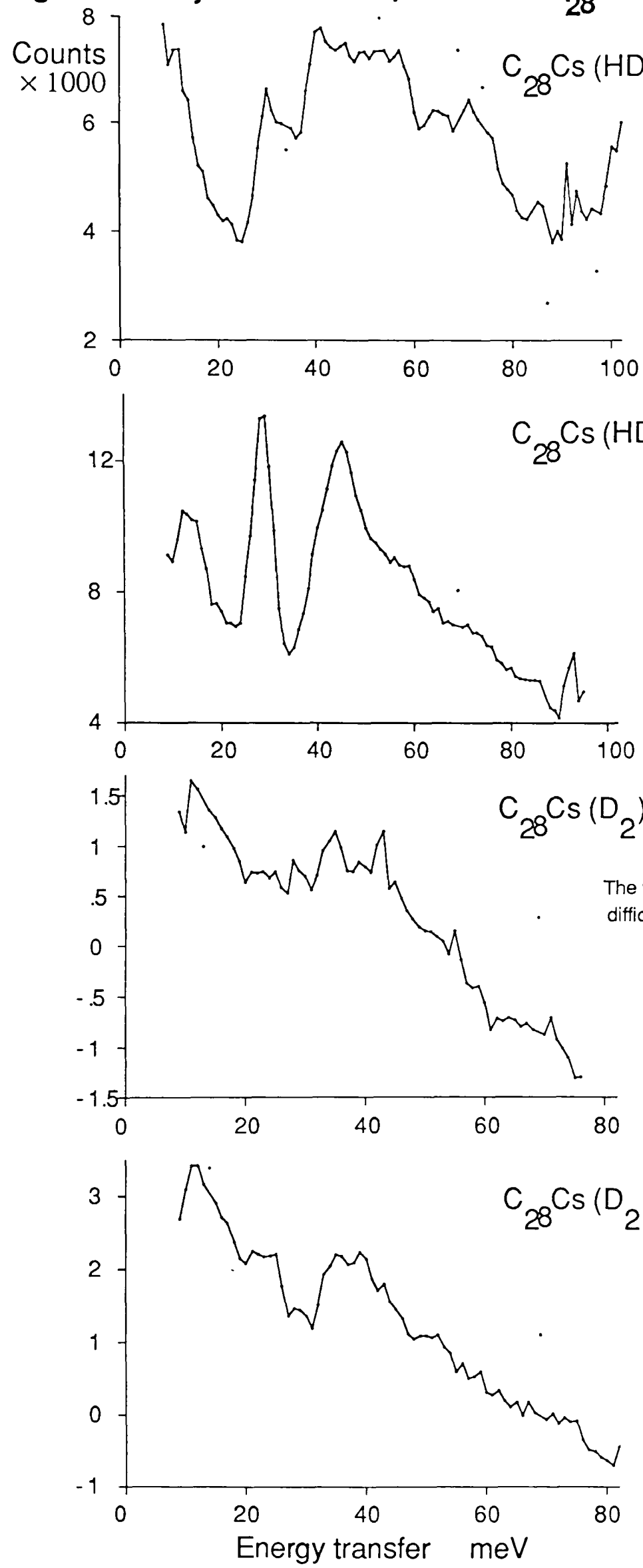

The compositions $C_{28}Cs(HD)_1$ and $C_{28}Cs(D_2)_1$ should be treated with considerable scepticism since it is very doubtful whether the samples were properly equilibrated.
Stray points are indicated by a dot.

The very weak scattering from deuterium causes difficulties in background subtraction.

interesting differences from the H_2 spectra. As expected, the spectra of D_2 are much weaker than those of H_2, owing to the much smaller incoherent scattering cross-section of deuterium; this causes difficulties in subtracting the background. The lack of a peak at 37 meV in the spectrum of $C_{24}Cs(HD)_2$ shows that the HD has not equilibrated to $H_2 + D_2$ to any great extent. The compositions $(HD)_1$ and $(D_2)_1$ should, however, be treated with considerable scepticism since the spectra were run at low temperature without proper equilibration of the samples.

7.3.5 $C_{24}Rb(H_2)_1$ and $C_{24}Rb(H_2)_2$

While the tunnelling spectra have concentrated on the rubidium intercalates, the librational spectra have focussed on the caesium intercalates. Accordingly, to get a complete picture of the beryllium filter spectroscopy of hydrogen in the rubidium intercalates, it has been necessary to use old data of varying quality[366,367]. Most of the Harwell spectra have 2 meV energy steps, instead of 1 meV, and poor statistics. Some of the spectra, however, were run on the unrebuilt IN1 spectrometer at the ILL using a hot neutron source, which gives much sharper high energy spectra, but does not scan below 30 meV. Breaks in the spectra mark changes in monochromator plane. All energies take account of the 3 meV filter correction.

The spectra of $C_{24}Rb(H_2)_1$ and $C_{24}Rb(H_2)_2$ show peaks at 21 and 42 meV similar to the peaks at 13 and 37 meV in $C_{24}Cs(H_2)_x$. However, the peaks at 57 meV and 85 meV are present in the spectra of both $C_{24}Rb(H_2)_1$ and $C_{24}Rb(H_2)_2$, unlike the peaks seen in the caesium intercalate spectrum at 51 and 71 meV, which only appear for $C_{24}Cs(H_2)_2$ and $C_{24}Cs(H_2)_1(N_2)_1$. This is at variance with the two site model for absorption, although both $C_{24}Rb(H_2)_1$ samples were run at low temperature and may be contaminated with $C_{24}Rb(H_2)_2$. (There is also a weak shoulder at 51 meV only present in $C_{24}Rb(H_2)_2$.) The spectra are shown in Fig 7.10 with peak positions in Table 7.2

Fig 7.10 Beryllium Filter Spectra of Hydrogen in Rubidium Intercalates

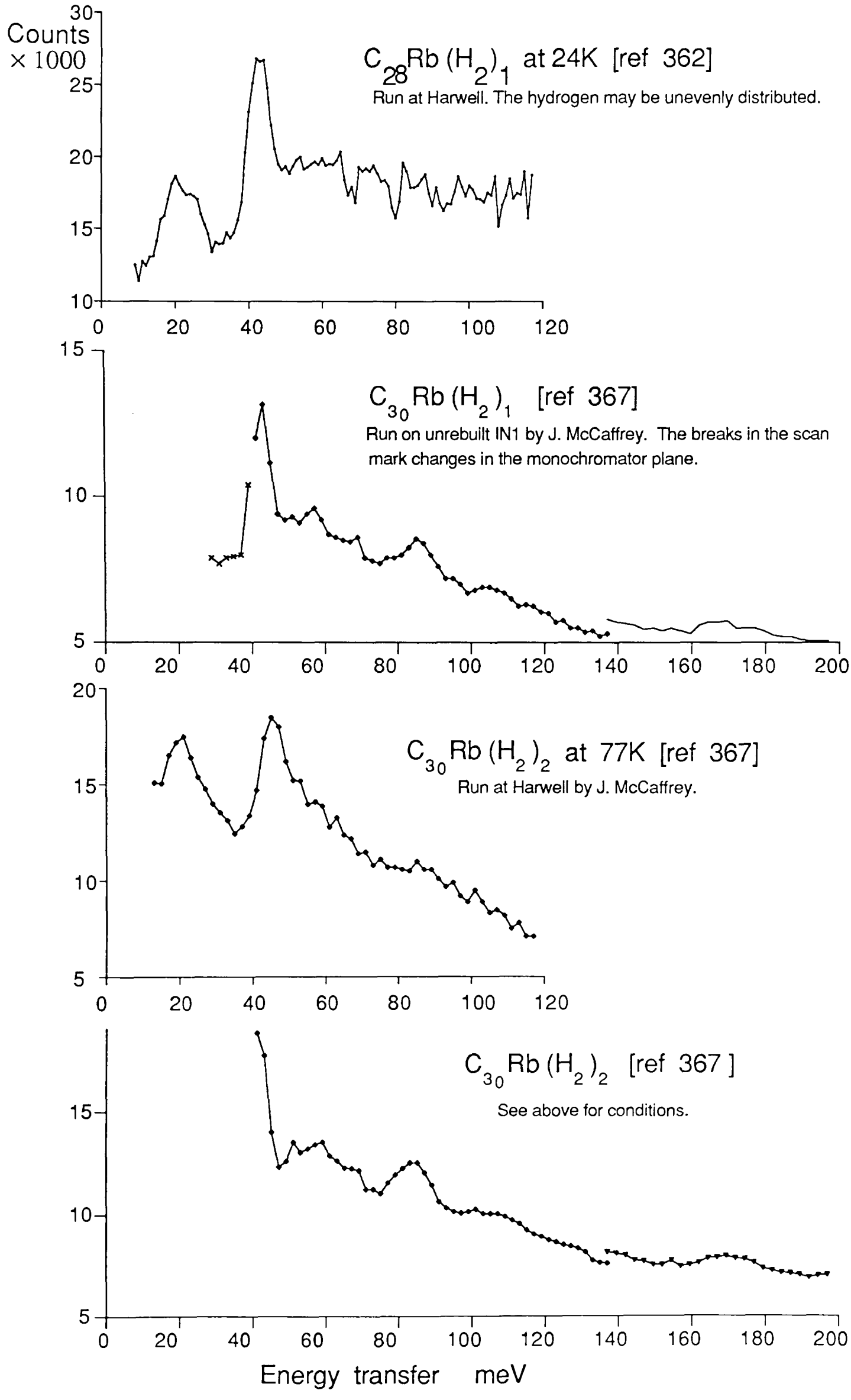

7.3.6 $C_{24}Rb(HD)_1$ and $C_{24}Rb(HD)_2$

The beryllium filter spectra of $C_{24}Rb(HD)_1$ and $C_{24}Rb(HD)_2$ were also measured by McCaffrey et al[367] on the unrebuilt IN1 spectrometer. While there are peaks at ≈35, 51 and 65 meV not observed in the $C_{24}Rb(H_2)_2$ spectrum, the H_2 peaks at ≈43, 57 and 87 meV also appear, indicating some equilibration to $H_2 + D_2$. The 35, 51 and 65 meV peaks in the HD spectrum are presumably the isotopically shifted 43, 57 and 87 meV peaks in the H_2 spectrum. Peak positions are listed in Table 7.2.

Fig 7.11 Beryllium Filter Spectra of HD in Rubidium Intercalates

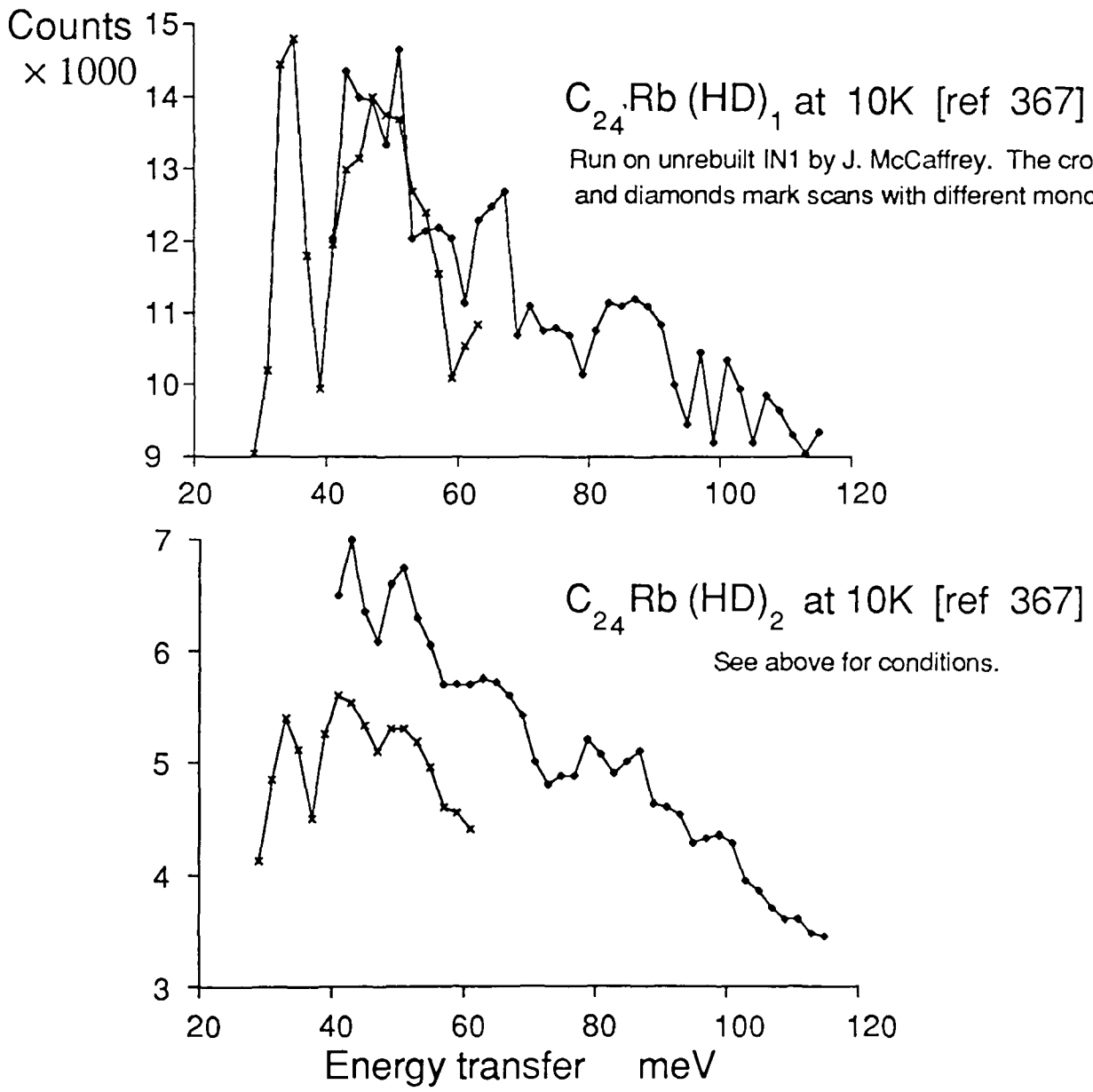

Table 7.2 Beryllium Filter Intercalate Data

Sample & ref	Temp	Peaks/mev and Intensity																
$C_{24}Cs(H_2)_1$	85K	14 s		36 s														
$C_{28}Cs(H_2)_1$ [362]	10K	13 vs	27 w	38 vs	49 s	61 vw	79 m				96 w	106 vw						
$C_{30}Cs(H_2)_2$ [367]	77K	18 s		35 vs	51 s		71 m											
$C_{26}Cs(H_2)_2$	4K			36 vs	51 s	62 m	72 s	84 vw	91 w	98 w	115 w	129 w	146 m	167 vvw	174 vw	180 vvw		
$C_{24}Cs(H_2)_1(N_2)_{0.18}$	85K	14 s		36 s	47 w													
$C_{24}Cs(H_2)_1(N_2)_{0.45}$	85K	14 vs		35 vs	48 m		71 vw											
$C_{24}Cs(H_2)_1(N_2)_{1.0}$	85K	15 s		35 vs	48 s		71 w											
$C_{28}Cs(HD)_1$ [362]	30K	12 m	22 vw	30 m	43 m	55 m	64 m	72 m	85 w	93 w								
$C_{28}Cs(HD)_2$ [362]	30K	13 vs	20 vw	29 vs	45 vs	57 vw		69 vw										
$C_{28}Cs(D_2)_1$ [362]	30K	11 s	23 w	28 w	35 s	41 m	52 w	59 vw	67 m									
$C_{28}Cs(D_2)_2$ [362]	30K	12 vs	23 w	28 w	37 s		50 w	59 vw										
$C_{28}Rb(H_2)_1$ [362]	24K	21 m	42 s		60 vvw			73 w	85 w	97 vvw								
$C_{30}Rb(H_2)_1$ [367]	?		42 vs	51 vvw	57 m	69 vvw	77 w	85 m			105 w	167 w						
$C_{30}Rb(H_2)_2$ [367]	10K	21 vs	45 s		58 sh			84 w										
$C_{30}Rb(H_2)_2$ [367]	?		42 vs	51 w	59 m	69 sh	77 sh	85 m			107 w	169 w						
$C_{24}Rb(HD)_1$ [367]	10K	35 vs	43 s	51 s	57 sh	65 s	73 w	87 m	99 m	109 w								
$C_{24}Rb(HD)_2$ [367]	10K	33 s	42 s	50 m		63 s	78 w	87 w	99 vw									

7.4 H_2 MOLECULAR VIBRATION

Taking advantage of the higher incident energies available on IN1B, the energy region 100-130 THz (3300-4300 cm^{-1}) was also scanned at the same time as the librational experiment to see whether the molecular vibration of hydrogen in $C_{26}Cs(H_2)_2$ at 4K could be observed, and if so, whether it was shifted from the free molecule value of 4162 cm^{-1} [121]. Even with the benefit of a hot neutron source, these energies are near the machine's upper limit, and the scanning speed at 110 THz using the Cu 220 monochromator plane was a factor of 15 down from the maximum at 20 THz, decreasing sharply with increasing energy. Preliminary findings indicated a very weak excitation at 109±2 THz (448±10 meV, 3610±70 cm^{-1}) but two subsequent experiments merely showed a sloping background in this energy region.

The expected intensity of the transition, as would be observed by beryllium filter spectroscopy, can be calculated as follows:

For a fundamental vibrational excitation:

$$S(\mathbf{Q},\omega) = \exp\{-Q^2\langle u_Q^2\rangle\} \times I_1(Q^2\langle u_Q^2\rangle) \times \delta(\hbar\bar{\nu} - \hbar\bar{\nu}_a) \qquad (6.9)$$

where $Q^2 = 0.05984\bar{\nu}_{inc} + 1.45\ A^{-2}$ and $\bar{\nu}_{inc} = \bar{\nu}_{tr} + 25\ cm^{-1}$ (6.16)

$\langle u_Q^2\rangle$ is best calculated here from a formula by Batley et al[368]:

$$\langle u_Q^2\rangle = \frac{h}{8\pi^2\mu\bar{\nu}c} \quad \text{and} \quad \langle u_Q^2\rangle = \tfrac{1}{3}\langle u^2\rangle \qquad (7.1)$$

where $\bar{\nu}$ is the excitation frequency in cm^{-1}, μ is the reduced mass of the hydrogen molecule, and c is the velocity of light in cm/sec. Following Griffin & Jobic [321] and Warner et al[322], it is assumed that $S(\mathbf{Q},\omega)$ for the vibration can be separated from the librational $S(\mathbf{Q},\omega)$ (Section 6.1.2), with $\bar{\nu} = 4162\ cm^{-1}$. This gives $Q^2 = 252\ A^{-2}$, $\langle u_Q^2\rangle = 0.000670\ A^2$ and $Q^2u^2 = 0.169$. For $Q^2u^2 \leqq 0.8$,

$$S(\mathbf{Q},\omega) = \tfrac{1}{2}Q^2\langle u_Q^2\rangle \times \exp\{-Q^2\langle u_Q^2\rangle\} \times \delta(\hbar\bar{\nu} - \hbar\bar{\nu}_a) \qquad (6.11)$$

and hence $S(\mathbf{Q},\omega) = 0.071$. This compares with 0.183 for the intense methyl group torsion at 140 cm^{-1} in solid acetonitrile (Fig 6.11, Table 6.6), and means that the H_2 molecular vibration would be expected to be observed with moderate intensity. (Larger values of $\langle u_Q^2 \rangle$ to take account of librational motion would cause an increase in $S(\mathbf{Q},\omega)$ - See Fig 6.1.) There must, therefore, be some other reason for the non-observance of the line.

The most probable explanation is the recoil of the hydrogen molecule. The $C_{24}Cs(H_2)_2$ librational spectrum (Fig 7.8) shows a "fade-out" of the peaks above 80 meV, and with an incident energy of 450 meV, this effect would be very serious. In the free molecule limit, the shifted transition would occur at double the unshifted energy (Equation 6.32), out of the range of observation, and the scattering cross-section would be reduced to $\frac{4}{9}$ of the bound value[291] (Section 6.1.2). Apart from the recoil effects, the scattering cross-section of the hydrogen atom falls off with increasing incident energy, and for 500 meV neutrons, it is only 22 barns [294]. (**Rotational** transitions in solid hydrogen have, however, been observed with 1900 meV incident neutrons[323].) It therefore appears unlikely that the transition will be observed, at least unless higher incident energies are used to take account of the recoil shift.

CHAPTER 8

THE DYNAMICS OF HYDROGEN PHYSISORBED BY INTERCALATES

INTRODUCTION

In Chapter 7, the low energy neutron spectrum of $C_{24}Rb(H_2)_x$ indicated transitions at ≈1.4 and 0.65 meV, which were attributed to rotational tunnelling in two distinct sites, termed A and B. The A site was filled preferentially, the 0.65 meV peak only appearing at concentrations above $(H_2)_{0.8}$. Furthermore, after the B site peak had appeared, the A site peak continued to grow in intensity. This two site picture was confirmed by the time of flight spectra of $C_{24}Cs(H_2)_1$ and $C_{24}Cs(H_2)_2$, in which the A and B site peaks occurred at ≈1.2 and 0.65 meV respectively.

Beryllium filter spectra of $C_{24}Cs(H_2)_1$ showed peaks at 13 and 37 meV, additional peaks appearing at 51 and 71 meV in the case of $C_{24}Cs(H_2)_2$ and $C_{24}Cs(H_2)_1(N_2)_x$. These peaks were tentatively assigned to librations in the A and B sites. In the case of $C_{24}Rb(H_2)_1$ and $C_{24}Rb(H_2)_2$, peaks appeared at 21, 42, 57, and 85 meV. Here, however, there were no intense peaks only present at high hydrogen concentrations. The aim, therefore, is to find a potential of the correct strength and symmetry to explain both the tunnelling and the librational results, and which appears physically reasonable in the structural model of the intercalates. The fine details of the potential are likely to be supplied by the tunnelling spectra, which are much more sensitive to small changes than the librational spectra.

8.1 THE MODEL POTENTIAL

In Figs 6.7 and 6.8, the splitting diagrams as a function of hindering potential were plotted for a homonuclear diatomic molecule in fields with axial, tetrahedral and octahedral symmetry. In this case, however, the rotational constant B is a constant 7.35 meV [121], and

because of the low temperature, all transitions take place either from the ground state or the excited tunnelling state. Since the tunnelling energies are small compared with the resolution of the beryllium filter spectrometer, the splitting diagrams can be replotted to show energy **differences** in meV from the ground state, allowing calculated and observed librational energies to be compared directly. Similarly, the tunnelling splittings have been plotted as a function of field strength.

It can be seen from Figs 8.1 and 8.2 that in the high symmetry tetrahedral and octahedral fields, the values of the barrier constant required to give tunnelling transitions at ≈1 meV predict fundamental librational transitions at energies greater than 100 meV, with barriers to rotation more than the hydrogen desorption energy (Table 1.1)! On the other hand, in an axially symmetric cos2θ potential, a tunnelling splitting of 1.25 meV predicts a fundamental libration energy of 42 meV (Fig 8.3), and the symmetry of the potential is easier to reconcile with the 2-D nature of the system than a potential with tetrahedral or octahedral symmetry. (Fig 6.6, Section 8.4)

Using Fig 8.3 to read off the transition energies according to this model, the A site in $C_{24}Rb(H_2)_x$ has an axially symmetric twofold barrier to rotation with a barrier constant K^2 of 14B, giving a tunnelling line at 1.25 meV and a fundamental libration at 42 meV, compared with the observed values of 1.2-1.4 meV (Fig 7.3, Table 7.1) and 42 meV respectively (Fig 7.10, Table 7.2). The B site has a stronger potential with K^2=18B, giving a tunnelling line at 0.65 meV and a fundamental libration at 50 meV. In the observed spectra of $C_{24}Rb(H_2)_x$ the B site tunnelling line occurs at 0.60-0.72 meV (Fig 7.3, Table 7.1); however, no librational lines were observed in $C_{24}Rb(H_2)_2$ **only**, although there was a peak at 58 meV and a small blip at 51 meV in both $C_{24}Rb(H_2)_1$ and $C_{24}Rb(H_2)_2$ (Fig 7.10, Table 7.2). The calculated barriers to rotation in

Fig 8.1 Splitting Pattern for the Rotational Energy Levels of a Hydrogen Molecule in a Potential field with Tetrahedral Symmetry replotted to show Transition Energies from the Ground State in meV [after ref 362].

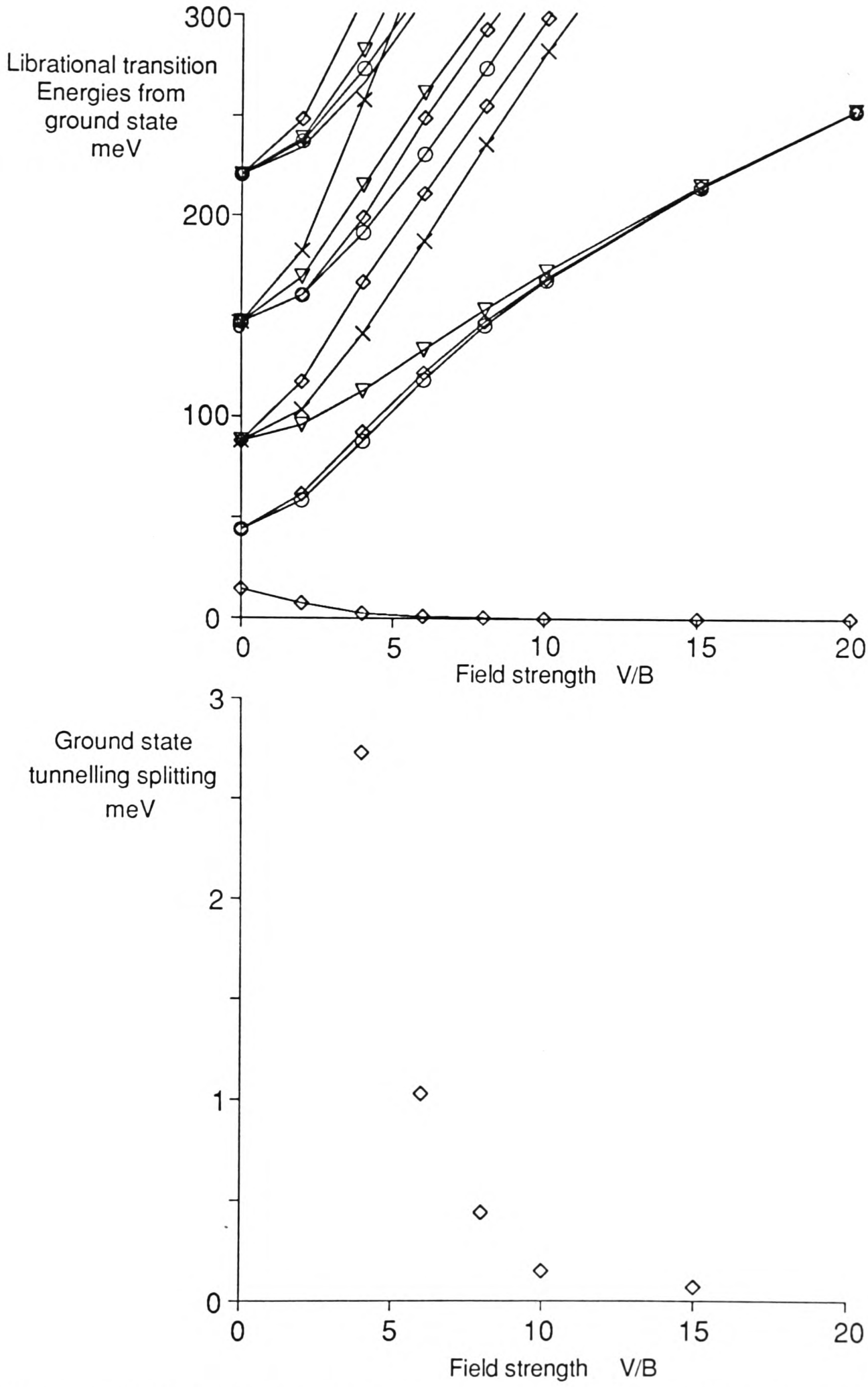

The ground state has A_1 symmetry. Transitions to A_1, E, T_1 and T_2 states are marked by crosses, circles, triangles and diamonds. The barrier to rotation is 3 -fold, value $10V / \sqrt{3}$. A tunnelling splitting of 1.03 meV predicts the first librational transition to occur at 119 meV with a barrier to rotation of 35B (255 meV; 25 KJ/mol). (Original splitting pattern in Fig 6.8.)

Fig 8.2 Splitting Pattern for the Rotational Energy Levels of a Hydrogen Molecule in a Potential field with Octahedral Symmetry Replotted to show Transition Energies from the Ground State in meV [after ref 362]

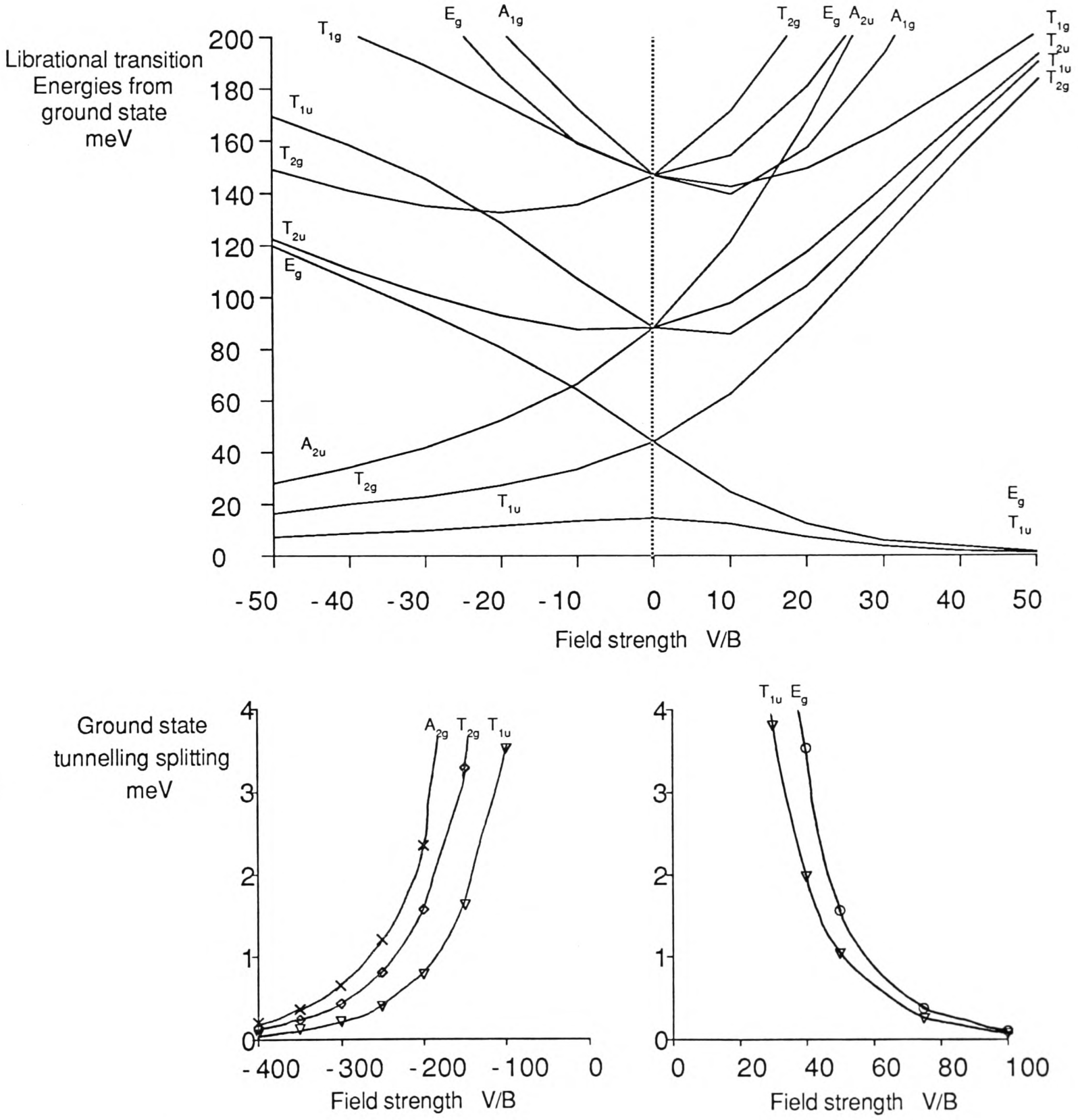

Rotational transitions up to J' = 4 are shown. The ground state has A_{1g} symmetry. The symmetries of the upper states are marked on the diagrams. If V > 0, the potential minima lie at the corners of the octahedron and there is a 4 -fold barrier to rotation of height 5V/ 4. If V < 0, the minima lie at the centres of the faces of the octahedron, and there is a 4 -fold barrier to rotation of height 5V/ 12 and a 3 -fold barrier to rotation of height 5V/ 3. The transition from the ground state to the T_{1u} tunnelling state occurs at ≈1 meV for V ≈ +50B or -180B predicting fundamental librations at 180 or >200 meV respectively. The lowest barriers to rotation in these cases are 62B or 75B (460 or 550 meV; 44 or 53 KJ/mol). (See Fig 6.8 for original splitting pattern.)

Fig 8.3 **Splitting Pattern for the Rotational Energy Levels of a Hydrogen Molecule in an Axially Symmetric cos2θ Potential replotted to show Transition Energies from the Ground State in meV**

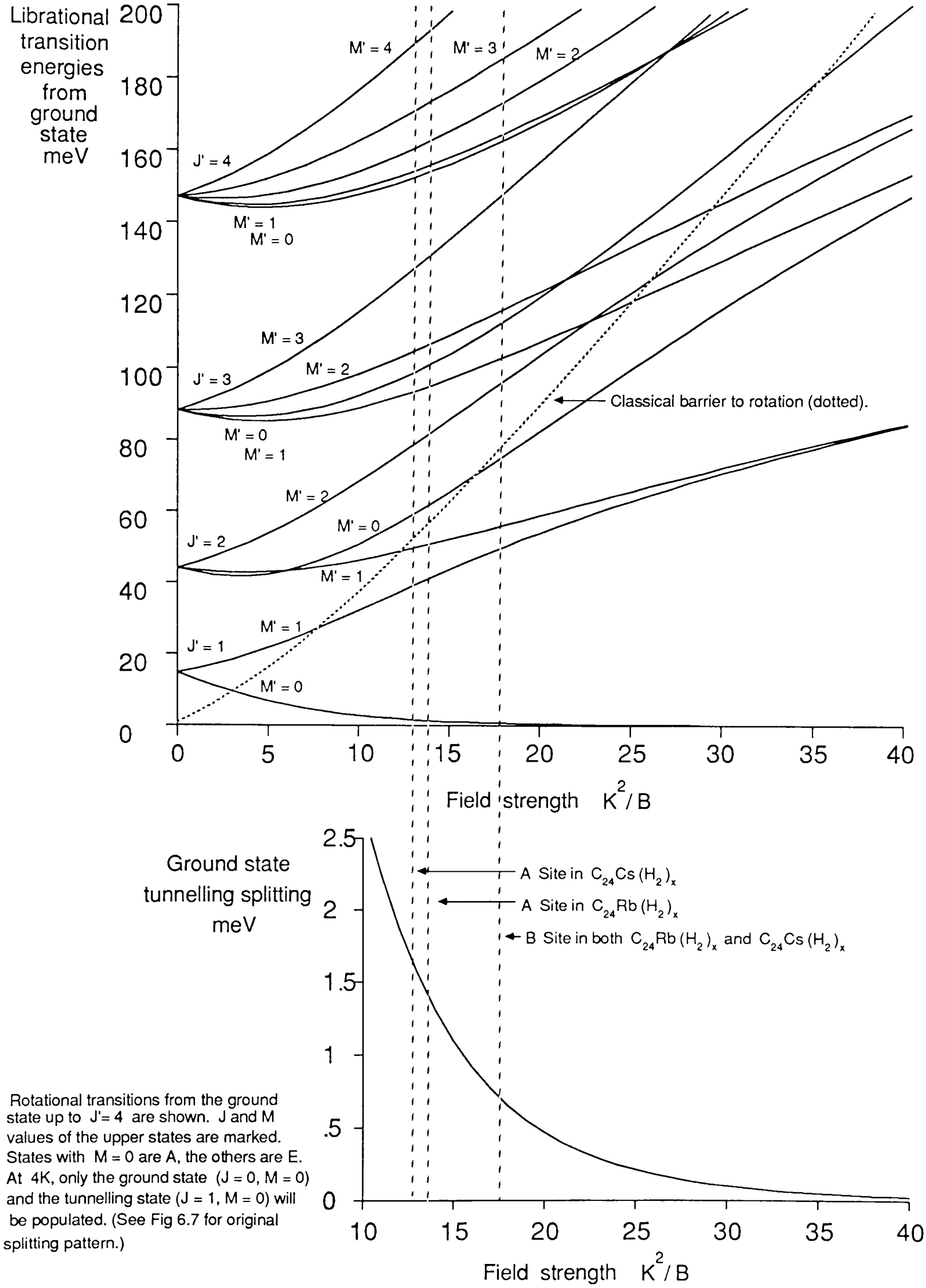

Rotational transitions from the ground state up to J'= 4 are shown. J and M values of the upper states are marked. States with M = 0 are A, the others are E. At 4K, only the ground state (J = 0, M = 0) and the tunnelling state (J = 1, M = 0) will be populated. (See Fig 6.7 for original splitting pattern.)

the A and B sites are 57 and 78 meV (5.5 and 7.5 KJ/mol). The calculated transition energies are compared with observed peak positions in Table 8.1 with, on the whole, excellent agreement.

Similar agreement can be obtained with the $C_{24}Cs(H_2)_2$ results (Table 8.1), the A and B sites having potentials with K^2=13B and 18B respectively, predicting tunnelling lines at 1.55 and 0.65 meV, and librations at 39 and 50 meV. (Tunnelling observed at 0.99-1.20 meV and 0.67 meV; librations at 35-38 meV and 49-51 meV in $C_{24}Cs(H_2)_1$ and $C_{24}Cs(H_2)_2$ (Figs 7.5 and 7.7, Table 7.2).) The barriers to rotation in the A and B sites are 51 and 78 meV (4.9 and 7.5 KJ/mol). The $C_{24}Cs(H_2)_x$ A site tunnelling and libration energies, however, are **both** lower than the $C_{24}Rb(H_2)_x$ A site tunnelling and libration energies, which is inconsistent with the model. Similarly, the $C_{24}Rb(H_2)_x$ and $C_{24}Cs(H_2)_x$ tunnelling and libration peaks all shift down in energy slightly on increasing the hydrogen concentration. The inconsistencies are, however, relatively minor and probably result from small deviations from the assumed cylindrical symmetry and sinusoidal shape of the potential. Similar complications are also hinted at by the fine structure of the $C_{24}Rb(H_2)_x$ tunnelling peaks.

The spectrum of $C_{24}Cs(H_2)_1(N_2)_1$ is very similar to the spectrum of $C_{24}Cs(H_2)_2$ in both the tunnelling and librational energy regions, except for the fact that the A site tunnelling peak is shifted down in energy even more than in $C_{24}Cs(H_2)_2$ (1.20→0.88 cf 0.99 meV), and a possible very weak excitation appears at 0.37 meV (Fig 7.5). The B site peak also appears to be slightly shifted down in energy, but this may not be statistically significant (0.62 cf 0.67 meV). The librational spectra of $C_{24}Cs(H_2)_1(N_2)_x$ ($0 \leq x \leq 1$) show the appearance of the B site peaks with increasing N_2 concentration, and a general sharpening of the spectrum, but no significant shifts in peak positions compared with $C_{24}Cs(H_2)_2$

(Fig 7.8, Table 7.2). It can therefore be concluded that in $C_{24}Cs(H_2)_1(N_2)_1$, the site structure is similar to $C_{24}Cs(H_2)_2$, with some hydrogen molecules in both A and B sites, the A sites undergoing the same distortions as in $C_{24}Cs(H_2)_2$ but to a greater extent. The $C_{24}Cs(H_2)_1(N_2)_1$ tunnelling and libration spectra are also included in Table 8.1

The main problem with the two absorption site hindered rotor explanation is that it fails to account to the low energy beryllium filter peak at 13 meV in $C_{24}Cs(H_2)_1$, 18 meV in $C_{24}Cs(H_2)_2$ and 21 meV in $C_{24}Rb(H_2)_1$. (The other problems are the hot band at 2.15 meV in $C_{24}Cs(H_2)_1$ (Fig 7.5) and the peak at 2.09 meV seen in $C_{24}Rb(H_2)_{2.00}$ but not $C_{24}Rb(H_2)_{1.78}$ (Fig 7.3). No good explanation exists for either of these.) 13 meV is the energy of the $J = 0 \rightarrow 1$ transition of a freely rotating hydrogen molecule, and one possibility is to propose a third site in which the hydrogen molecule can rotate almost freely, the values for K^2 in $C_{24}Cs(H_2)_1$, $C_{24}Cs(H_2)_2$ and $C_{24}Rb(H_2)_1$ being ≈ 0, 3B and 4.5B. (In these cases, the "tunnelling" lines would occur at energies of 7 meV or more, and would lie between the energy ranges of the time of flight and beryllium filter spectra.) The plot of the ≈ 1.4 meV tunnelling peak intensity versus filling (Fig 7.4) has an intercept of zero intensity at composition $(H_2)_{0.08}$, suggesting that some hydrogen may not be tunnelling, but this is by no means enough to account for the intensity of the beryllium filter peak, especially in $C_{24}Cs(H_2)_1$. The increase in intensity of the 1.4 meV peak has no breaks or plateaux which might indicate the filling of another site, and it is also difficult to see how such an isotropic site could exist in a highly anisotropic material such as a graphite intercalate. As a result of these considerations, therefore, the free rotor hypothesis has to be rejected.

A second possibility is that **both** the low energy "librational" lines, 13 and 37 meV in $C_{24}Cs(H_2)_1$, 18 and 35 meV in $C_{24}Cs(H_2)_2$ and 21 and 42 meV in $C_{24}Rb(H_2)_1$ are the two branches of a weakly hindered J = 0→1 rotation, heavily shifted by recoil. If the apparent mass of the hydrogen molecule is assumed constant with energy,[+] the unshifted energies for $C_{24}Cs(H_2)_1$ are 6.7 and 23 meV, the barrier constant K^2 = 5.1B, and the apparent mass of the hydrogen molecule is 3.0. Similar calculations give unshifted energies of 8.8 and 19.3 meV with K^2 = 3.5B and a hydrogen mass of 2.6 for $C_{24}Cs(H_2)_2$, and energies of 8.1 and 19.1 meV with K^2 = 3.7B and a hydrogen mass of 2.1 for $C_{24}Rb(H_2)_1$.

The problem with this argument is that it does not account for the tunnelling spectra, unless a further A site is proposed of high symmetry with a large potential barrier and no observable librational spectrum. Second, it requires large recoil shifts to occur at relatively low momentum transfers. In solid hydrogen using 5 meV neutrons, the J = 1→0 transition was observed as a free rotation at 15 meV independent of the scattering angle (Section 6.2.2). This has the same momentum transfer as the 13 meV transition in $C_{24}Cs(H_2)_1$. Furthermore, all intercalate tunnelling data to date have shown little or no **Q** dependence[361]. For recoil effects to be so drastic in a beryllium filter experiment with 13 meV energy transfer, ($Q = 3.0Å^{-1}$) some effect would be expected in the tunnelling spectrum, where a 3 meV incident neutron scattered through 90° with a 1 meV energy gain has $Q = 1.8Å^{-1}$.

Having rejected the two alternative explanations, one is forced to conclude that another type of excitation, possibly a whole molecule translation is responsible for the low energy band in the beryllium

---

+ In fact, the apparent mass of the hydrogen molecule would decrease with increasing momentum transfer to reach a limiting value of 2. This would alter the unshifted energies and decrease K^2, but does not affect the validity of the argument.

filter spectra. This is confirmed by the presence of weak bands in the low temperature beryllium filter spectra of $C_{24}Cs(H_2)_1$ and $C_{24}Cs(H_2)_2$ which can be attributed to overtones and combinations eg 27 meV in $C_{24}Cs(H_2)_1$, 62 meV in $C_{24}Cs(H_2)_2$. The possibilities of whole molecule translational vibrations and translational tunnelling are discussed in Section 8.5.

So far, only fundamental excitations have been considered in the librational spectrum, whereas Fig 8.3 can also be used to compare calculated overtone energies with observed peaks. The value of this, however, is limited by the complexity of the splitting pattern, the poor resolution of the spectrometer and uncertainties about recoil effects. It would be ultimately desirable to calculate peak intensities as was done for acetonitrile (Section 6.5.4), since some of the transitions will be forbidden. In the case of acetonitrile, the splitting pattern was relatively simple and the potential barrier large enough for the librations to be approximated to harmonic oscillations. In the present case, however, the situation is intermediate between the free rotor and the harmonic oscillator, each limit predicting a totally different result, and neither of them a sufficiently good approximation to use. It would be possible, though difficult, to calculate scattering intensities directly. This would involve using the eigenvectors of each librational level to break it down into its rotational components. The transition moment for each component could then be calculated using Equations 6.23 and 6.27 with an appropriate value of **Q**. This would have to be repeated for all values of K^2, and would be a long process which has yet to be attempted for **any** system.

Subject to the above-mentioned limitations, the calculated overtones for $C_{24}Rb(H_2)_X$ and $C_{24}Cs(H_2)_X$ are compared with observed peaks in Table 8.1. While a theoretical line can be found to fit most of the

Table 8.1 Calculated and Observed Transition Energies (meV) for the Hindered Rotation of Absorbed Hydrogen Molecules using an Axially Symmetric cos2θ Model Potential

$C_{24}Rb(H_2)_x$

Calculated		Observed							
Site A	Site B								
K^2=14.2B	K^2=18B	$C_{24}Rb(H_2)_1$				$C_{24}Rb(H_2)_2$			
						s	0.60		
	0.65					m	0.70		
						m	1.05		
1.27						vs	1.22		
				vs	1.42	m	1.50		
						s	2.05		
		m	21			vs	21		
41		s	42	vs	42	s	45	vs	42
51	50			vvw	51			w	51
63	56	vvw	60	m	57	sh	58	m	59
				vvw	69			sh	69
	76	w	73	w	77			sh	77
83		w	85	m	85	w	84	m	85
95	97	vvw	97						
101	102			w	105			w	107
108	113								
	116								
133									
153	149								
155									
163	163								
	166								
173	173			w	169			w	169
	185								
194									

This table gives a summary only. The observed spectra are shown in full in Figs 7.3 and 7.10. Details of the calculation are given in Section 6.4.1 and Fig 8.3. K^2 is the barrier constant and B the rotation constant for the hydrogen molecule.

Table 8.1 (cont'd) Calculated and Observed Transition Energies (meV) for the Hindered Rotation of Absorbed Hydrogen Molecules using an Axially Symmetric cos2θ Model Potential

Calculated		$C_{24}Cs(H_2)_x$ Observed		
Site A K^2=13B	Site B K^2=18B	$C_{24}Cs(H_2)_1$	$C_{24}Cs(H_2)_2$	$C_{24}Cs(H_2)_1(N_2)_1$
				vw 0.37
	0.65		m 0.67	m 0.62
1.57		s 1.20	s 0.99	s 0.88
		w 2.14		
		s 14 vs 13	s 18 -	s 15
		w 27		
39		s 36 vs 38	vs 35 vs 36	vs 35
49	50	s 49	s 51 s 51	s 48
59	56	vw 61	m 62	
79	76	m 79	m 71 s 72	w 71
			vw 84	
94			w 91	
99	97	w 96	w 98	
105	102	vw 106		
	113			
	116			w 115
128				w 129
152	149			m 146
154				
160	163			vvw 167
	166			
171	173			vw 174
189	185			vvw 180

This table gives a summary only. The observed spectra are shown in full in Figs 7.5, 7.7 and 7.8. Details of the calculation are given in Section 6.4.1 and Fig 8.3. K^2 is the barrier constant and B the rotation constant for the hydrogen molecule.

observed peaks (assuming no recoil of the hydrogen molecule), this is probably attributable more to the complexity of the calculated splitting pattern and the poor resolution of the spectrometers, rather than to the accuracy of the potential. It appears, therefore that theoretical peak intensities will be needed for an accurate comparison.

8.2 ISOTOPIC SHIFTS

On substitution of HD or D_2 for H_2, three effects will occur: the mass effect, the much weaker scattering of neutrons by the deuterium nucleus than the proton and the change in nuclear spin statistics. The change in mass leaves the absolute potential barrier constant,# but the rotational constant B is scaled by a factor of 2 for D_2 and $\frac{4}{3}$ or $\frac{3}{2}$ for HD, depending on whether the librations take place about the molecular centre of mass or the geometrical bond centre. Since the splitting diagrams for H_2 (Figs 8.1-8.3) have been calculated entirely in terms of B, the same diagrams can be used to calculate the expected transition energies for HD and D_2 provided that K^2/B is **multiplied** by the relevant factor, followed by **division** of the transition energies by the same factor (2, $\frac{4}{3}$ or $\frac{3}{2}$). In the limit of a large hindering potential, the isotopic shift for librations will approach $\sqrt{\frac{4}{3}}$ or $\sqrt{\frac{3}{2}}$ for HD and $\sqrt{2}$ for D_2, as expected for a harmonic oscillator.

The change in nuclear spin statistics affects the librational intensities. In H_2 the J = 0→2, 4, 6... transitions are forbidden for incoherent scattering, but for HD and D_2 all combinations of J odd→odd, odd→even, even→odd and even→even transitions give incoherent scattering (Section 6.2.1). They will thus give librational lines in proportion to their contribution to each of the librational states, subject to thermal population constraints.

This may not be true for HD rotating about its centre of mass, where the path traced out by the nuclei is different.

Starting with the $C_{24}Rb(HD)_x$ tunnelling results, the A and B site barriers, K^2 = 14B and 18B in $C_{24}Rb(H_2)_x$, scale to K^2 = 18.9B and K^2 = 24B for centre of mass librations, predicting an A site line at 0.41 meV and a B site line at 0.19 meV. For bond centre librations, the A and B site barriers are 21.3B and 27B, with lines predicted at 0.26 meV and 0.11 meV. $C_{24}Rb(HD)_1$ actually gives a single observed line at 0.417 meV, precisely in the position predicted by the centre of mass model. $C_{24}Rb(HD)_2$, however, gives peaks at 0.138, 0.218 and 0.345 meV (Fig 7.3, Table 7.1), which is within the predicted range, but does not correspond exactly with either model.

Librational isotopic shifts can be similarly predicted. The A and B site fundamental librations at 42 and (possibly) 51 meV in $C_{24}Rb(H_2)_x$, should occur in $C_{24}Rb(HD)_x$ at 39 and 46 meV (centre of mass), or 38 and 45 meV (bond centre). The observed values, however, are 33-35 meV and 50 meV (Fig 7.11, Table 7.2), with a clear down-shift in the A site fundamental libration energy. In this case, however, there are also peaks at 43, 57, 73 and 87 meV, indicating contamination by H_2; this may obscure the true shifted B site peak. The low energy peak, observed at 21 meV in $C_{24}Rb(H_2)_x$, if it is a whole molecule translational excitation, will scale as a harmonic oscillation by a factor of $\sqrt{\frac{3}{2}}$ to 17 meV. This has yet to be tested, as the $C_{24}Rb(HD)_x$ spectra were measured on IN1. Comparison of librational overtones is made difficult by the changes in selection rules caused by the nuclear spin statistics. For the sake of completeness, however, they are included in Table 8.2.

In the case of $C_{24}Cs(HD)_x$, the barriers for the A and B sites of K^2 = 13B and 18B in $C_{24}Cs(H_2)_x$ scale to K^2 = 17.3B and 24B in the centre of mass model, and K^2 = 19.5B and 27B in the bond centre model. Tunnelling data are not available, but lines are predicted for the A and B sites at 0.55 and 0.19 meV (centre of mass) or 0.38 and 0.11 meV

(bond centre). Librational fundamentals are predicted for the A and B sites at 37 and 46 meV (centre of mass) or 35 and 44 meV (bond centre). The observed $C_{24}Cs(HD)_2$ spectrum gives intense peaks at 29 and 45 meV (Fig 7.9, Table 7.2). Here again, there is a clear down-shift in the A site librational fundamental, but the B site peak is as predicted. (The lack of lines at 37 and 49 meV, however, does at least indicate no contamination by H_2.) The low energy peak at 18 meV in the $C_{24}Cs(H_2)_2$ spectrum scales as a whole molecule translational excitation to 15 meV; the observed value is 13 meV, nearer the position expected from the $C_{24}Cs(H_2)_1$ spectrum. The calculated and observed spectra are compared in Table 8.2.

The D_2 spectra are simpler to interpret than the HD spectra, since the uncertainties over centre of mass versus bond centre rotation and possible equilibration to $H_2 + D_2$ are removed. They are, however, much weaker, and the tunnelling energies are so low as to be close to the limit of observation on IN5, where the elastic peak has a FWHM of 0.04 meV with 8A incident neutrons (Fig 7.3). In $C_{24}Rb(D_2)_X$, the barriers for the A and B sites scale to $K^2 = 28.4B$ and 36B, and tunnelling is predicted at 0.07 and 0.02 meV (probably unobservable). In the tunnelling spectrum of $C_{24}Rb(D_2)_2$, a weak line is observed at 0.21 meV (Fig 7.3, Table 7.1); this is the energy of the B site tunnelling peak in $C_{24}Rb(HD)_2$ (Table 8.2). Librational lines are predicted at 34 and 40 meV for the two sites, with the low energy peak at 16 meV, but no experimental data are available for comparison.

In $C_{24}Cs(D_2)_X$, the A and B site barriers scale to $K^2 = 26B$ and 36B. No tunnelling data are available, but lines are predicted at 0.09 and 0.02 meV for the two sites. The A and B site librations are predicted at 33 and 40 meV, compared with peaks observed for $C_{24}Cs(D_2)_2$ at 35 and 41 meV (Fig 7.9, Table 7.2). The low energy peak is observed at 12 meV, compared with a calculated energy of 13 meV.

Table 8.2 Isotopic Shifts in the Neutron Spectrum of $C_{24}Rb(HD)_x$

	Centre of mass		**Bond Centre**		**Observed spectrum**	
	A Site	B Site	A Site	B Site		
$(H_2)_2$	K^2=18.9B	K^2=24B	K^2=21.3B	K^2=27B	$(HD)_1$	$(HD)_2$
0.6-0.7		**0.19**		**0.11**		0.138,0.218
1.05-1.5	**0.41**		**0.26**		0.418	0.345
2.05						
vs 21	(Whole molecule vibration at 17)					
	39		**38**		vs 35	s 33
vs 42	44	**46**	41	**44**	s 43	s 42
w 51		48		45	s 51	m 50
m 59	59		58		sh 57	
	75	73	73	71	s 65	s 63
w 77	78				w 73	w 78
			83	82		
m 85	87	88		85	m 87	w 87
	89			93		
		98		97	m 99	vw 99
		101				
w 107			109		w 109	
	115		114			

The first column summarizes the $C_{24}Rb(H_2)_x$ neutron data (Figs 7.3, 7.10; Tables 7.1, 7.2). The columns labelled **Centre of mass** and **Bond Centre** give predicted $C_{24}Rb(HD)_x$ line positions calculated using Fig 8.3, according to whether the HD molecule librates about its centre of mass or the geometrical bond centre. In $C_{24}Rb(H_2)_x$, the A site has barrier constant K^2 = 14.2B and the B site K^2 = 18B (Table 8.1). For HD, values of K^2 are multiplied by, and transition energies from Fig 8.3 divided by a factor f, the ratio of B in H_2 and HD. For centre of mass rotations, f = $\frac{4}{3}$ and for bond centre rotations f = $\frac{3}{2}$. Predicted fundamental excitations are shown in **bold type**. The right hand columns summarize the observed HD spectra (Fig 7.3, 7.11); the beryllium filter spectra show extensive contamination by H_2, as well as having unreliable effective concentrations of absorbed HD. Energies are in meV throughout.

Table 8.2 (cont'd) Isotopic Shifts in the Neutron Spectrum of $C_{24}Cs(HD)_x$

	Centre of mass		Bond Centre		Observed spectra	
	A Site	B Site	A Site	B Site		
$(H_2)_2$	K^2=17.3B	K^2=24B	K^2=19.5B	K^2=27B	$(HD)_1$	$(HD)_2$
0.67		**0.19**		**0.11**		
0.99-1.2	**0.55**		**0.38**			
s 18	(Whole molecule vibration at 15)				m 12	vs 13
(w 27)					vw 22	vw 20
vs 36	**37**		**35**		m 30	vs 29
s 51	42	**46**	39	**44**	m 43	vs 45
m 62		48		45		
s 72	55		54		m 55	vw 57
					m 64	
vw 84			68			vw 69
w 91	71	73	71	71	m 72	
w 98	76		79			
	83			82		
	86	88		85	w 85	
		98		93	w 93	
w 115	109	101	103	97		

See previous page for key to column headings. $C_{24}Cs(H_2)_x$ and $(HD)_x$ data are shown in full in Figs 7.5, 7.7, 7.9 and Table 7.2. In $C_{24}Cs(H_2)_x$, the A site has K^2 = 13B and the B site K^2 = 18B. HD tunnelling spectra are not available. The beryllium filter spectra have unreliable effective concentrations of HD, but show no trace of H_2 contamination. Energies are in meV throughout.

Table 8.3 Isotopic Shifts in the Beryllium Filter Spectrum of $C_{24}Cs(D_2)_x$

(Energies in meV. Fundamentals in **bold**)

	Calculated		**Observed**	
	A Site	B Site		
$(H_2)_2$	$K^2=26B$	$K^2=36B$	$(D_2)_1$	$(D_2)_2$
0.67		**0.021**		
0.99-1.2	**0.090**			
s 18	(Vibration gives 13)		s 11	vs 12
vs 36			w 23	w 23
s 51	**33**		s 35	s 37
m 62		**40**	m 41	
s 72	52		w 52	w 50
vw 84	59		vw 59	vw 59
w 91	62			
w 98		68		m 67

Overall, therefore, the comparison of calculated and observed isotopic shifts offers qualified support for the hindered rotation model. The notable exception to this is the lowering (from prediction) of the A site libration peaks in $C_{24}Rb(HD)_2$ and $C_{24}Cs(HD)_2$.

8.3 COMPARISON WITH X-RAY RESULTS [369]

A series of X-ray diffraction experiments on Papyex[++] intercalated with rubidium to form $C_{24}Rb$ has been done[369]. The intercalate sample was contained in a centre-stick adapted for gas handling capable of being cooled to liquid helium temperatures[370]. This allowed the structure of $C_{24}Rb(H_2)_x$ to be studied in situ as a function of both temperature and H_2 concentration. The sample was oriented so that only the hk0 lines were visible. As well as the $C_{24}Rb$ order-disorder transition reported at 165K (See Section 1.4.1), the $C_{24}Rb(H_2)_2$ sample

---

++ Papyex is a form of graphite ordered in the c direction, but disordered in the ab plane, similar to HOPG. (See footnote in Section 1.4.1.)

underwent a further change in the metallic layer packing in the presence of excess hydrogen gas. Above 110K, the mean metal-metal spacing was indicated by a single broad line, but below this temperature the broad line persisted at reduced intensity and two distinct peaks also emerged in the same region of 2θ. The packing densities associated with these peaks allow the hydrogen- and alkali-rich phases to be compared with the unchanged $C_{24}Rb$. At low hydrogen fillings, no resolution of the broad peak was observed. A set of diffraction patterns is shown in Fig 8.4, and the results are summarized below:

At room temperature, the "$C_{24}Rb$" sample had a metal-metal spacing of 6.15Å, giving a stoichiometry $C_{25.0}Rb$. This is somewhat larger than the metal-metal distance of 6.05Å reported by Suzuki[79], and nearer the value in the Naylor model of 6.097Å (Fig 1.9, Section 1.4.1). For samples of $C_{24}Rb(H_2)_x$ where $x < 1$, the metal ion peak remained unresolved with a metal-metal distance under 6.24Å. Under excess hydrogen however, the low temperature structure contained 50% of a phase with a metal-metal distance of 6.18Å (almost unchanged), 30% of a 6.54Å phase (expanded), 20% of 5.98Å (compressed), and ≦5% of 4.92Å. (These proportions are estimated from the relative diffraction line intensities and are only approximate.) The metal-metal distances of 6.18Å and 5.98Å correspond to incommensurate phases, but 6.54Å and 4.92Å are the metal-metal distances in the $(\sqrt{7}\times\sqrt{7})R19.1°$ $C_{28}M$ commensurate structure (metal-metal distance 6.51Å), and the $(2\times2)R0°$ C_8M structure which also occurs in the stage I compounds (Figs 1.7, 1.5). The appearance at high hydrogen concentrations of the compressed phase with a 5.98Å metal-metal spacing should be compared with the appearance of the B site tunnelling peak at ≈0.65 meV only seen in $C_{24}Rb(H_2)_x$ when $x > 0.8$ (Figs 7.3, 7.4).

A simple check can be carried out on the above metal-metal distances. Since alkali metal intercalation is always carried out at

Fig 8.4 In-plane diffraction pattern of $C_{24}Rb(H_2)_x$ under excess Hydrogen as a function of temperature [ref 369]

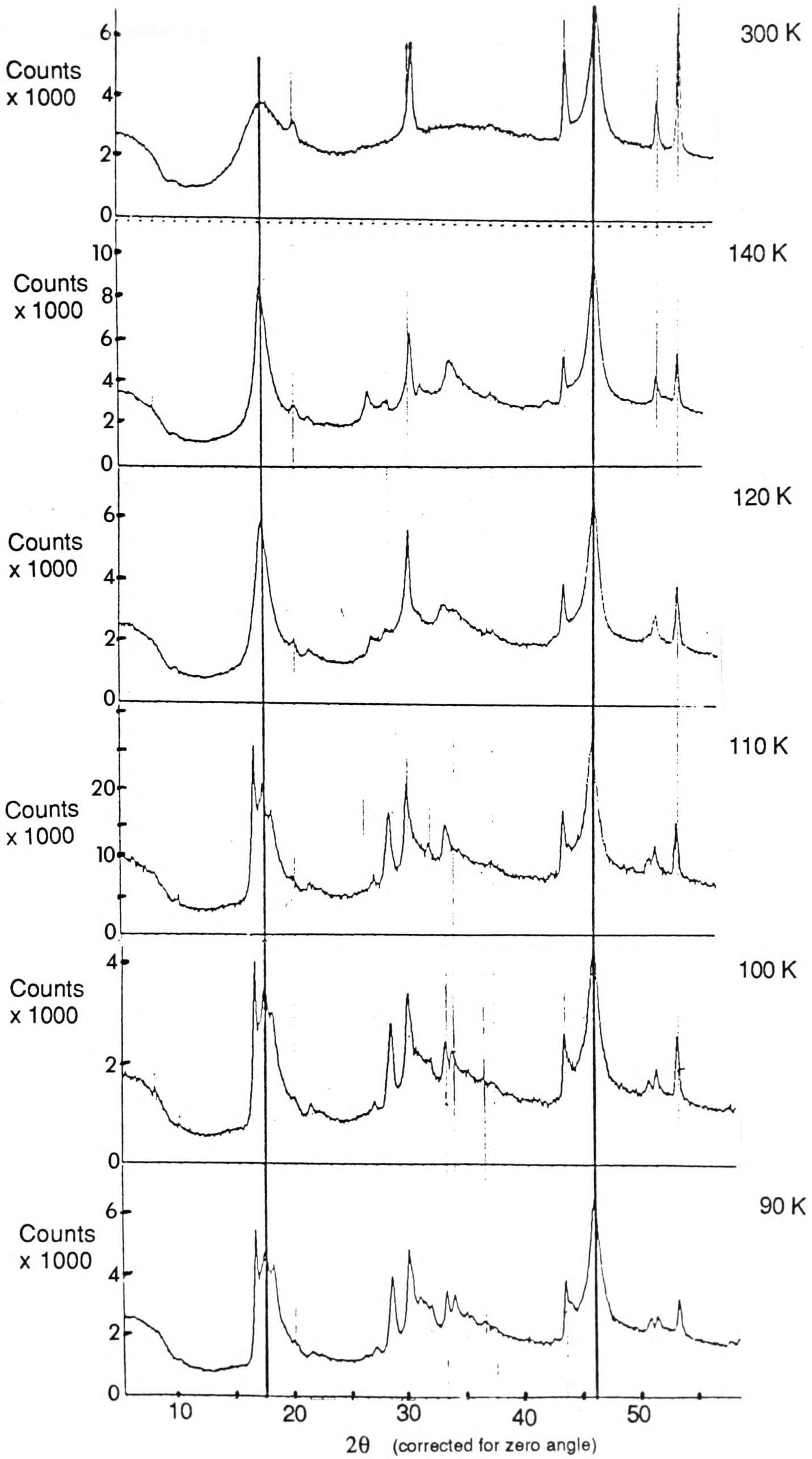

elevated temperatures, it can be assumed that no metal is absorbed or desorbed on physisorption of H_2 at ≈100K. Neutron powder diffraction from the 00ℓ planes further shows that no change in staging occurs on gas physisorption (Section 1.5.2), and this means that the average in-plane metal-metal distance must remain constant, any patches of denser packing being balanced by rarefied patches. This is precisely what is observed. The carbon to caesium ratio is proportional to the square of the metal-metal distance, and the mean metal-metal distance d is given by the equation below. (Compositions have been slightly adjusted so as to add up to 100%):

$$0.2 \times 5.98^2 + 0.3 \times 6.54^2 + 0.45 \times 6.18^2 + 0.05 \times 4.92^2 = d^2 \quad (8.1)$$

This makes d = 6.195A.

The calculation shows that in this model, a small proportion of the (2×2)R0° structure is needed to maintain the stoichiometry at the room temperature value; this is not necessarily the most energetically favoured stoichiometry for this stage in the ordered phases below 165K.

8.4 SITE STRUCTURE OF THE INTERCALATES

8.4.1 Numbers of Sites

Considering limiting cases first, the $(\sqrt{7}\times\sqrt{7})$R19.1° $C_{28}M$ structure (Fig 1.7) consists of a commensurate triangular lattice of metal ions with a metal-metal distance of 6.51Å and two triangular sites per metal ion. These sites are denoted Y sites, and if every triangle contained one hydrogen molecule, a stoichiometry $C_{28}M(H_2)_2$ would result (Fig 8.5). (A rhombus shaped site could be made by joining two triangular sites together with stoichiometry $C_{28}M(H_2)_1$, but in the absence of distortion, the dimensions are the same as for absorption into the edge of a Y site; it is not considered separately.) The (2×2)R0° structure (Fig 1.5), which would give a stage II stoichiometry $C_{16}M$, also consists of a

Fig 8.5 Sites in the (2 x 2) R0° and (√7 x √7) R19.1° Structures

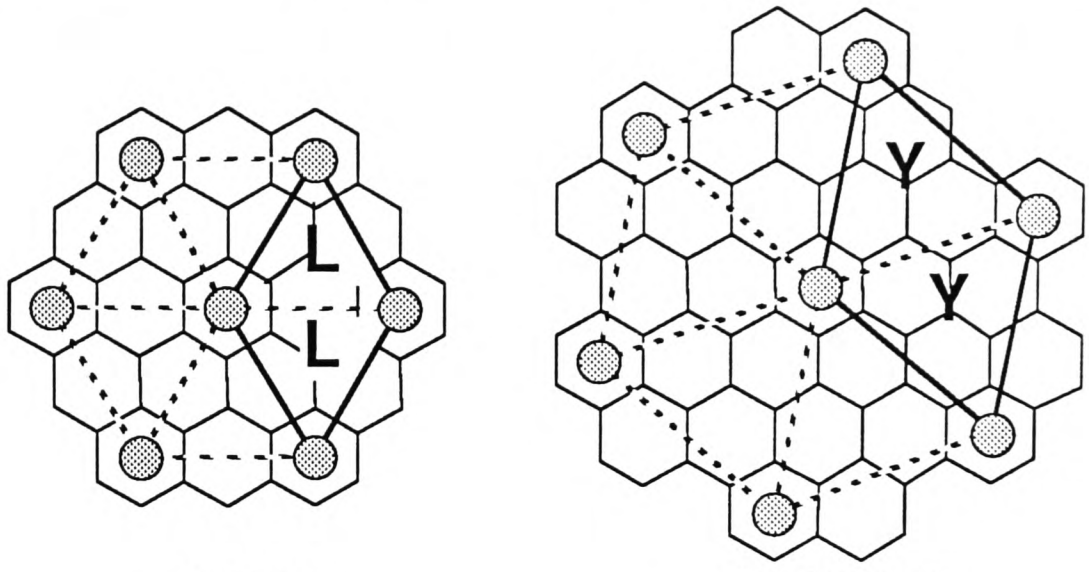

(2 x 2) R0°
2 L sites per metal ion

(√7 x √7) R19.1°
2 Y sites per metal ion

Metal ions are shown as filled circles on the hexagonal graphite lattice. The unit cell is shown by heavy lines, and sites are marked by dotted lines. The unit cell has been moved sideways for clarity. (c.f. Figs 1.5, 1.7)

commensurate triangular lattice with two sites per metal ion, but the metal-metal distance is only 4.92Å; these small triangular sites are denoted L sites. In between these two extremes lie the incommensurate room temperature structures of the stage II intercalates with stoichiometries $C_{22.0}M$ to $C_{25.5}M$ and metal-metal distances of 5.79-6.24Å depending on the metal ion. These structures have two triangular sites per metal ion of intermediate size (I sites). The site structures and dimensions are shown in Figs 8.5, 8.6 and 8.9.

In the case of the low temperature domain structures of the stage II intercalates, things are a little more complex. The Naylor model[96] for $C_{24}Rb$ has hexagonal 7 atom fragments of the (√7×√7)R19.1° structure separated by domain walls (Fig 1.9). If the metal ion superlattice does not change with the introduction of small quantities of hydrogen, a unit cell containing 7 Rb^+ ions can be identified with 6 Y sites, 3 nearly rectangular sites denoted Z and 2 L sites.## The stoichiometries per

---

The stage I intercalates with an L site structure do not physisorb gases. They also, however, have a commensurate room temperature structure and low metal ion mobility.

Fig 8.6 Site structure in an Incommensurate Lattice

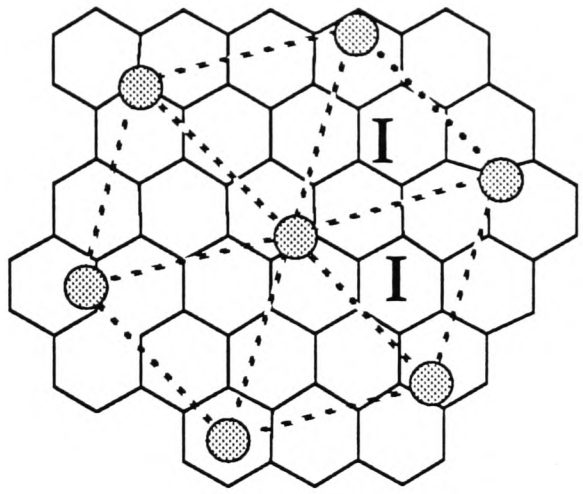

2 I sites per metal ion

The metal - metal distance varies with the metal ion, and there is no long range order.
The metal - metal distance shown here is 6.05 Å.

Fig 8.7 Sites in Naylor's domain structure for $C_{24}Rb$ at low temperature

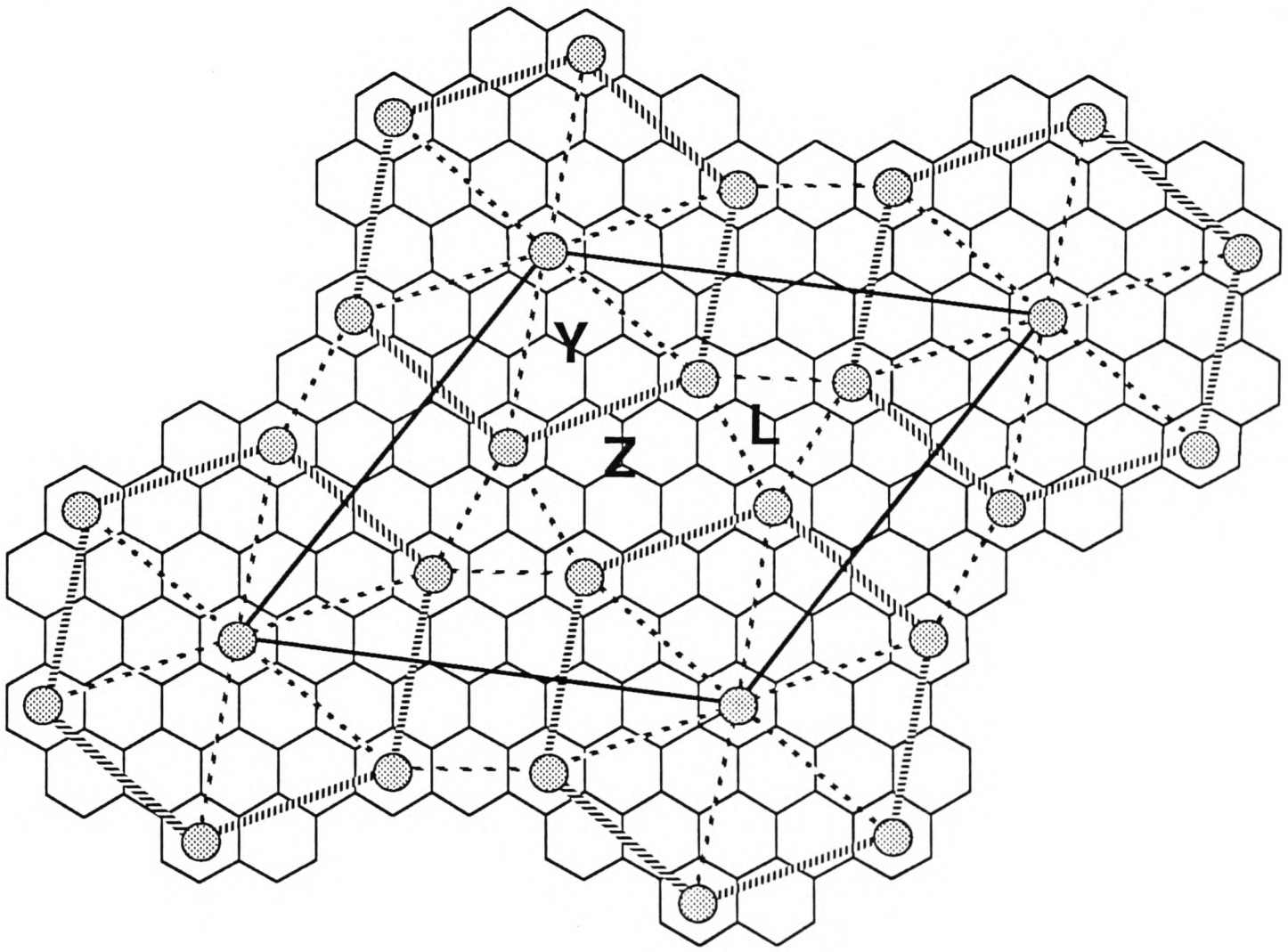

Metal ions are shown as filled circles on the hexagonal graphite lattice. The unit cell containing 7 Rb^+ ions is shown by heavy lines, and sites are marked by dotted lines. Each unit cell has 6 Y sites, 3 Z sites and 2 L sites, giving stoichiometries per metal ion 0.86, 0.43 and 0.29 respectively, total 1.57, or 1.29 excluding L sites. If the Z sites were double filled a stoichiometry 2.00 would result. (c.f. Fig 1.9)

metal ion of the Y, Z and L sites are 0.86, 0.43 and 0.29 respectively, total 1.57, or 1.29 excluding L sites. The stoichiometry of 0.86 for Y sites is significant because the zero intensity intercept for the B site peak in the neutron time of flight spectrum (≈0.65 meV) occurs at a filling $(H_2)_{0.81}$ (Fig 7.4). The site structure for $C_{24}Rb$ is shown in Fig 8.7.

In the case of $C_{24}Cs$, Clarke's structure in the low temperature limit[84,92] (Fig 1.8) gives a 19 ion unit cell with 24 Y sites, 6 Z sites and 2 L sites with stoichiometries per metal ion 1.26, 0.32, and 0.11, total 1.69, or 1.58 excluding L sites. This is shown in Fig 8.8.

These figures can be explained by reference to a general topological principle: to get a limiting stoichiometry $C_xM(H_2)_2$ in a single plane, the co-ordination numbers of the metal ions and the hydrogen molecules must be in a 2:1 ratio, irrespective of the metal: carbon ratio and the exact site structure. In the context of underlying hexagonal geometry, the only regular site structure in which this occurs is a triangular lattice of metal ions with a hydrogen molecule in the centre of every triangle as in the (2×2)R0° and (√7×√7)R19.1° commensurate structures and the room temperature incommensurate structure (co-ordination numbers 6 and 3). This explains why structures including Z sites cannot give a stoichiometry $C_{24}M(H_2)_2$ unless some sites are double filled, absorption occurs along site edges (co-ordination number 2), or clusters of hydrogen molecules form containing a reduced concentration of metal ions. To get a greater filling than $(H_2)_2$, hinted at by Watanabe[116], (Table 1.1), one of these latter effects would have to occur.

8.4.2 Site Dimensions

In their paper on gas physisorption by stage II intercalates, Watanabe et al[116] stated that the stage I intercalates C_8M do not physisorb hydrogen because the metal-metal distance is too small to

Fig 8.8 Sites in Clarke's domain structure for $C_{24}Cs$ at low temperature

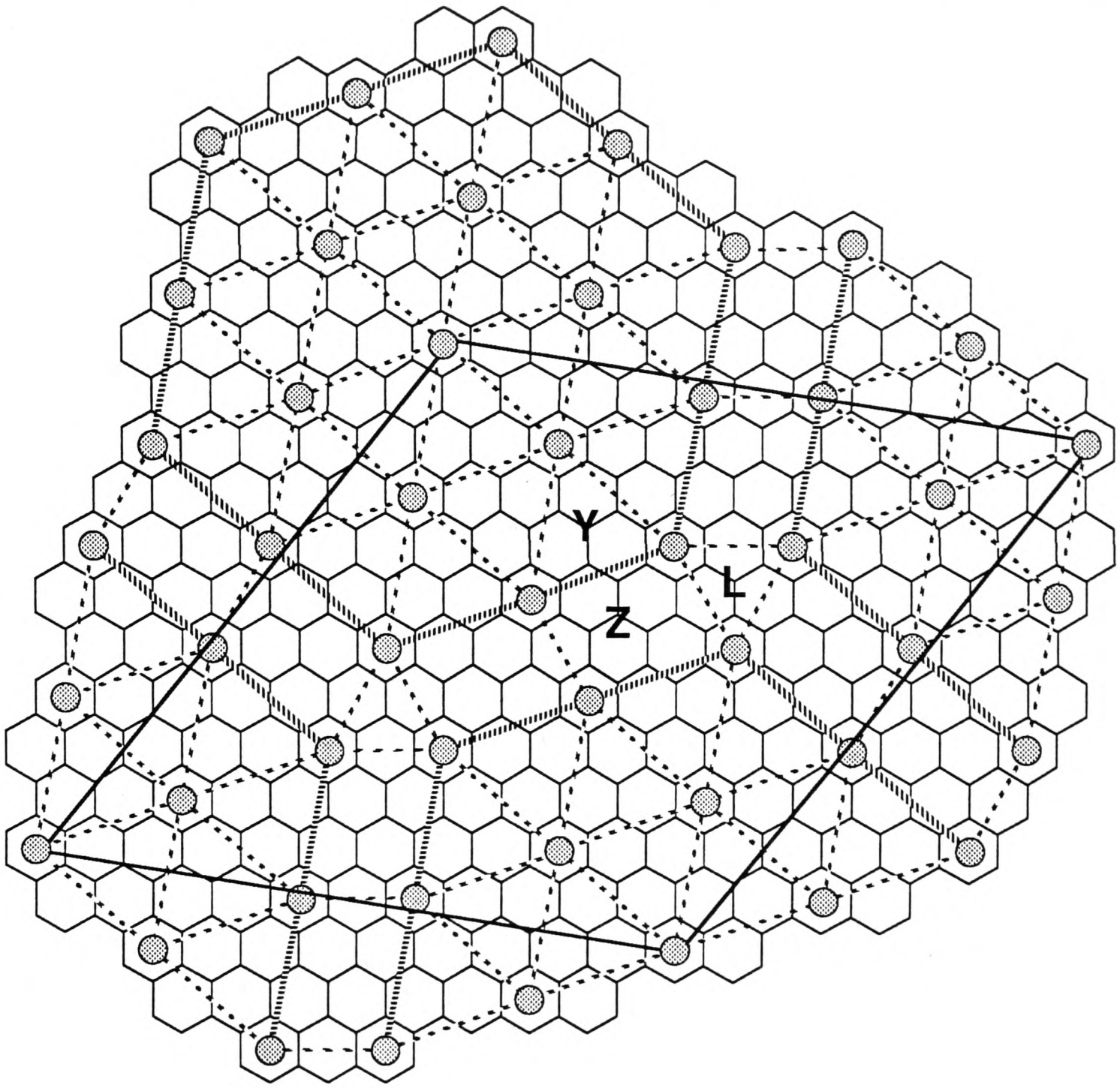

Metal ions are shown as filled circles on the hexagonal graphite lattice. To save space, only one domain of caesium ions has been shown in full. The unit cell containing 19 Cs^+ ions is shown by heavy lines, and sites are marked by dotted lines. Each unit cell has 24 Y sites, 6 Z sites and 2 L sites. Site stoichiometries per metal ion are 1.26, 0.32 and 0.11, total 1.69, or 1.58 excluding L sites. (c.f. Fig 1.8)

allow a hydrogen molecule to pass through the lattice. This is a kinetic effect and is likely to be important in the stage I compounds because the metal ions are rigidly fixed. In the stage II compounds, however, the metal ions are much freer to move, and thermodynamic considerations of whether a site is large enough to accommodate the molecule in question are likely to dominate. Site dimensions to atomic centres are shown in Fig 8.9; the in-plane size of the commensurate Y, Z and L sites does not vary with the metal ion. The next step is to insert the Van de Waals' diameters of the metal ions and graphite layers, and to compare the space left with the Van de Waals' diameters of the gas molecules.

Considering the c axis first, the expansion in the distance between the graphite layers on intercalation to C_8K, Rb, Cs is only 2.05, 2.33 2.59A respectively. This is significantly less than the diameters of the metal ions of 2.66, 2.98 and 3.30A [29] (See Fig 1.2 and Section 1.3.4) and also less than the Van de Waals' diameters of hydrogen, nitrogen, argon and methane of 2.40, 3.00, 3.80 and 4.00 A respectively[116] (Table 1.1). (The Van de Waals' shape of hydrogen is nearly spherical, although this is less true for nitrogen[121].) All this, together with the expansion in the c axis parameter of $C_{24}K$ from 8.67 to 8.96A on deuterium absorption[116], suggests that the non-absorption of nitrogen, argon and methane by $C_{24}K$ is determined by its small c axis.

In the ab plane, however, the position is reversed: the commensurate Y, Z and L sites are smallest for $C_{24}Cs$, owing to the greater size of the Cs^+ ion. The Van de Waals' sizes of Y, Z, L and I sites are shown for all $C_{24}M$ in Fig 8.9. All the sites including the L site are large enough to accommodate a hydrogen molecule, although the L site is too small to allow it to pass through. Furthermore, all the sites except the L and R sites, and possibly the I site in $C_{24}Cs$, will accommodate a methane molecule. A continuous lattice of Y or I sites is, however, too

Fig 8.9 Site geometries to atomic centres

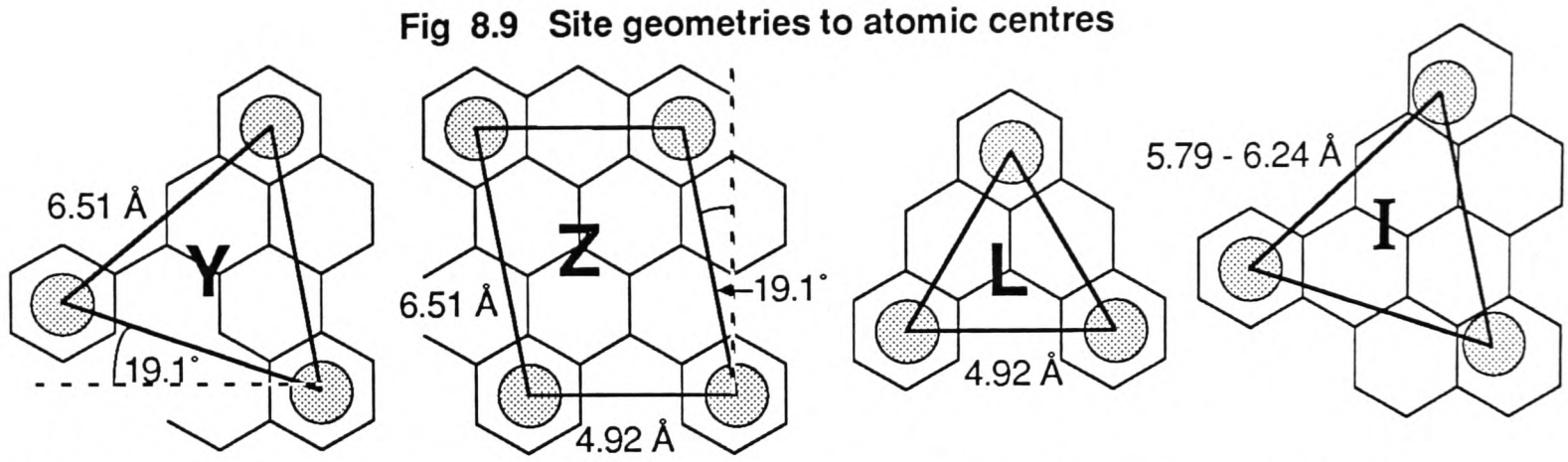

Site dimensions to atomic centres in the *ab* plane for the commensurate Y, Z and L sites are independent of the metal ion as shown. The size of the I site, however, varies from 5.79 Å in $C_{24}K$ to 6.05 Å in $C_{24}Rb$ and 6.24 Å in $C_{24}Cs$. The *c* axes for all sites are 5.40, 5.68 and 5.94 Å in $C_{24}K$, Rb, Cs

Van de Waals' sizes of Sites

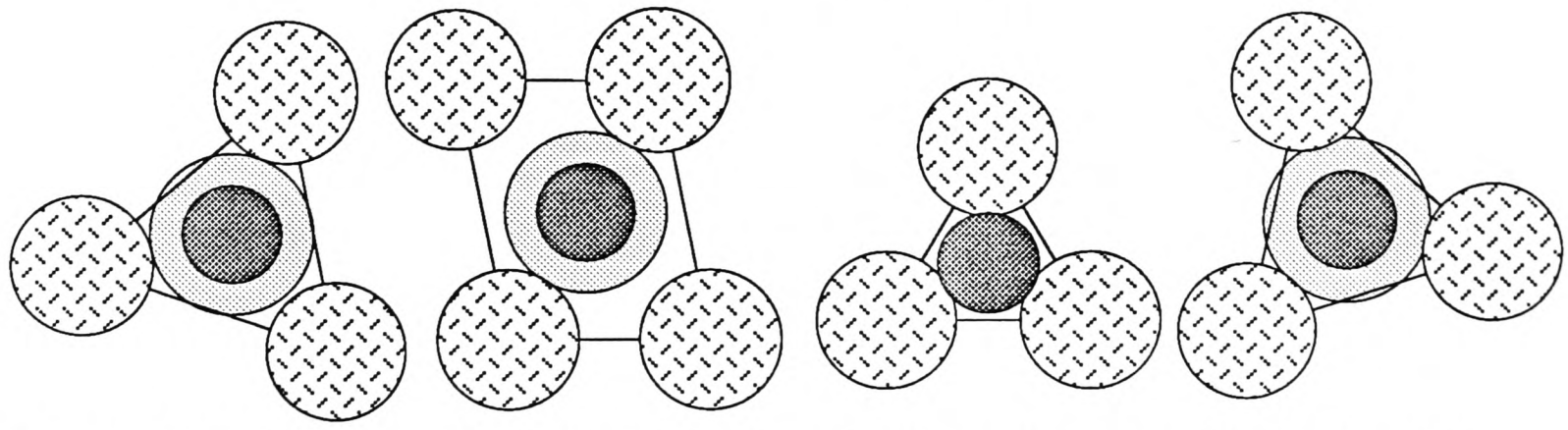

The filled circles indicate the Van de Waals' size of caesium ions, with hydrogen (dark) and methane (light) molecules in the site. (The I site size to atomic centres has been adjusted accordingly.) In potassium and rubidium intercalates, the metal ions will be smaller, and the sites correspondingly larger in the *ab* plane.

	Site Centre				Site edge			
	Y	Z	L	I	Y	Z	L	I
K	4.86*	4.72	3.02*	4.03*	3.85	**	2.26	3.13
Rb	4.54*	4.40	2.70	4.01*	3.53	**	1.94	3.07
Cs	4.22*	4.08	2.38	3.91*	3.21	**	1.62	2.94

The figures give the diameter of the largest circle which can be fitted into a site in the plane of the metal ions.

Van de Waals' diameters of H_2, N_2, Ar, CH_4 = 2.40, 3.00, 3.80, 4.00 A [116]

Van de Waals' diameters of K^+, Rb^+, Cs^+ = 2.66, 2.98, 3.30 A [29]

* Figures for an isolated gas molecule. For molecules in adjacent sites, the maximum is 3.76A for any Y site, 2.84A for an L site. For I sites, it is 3.34, 3.49, 3.60 A for K, Rb, Cs intercalates.

** Z sites have a long edge equivalent to a Y site and a short edge equivalent to an L site.

The c axis is 2.05, 2.33, 2.59 A for all sites in $C_{24}K$, Rb, Cs (excluding any swelling on gas absorption).

small to accommodate a full complement of methane molecules. A further consequence of the relatively large dimensions of the sites is to make attractive forces important in calculating stabilization energies.

8.4.3 Site Geometries: The Calculated Barrier to Rotation

The explanation of the tunnelling and librational spectra has invoked the model of a two-fold hindered rotor in an axially symmetric potential (Fig 6.6). The most reasonable interpretation of this in terms of the intercalate structure is to propose that the most stable orientation of the hydrogen molecule is perpendicular to the graphite plane, and that if it is rotated so as to lie in the plane, its energy is independent of its orientation relative to the metal ion and graphite lattices (Fig 8.10). (For a triangular site, a stable in-plane orientation would give a sixfold barrier to rotation.)

The potential energy of a single hydrogen molecule in a $(\sqrt{7}\times\sqrt{7})R19.1°$ $C_{28}Cs$ superlattice (ie a Y site) has been calculated by Trouw[371] on the basis of interactions of the hydrogen quadrupole with the charges on the caesium ions and the graphite lattice, and also Van de Waals' forces. (The caesium ions had charge +1, the negative charges residing wholly on the graphite lattice. The hydrogen molecule was neutral overall, the quadrupole represented by a charge of +0.47 at each atomic nucleus and -0.94 at the bond centre.) He found that the most stable orientation of the hydrogen molecule was perpendicular to the graphite plane, and that the coplanar orientation was less stable by 7.8-8.7 KJ/mol (81-91 meV; 11-12B) with an approximately sinusoidal potential and a relatively small dependence on the in-plane orientation (Fig 8.10). This is very close to the model potential chosen for the A site in $C_{24}Cs(H_2)_x$ which was sinusoidal with K^2 = 13B and no energy variation with in-plane orientation (Section 8.1). It remains, however, to calculate the energies of hydrogen molecules in Z and L sites as a

Fig 8.10 Scale representation of a Hydrogen molecule perpendicular and parallel to the graphite plane in a ($\sqrt{7}$ x $\sqrt{7}$) R19.1° Site in a Caesium Intercalate

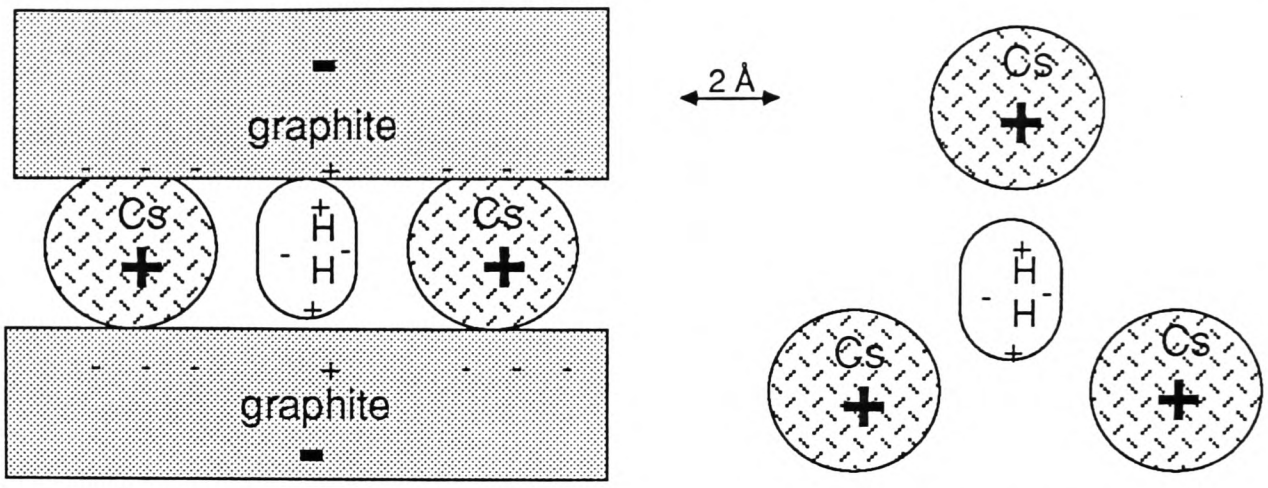

Integral charges are shown in bold, fractional charges and polarizations in small type. The geometry of the hydrogen molecule is only approximate. (For further information on the shape of the hydrogen molecule see Silvera [121].)

Calculated energy of a Hydrogen molecule in a ($\sqrt{7}$ x $\sqrt{7}$) R19.1° Site in $C_{24}Cs$ as a function of its orientation

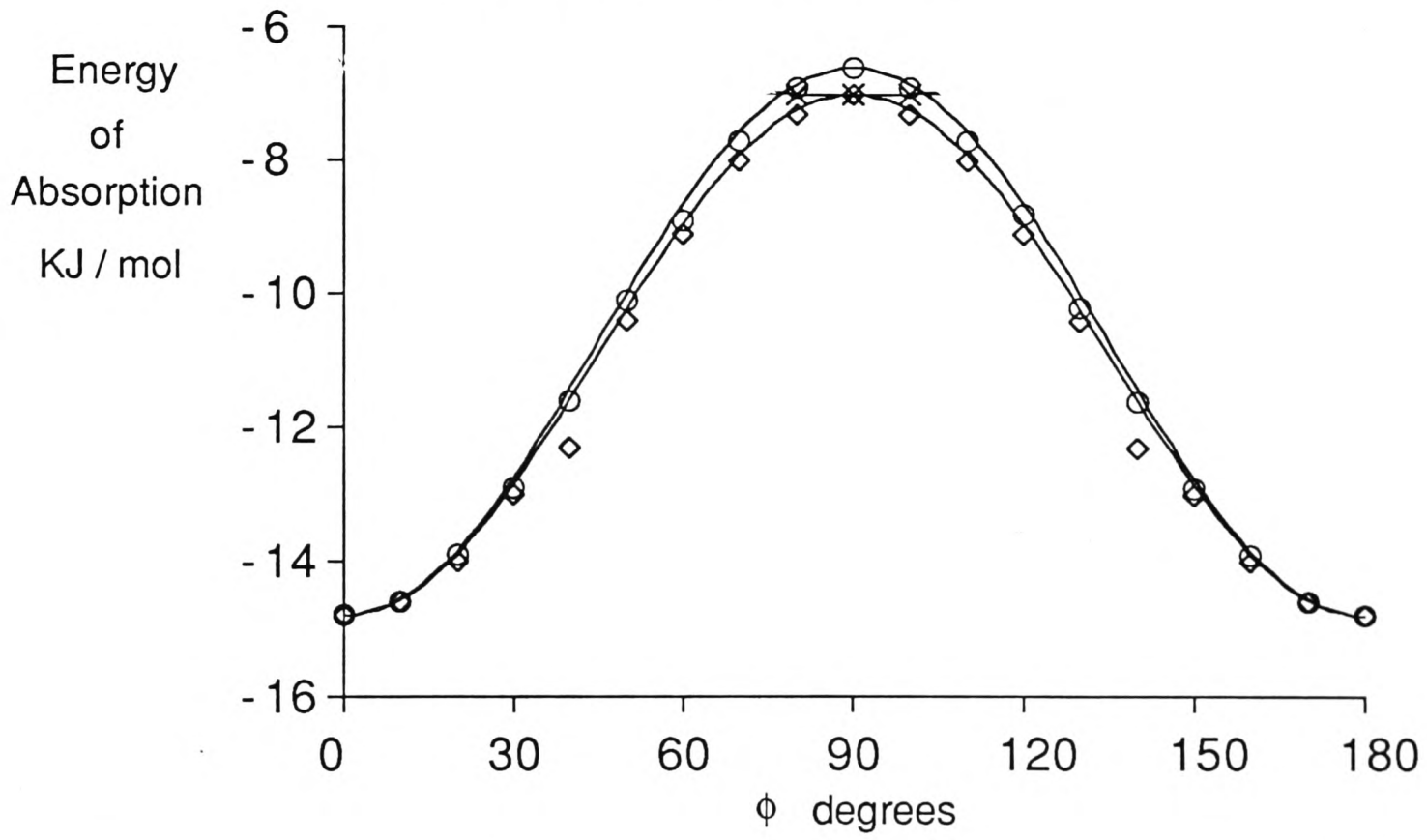

The symbols are Trouw's figures[371] with ϕ the angle between the internuclear axis of the hydrogen molecule and a line normal to the graphite plane. The stable conformation is perpendicular to the graphite plane. The diamonds and circles show the effect of rotation from this conformation through the plane of the metal ions, so that the internuclear axis points respectively between two metal ions and directly at a metal ion. The lines are cosine curves fitted to the tops and bottoms of the potential wells only.

function of angle of rotation as well as the calculation of the barrier to rotation as a function of site size in an I site, but we conclude that a fairly good model for the hydrogen rotational potential can be developed by the above procedure.

8.5 TRANSLATIONAL MOTION OF HYDROGEN MOLECULES

8.5.1 The Potential

So far, the discussion has centred on the rotational excitations, whereas the translational motion must also be considered, in particular with reference to the lines at 13 meV in $C_{24}Cs(H_2)_1$ and 22 meV in $C_{24}Rb(H_2)_1$ not explained by the hindered rotor model (Section 8.1). Trouw[371] also calculated the energy of a hydrogen molecule oriented perpendicular to the graphite plane in a $(\sqrt{7}\times\sqrt{7})R19.1°$ $C_{28}Cs$ structure (Y site) as a function of distance parallel to the graphite plane from a Cs^+ ion along the median of the site. (The distance between the caesium nucleus and the site edge along this line is 5.64Å.) The potential is shown in Fig 8.11 and gives a very flat potential minimum 3.6Å from the Cs^+ nucleus and a barrier between Y sites of only 1.27 KJ/mol (13.2 meV)

Fig 8.11 Calculated energy of a Hydrogen molecule in a $(\sqrt{7} \times \sqrt{7})$ R19.1° Site in $C_{24}Cs$ as a function of position in metal ion plane

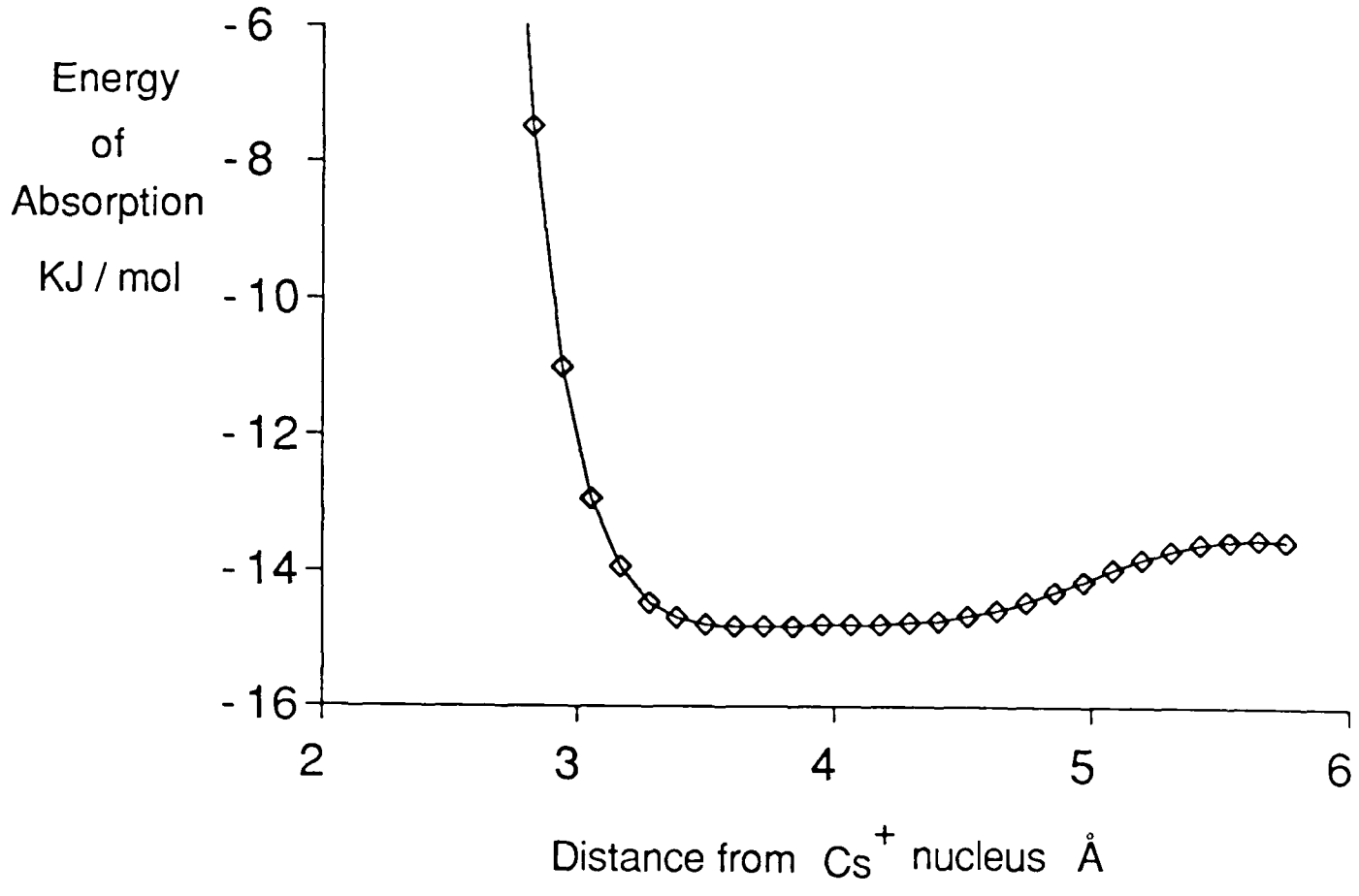

much lower than both the barrier to rotation and the gas absorption energy. This means that the in-plane translational potential consists of a $(\sqrt{7}\times\sqrt{7})R19.1°$ lattice of potential minima, similar to the lattice of Cs^+ ions, with low saddles joining the minima. This lattice of minima is too complex for direct calculation of the energy levels, so as an approximation, a simple double well potential was chosen. Various well shapes with easily calculable levels were used, but none of them were wholly satisfactory as the Trouw potential is difficult to model, owing to its very flat minimum.

8.5.2 Possible Excitations: the Harmonic Approximation

First, the two halves of the double well were approximated to harmonic oscillators. This gave a v = 0→1 transition at 5.8 meV (Fig 8.13). In addition, the interaction between the wells in the ground state was calculated using the formula of Gomez et al[372].

The potential in the two wells can be described as follows:

$$V = V_A = \tfrac{1}{2}m\omega^2(x+x_0)^2 \text{ for } x<0 \qquad (8.2)$$

$$V = V_B = \tfrac{1}{2}m\omega^2(x-x_0)^2 \text{ for } x>0$$

with V_A and V_B the potential in the two wells, m the mass of the tunnelling species, x its displacement and $2x_0$ the well separation.

The non-interacting ground state wavefunctions are then given by:

$$\psi_A = c\ \exp[(-m\omega/2\hbar)(x+x_0)^2] \qquad (8.3)$$

$$\psi_B = c\ \exp[(-m\omega/2\hbar)(x-x_0)^2]$$

with c as the normalization constant and $\hbar\omega$ as the v=0→1 energy.

If the wells are now allowed to interact, the energy levels for the ground state, $E_\pm$ are now given by:

$$E_+ = \tfrac{1}{2}\hbar\omega + \eta' \quad \text{and} \quad E_- = \tfrac{1}{2}\hbar\omega - \eta' \qquad (8.4)$$

where $2\eta'$ is the tunnelling splitting and $\eta' << \hbar\omega$.

$$\eta' = -Kc^2\ \exp[-(m\omega/\hbar)x_0^2] \ /\ 2(m\omega/\hbar) \qquad (8.5)$$

where $K = 2m\omega^2x_0$.

c, the normalization constant is defined as follows[373]:

$$c^2 = \alpha/\sqrt{\pi} \quad \text{where} \quad \alpha = (m\omega/\hbar)^{\frac{1}{2}} \tag{8.6}$$

The tunnelling splitting calculated by this method was found to be 3.85 J/mol or 40 μeV.

8.5.3 Possible Excitations: the Double Well Approximation

Another approach used Manning's double well potential, originally used to calculate the energy levels for the inversion mode of ammonia. This is well documented in the original[374], so only an outline of the solution is given here.

The potential V in cm^{-1} as a function of displacement r is given by:

$$V = \frac{1}{k\rho^2}\left[-\frac{\beta}{2}\left(\frac{\beta}{2} + \frac{1}{2}\right) \operatorname{sech}^2\left(\frac{r}{2\rho}\right) - D\left(\operatorname{sech}^2\left(\frac{r}{2\rho}\right) - \operatorname{sech}^4\left(\frac{r}{2\rho}\right) \right) \right] \tag{8.7}$$

$k = 8\pi^2 cm/h$ where c is now the speed of light in cm/sec, m is the mass of the hydrogen molecule and ρ, β, and D are fitting parameters. The potential, symmetric in r and zero at $r = \pm\infty$ and is large and negative at small absolute values of r with minima at $\pm r_0$ (Fig 8.12). To fit Trouw's calculated potential, a large positive constant C was added and V was converted to KJ/mol (1 cm^{-1} = 11.96 KJ/mol).

Fig 8.12 General Form of Manning's Potential [ref 374]

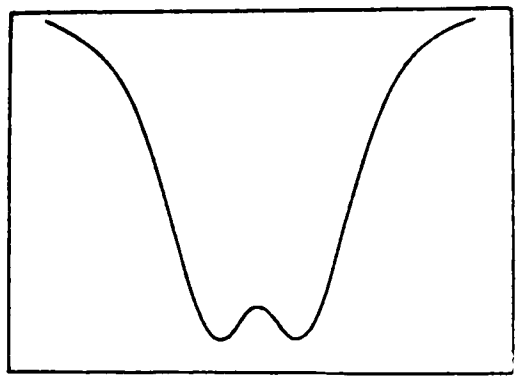

r_0 is given by:

$$\operatorname{sech}^2\left(\frac{r_0}{2\rho}\right) = \frac{(\beta/2)(\beta/2 + \frac{1}{2}) + D}{2D} \tag{8.8}$$

and the barrier between the two wells is:

$$\frac{1}{k\rho^2} \frac{\left[D - (\beta/2)(\beta/2)\right]^2}{4D} \tag{8.9}$$

The Schrodinger equation for the vibration can be solved by making the substitution $x = \tanh^2(r/2\rho)$ and expanding in integral powers of x for symmetric solutions and half-integral powers of x for antisymmetric solutions. The coefficients are found by a recursion relation which can be reduced to a continued fraction with eigenvalues λ.

The coefficient of x^n is given by:

$$0 = 1 - \cfrac{Q_0}{1 - \cfrac{Q_1}{1 - \cfrac{Q_2}{1 - \ldots}}} \qquad (8.10)$$

where $$Q_n = \frac{(m + n + 1)(m + n + \frac{1}{2})}{P_n P_{n+1}} D \qquad (8.11)$$

where $$P_n = (m + n - \lambda)(m + n + \beta + \tfrac{1}{2} - \lambda)$$

For symmetric levels, $m = 0$ and for antisymmetric levels, $m = \frac{1}{2}$. As n increases, Q_n decreases until it becomes negligible in comparison with unity.

The first step in the solution was to find values of ρ, β, D and C so as to fit Trouw's data. This was done using program MINMAX [375] employing a NAG fitting routine[376]. It was found that the four parameters allowed insufficient flexibility for good fitting and that the closest values were $\rho = 1.964\times10^{-6}$, $\beta = 72.53$, $D = 1975.7$, $C = 36024$ (Fig 8.13). (cf Manning's values for ammonia $\rho = 4.17\times10^{-9}$, $\beta = 70$, $D = 1920$.)

The continued fraction was solved for each energy level by an iterative procedure using program NH3FIT in a method similar to the solution of the hindered rotor wave equation by ROTFIT (Section 6.4.1). Which level was converged upon depended entirely on the initial guesses for λ. It was found that for the ground state, the continued fraction was negative only over a very narrow range of λ with singularities nearby, so good initial guesses were needed. In the ground state, λ was

approximately -0.764 and in the first excited state it was -0.41, becoming positive in the higher excited states. For the initial guesses, Q was calculated to 100 terms, and then in the final calculation to 100,000 terms, with final Q values $<2\times10^{-6}$ and energies bracketed to within 0.003 J/mol in the ground state, less accurately in the excited states.

The energy levels are shown in Fig 8.13. The tunnelling splitting in the ground state is 1.37 J/mol or 14.1 μeV, with a vibration at 6.87/7.35 meV, the tunnelling splitting in the first excited state being 480 μeV. The entire diagram could be calculated in a few minutes using a VAX 11/780.

8.5.4 Discussion

The two model potentials predict fairly similar sets of energy levels, with a ground state level split by tunnelling of 14-40 μeV, one or two excited vibrational levels localized in each potential well and a $v = 0\rightarrow1$ transition at 6-7 meV. The calculated $v = 0\rightarrow1$ transition energy, however, is at least a factor of two down on the low energy peak in the beryllium filter spectrum of $C_{24}Cs(H_2)_x$ at 13-18 meV, and no peaks have been observed at the predicted tunnelling and vibration energies. (This might, however, be caused by the choice of instruments.) The energy levels for vibration of the hydrogen molecule perpendicular to the graphite layers have still to be calculated, and this may account for the peaks at 13-18 meV and 21 meV in the spectra of $C_{24}Cs(H_2)_x$ and $C_{24}Rb(H_2)_x$.

The calculated potentials also indicate that the hydrogen molecule is weakly bound into each site, and that considerable recoil might be expected at high energy transfers in beryllium filter spectroscopy. Furthermore, the vibrational states for $v > 1$ are delocalized, so a continuum of translational states will form at energies higher than

Fig 8.13 Translational Energy levels of a Hydrogen Molecule in Double Well approximations of the Intercalate Potential

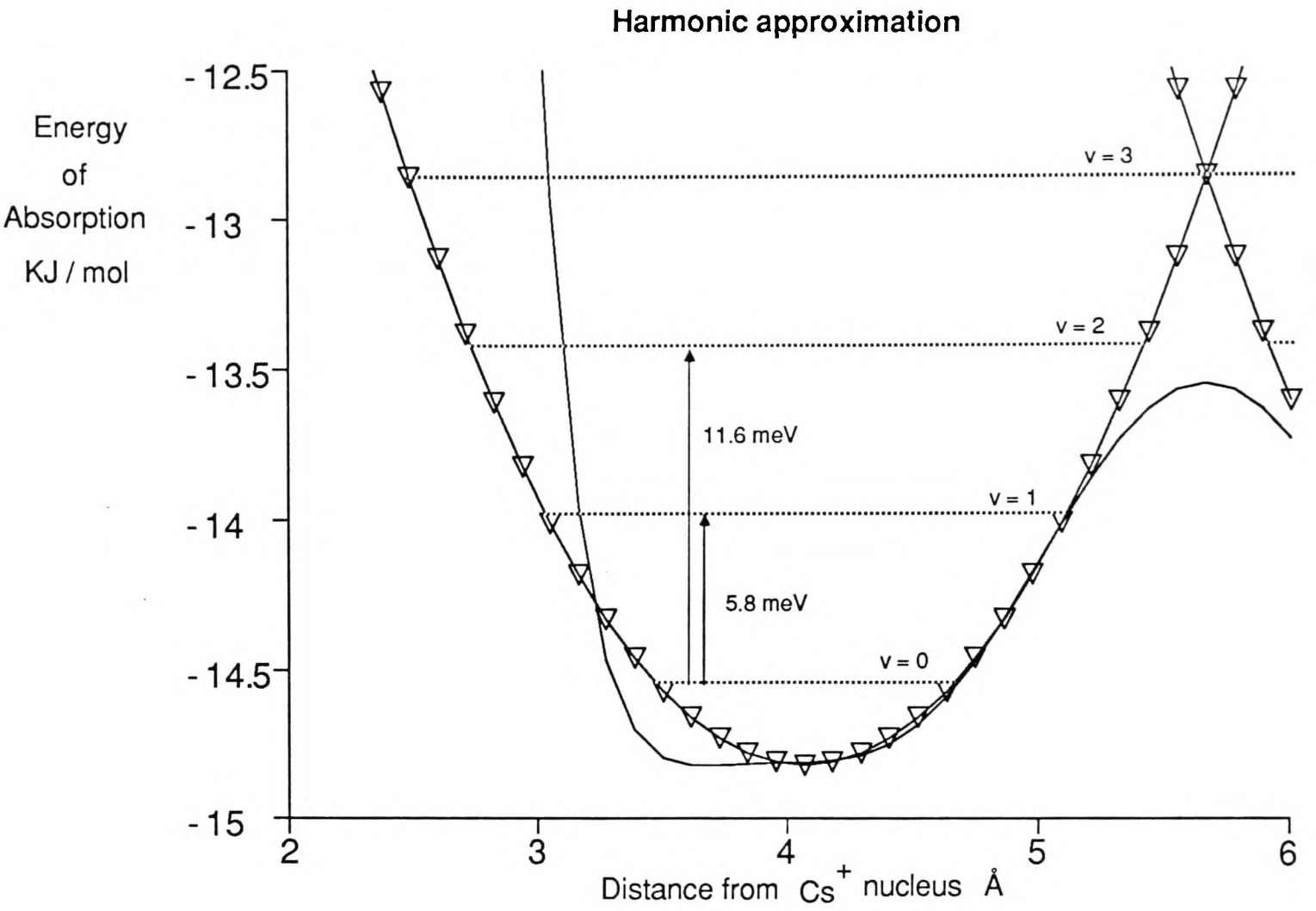

The plain line shows Trouw's calculated potential, the lines with symbols the model potentials and the dotted lines the energy levels. Interactions between the two wells have been omitted from the diagram of the harmonic approximation. The superscripts ± indicate symmetric and antisymmetric levels. The ground state tunnelling splittings in the two model potentials are 40 and 14 μeV (1 meV = 96.487 J/ mol).

13 meV, similar to an electron band structure in a metal. Finally, the relatively large translational tunnelling splitting predicts a very high hydrogen mobility through an intercalate layer, independent of the temperature. Thus the rate of sample equilibration for a fixed non-limiting amount of absorbed hydrogen is governed by the rate of transfer between layers, determined by the gas vapour pressure over the sample. This tunnelling effect will not occur for nitrogen, argon and methane, and the kinetics of absorption will be different in these cases.

8.6 CONCLUSION: THE STRUCTURAL MODEL

In their original paper, Beaufils et al[361] assigned the time of flight spectra of hydrogen in $C_{24}Rb(H_2)_x$ and $C_{24}Cs(H_2)_x$ to rotational tunnelling in a two site model. Similarly, beryllium filter spectra of $C_{24}Rb(H_2)_x$ and $C_{24}Cs(H_2)_x$[362,367] were assigned to librational transitions of the hydrogen molecule in the two sites[362]. The two site model has been confirmed by the more recent tunnelling spectra of $C_{24}Rb(H_2)_x$ and the librational spectra of $C_{24}Cs(H_2)_1(N_2)_x$, both measured as a function of increasing gas concentration (Figs 7.3, 7.8; Tables 7.1, 7.2). Both sets of spectra indicate one and two peaks respectively at low gas concentrations, assigned to transitions in the A site, and at high fillings these are joined by further peaks, assigned to transitions in the B site.

Originally, the A site was proposed as being tetrahedral, and the B site octahedral[361]. Examination of the splitting patterns for the rotational levels of hydrogen in potential fields of these symmetries, however, shows that these site geometries cannot be reconciled with the observed neutron spectra, and that a lower symmetry field is required (Section 8.1 and [ref 362]). An axially symmetric cos2θ potential fulfils this requirement, and accounts for both the tunnelling and the librational spectra in $C_{24}Rb(H_2)_x$ and $C_{24}Cs(H_2)_x$, the barriers to

rotation in $C_{24}Rb(H_2)_x$ being 57 and 78 meV (5.5 and 7.5 KJ/mol) in the A and B sites, and in $C_{24}Cs(H_2)_x$ 51 and 78 meV (4.9 and 7.5 KJ/mol) (Section 8.1).

The axial site symmetry with a twofold barrier to rotation can be fitted with the staging model for the intercalates by proposing that the hydrogen molecules are accommodated within the plane of the metal ions [116], and that the minimum energy orientation has the H-H internuclear axis perpendicular to the plane of the metal ions. To maintain axial or near-axial symmetry, the energy of a hydrogen molecule constrained so as to be coplanar with the metal ions would have to vary very little with its in-plane orientation. The proposals and barrier heights are consistent with the modest c axis expansion on hydrogen absorption (Section 1.5.2), the hydrogen absorption energy of 9-12 KJ/mol (Table 1.1) and potential calculations by Trouw (Section 8.4.3).

The A site can be identified in the domain model of the intercalate structure (Figs 8.7, 8.8). X-ray data from $C_{24}Rb(H_2)_x$ show that the $C_{24}Rb$ in-plane structure remains unaltered at hydrogen concentrations less than about $(H_2)_1$ (Section 8.3). This means that the A site must exist in the undisturbed $C_{24}Rb$ domain structure; the only single site common enough is the $(\sqrt{7}\times\sqrt{7})R19.1°$ Y site, of which there are 0.86 per Rb^+ ion. Further evidence associating the A site transitions in the neutron spectra with the Y site in the structural model is Trouw's potential calculation on a hydrogen molecule in a Y site in $C_{28}Cs$ (Section 8.4.3), and the fact that the B site peak in the tunnelling spectrum of $C_{24}Rb(H_2)_x$ has an intercept of zero intensity at hydrogen concentration $(H_2)_{0.81}$ (Fig 7.4). (In $C_{24}Cs$, the domains are larger and there are 1.26 Y sites per Cs^+ ion (Fig 8.8). Tunnelling data from $C_{24}Cs(H_2)_x$ as a function of increasing hydrogen concentration show that the B site peak first appears at a concentration $(H_2)_{1.30}$ [363].)

It might be tempting to identify the B site peaks in the neutron spectra with the Z or L sites in the domain model. Low temperature X-ray data from $C_{24}Rb(H_2)_2$, however, show three or four possible phases, each characterized by its own metal-metal distance: 50% of 6.18A [unchanged], 30% of 6.54A [$(\sqrt{7}\times\sqrt{7})R19.1°$], 20% of 5.98A [compressed incommensurate] and ≦5% of 4.92A [$(2\times2)R0°$] (Section 8.3). The $C_{24}Rb(H_2)_X$ tunnelling data also exhibit curious behaviour: at concentrations above $(H_2)_{0.8}$, the A site peak continues to grow in intensity along with the B site peak (Figs 7.3, 7.4). The 30% of 6.54A phase in the X-ray data would therefore seem to indicate the aggregation of $(\sqrt{7}\times\sqrt{7})R19.1°$ domains to form more Y sites (A sites). Since the overall metal to carbon ratio does not change, the large patches of expanded $(\sqrt{7}\times\sqrt{7})R19.1°$ structure would have to be balanced by patches of compressed phase. The 5.98A phase, then, is the obvious choice for the B sites. The 50% of 6.18A phase corresponds to patches of unchanged $C_{24}Rb$ with no absorbed hydrogen. (The diffraction patterns were recorded under excess hydrogen without measuring the exact quantity absorbed. The samples used in the neutron experiments often absorbed less than the stoichiometric quantity of hydrogen - see Section 7.1.) The disruption of the domain structure also accounts for the shift in the A site peaks at high hydrogen concentrations from 1.4 to 1.2 meV in the tunnelling spectra of $C_{24}Rb(H_2)_X$, and from 1.3 to 1.0 meV in $C_{24}Cs(H_2)_X$.

Various problems remain, however. The low energy beryllium filter peak at 13-18 meV in $C_{24}Cs(H_2)_X$ and 21 meV in $C_{24}Rb(H_2)_1$ (Figs 7.7, 7.10; Table 7.2) still has to be assigned properly, and there is as yet no explanation for the hot band at 2.15 meV in $C_{24}Cs(H_2)_1$ (Fig 7.5), and the peak at 2.05 meV in $C_{24}Rb(H_2)_{2.00}$ (Fig 7.3). The agreement between observed and calculated isotopic shifts, while good in places, leaves something to be desired overall (Tables 8.2, 8.3). It has also not yet

proved possible to calculate expected intensities for the librational transitions, to compare with the observed spectra. In spite of these problems, however, the model still manages to link much diverse data.

ACKNOWLEDGEMENTS

I should like to thank my supervisor, Prof. J.W. White most warmly for his continued enthusiasm and much-needed advice and help. I am also grateful to my co-supervisor and former tutor, Dr. R.K. Thomas for introducing me to neutron scattering, and for his encouragement and sense of humour.

I thank the members, both past and present of the PCL neutron scattering groups for their assistance, in particular Dr. Frans Trouw and Ian Jackson. Thanks are also extended to the staff of AERE Harwell and the ILL in Grenoble for their technical help, which enabled most of the experiments to go smoothly.

The financial support of a CASE joint studentship from the SERC and RSRE Malvern is gratefully acknowledged, as is the provision of a Visiting Fellowship from the Australian National University, Canberra.

Thanks are also due to those who helped in the production of this thesis: the computer staff in Canberra at the RSC who answered my many questions about the MASS11 word processing package, and Dr. D.J. Evans who gave me his Macintosh plotting program.

Finally, and most important, I should like to thank my parents for their continued encouragement and support, especially during the initial stages of writing up.

REFERENCES

1. C. Kittel, "Introduction to Solid State Physics", 5th Edn., Wiley (New York) 1976.
2. J.C.W. Chien, "Polyacetylene: Chemistry, Physics and Materials Science", UK Edn. Academic Press (London) 1984.
3. M.S. Whittingham, Prog. Solid State Chem. 12, 41 (1978)
4. F.R. Gamble and T.H. Geballe, "Treatise on Solid State Chemistry" Vol 3 pp. 89ff, ed. N.B. Hannay, Plenum (New York) 1976.
5. "Extended Linear Chain Compounds" Vols I-III, ed. J.S. Miller, Plenum (New York) 1982/3.
6. E. McRae, D. Billaud, J.F. Marêché, A. Hérold, Physica 99B, 489 (1980)
7. F.L. Vogel, R. Wachnik, L.A. Pendrys, "Physics of Intercalation Compounds" p. 288, ed. L. Pietrono and E. Tosati, Springer Series in Solid State Sciences 38, Springer-Verlag (Berlin) 1981.
8. D.G. Onn, G.M.T. Foley, J.E. Fischer, Phys. Rev. B19, 6474 (1979)
9. J.W. Milliken and J.E. Fischer, J. Chem. Phys. 78, 5800 (1983)
10. C. Zeller, A. Denenstein, G.M.T. Foley, Rev. Sci. Inst. 50, 602 (1979)
11. D.W. Murphy, F.J. DiSalvo, G.W. Hull Jr., J.V. Waszczak, Inorg. Chem. 15, 17 (1976)
12. A.H. Thompson, F.R. Gamble, R.F. Koehler Jr., Phys. Rev. B5, 2811 (1972)
13. F. Kanamaru, M. Shimada, M. Koizumi, M. Takano, T. Takada, J. Sol. State Chem. 7, 297 (1973)
14. M.B. Dines and M. Marrocco, ref 5 Vol II pp. 1ff
15. A.G. Freeman and J.P. Larkindale, Inorg. Nucl. Chem. Lett. 5, 937 (1969)
16. N. Bartlett, R.N. Biagoni, B.W. McQuillan, A.S. Robertson, A.C. Thompson, J. Chem. Soc. Chem. Comm. 1978, 200

17. L.D. Ellerbeck, H.R. Shanks, P.H. Sidles, G.C. Danielson, J. Chem. Phys. 35, 298 (1961)

18. G.B. Street, T.C. Clarke, M. Krounbi, K. Kanazawa, V. Lee, P. Pfluger, J.C. Scott, G. Weiser, Mol. Cryst. Liq. Cryst. 83, 253 (1982)

19. G. Tourillon and F. Garnier, J. Electroanal. Chem. 135, 173 (1982)

20. T.J. Marks and D.W. Kalina, ref 5 Vol I p. 197

21. G.B. Street and W.D. Gill in "Molecular Metals" p. 301, ed. W.E. Hatfield, Nato Conf. Series VI:1, Plenum (New York) 1979 and refs therein.

22. M. Murakami and S. Yoshimura, Mol. Cryst. Liq. Cryst. 118, 95 (1982)

23. J.M. Williams, A.J. Schulz, A.E. Underhill, K. Carneiro, ref 5 Vol I p. 73

24. J.H. O'Neill, A.E. Underhill, G.A. Toombs, Sol. State Commun. 29, 557 (1979)

25. J.H. Perlstein, Angew. Chem. Int. Edn. Engl. 16, 519 (1977)

26. J. Ferraris, D.O. Cowan, V. Walatka Jr., J.H. Perlstein, J. Am. Chem. Soc. 95, 948 (1973)

27. S.A. Solin, Adv. Chem. Phys. 49, 455 (1982)

28. Yu.N. Novikov and M.E. Vol'pin, Russ. Chem. Rev. 40, 733 (1971)

29. M.A.M. Boersma, Catal. Rev. 10, 243 (1974)

30. S. Basu, C. Zeller, P. Flanders, C.D. Fuerst, W.D. Johnson, J.E. Fischer, Mater. Sci. Eng. 38, 275 (1979)

31. S.Y. Leung, M.S. Dresselhaus, C. Underhill, T. Krapchev, G. Dresselhaus, B.J. Wuensch, Phys. Rev. B24, 3505 (1981)

32. D. Guérard, M. Chaabouni, P. Lagrange, M. el Makrini, A. Hérold, Carbon 18, 257 (1980)

33. M. el Makrini, D. Guerard, P. Lagrange, A. Hérold, Physica 99B, 481 (1980)

34. B.R. York, S.K. Hark, S.A. Solin, Phys. Rev. Lett. 50, 1470 (1983)

35. D. Neumann, H. Zabel, J.J. Rush, N. Berk, Phys. Rev. Lett. 53, 56 (1984)

36. S.A. Solin, P. Chow, H. Zabel, Phys. Rev. Lett. 53, 1927 (1984)

37. A. Hérold, D. Billaud, D. Guérard, P. Lagrange, M. el Makrini, Physica 105B, 253 (1981)

38. E. Stumpp, Physica 105B, 9 (1981)

39. F. Beck, H. Krohn, W. Kaiser, J. Electroanal. Chem. 165, 93 (1984)

40. M.J. Bottomley, G.S. Parry, A.R. Ubbelohde, D.A. Young, J. Chem. Soc. 1963, 5674

41. D. Billaud, A. Chenite, A. Metrot, Carbon 20, 493 (1982)

42. M.J. Moran, J.E. Fischer, W.R. Salaneck, J. Chem. Phys. 73, 629 (1980)

43. E.J. Samuelsson, R. Moret, R. Comès, H. Fuzellier, M. Klatt, M. Lelaurin, A. Hérold, Synth. Met. 10, 13 (1984)

44. D.E. Nixon and G.S. Parry J. Phys. C2, 1732 (1969)

45. W. Rüdorff and E. Schulz, Z. Anorg. Chem. 277, 156 (1954)

46. T.D. Trewern, M.Sc. Thesis, Oxford 1978.

47. P. Lagrange and A. Hérold, Carbon 16, 235 (1978)

48. T. Trewern, R.K. Thomas, G. Naylor, J.W. White, J. Chem. Soc. Faraday Trans. I 78, 2369 (1982)

49. A. Hérold, Bull. Chim. Soc. Fr. 1955, 999

50. D.E. Nixon and G.S. Parry J. Phys. D1, 291 (1968)

51. N. Caswell, Phys. Rev. B22, 6308 (1980)

52. D. Guérard and A. Hérold, Carbon 13, 337 (1975)

53. R. Nishitani, Y. Uno, H. Suematsu, Phys. Rev. B27, 6572 (1983)

54. S.E. Millman and G. Kirczenow, Phys. Rev. B26, 2310 (1982)

55. J.M. Thomas, G.R. Millward, R.F. Schlögl, H.P. Boehm, Mater. Res. Bull. 15, 671 (1980)

56. W. Metz and D. Hohlwein, Carbon 13, 87 (1975)

57. S.A. Safran, Phys. Rev. Lett. 44, 937 (1980)

58. N. Daumas and A. Hérold, Bull. Soc. Chim. Fr. 1971, 1598

59. G. Kirczenow, Phys. Rev. Lett. 55, 2810 (1985)

60. R.J. Nemanich, S.A. Solin, D. Guérard, Phys. Rev. B16, 2965 (1977)

61. S.B. DiCenzo, G.K. Wertheim, S. Basu, J.E. Fischer, Phys. Rev. B24, 2770 (1981)

62. S.B. DiCenzo, S. Basu, G.K. Wertheim, D.N.E. Buchanan, J.E. Fischer, Phys. Rev. B25, 620 (1982)

63. G.R. Hennig, J. Chem. Phys. 43, 1201 (1965)

64. G.P. Carver, Phys. Rev. B2, 2284 (1970)

65. J. Conard, H. Estrade, P. Lauginie, H. Fuzellier, G. Furdin, R. Vasse, Physica 99B, 521 (1980)

66. U. Mizutani, T. Kondow, T.B. Massalski, Phys. Rev. B17, 3165 (1978)

67. H. Kamimura, K. Nakoa, T. Ohno, T. Inoshita, Physica 99B, 401 (1980)

68. N. Wada and S.A. Solin, Physica 105B, 268 (1981)

69. M.E. Preil and J.E. Fischer, Phys. Rev. Lett. 52, 1141 (1984)

70. M. Posternak, A. Baldereschi, A.J. Freeman, E. Wimmer, M. Weinert, Phys. Rev. Lett. 50, 761 (1983)

71. Th. Fauster, F.J. Himpsel, J.E. Fischer, E.W. Plummer, Phys. Rev. Lett. 51, 430 (1983)

72. Nan Xian and Sohrab Rabii, Phys. Rev. Lett. 52, 2386 (1984)

73. D.P. DiVincenzo and E.J. Mele, Phys. Rev. Lett. 53, 52 (1984)

74. G. Kaindl, J. Feldhaus, U. Ladewig, K.H. Frank, Phys. Rev. Lett. 50, 123 (1983)

75. H. Zabel, Y.M. Jan, S.C. Moss, Physica 99B, 453 (1980)

76. H. Zabel, S.C. Moss, N. Caswell, S.A. Solin, Phys. Rev. Lett. 43, 2022 (1979)

77. M. Mori, S.C. Moss, Y.M. Jan, H. Zabel, Phys. Rev. B25, 1287 (1982)

78. Y. Yamada, I. Naiiki, T. Watanabe, T. Kiichi, H. Suematsu, Physica 105B, 277 (1981)

79. M. Suzuki, H. Ikeda, H. Suematsu, Y. Endoh, H. Shiba, Physica 105B, 280 (1981)

80. Roy Clarke, N. Caswell, S.A. Solin, P.M. Horn, Phys. Rev. Lett. 43, 2018 (1979)

81. Roy Clarke, N. Caswell, S.A. Solin, P.M. Horn, Physica 99B, 457 (1980)

82. M.J. Winokur, J.H. Rose, Roy Clarke, Phys. Rev. B25, 3703 (1982)

83. H. Zabel, A. Magerl, A.J. Dianoux, J.J. Rush, Phys. Rev. Lett. 50, 2094 (1983)

84. Roy Clarke, J.N. Gray, H. Homma, M.J. Winokur, Phys. Rev. Lett. 47, 1407 (1981)

85. N. Kambe, G. Dresselhaus, M.S. Dresselhaus, Phys. Rev. B21, 3491 (1980)

86. Per Bak, Rep. Prog. Phys. 45, 587 (1982)

87. G.S. Parry, Mat. Sci. Eng. 31, 99 (1977)

88. N. Kambe, H. Mazurek, M.S. Dresselhaus, G. Dresselhaus, Physica 105B, 272 (1981)

89. M. Suzuki and H. Suematsu, J. Phys. Soc. Japan 52, 2761 (1983)

90. M. Suzuki, Phys. Rev. B33, 1386 (1986)

91. H. Suematsu, M. Suzuki, H. Ikeda, J. Phys. Soc. Japan 49, 835 (1980)

92. M.J. Winokur and Roy Clarke, Phys. Rev. Lett. 54, 811 (1985)

93. G.S. Parry, Physica 105B, 261 (1981)

94. I. Naiki and Y. Yamada, J. Phys. Soc. Japan 51, 257 (1982)

95. Y. Yamada and I. Naiki, J. Phys. Soc. Japan 51, 2174 (1982)

96. G.R.S. Naylor and J.W. White, unpublished results.

97. J.B. Hastings, W.D. Ellenson, J.E. Fischer, Phys. Rev. Lett. 42, 1552 (1979)

98. G.S. Parry, D.E. Nixon, K.M. Lester, B.C. Levine, J. Phys. C2, 2156 (1969)

99. Roy Clarke, N. Caswell, S.A. Solin, Phys. Rev. Lett. 42, 61 (1979)

100. F.J. Salzano and S. Aronson, J. Inorg. Nucl. Chem. 26, 1456 (1964)

101. W.D. Ellenson, O. Semmingsen, D. Guérard, D.G. Onn, J.E. Fischer, Mater. Sci. Eng. 31, 137 (1977)

102. R. Nishitani, Y. Uno, H. Suematsu, Y. Fujii, T. Matsushita, Phys. Rev. Lett. 52, 1504 (1984)

103. C. Ayache, E. Bonjour, R. Lagnier, J.E. Fischer, Physica 99B, 547 (1980)

104. K.C. Woo, W.A. Kamitakahara, D.P. DiVincenzo, D.S. Robinson, H. Mertwoy, J.W. Milliken, J.E. Fischer, Phys. Rev. Lett. 50, 182 (1983)

105. Roy Clarke, N. Wada, S.A. Solin, Phys. Rev. Lett. 44, 1616 (1980)

106. N. Wada, Phys. Rev. B24, 1065 (1981)

107. C.D. Fuerst, J.E. Fischer, J.D. Axe, J.B. Hastings, D.B. McWhan, Phys. Rev. Lett. 50, 357 (1983)

108. D. Saehr and A. Hérold, Bull. Soc. Chim. Fr. 1965, 3130

109. M. Colin and A. Hérold, Bull. Soc. Chim. Fr. 1971, 1982

110. P. Lagrange, A. Métrot, A. Hérold, Comptes Rendus Acad. Sci. Paris, Série C 278, 701 (1974)

111. J. Conard, H. Estrade-Szwarckopf, P. Lauginie, M. el Makrini, P. Lagrange, D. Guérard, Physica 105B, 290 (1981)

112. T. Enoki, M. Sano, H. Inokuchi, J. Chem. Phys. 78, 2017 (1983)

113. J.-P. Beaufils, T. Trewern, R.K. Thomas, J.W. White, J. Chem. Soc. Faraday Trans. I 78, 2387 (1982)

114. T. Trewern, R.K. Thomas, J.W. White, J. Chem. Soc. Farad. Trans. I 78, 2399 (1982)

115. K. Watanabe, M. Soma, T. Onishi, K. Tamaru, Nature Phys. Sci. 233, 160 (1971)

116. K. Watanabe, T. Kondow, M. Soma, T. Onishi, K. Tamaru, Proc. Roy. Soc. (Lond) A333, 51 (1973)

117. D.A. Whan, Chem. Br. 17, 531 (1981)

118. T. Kondow, K. Ando, Y. Tomono in "Physics of Intercalation Compounds", ed. L. Pietronero and E. Tosati, Springer Series in Solid State Sciences 38, Springer-Verlag (Berlin) 1981.

119. L. Christiany, H. Fuzellier, P. Lagrange, A. Hérold, Physica 99B, 477 (1980)

120. H. Inokuchi, N. Wakayama, T. Kondow, Y. Mori, J. Chem. Phys. 46, 837 (1967)

121. I.F. Silvera, Rev. Mod. Phys. 52, 393 (1980)

122. K. Watanabe, T. Kondow, M. Soma, T. Onishi, K. Tamaru, J. Chem. Soc. Chem. Commun. 1972, 39

123. N. Okuyama, T. Takahasi, S. Kanayama, H. Yasanga, Physica 105B, 298 (1981)

124. L. Facchini, M.F. Quinton, A.P. Legrand, F. Bégun, R. Setton, Physica 99B, 525 (1980)

125. A.L. Blumenfeld, Yu.V. Isaev, Yu.N. Novikov, Synth. Met. 10, 193 (1985)

126. R. Diebold and A. Hérold, Bull. Soc. Chim. Fr. 1963, 578

127. Yu.N. Novikov and M.E. Vol'pin, Physica 105B, 471 (1981)

128. G.J. Schulz, Rev. Mod. Phys. 45, 423 (1973)

129. G. Herzberg, "Spectra of Diatomic Molecules", 2nd Edn. p. 221, Van Nostrand (New York) 1950.

130. T.E. Sharp, Atomic Data 2, 129 (1971)

131. H. Ehrhardt, L. Langhans, F. Linder, H.S. Taylor, Phys. Rev. 173, 222 (1968)

132. C.E. Kuyatt, J.A. Simpson, S.R. Mielczarek, J. Chem. Phys. 44, 437 (1966)

133. I. Eliezer, H.S. Taylor, J.K. Williams Jr., J. Chem. Phys. 47, 2165 (1967)

134. O. Nehmé, D.Phil. Thesis, Oxford 1984.

135. T. Ito, H. Shirakawa, S. Ikeda J. Polym. Sci. Polym. Chem. Ed. 12, 11(1974)

136. L.B. Luttinger, Chem. Ind.(Lond) 1960, 1135

137. L.B. Luttinger, J. Org. Chem. 27, 1591 (1962)

138. G. Lieser, G. Wegner, W. Müller, V. Enkelmann, Makromol. Chem. Rapid Commun. 1, 621 (1980)

139. A.J.N. Tansley, Chemistry Part II Thesis, Oxford 1984.

140. J.H. Edwards and W.J. Feast, Polymer 21, 595 (1980)

141. D.C. Bott, C.K. Chai, J. Edwards, W.J. Feast, R.H. Friend, M.E. Horton, J. Physique Colloque C3, 143 (1983)

142. H. Kahlert and G. Leising, Mol. Cryst. Liq. Cryst. 117, 1 (1985)

143. T. Ito, H.Shirakawa, S. Ikeda, J. Polym. Sci. Polym. Chem. Ed. 13, 1943 (1975)

144. A. Feldblum, A.J. Heeger, T.-C. Chung, A.G. MacDiarmid, J. Chem. Phys. 77, 5114 (1982)

145. H. Shirakawa and S. Ikeda, Polym. J. 2, 231 (1971)

146. C.R. Fincher Jr., C.-E. Chen, A.J. Heeger, A.G. MacDiarmid, Phys. Rev. Lett. 48, 100 (1982)

147. C.S. Yannoui and T.C. Clarke, Phys. Rev. Lett. 51, 1191 (1983)

148. A. Karpfen and R. Höller, Sol. Stat. Commun. 37, 179 (1982)

149. J.L. Brédas, R.R. Chance, R.H. Baughman, R. Silbey, J. Chem. Phys. 76, 3673 (1982)

150. R.H. Baughman, S.L. Hsu, G.P. Pez, A.J. Signorelli, J. Chem. Phys. 68, 5405 (1978)

151. C. Riekel, H.W. Hässlin, K. Menke, S. Roth, J. Chem. Phys. 77, 4254 (1982)

152. K. Soga, S. Kawakami, H. Shirakawa, S. Ikeda, Makromol. Chem. Rap. Commun. 1, 523 (1980)

153. K. Harper and P.G. James, Mol. Cryst. Liq. Cryst. 117, 55 (1985)

154. M.A. Druy, C.-H. Tsang, N. Brown, A.J. Heeger, A.G. MacDiarmid, J. Polym. Sci. Polym. Phys. Ed. 18, 429 (1980)

155. S.L. Hsu, A.J. Signorelli, G.P. Pez, R.H. Baughman, J. Chem. Phys. 69, 106 (1978)

156. H. Shirakawa, E.J. Louis, A.G. MacDiarmid, C.K. Chiang, A.J. Heeger, J. Chem. Soc. Chem. Comm. 1977, 578

157. C.K. Chiang, C.R. Fincher Jr., Y.W. Park, A.J. Heeger, H. Shirakawa, E.J. Louis, S.C. Gau, A.G. MacDiarmid, Phys. Rev. Lett. 39, 1098 (1977)

158. C.K. Chiang, M.A. Druy, S.C. Gau, A.J. Heeger, E.J. Louis, A.G. MacDiarmid, Y.W. Park, H. Shirakawa, J. Am. Chem. Soc. 100, 1013 (1978)

159. J.C.W. Chien, J.M. Warakomski, F.E. Karasz, W.L. Chia, C.P. Lillya, Phys. Rev. B28, 6937 (1983)

160. C.K. Chiang, S.C. Gau, C.R. Fincher Jr., Y.W. Park, A.G. MacDiarmid, A.J. Heeger, Appl. Phys. Lett. 33, 18 (1978)

161. A.J. Epstein, H. Rommelman, M.A. Druy, A.J. Heeger, A.G. MacDiarmid, Sol. Stat. Commun. 38, 683 (1981)

162. R.H. Baughman, N.S. Murthy, G.G. Miller, J. Chem. Phys. 79, 515 (1983)

163. B. Francois, M. Bernard, J.J. André, J. Chem. Phys. 75, 4142 (1981)

164. R.B. Kaner and A.G. MacDiarmid, J. Chem. Soc. Faraday Trans. I 80, 2109 (1984)

165. K. Kaneto, M. Maxfield, D.P. Nairns, A.G. MacDiarmid, A.J. Heeger, J. Chem. Soc. Faraday Trans. I 78, 3417 (1982)

166. G.C. Farrington, B. Scrosati, D. Frydrych, J. de Nuzzio, J. Electrochem. Soc. 131, 7 (1984)

167. J.H. Kaufman, J.W. Kaufer, A.J. Heeger, R. Kaner, A.G. MacDiarmid, Phys. Rev. B26, 2327 (1982)

168. A.G. MacDiarmid, R.J. Mammone, J.R. Krawczyk, S.J. Porter, Mol. Cryst. Liq. Cryst. 105, 89 (1984)

169. S. Lefrant, L.S. Lichtmann, H. Temkin, D.B. Fitchen, D.C. Miller, G.E. Whitwell II, J.B. Burlitch, Sol. Stat. Commun. 29, 191 (1979)

170. H. Shirakawa, T. Sasaki, S. Ikeda, Chem. Lett. Jpn. 1978, 1113

171. I. Harada, Y. Furukawa, M. Tasumi, H. Shirakawa, S. Ikeda, J. Chem. Phys. 73, 4746 (1980)

172. W.R. Salaneck, H.R. Thomas, R.W. Bigelow, C.B. Duke, E.W. Plummer, A.J. Heeger, A.G. MacDiarmid, J. Chem. Phys. 72, 3674 (1980)

173. T. Matsuyama, H. Sukai, H. Yamaoka, Y. Maeda, H. Shirakawa, Sol. Stat. Commun. 40, 563 (1981)

174. G. Kaindl, G. Wortmann, S. Roth, K. Menke, Sol. Stat. Commun. 41, 75 (1982)

175. W.R. Salaneck, H.R. Thomas, C.B. Duke, A. Paton, E.W. Plummer, A.J. Heeger, A.G. MacDiarmid, J. Chem. Phys. 71, 2044 (1979)

176. M. Monkenbusch, B.S. Morra, G. Wegner, Makromol. Chem. Rap. Commun. 3, 69 (1982)

177. J.C.W. Chien, F.E. Karasz, K. Shimamura, Macromolecules 15, 1012 (1982)

178. F.H. Herbstein, M. Kaftory, M. Kapon, W. Saenger, Z. Kristallogr. 154, 11 (1980)

179. P. Coppens in "Extended Linear Chain Compounds", ed. J.S. Miller, Vol I p. 335, Plenum (New York) 1982.

180. R.H. Baughman, N.S. Murthy, G.G. Miller, L.W. Shacklette, J. Chem. Phys. 79, 1065 (1983)

181. J.M. Pochan, H.W. Gibson, F.C. Bailey, J. Polym. Sci. Polym. Lett. Edn. 18, 447 (1980)

182. J.M. Pochan, D.F. Pochan, H. Rommelman, H.W. Gibson, Macromolecules 14, 110 (1981)

183. Y.W. Park, A.J. Heeger, M.A. Druy, A.G. MacDiarmid, J. Chem. Phys. 73, 946 (1980)

184. H.K. Müller, J. Hocker, K. Menke, K.Ehinger, S. Roth, Synth. Met. 10, 273 (1985)

185. W. Wanqun, R.J. Mammone, A.G. MacDiarmid, Synth. Met. 10, 235 (1985)

186. M.J. Kletter, T. Woerner, A. Pron, A.G. MacDiarmid, A.J. Heeger, Y.W. Park, J. Chem. Soc. Chem. Comm. 1980, 426

187. H. Shirakawa, A. Hamano, S. Kawakami, M. Sato, K. Soga, S. Ikeda, Z. Phys. Chem.(Frankfurt) 120, 235 (1980)

188. H. Shirakawa, M. Sato, A. Hamano, S. Kawakami, K. Soga, S. Ikeda, Macromolecules 13, 457 (1980)

189. K. Soga, S. Kawakami, H. Shirakawa, Makromol. Chem. Rapid Commun. 1, 643 (1980)

190. Y. Furukawa, T. Arakawa, H. Takeuchi, I. Harada, H. Shirakawa, J. Chem. Phys. 81, 2907 (1984)

191. I. Harada, Y. Furukawa, T. Arakawa, H. Takeuchi, H. Shirakawa, Mol. Cryst. Liq. Cryst. 117, 335 (1985)

192. J.C.W. Chien, P.C. Uden, Ju-Li Fan, J. Polym. Sci. Polym. Chem. Edn. 20, 2159 (1982)

193. A.F. Diaz and K.K. Kanazawa in "Extended Linear Chain Compounds", ed. J.S. Miller, Vol III p. 147, Plenum (New York) 1983.

194. A.F. Diaz, K.K. Kanazawa, G.P. Gardini, J. Chem. Soc. Chem. Comm. 1979, 635

195. K.K. Kanazawa, A.F. Diaz, R.H. Geiss, W.D. Gill, J.F. Kwak, J.A. Logan, J.F. Rabolt, G.B. Street, J. Chem. Soc. Chem. Comm. 1979, 854

196. A.F. Diaz, J.I. Castillo, J.A. Logan, W-Y. Lee, J. Electroanal. Chem. 129, 115 (1981)

197. M. Salmón, A.F. Diaz, J.A. Logan, M. Krounbi, J. Bargon, Mol. Cryst. Liq. Cryst. 83, 265 (1982)

198. "Vogel's Practical Organic Chemistry", 4th Edn., Revised B.S. Furness, A.J. Hannaford, V. Rogers, P.W.G. Smith, A.R. Tatchell, Longman (London) 1978.

199. R.A. Bull, Fu-Ren F. Fan, A.J. Bard, J. Electrochem. Soc. 129, 1009 (1982)

200. D.B. Fraser and H.D. Cook, J. Electrochem. Soc. 119, 1368 (1972)

201. J. Prejza, I. Lundström, T. Skotheim, J. Electrochem. Soc. 129, 1685 (1982)

202. R.N. Adams, "Electrochemistry at Solid Electrodes", Marcel Dekker (New York) 1969.

203. A.F. Diaz, Chemica Scripta 17, 145 (1981)

204. E.M. Genies, G. Bidan, A.F. Diaz, J. Electroanal. Chem. 149, 101 (1983)

205. A.F. Diaz and J.I. Castillo, J. Chem. Soc. Chem. Comm. 1980, 397

206. A.F. Diaz, K.K. Kanazawa, J.I. Castillo, J.A. Logan, Polym. Sci. Technol. 15, 149 (1981)

207. P. Pfluger and G.B. Street, J. Chem. Phys. 80, 544 (1984)

208. G.B. Street, R.H. Geiss, S.E. Lindsey, A. Nazzal, P. Pfluger in "Organic Molecular Aggregates: Electronic Excitation and Interaction Processes", p. 242, ed. P. Reineker, H. Haken, H.C. Wolf, Springer Series in Solid State Sciences 49, Springer-Verlag (Berlin) 1983.

209. K. Hyodo and A.G. MacDiarmid, Synth. Met. 11, 167 (1985)

210. R.A. Bull, F.-R. Fan, A.J. Bard, J. Electrochem. Soc. 130, 1636 (1983)

211. S. Asavapiriyanont, G.K. Chandler, G.A. Gunawardena, D. Pletcher, J. Electroanal. Chem. 177, 229 (1984)

212. M.M. Dall'Olio, G. Dascola, V. Varacca, V. Bocchi, Compt. Rendus C267, 433 (1968)

213. A. Angeli and L. Alessandri, Gazz. Chim. Ital. 46, 283 (1916)

214. G.P. Gardini, Adv. Heterocyclic Chem. 15, 67 (1973)

215. R.A. Jones and G.P. Bean, "The Chemistry of Pyrrole", Academic Press (New York) 1977

216. R.B. Bjorklund and I. Lundström, J. Electronic Mat. 13, 211 (1984)

217. M. Salmón, K.K. Kanazawa, A.F. Diaz, M. Krounbi, J. Polym. Sci. Polym. Lett. Edn. 20, 187 (1982)

218. G. Wegner, Mol. Cryst. Liq. Cryst. 106, 269 (1984)

219. R. Mc Neill, R. Siudak, J.H. Wardlow, D.E. Weiss, Aust. J. Chem. 16, 1056 (1963)

220. B.A. Bolto and D.E. Weiss, Aust. J. Chem. 16, 1076 (1963)

221. B.A. Bolto, R. Mc Neill, D.E. Weiss, Aust. J. Chem. 16, 1090 (1963)

222. P. Audebert and G. Bidan, Mol. Cryst. Liq. Cryst. 118, 187 (1985)

223. B.L. Funt and S.V. Lowen, Synth. Met. 11, 129 (1985)

224. A.F. Diaz, J. Crowley, J. Bargon, G.P. Gardini, J.B. Torrance, J. Electroanal. Chem. 121, 355 (1981)

225. A.F. Diaz, A. Martinez, K.K. Kanazawa, M. Salmón, J. Electroanal. Chem. 130, 181 (1981)

226. G.B. Street, S.E. Lindsey, A.J. Nazzal, K.J. Wynne, Mol. Cryst. Liq. Cryst. 118, 137 (1985)

227. O. Inganäs, R. Erlandsson, C. Nylander, I. Lundström, J. Phys. Chem. Solids 45, 427 (1984)

228. K. Yakushi, L.J. Lauchan, G.B. Street, J.L. Brédas, J. Chem. Phys. 81, 4133 (1984)

229. A. Nazzal and G.B. Street, J. Chem. Soc. Chem. Comm. 1984, 83

230. A.F. Diaz, J. Castillo, K.K. Kanazawa, J.A. Logan, M. Salmón, O. Fajardo, J. Electroanal. Chem. 133, 233 (1982)

231. M. Ogasawara, K. Funahashi, K. Iwata, Mol. Cryst. Liq. Cryst. 118, 159 (1985)

232. M. Tanaka, A. Watanabe, H. Fujimoto, J. Tanaka, Mol. Cryst. Liq. Cryst. 83, 277 (1982)

233. N. Mott, "Metal-Insulator Transitions", p. 35, Taylor & Francis (London) 1974.

234. R. Erlandsson, O. Inganäs, I. Lundström, W.R. Salaneck, Synth. Met. 10, 303 (1985)

235. P. Pfluger and G.B. Street, Polymer Preprints Am. Chem. Soc. 23, 122 (1982)

236. P. Pfluger, M. Krounbi, G.B. Street, G. Weiser J. Chem. Phys. 78, 3212 (1983)

237. G. Tourillon and F. Garnier J. Electrochem. Soc. 130, 2042 (1983)

238. R.H. Geiss, G.B. Street, W. Volksen, J. Economy, IBM J. Res. Dev. 27, 321 (1983)

239. R.J. Waltman, J. Bargon, A.F. Diaz, J. Phys. Chem. 87, 1459 (1983)

240. F. Garnier, G. Tourillon, M. Gazard, J.C. Dubois, J. Electroanal. Chem. 148, 299 (1983)

241. S.W. Feldberg, J. Am. Chem. Soc. 106, 4671 (1984)

242. J.H. Kaufman, K.K. Kanazawa, G.B. Street, Phys. Rev. Lett. 53, 2461 (1984)

243. E.M. Genies and J.M. Pernaut, Synth. Met. 10, 117 (1984)

244. K. Yakushi, L.J. Lauchlan, T.C. Clarke, G.B. Street, J. Chem. Phys. 79, 4774 (1983)

245. J.C. Scott, P. Pfluger, M.T. Krounbi, G.B. Street, Phys. Rev. B28, 2140 (1983)

246. R.A. Jones, Adv. Heterocyclic Chem. 11, 443 (1970)

247. P. Pfluger, U.M. Gubler, G.B. Street, Sol. Stat. Commun. 49, 911 (1984)

248. W.K. Ford, C.B. Duke, W.R. Salaneck, J. Chem. Phys. 77, 5030 (1982)

249. H. Münstedt, H. Naarmann, G. Köhler, Mol. Cryst. Liq. Cryst. 118, 129 (1985)

250. E.M. Genies and A.A. Syed, Synth. Met. 10, 21 (1984)

251. W. Wernet, M. Monkenbusch, G. Wegner, Makromol. Chem. Rap. Comm. 5, 157 (1984)

252. W. Wernet, M. Monkenbusch, G. Wegner, Mol. Cryst. Liq. Cryst. 118, 193 (1985)

253. G. Ahlgren and B. Krische, J. Chem. Soc. Chem. Comm. 1984, 946

254. B. Krische and G. Ahlgren, Mol. Cryst. Liq. Cryst. 121, 325 (1985)

255. O. Niwa and T. Tamamura, J. Chem. Soc. Chem. Comm. 1984, 817

256. M.-A. de Paoli, R.J. Waltman, A.F. Diaz, J. Bargon, J. Chem. Soc. Chem. Comm. 1984, 1015

257. R.A. Simon, A.J. Ricco, M.S. Wrighton, J. Am. Chem. Soc. 104, 2031 (1982)

258. M.V. Rosenthal, T.A. Skotheim, A. Melo, M.I. Florit, M. Salmón, J. Electroanal. Chem. 185, 297 (1985)

259. O. Inganäs and I. Lundström, J. Electrochem. Soc. 131, 1129 (1984)

260. K. Kaneto, K. Yoshino, Y. Inuishi, Jap. J. Appl. Phys. 22, L412 (1983)

261. M. Okano and A. Fujishima, J. Electroanal. Chem. 185, 393 (1985)

262. A. Hooper, "Electronically Conducting Polymers", Harwell Product Sheet, 1985.

263. A.J. Frank, Mol. Cryst. Liq. Cryst. 83, 341 (1982)

264. T. Skotheim, L.-G. Petersen, O. Inganäs, I. Lundström, J. Electrochem. Soc. 129, 1737 (1982)

265. T. Skotheim and I. Lundström, J. Electrochem. Soc 129, 894 (1982)

266. M. Kaneto, K. Okuzumi, A. Yamada, J. Electroanal. Chem. 183, 407 (1985)

267. W.H. Meyer, H. Kiess, B. Binggeli, E. Meier, G. Harbeke, Synth. Met. 10, 255 (1985)

268. I.B. Goldberg, H.R. Crowe, P.R. Newman, A.J. Heeger, A.G. MacDiarmid, J. Chem. Phys. 70, 1132 (1979)

269. B.R. Weinberger, E. Ehrenfreund, A. Pron, A.J. Heeger, A.G. MacDiarmid, J. Chem. Phys. 72, 4749 (1980)

270. W.P. Su, J.R. Schrieffer, A.J. Heeger, Phys. Rev. Lett. 42, 1698 (1979)

271. W.P. Su, J.R. Schrieffer, A.J. Heeger, Phys. Rev. B22, 2099 (1980)

272. M.J. Rice, Phys. Lett. 71A, 152 (1979)

273. M.J. Rice and E.J. Mele, Sol. Stat. Commum. 35, 487 (1980)

274. N. Suzuki, M. Ozaki, S. Etemad, A.J. Heeger, A.G. MacDiarmid, Phys. Rev. Lett. 45, 1209 (1981)

275. I. Harada, Y. Furukawa, M. Tasumi, H. Shirakawa, S. Ikeda, J. Chem. Phys. 73, 4746 (1980)

276. C.R. Fincher Jr., M. Ozaki, A.J. Heeger, A.G. MacDiarmid, Phys. Rev. B19, 4140 (1979)

277. J.D. Flood and A.J. Heeger, Phys. Rev. B28, 2356 (1983) and refs. therein.

278. J.C.W. Chien, F.E. Karasz, G.E. Wnek, Nature 285, 390 (1980)

279. D.K. Campbell and A.R. Bishop, Phys. Rev. B24, 4859 (1981)

280. J.L. Brédas, B. Thémans, J.G. Fripiat, J.M. André, R.R. Chance, Phys. Rev. B29, 6761 (1984)

281. J.L. Brédas, Mol. Cryst. Liq. Cryst. 118, 49 (1985)

282. J.C. Scott, J.L.Brédas, J.H. Kaufman, P. Pfluger, G.B. Street, K. Yakushi, Mol. Cryst. Liq. Cryst. 118, 163 (1985)

283. J.H. Kaufman, N. Colerani, J.C. Scott, G.B. Street, Phys. Rev. Lett. 53, 1005 (1984)

284. J.L. Brédas, J.C. Scott, K. Yakushi, G.B. Street, Phys. Rev. B30, 1023 (1984)

285. J.C.W. Chien and G.N. Babu, J. Chem. Phys. 82, 441 (1985)

286. J.C.W. Chien, G.N. Babu, J.A. Hirsch, Nature 314, 723 (1985)

287. R.H. Baughman, L.W. Shacklette, N.S. Murthy, G.G. Miller, R.S. Elsenbaumer, Mol. Cryst. Liq. Cryst. 118, 253 (1985)

288. S. Flandrois, C. Hauw, B. Francois, Mol. Cryst. Liq. Cryst. 117, 91 (1985)

289. L.W. Shacklette and J.E. Toth, Phys. Rev. B32, 5892 (1985)

290. G.E. Bacon, "Neutron Diffraction", 3rd Edn., OUP 1975.

291. G.E. Bacon, "Neutron Scattering in Chemistry", Butterworths (London) 1977.

292. "Chemical Appplications of Thermal Neutron Scattering", ed. B.T.M. Willis, OUP (London) 1973.

293. O. Nehmé, private communication.

294. "Neutron Cross-Sections", comp. D.J. Hughes, B.A. Magurno, M.K. Brussel, 2nd Edn., Brookhaven Nat. Lab. Rep. BNL 325 (1958)

295. A.F. Wells, "Structural Inorganic Chemistry", 4th Edn., OUP 1975.

296. J. Twisleton, D.Phil Thesis, Oxford 1973.

297. F.A. Cotton and G. Wilkinson, "Advanced Inorganic Chemistry", 4th Edn., Wiley (New York) 1980.

298. R.K. Wyckoff, "Crystal Structures", Vol I p. 351, 2nd Edn., Wiley (New York) 1963.

299. M. von Stackelberg, Z. Phys. Chem. B9, 437 (1930)

300. C.G. Windsor in "Chemical Applications of Thermal Neutron Scattering", p. 1, ed. B.T.M. Willis, OUP (London) 1973.

301. "International Tables for Crystallography", Vol A: Space Group Symmetry, ed. Theo Hahn, Reidel (Dordrecht) 1983.

302. B.T.M. Willis and A.W. Pryor, "Thermal Vibrations in Crystallography", p. 209, Cambridge 1975.

303. "Eight Peak Index of Mass Spectra", 2nd Edn., Mass Spectrometry Data Centre, AWRE Aldermaston 1974.

304. J.W. Otvos and D.P. Stevenson, J. Am. Chem. Soc. 78, 546 (1956)

305. L. Ebersen and H. Schäfer, Fortschritte der Chemischen Forschung 21 (1971)

306. R.W. Berry, P.M. Hall, M.T. Harris, "Thin Film Technology", Van Nostrand 1968.

307. S. Flandrois in "Physics of Intercalation Compounds", ed. L. Pietronero and E. Tosati, Springer Series in Solid State Sciences 38, Springer-Verlag (Berlin) 1981.

308. D. Billaud and D. Begin, Mol. Cryst. Liq. Cryst. 117, 103 (1985)

309. G. Wegner in "Molecular Metals", p. 209, ed. W.E. Hatfield, Nato Conf. Series VI:1, Plenum (New York) 1979.

310. A.C. Zemach and R.J. Glauber, Phys. Rev. 101, 118 (1956)

311. V.F. Sears, Canad. J. Phys. 44, 1279 (1966)

312. W. Press, "Single Particle Rotations in Molecular Crystals", Springer Tracts in Modern Physics 92, Springer-Verlag (Berlin) 1981.

313. H.F. King and D.F. Hornig, J. Chem. Phys. 44, 4520 (1966)

314. Many papers by D. Smith in J. Chem. Phys. 65 (1976) onwards.

315. V.F. Sears, Canad. J. Phys. 44, 1299 (1966)

316. A. Hüller, Sol. Stat. Commun. 23, 765 (1977)

317. J. Howard and T.C. Waddington in "Advances in Infra-red and Raman Spectroscopy", Vol 7, ed. R.J.H. Clark and R.E. Hester, Heyden 1980.

318. H. Jobic, R.E. Ghosh, A. Renouprez, J. Chem. Phys. 75, 4025 (1981)

319. J.R. Cockbain, R. Lechner, M. Owen, R.K. Thomas, J.W. White, Mol. Phys 45, 1035 (1982)

320. "Handbook of Mathematical Functions", ed. M. Abramowitz and I.A. Stegun, NBS 1964; Wiley 1972.

321. A. Griffin and H. Jobic, J. Chem. Phys. 75, 5940 (1981)

322. M. Warner, S.W. Lovesey, J. Smith, Z. Phys. B51, 109 (1983)

323. W. Langel, D.L. Price, R.O. Simmons, P.E. Sokol, Argonne Nat. Lab. Exp. Rep. No. 419 (1985)

324. H. Jobic, Chem. Phys. Lett. 106, 321 (1984)

325. P.H. Gamlen, N.F. Hall, A.D. Taylor, "Molecular Spectroscopy by the Beryllium Filter Machine", AERE Harwell Rep. RRL 74/693 (1974)

326. J.A. Young and J.U. Koppel, Phys. Rev. 135A, 603 (1964)

327. E.U. Condon and G.H. Shortley, "The Theory of Atomic Spectra", pp. 73ff, Cambridge 1935.

328. P.J. Wheatley, "The Chemical Consequences of Nuclear Spin", North Holland 1970.

329. P.A. Egelstaff, B.C. Haywood, F.J. Webb, A.H. Baston, Phys. Lett. 12, 188 (1964)

330. A.W. McReynolds and W.L. Whittemore in "Proc. Symp. Inelastic Scattering of Neutrons from Solids and Liquids" Vol I p. 263, International Atomic Energy Agency (Vienna) 1963.

331. W.L. Whittemore and H.R. Danner, ibid p. 273

332. A. Hüller and W. Press in "Proc. Symp. Neutron Inelastic Scattering 1977", Vol I p. 231, IAEA (Vienna) 1978.

333. R.K. Thomas, Chem. Soc. Spec. Per. Rep., Molecular Spectroscopy 6, 232, ed. R.F. Barrow, D.A. Long, J. Sheridan (1979)

334. A.J. Leadbetter and R.E. Lechner in "The Plastically Crystalline State" p. 285, ed. J.N. Sherwood, Wiley (Chichester) 1979.

335. E.O. Stejskal and H.S. Gutowsky, J. Chem. Phys. 28, 388 (1958)

336. S.J. Roser, D.Phil. Thesis, Oxford 1983.

337. M.P. Allen, private communication.

338. R.P. Bell, "The Tunnel Effect in Chemistry", Cambridge 1980.

339. G. Herzberg, "Infra-red and Raman Spectra", Van Nostrand (New York) 1945.

340. M. Batley, R.K. Thomas, A. Heidemann, A.H. Overs, J.W. White, Mol. Phys 34, 1771 (1977)

341. N. Boden in "The Plastically Crystalline State" p. 147, ed. J.N. Sherwood, Wiley (Chichester) 1979.

342. T.E. Stern, Proc. Roy. Soc. (Lond) A130, 551 (1930)

343. A.H. Wilson, Proc. Roy. Soc. (Lond) A117, 628 (1928)

344. D. Smith, J. Chem. Phys. 68, 3222 (1978)

345. P. Sauer, Z. Phys. 194, 360 (1966)

346. A.F. Devonshire, Proc. Roy. Soc. (Lond) A153, 601 (1936)

347. H. Michel and E. Lippert in "Organic Liquids", p. 293, ed. A.D. Buckingham, E. Lippert, S. Bratos, Wiley (Chichester) 1978.

348. W.E. Putnam, D.M. McEarchern Jr., J.E. Kilpatrick, J. Chem. Phys. 42, 749 (1965)

349. E.L. Pace and L.J. Noe, J. Chem. Phys. 49, 5317 (1968)

350. R.J. Jakobsen and Y. Mikawa, Appl. Optics 9, 17 (1970)

351. D.E. Milligan and M.E. Jacox, J. Mol. Spectros. 8, 126 (1962)

352. M.P. Marzocchi and S. Dobas, Spectrochim. Acta 30A, 1437 (1974)

353. A. Anderson, B. Andrews, B.H. Torrie, J. Mol. Struct. 79, 409 (1982)

354. M.P. Marzocchi and M.G. Migliorini, Spectrochim. Acta 29A, 1643 (1973)

355. T.B. Freedman and E.R. Nixon, Spectrochim. Acta 28A, 1375 (1972)

356. D. Leutloff, R. Wittenbeck, E. Knözinger, Proc. SPIE 289, 10 (1981)

357. P.H. Gamlen, D.Phil. Thesis, Oxford 1978

358. "Neutron Beam Instruments at Harwell", ed A.H. Baston and D.H.C. Harris, UKAEA 1978.

359. E.O. Stejskal, D.E. Woessner, T.C. Farrar, H.S. Gutowsky, J. Chem. Phys. 31, 55 (1959)

360. T.E. Bull and J.A. Jonas, J. Chem. Phys. 53, 3315 (1970)

361. J.P. Beaufils, T. Crowley, T. Rayment, R.K. Thomas, J.W. White, Mol. Phys. 44, 1257 (1981)

362. W.J. Stead, Chemistry Part II Thesis, Oxford 1982.

363. I.P. Jackson, D.Phil. Thesis, Oxford, in preparation.

364. D. Cebula, D.Phil. Thesis, Oxford 1979.

365. R. Scherm, A.J. Dianoux, C. Carlile, J. Suck, J.W. White, ILL Annual Report, 1979

366. J.W. White, private communication.

367. J. McCaffrey, Chemistry Part II Thesis, Oxford 1981.

368. M. Batley, S. Mraw, L.A.K. Staveley, A.H. Overs, R.K. Thomas, J.W. White, Mol. Phys. 45, 1015 (1982)

369. J.W. White, unpublished results.

370. C.W. Mowforth, D.Phil. Thesis, Oxford 1982.

371. F. Trouw, D.Phil. Thesis, Oxford 1986.

372. M. Gomez, S.P. Bowen, J.A. Krumhansl, Phys. Rev. 153, 1009 (1967)

373. H. Eyring, J. Walter, G.E. Kimball, "Quantum Chemistry", p. 77, Wiley (New York) 1944.

374. M.F. Manning, J. Chem. Phys. 3, 136 (1935)

375. F.B. van Swol, private communication.

376. NAG FORTRAN Library Routine E04FDF, Numerical Algorithms Group, Oxford.

377. L.A. Woodward, "Introduction to the Theory of Molecular Vibrations and Vibrational Spectroscopy", Oxford 1972.

378. E.B. Wilson, J.C. Decius, P.C. Cross, "Molecular Vibrations", McGraw-Hill (New York) 1955.

379. J.C. Decius and R.M. Hexter, "Molecular Vibrations in Crystals", McGraw-Hill (New York) 1977.